EFFECTS OF IONOSPHERIC CONDUCTANCE IN HIGH-LATITUDE PHENOMENA

A THESIS

SUBMITTED TO THE COLLEGE OF GRADUATE STUDIES AND RESEARCH

IN PARTIAL FULFILLMENT OF THE REQUIREMENTS

FOR THE DEGREE OF DOCTOR OF PHILOSOPHY

IN THE DEPARTMENT OF PHYSICS AND ENGINEERING PHYSICS

UNIVERSITY OF SASKATCHEWAN, SASKATOON

BY

LEONID BENKEVITCH

© Copyright Leonid Benkevitch, February 2006. All rights reserved.

PERMISSION TO USE

In presenting this thesis in partial fulfillment of the requirements for the degree of Doctor of Philosophy in the Department of Physics and Engineering Physics, University of Saskatchewan, I agree that the Libraries of this University may make it freely available for inspection. I further agree that permission for copying of this thesis in any manner, in whole or in part, for scholarly purposes may be granted by the professor or professors who supervised my thesis work or, in their absence, by the Head of the Department or the Dean of the College in which my thesis work was done. It is understood that any copying or publication or use of this thesis or parts thereof for financial gain shall not be allowed without my written permission. It is also understood that due recognition shall be given to me and to the University of Saskatchewan in any scholarly use which may be made of any material in my thesis.

Requests for permission to copy or to make other use of material in this thesis in whole or part should be addressed to:

Head of the Department of Physics and Engineering Physics
University of Saskatchewan
Saskatoon, Saskatchewan, S7N 5E2

ABSTRACT

In this thesis, the relationship between several high-latitude phenomena and the ionospheric conductance in both hemispheres is studied theoretically and experimentally.

Theoretically, the high-latitude electrodynamics is studied by considering currents in the magnetosphere-ionosphere system resulting from the ionospheric sheet current redistribution between the conjugate ionospheres. It is shown that strong flow between the conjugate ionospheres, the interhemispheric currents (IHC), can be set up if the conductance distribution is asymmetric in the conjugate ionospheric regions. Such conditions are typical for solstices owing to the differences in the solar illumination. Analytical and numerical modeling shows that IHCs can appear in the regions of strong conductance gradient, more specifically around the solar terminator line, and that the intensity of the IHCs can be comparable to the intensity of the well known Region 1/Region 2 currents. The effect of IHC excitation on observable magnetic perturbations on the ground is investigated. It is shown that in the vicinity of the solar terminator line, the pattern of magnetic perturbation can be such that an apparent equivalent current vortex can be detected. In addition, strong conductance gradients are shown to affect significantly the quality of the ionospheric plasma flow estimates from the ground-based magnetometer data.

Experimentally, the effect of the nightside ionospheric conductance on occurrence of substorms, global storm sudden commencement and radar auroras is investigated. To characterize substorm occurrence, new parameters, the derivatives of the classical AE and AO indices, are introduced. It is shown that the seasonal and diurnal variations of these parameters are controlled by the total nightside ionospheric conductance in the conjugate regions. The substorm onsets preferentially occur at low levels of the total conductance, which is consistent with the idea of the substorm triggering through the magnetosphere-ionosphere feedback instability. It is hypothesized that the total conductance affects the global storm onsets as well. To check this idea, the 33-year sudden storm commencement (SSC) data are considered. The semiannual, annual, semidiurnal, and diurnal variations in the SSC occurrence rate are found to be significant and these components exhibit a strong relationship with the total conductance of the high-latitude ionospheres. Finally, the SuperDARN midnight echo occurrence is shown to correlate, for some radars, with the total conductance minima and presumably with electric field maxima, which is consistent with general expectation that the F-region irregularities occur preferentially during times of enhanced electric fields. The gradients of the high-latitude conductance can also lead to significant errors in the plasma convection estimates from the ground-based magnetometers, and to investigate this effect a statistical assessment of the difference between the true plasma convection (SuperDARN) and the magnetometer-inferred equivalent convection direction is performed. The largest differences are found for the transition region between the dark and sunlit ionospheres and in the midnight sector where strong conductance gradients are expected due to particle precipitation. Consideration of regular conductance gradients due to solar illumination improves the agreement between the radar and magnetometer data. Finally, an attempt is made to

demonstrate the effects of conductance upon the properties of traveling convection vortices (TCVs). Joint SuperDARN and magnetometer data reveal that there is resemblance between the magnetometer and radar inferred TCV images on a scale of thousands of kilometers. However, on a smaller scale of hundreds of kilometers, significant differences are observed.

ACKNOWLEDGEMENTS

I would like to thank my supervisor Dr. A.V. Koustov for his permanent guidance and support in my studies.

I would also like to give thanks to many people in the SuperDARN group at the Institute of Space and Atmospheric Studies at Department of Physics and Engineering Physics, who have assisted me in the course of this work. I am grateful to Drs. G.J. Sofko, M. Watanabe, J.P. St. Maurice, G.C. Hussey, D. Andre, and K.A. McWilliams for many useful discussions. Dr. Sofko has a special talent in creation of inspiring atmosphere in our group. I would like to thank my fellow graduate students, J. Liang, D. Danskin, R. Makarevitch, T. Schelkova, R. Drayton, B. Schwab, and R. Gillies for stimulating discussions.

My special thanks are extended to the people who were involved in this research work. Dr. W. B. Lyatsky used to be my first teacher in Space Physics and my ex-supervisor. Many of the ideas in this thesis belong to him. In my work on Chapter 5, I fruitfully collaborated with Dr. G. Y. Khachikyan. And, of course, I appreciate very much our collaboration with my fellow graduate student, now Dr. Jun Liang. A considerable part of Chapter 5 is a result of our joint effort. He also used to be a congenial companion in our studentship in U of S.

I am grateful to many other people. I would like to thank Dr. A. Smolyakov from the Plasma Physics Group for his friendly assistance in clarifying theoretical questions; his graduate students, Yuriy Tyshetskiy, Dmitriy Sidorenko, and Ivan Khalzov for our discussions of various ideas. I am thankful to Dr. Manson for his encouraging comments to my PhD presentation. I very much appreciate general friendly support from Dr. S. Petelina. For the same reason I must mention our engineers, W. Marshall, H. Olivier, and Jan Wiid.

The Natural Sciences and Engineering Research Council of Canada (NSERC) provided financial assistance that enabled my studies with research grants to A.V. Koustov. I thank all the national funding agencies and individuals who make the SuperDARN convection measurements available.

In these studies I used ground-based magnetometer data from various institutions worldwide. I would like to acknowledge the following data providers: Geophysical Institute Magnetometer Array (GIMA) project, University of Alaska; CANOPUS project, Canadian Space Agency; the SAMNET team for magnetometer data, PPARC National Facility, Lancaster University; the institutes who maintain the IMAGE magnetometer array. I would like to personally appreciate the kind help in access to the data: Dr. M. J. Engebretson, Magnetometer Array for Cusp and Cleft Studies (MACCS) project, Augsburg College and Dr. Geoff Hughes, Boston University; Dr. J. Watermann, Greenland magnetometer chain project, Danish Meteorological Institute (DMI); Dr. R. Coles, Canadian Magnetic Observatory System (CANMOS) project, Geophysical Survey of Canada (GSC), Natural Resources Canada (NRCAN).

I would also like to thank my family and friends for their constant understanding and encouragement.

TABLE OF CONTENTS

LIST OF TABLES

LIST OF FIGURES

LIST OF ABBREVIATIONS

AACGM	Altitude-Adjusted Corrected Geomagnetic
ACF	Advanced Composition Explorer
ACF	Auto-Correlation Function
BPS	Boundary Plasma Sheet
CANMOS	CANadian Magnetic Observatory System
CANOPUS	Canadian Auroral Network for the OPEN Program Unified Study
CCW	Counter-ClockWise
CGM	Corrected GeoMagnetic
CPS	Central Plasma Sheet
CW	ClockWise
DMI	Danish Meteorological Institute
DMSP	Defense Meteorological Satellite Program
EISCAT	European Incoherent Scatter
EMR	Energy, Mines and Resources
FAC	Field-Aligned Current
FFT	Fast Fourier Transform
FoV	Field of View
GD	Gradient Drift
GDI	Gradient-Drift Instability
GGS	Global Geospace Science Initiative
GIMA	Geophysical Institute Magnetometer Array
GSC	Geological Survey of Canada
GSE	Geocentric Solar Ecliptic
GSM	Geocentric Solar Magnetospheric
HBL	High-Latitude Boundary Layer

HF	High Frequency
IHC	Interhemispheric Current
IMAGE	International Monitor for Auroral Geomagnetic Effects
IMF	Interplanetary Magnetic Field
INTERMAGNET	INTErnational Real-time MAGnetic observatory NETwork
ISTP	International Solar-Terrestrial Physics Program
LLBL	Low-Latitude Boundary Layer
LOS	line-of-sight
MACCS	Magnetometer Array for Cusp and Cleft Studies
MARIA	Magnetometer and Riometer Array
MEC	Magnetic Equivalent Convection
MFI	Magnetic Fields Investigation
MI	Magnetosphere-Ionospheric
MIE	Magnetic Impulse Event
MLAT	Magnetic Latitude
MLON	Magnetic Longitude
MLT	Magnetic Local Time
NASA	National AeroSpace Agency
NRCAN	Nature Resources Canada (see also EMR and CANMOS)
OCFLB	Open-Closed Field Line Boundary
PACE	Polar Anglo-American Conjugate Experiment
PDE	Partial Differential Equation
PMAF	Poleward-Moving Auroral Forms
PolarDARN	Polar Dual Auroral Radar Network
PPMP	Poleward-Propagating Magnetic Perturbations
PSBL	Plasma Sheet Boundary Layer
PWM	Pulse Width Modulation
R_E	Earth's Radius
RM	Russell-McPherron Model
SAMNET	Sub-Auroral Magnetometer NETwork
SCHA	Spherical Cap Harmonics Analysis

SDC	SuperDARN-observed Convection
SSC	Storm Sudden Commencement
STARE	Scandinavian Twin Auroral Radar Experiment
SuperDARN	Super Dual Auroral Radar Network
SW	Solar Wind
SWE	Solar Wind Experiment
SWEPAM	Solar Wind Electron-Proton-Alpha Monitor
TCV	Traveling Convection Vortex
UT	Universal Time
UV	Ultra Violet
VHF	Very High Frequency

CHAPTER 1

INTRODUCTION

This thesis presents investigation of several high-latitude ionospheric and magnetospheric phenomena that are ultimately related to the conductance of the earth's ionosphere. This introductory chapter describes fundamental concepts of the magnetosphere-ionospheric physics relevant to the undertaken research. We briefly consider the solar wind, formation of the earth's magnetosphere, plasma circulation within the magnetosphere and in the high-latitude ionosphere as well as magnetosphere-ionospheric coupling via the field-aligned currents. Finally, we state the goals of the thesis and provide a brief thesis outline.

1.1 Solar wind and formation of the earth's magnetosphere

The physical processes in the earth's space environment have intimate relation to the sun. In the solar system, the third planet from the sun is the earth, which rotates around the sun in an approximately circular orbit. The radius of this orbit is ~ 1.5×10^{11} m, which is used as a measurement unit named the *astronomical unit*, 1 AU. Despite this enormous distance, the earth is constantly exposed to two major inputs from the sun: the solar radiation and the solar plasma flow called the solar wind.

The solar wind is a result of the huge difference in gas pressure between the solar corona and the interstellar medium. This pressure difference permanently drives flux of the solar plasma outward into space. According to measurements near the orbit of the earth, the solar wind is basically composed of electrons and ionized hydrogen (protons) in approximately equal ratio

with ~ 5% (by number) admixture of ionized helium. The ions of heavier elements are also present but in much fewer numbers. The proton density is ~ 6 – 7 particles per cubic centimetre, and the proton and electron temperatures are of the order of 10^5 K. The solar wind flow velocity is about 450 m/s on average, but it can have values from 300 km/s to more than 2000 km/s.

The solar wind carries with it a weak magnetic field, the *interplanetary magnetic field* (IMF), amounting to a few nano-Teslas (nTs). The IMF is "frozen in" to the plasma so that it moves together with the plasma. The reason is the very high conductivity, which leads to a very strong induced current that opposes plasma flow across the magnetic field lines. The IMF can be described by the equation

$$\frac{\partial \mathbf{B}}{\partial t} = \nabla \times (\mathbf{v} \times \mathbf{B}) , \tag{1.1}$$

often referred to as the "frozen-in" law [*Sturrock*, 1994]. Although the solar wind flows out almost radially from the sun, the solar rotation (with the period of about 27 days) gives the magnetic field a spiral form.

The sun's own magnetic field (especially in the time between the solar maxima) has a dominant dipole structure, with the dipole axis approximately collinear with the sun's rotation axis so that the IMF direction can be either inward or outward with respect to the sun. However, satellite measurements have revealed the existence of several distinct sectors, the field being inward and outward in alternative sectors. This anomaly was resolved by offering a concept of the "ballerina model". According to this, the solar magnetic field has the form of extending loops connecting the north and south of the solar dipole. There also exists a heliospheric current sheet in or near the equatorial plane which effectively divides the outward field (above the plane) from the inward field (below it). If the solar magnetic dipole is tilted from the rotation axis, the current sheet will be tilted from the ecliptic plane and a spacecraft near the earth will observe a two-sector structure as the sun rotates. When more than two sectors are seen, it is thought that the current sheet has developed undulations as in the skirt of a pirouetting ballerina; hence is the concept name. A good review on the heliospheric current sheet is given in *Smith* [2001].

The earth's magnetic field has a multipole structure with predominant centred dipole, which gives about 90% contribution to the entire field. In mid 1996 the magnetic pole positions in the north and south polar regions were 79.3° North, 71.5° West and 79.3° South, 108.5° East,

respectively. The earth's dipole magnetic induction at the earth's surface is ~ 62,000 nT at the poles and ~ 31,000 nT at the equator.

As the solar wind approaches the earth, it interacts with the terrestrial magnetic field. Being unable to penetrate it, the solar wind nevertheless deforms it into a bell-shaped cavity. This cavity containing all of the earth's magnetic field is called the *magnetosphere*; its surface is known as the *magnetopause*. The resultant configuration of the magnetospheric field is very different from that of a dipole. On the upstream side, the magnetopause is observed at a geocentric distance of ~ 10 R_E (R_E being the earth's radius, ~6400 km). The radius of the magnetosphere dawn-dusk cross section is 12-13 R_E, rising to ~ 30 R_E farther down the tail. The entire length of the magnetospheric tail is estimated to be more than 220 R_E [*Kivelson and Russell*, 1996]. The closed field line portion of the magnetotail is usually less than about 60 R_E.

The solar wind velocity at the orbit of earth exceeds that of any waves that can propagate in it; the flow is said to be "supersonic" and "superAlfvén". For example, the Alfvén speed given by $v_A = B/\sqrt{\mu_0 \rho}$ (where B is the magnetic flux density and ρ is the particle mass density) is ~ 50 km/s and the Alfvén Mach number is 8 for a solar wind speed of 400 km/s. For this reason, a shock wave, *the bow shock,* is formed in front of the magnetosphere. The bow shock is a discontinuity in the solar wind medium; after it the solar wind plasma slows down to ~250 km/s (the speed depends on location/distance from the subsolar point) and its kinetic energy is dissipated as thermal energy (due to turbulent processes) so that the plasma temperature is increased to 5×10^6 K. The region between the bow shock and the magnetopause is named the *magnetosheath*. The thickness of the magnetosheath is 2-3 R_E upstream. Fig. 1.1 shows typical scales of various regions formed when the solar wind interacts with the geomagnetic field.

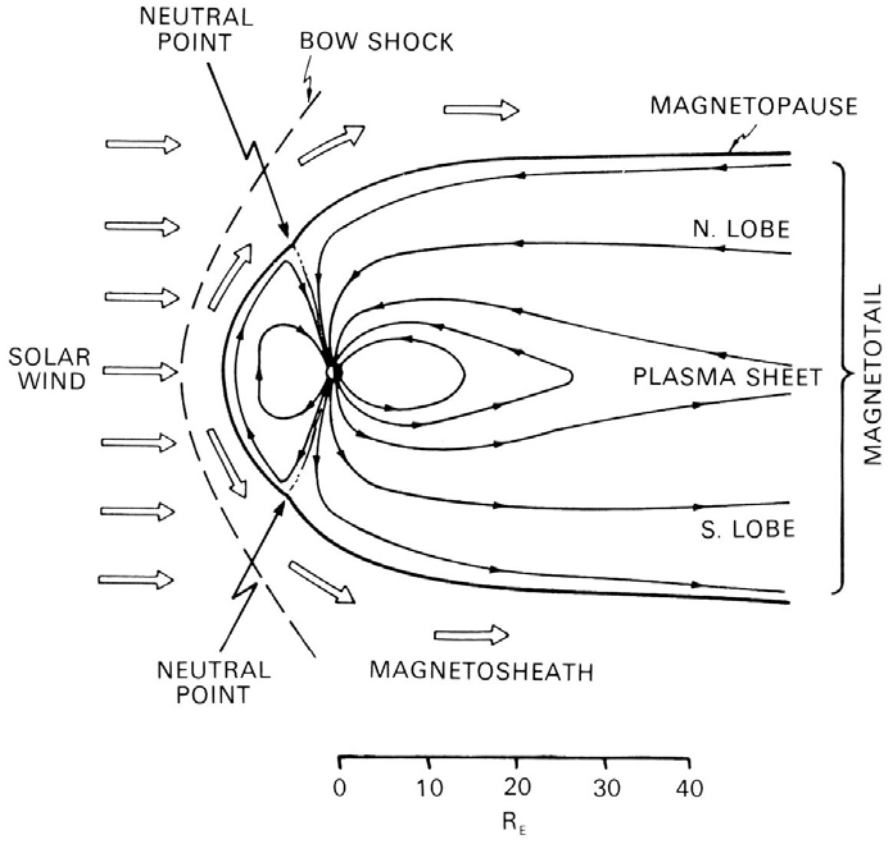

Figure 1.1. Cross-section of the geomagnetic cavity and plasma flow showing the magnetopause and the bow shock. (After *Vasyliunas* [1983], p. 243)

1.2 Magnetospheric regions

The magnetosphere has a complex structure. The particle motion there is determined by the earth's magnetic field. Due to the particle and energy input from the solar wind and the sun's radiation, the magnetosphere contains particle populations with a vast spectrum of energies. The charged and neutral particles of different energies behave differently in the geometry of magnetosphere, which leads to formation of special magnetospheric regions and the magnetospheric current systems.

The magnetosphere can be divided into two large regions, one containing closed field lines and the other containing open field lines. Each of the regions has its ionospheric mapping. The ionospheric footprints of the open-field-line regions are called *polar caps*. The closed-line region extends to relatively low magnetic latitudes, starting from ~ ±75° equatorward, whereas the open-line region maps to the latitudes approximately above ~ ±75°. The latitude of this

OCFLB (open-closed field line boundary) is not constant and can change dramatically during the magnetosphere dynamic evolutions.

According to the contemporary point of view, the magnetosphere is not completely closed with respect to the solar wind magnetic field, but there is an ongoing input of magnetic field lines from the magnetospheric subsolar side and there is also ongoing output of the terrestrial field lines from the magnetotail into space. These two phenomena occur via the *reconnection* or *merging* process.

A schematic 3-dimensional representation of the magnetosphere is given in Figure 1.2. Such magnetospheric regions as the *plasmasphere* and *central plasma sheet* (CPS) are closed-line regions while *tail lobes* and *mantle* are open-line regions. The *boundary plasma sheet* (BPS) and *low latitude boundary layer* (LLBL; not shown in the Fig.) are transition regions because they contain the field lines of both types.

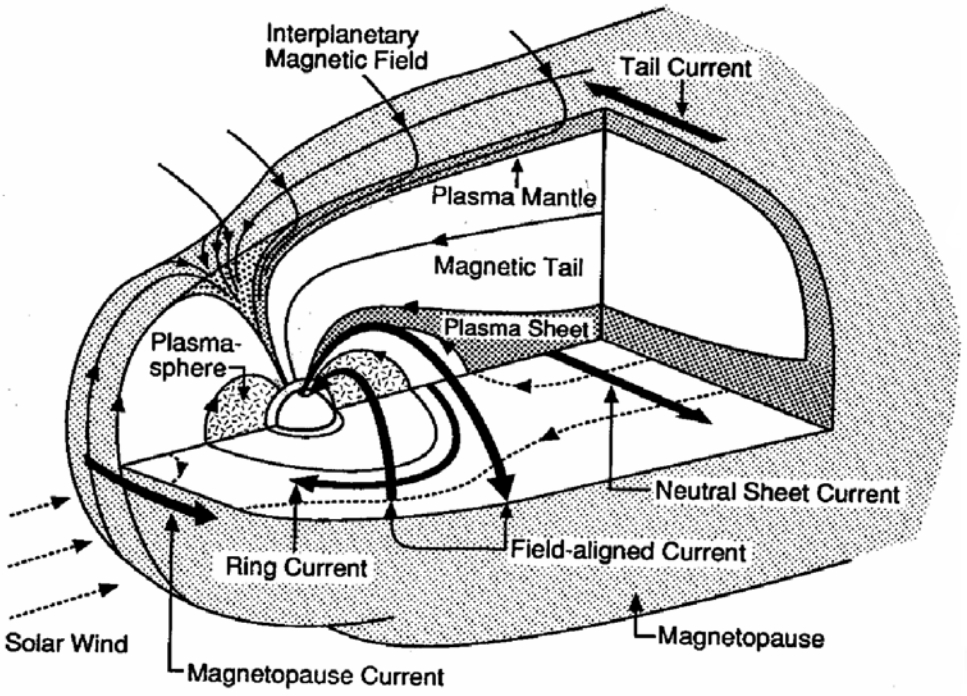

Figure 1.2. Three-dimensional cutaway view of the magnetosphere showing currents, fields, and plasma regions. (From *Kivelson and Russell* [1995])

The mantle contains the most recently reconnected field lines that are dragged tailward by the solar wind. The region of dayside reconnection (and its ionospheric projection) is called the *cusp*. It projects to a short (±2 hours around noon MLT) strip at ±(76°–77°) of magnetic latitude.

This ionospheric mapping of the magnetospheric regions was originally given by *Vasyliunas* [1979, see Fig. 2]. *Newell and Meng* [1994] later conducted a thorough study and subsequent region mapping with the use of DMSP satellite data.

The magnetospheric regions can be briefly characterized as follows. The plasmasphere is the innermost part. The equatorial projection of the plasmapause (i.e. its outer boundary) is typically found near 3-6 R_E. The *inner plasmasphere* is a region inside of the plasmasphere that corotates with the earth. Electron density in the plasmasphere is of the order of ~ 100 cm^{-3} and falls off by 2-3 orders of magnitude across the plasmapause. The plasmasphere contains the major part of the trapped and bouncing charged particles forming the Van Allen radiation belts.

The central plasma sheet or CPS extends tailward for several tens of R_E in the form of a slab. The CPS contains the so-called *cross-tail current sheet*. Electron density in the CPS is ~ 0.1 - 1 cm^{-3}. It contains hot particles with the energies up to tens of keV. The ionospheric projection of the CPS is observed at ~ 65° – 75° of geomagnetic latitude.

The boundary plasma sheet, BPS, is the region between the CPS and mantle. In the BPS the tail reconnection occurs, so the open field lines of the outer BPS become closed and move toward the CPS. Sharp ion streams are characteristic of the BPS, average energy being a few keV. The BPS ionospheric projection is observed at ~ 67° – 77° of geomagnetic latitude.

The northern tail lobe and the southern tail lobe are the regions adjacent to the CPS, containing open field lines in the earthward and tailward directions, respectively. Plasma densities are low (< 0.1 cm^{-3}) in this region, and the ion and electron energy spectra are very soft, typically ~ 20 eV.

The mantle is a boundary layer several thousand kilometers thick just inside the magnetopause. It contains particles of low densities, less than 0.1 cm^{-3}, with energies up to hundreds of eV. Its ionospheric projection on the dayside is between 77° and 81°. The mantle is a region of newly-reconnected open flux lines. Its lines of force are dragged tailward by the solar wind flux lines.

The low-latitude boundary layer, LLBL, is a relatively thin (0.5 – 1 R_E) boundary layer located earthward of the magnetopause. Its ionospheric projection is a thin semicircle called the *cleft*, observed at about 77° between ~ 10 and 14 MLT. Its characteristic electron densities are ~ 0.5 - 10 cm^{-3} with the energies from less than 100 eV to 1000-2000 eV. The LLBL is a current-generator region because it maintains the process of charge separation inside of itself.

The magnetosphere also includes several current systems, which are schematically shown in Fig. 1.2 along with the magnetospheric regions. Across the magnetopause the magnetic field undergoes a sharp change, therefore according to Ampere's law it contains a sheet of electrical current named *the magnetopause current sheet*, which covers the dayside magnetopause. The *tail current sheet* covers the magnetotail. Also, the *cross-tail current sheet* divides the magnetotail at the magnetic equatorial plane into two lobes with oppositely directed magnetic field lines. Thus, the magnetotail cross-section reveals two vortex current cells with opposite senses. The westward *ring current* flows inside the CPS around the earth. Its sense is opposite to that of the magnetopause current. Some magnetospheric currents lead to field-aligned currents (FACs), which close in the earth's ionosphere through the Birkeland field-aligned currents that have their ionospheric footprints at ~65 - 75° of geomagnetic latitude. These current systems are considered in more detail in Sections 1.4 and 1.6.

1.3 Plasma convection

There are two possible solar wind energy transfer mechanisms pertaining to the generation of convection in the magnetosphere: the *viscous interaction* and *reconnection*.

In the viscous interaction theory (first introduced by *Axford and Hines* [1961]) it is assumed that the solar wind transfers momentum and energy into the magnetosphere in a process similar to that within a falling raindrop, in which the fluid is swept back at the surface and returned inside the drop. Fig. 1.3a illustrates the viscous process. There are problems about this theory because the solar wind is too tenuous to cause a sufficient collisional force: the mean free path is ~10^9 km and collisions are virtually absent.

According to the other theory proposed by *Dungey* [1961], the IMF lines reconnect with the terrestrial field lines at the subsolar region of the magnetopause, making "open flux tubes", Fig. 1.3b. The open tubes are then carried downstream by the magnetosheath flow and stretched into a long cylindrical tail. Eventually, the open tubes close again by reconnection in the centre of the tail (presumably, in the BPS region). As a result of reconnection, some of the open field lines are convected back to regular IMF lines in the solar wind (line A in Fig. 1.3b). The other portion of the reconnected lines becomes closed terrestrial field lines, which return to the CPS. These field lines shrink as they move sunward along the magnetosphere flanks and eventually get into the dayside subsolar part of the magnetosphere, where they become subject to the dayside

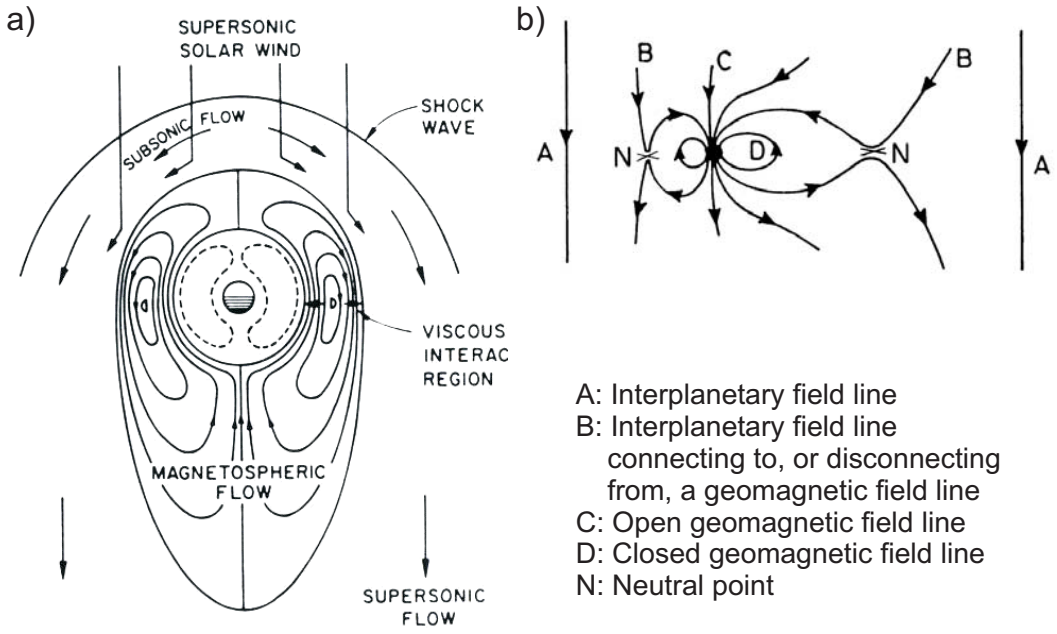

Figure 1.3. Two models of the solar wind − terrestrial magnetic field interaction: (a) viscous processes (From *Kelley* [1989]) and (b) magnetic reconnection. (After *C. T. Russell* [1972] and *R. H. Levy* [1964])

reconnection again. Therefore the reconnection process excites the cyclical flow in the interior called *plasma convection*. The overall flow cycle is ~ 12 hours, of which field lines remain open mapping into the tail lobe for ~ 4 hours and then take ~ 8 hours to convect back from the tail to the dayside. Under the solar wind conditions favourable for the reconnection the ionospheric image of the magnetospheric flow consists of two convection cells with antisunward flow of open field lines over the polar cap and a return sunward flow of closed field lines at lower latitudes.

This convective flow is associated with a large-scale electric field in the plasma directed from dawn to dusk. The voltage between the foci of the cells is of order 100 kV and is associated with the ionospheric flows of several hundreds m/s. Generally, the drift velocity **v**, electric field **E**, and magnetic field **B** are associated in the equation

$$\mathbf{v} = \frac{1}{B^2}\mathbf{E} \times \mathbf{B}\,. \tag{1.2}$$

This equation describes the Hall drift of charged particles in the direction perpendicular to those of the electric and magnetic fields. However, the described processes occur under the condition of stable negative IMF B_Z only. The charged particle populations, travelling with the reconnecting IMF field lines, penetrate into the magnetosphere, carrying the momentum and

energy from the solar wind. Hence the term "open magnetosphere" describing its state under negative IMF B_Z.

During the periods of positive IMF B_Z, the reconnection process at the subsolar region of the magnetopause ceases, and so does the input of particles, energy, and momentum. Therefore this state is referred to as closed magnetosphere. The IMF field lines do not merge with those of magnetopause, but slide down the magnetotail with solar wind without interaction with the earth's magnetosphere. The magnetosphere-ionospheric system also undergoes a number of changes, among which is vanishing of the Region 1 Birkeland field-aligned currents (to be considered later).

1.4 Magnetospheric current systems

The combination of constant solar wind plasma flow and the earth's magnetic field creates several current systems. Fig. 1.4 schematically sketches them, relative to the earth size. These systems can be identified as (a) the magnetopause current, (b) the ring current, (c) the tail current. Not shown in Fig. 1.4 are the magnetosphere-ionospheric current systems, involving the Birkeland field-aligned currents.

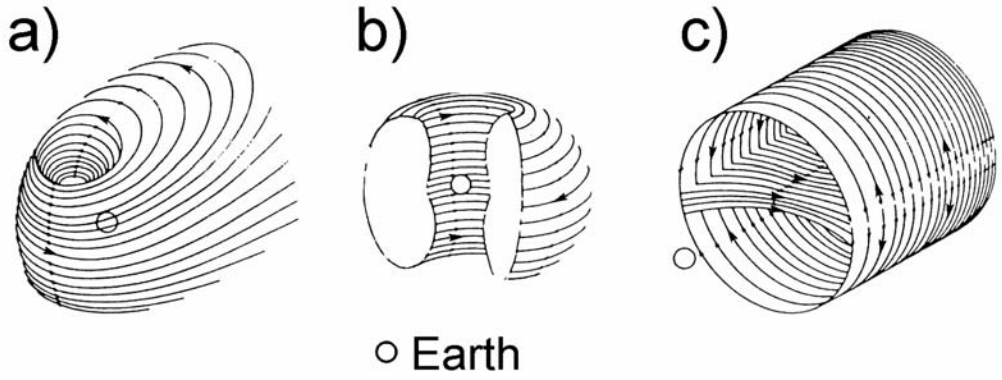

Figure 1.4. Magnetospheric current systems: a) magnetopause current; b) ring current; c) tail current. The small circle stands for the earth ionosphere. (After W. P. Olsen, *Adv. Space Res.*, 2, 13, 1987)

1.4.1 The magnetopause current

The magnetopause current, Fig. 1.4a, flows along the surface of the magnetopause so that its magnetic effect cancels the geomagnetic field outside the magnetosphere. In the inner magnetosphere, where the magnetic field is almost dipolar, the contribution from the

magnetopause current to the total field is small compared to that from the earth's internal dipole. Fig. 1.5 explains emergence of the magnetopause current. For simplicity we assume that the SW plasma is unmagnetized. Generally speaking, a flow of any high conducting fluid leads to emerging a magnetopause in front of a magnet fixed in the fluid and not moving with it. The schematic shows a rectangular fragment of cross-section of the magnetosphere in the *XZ* plane in the GSM coordinate system (for the GSM system see e.g. *Kivelson and Russell* [1996]). The magnetopause is shown as a thick grey vertical line. The subsolar area on the left contains no terrestrial magnetic field, whereas the magnetosphere on the right is filled with the earth's magnetic field lines. According to Maxwell's equation (with the term $\varepsilon_0\mu_0\partial\mathbf{E}/\partial t$ zero due to assumed stationary conditions):

$$\nabla\times\mathbf{B}=\mu_0\mathbf{j}. \tag{1.3}$$

Curl **B** can be estimated by replacing it with the circulation integral of **B** along a thin contour confining a segment of the magnetopause cross-section. The contour is shown as a dashed rectangular path in Fig. 1.5.

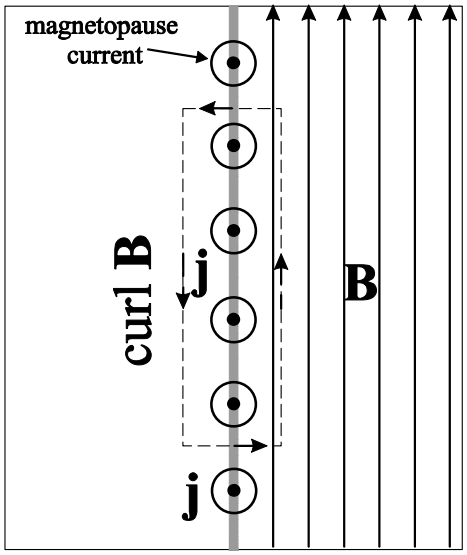

Figure 1.5. Formation of the magnetopause current **j**. The surface of magnetopause separates the interplanetary medium (on the left) and the earth's magnetic field **B** (on the right), therefore the magnetopause must contain the sheet current **j**.

The arrows specify the positive travel direction. Obviously, only the magnetic field inside the magnetosphere (on the right) contributes to the **B** circulation integral, because the horizontal segments of the contour and its subsolar segment have zero **B** projections. Hence the **B**

circulation and the curl **B** reach maximum at the surface of the magnetopause, and by equation (1.3) the surface must contain the current **j** with the streamlines perpendicular to the **B** lines of force, as shown by the circles with dots in Figure 1.5. The magnetopause current has counterclockwise sense of rotation if viewed from above the North Pole. It makes up two "funnels" near the dipole poles. These funnels indicate the positions of the earth's geomagnetic field cusps.

1.4.2 The tail current

The earth's magnetic field due to the solar wind action is extended far away from the sun (> 220 R_E), forming a tube-like tail. The northern half of this tail confines the magnetic lines of force directed towards the earth, and the southern half confines the lines directed outwards. Due to the properties of magnetic field, described in Section 1.4.1, such confined configuration only exists if there are surface currents. The latter are called tail currents. They form two solenoids, coalescent with the magnetopause and

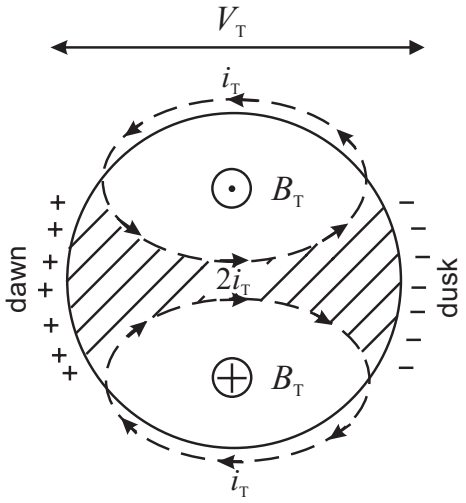

Figure 1.6. Tail current as seen from the earth (in antisunward direction). (After L. Svalgaard, *NASA Report SP-366*, 1975)

cusp currents, bounding the northern and southern magnetic flux tubes as shown in Fig. 1.6. The schematics in Fig. 1.6 facilitates approximate calculations of the tail current sheet density i_T (A/m) from the magnetic flux density B_T inside of the tail. These quantities are related as $B_T = \mu_0 i_T$. Note that the tail current in the CPS and BPS regions is $2i_T$. Since $B_T \approx 20\,nT$,

$i_T \approx 1.6 \times 10^{-2}$ A m^{-1}, the current density is $\sim 3.2 \times 10^{-2}$ A m^{-1} in the plasma sheet. With the reasonable tail length the total tail current is ~ 10^8 A.

1.4.3 The ring current

The ring current flows around the earth clockwise (from the viewpoint over the North Pole), as shown in Fig. 1.4b. Its magnetic field is such that it acts to oppose the earth's magnetic field. The action of the ring current reveals itself during the global magnetic storms that are characterized by sudden increase in the ground-level magnetic field (due to the initial compression of the magnetosphere from increased solar wind pressure) and its subsequent decompression lasting from several hours to days. For a loop current I generating the field variation ΔB under the assumption that the mirror currents are induced in the conductive ground, the ring current and its magnetic effect are approximately related as $\Delta B \approx Ir$ [*Hargreaves*, 1992]. A moderate magnetic storm may cause a depression of ~30 nT at the surface, therefore the ring current intensification should be 10^6 A at the geocentric distance $r \approx 4.5 R_E$.

The ring current consists of the trapped particles drifting at distances of (4-6) R_E from the earth's surface, between the inner edge of the CPS and the outer edge of the trapping zone. In the course of magnetospheric convection, the particles are accelerated earthward from the tail reconnection point. However, as they enter the regions of stronger magnetic field, they are trapped and join the ring current particle population. The total ring current is proportional to the total energy of the particles.

1.5 Ionosphere

The ionised part of the atmosphere is called the ionosphere. Actually, the ionosphere is the innermost shell of the magnetosphere, spanning the altitude range from ~ 60 up to ~ 500 km. The sources of ionisation include solar radiation and energetic particle precipitation.

1.5.1 General properties

A typical vertical ionospheric structure determined by the electron density is shown in Fig. 1.7. The ionospheric regions are designated D, E, F1 and F2. Table 1.1 shows the charged particle densities and collision frequencies for all the ionospheric regions. The lowest D region

spreads from ~ 60 to ~90 km of altitude. The E region occupies the altitudes from ~ 90 to ~ 160 km. The F region is located from ~ 160 up to 300 and even more km. The F region itself is subdivided into the F1 region, from 160 to 180 km and the F2 region, above 180 km. The D and F1 regions vanish at night, and the E region weakens, whereas the F2 region persists at reduced density.

This layered structure reflects differences in the ionospheric plasma behaviour due to the ion- and electron-neutral collision rates. In the densest D region, both electrons and ions are predominantly collisionally controlled and their motion is not affected by the earth's magnetic field. In the rarer plasma of the E region, the motion of electrons is controlled by the geomagnetic field (they are magnetised) since the electron-neutral collision rates are not large. The ions are still collisionally-controlled and their Hall-drift motion is negligible. The relative electron-ion drift in the E region causes the electric currents.

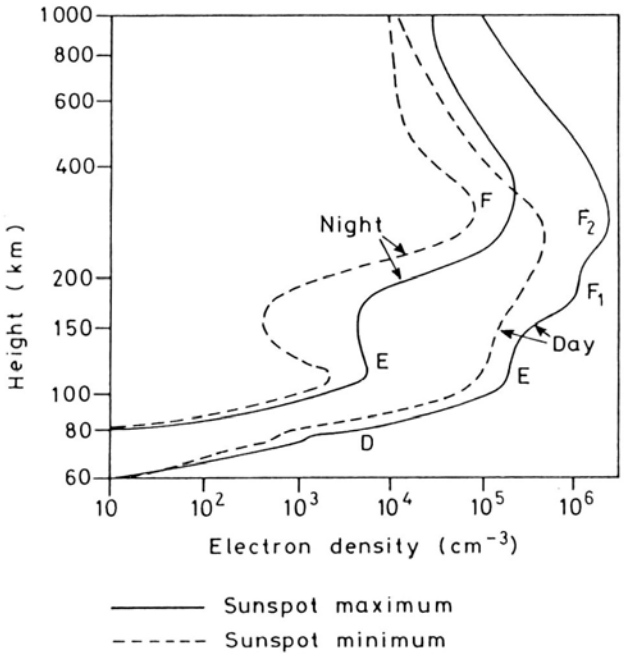

Figure 1.7. Vertical profiles of electron number density in the mid-latitude ionosphere. (After *W. Swider*, Wallchart Aerospace Environment, *US Air Force Geophysics Laboratory*)

In the F region both electrons and ions are magnetised. Since the $\mathbf{E}\times\mathbf{B}$-drift velocity has the same magnitude and direction for charges of the opposite signs, the plasma convection in the F region is not accompanied with the Hall current (though there is still very small Pedersen current that is often neglected).

Table 1.1. Typical ionospheric parameters for different regions [*Kivelson et al.*, 1996].

Region	Altitude, km	Electron density, cm^{-3}	Ion-neutral collision frequency ν_i, s^{-1}	Electron-neutral collision frequency ν_e, s^{-1}
D	60 - 90	10^2-10^4	$>3\times10^3$	$>10^5$
E	90 – 160	10^5	1.5×10^3	5×10^4
F	160 - 300	10^5-10^6	1	10^3

The current flow in the earth's space environment obeys the law of continuity and Ohm's law. The ionosphere-magnetospheric medium is strongly anisotropic in the sense of freedom of motion for electric charges. The frozen-in equation (1.1) implies that the motion of charged particles along the magnetic lines of force is hampered by collisions only, while their motion across the lines obeys the drift law (1.2), besides the collisions, and therefore the horizontal motion is much more restricted. This difference in electrical properties is expressed as a difference in the conductivities along and across the magnetic field lines, which shall be discussed in detail below.

The conductive anisotropy of the ionosphere suggests a natural decomposition of the three-dimensional currents $\mathbf{j}$ into one-dimensional currents $j_\parallel$ flowing along the (essentially vertical) geomagnetic field lines and two-dimensional ionospheric sheet currents $\mathbf{J}$ flowing across the field lines. The currents along the magnetic field $j_\parallel$ are called *field-aligned currents* (FACs). This decomposition simplifies the calculations related to the magnetosphere-ionospheric coupling and allows considering 2-D height-integrated conductances instead of 3-D ones.

1.5.2 Relationship between ionospheric vertical and horizontal currents

Consider a thin cylindrical ionospheric flux tube of volume *V*, whose axis is aligned with the geomagnetic field and whose top and bottom plates are at the altitudes h_1 and h_2 and have the areas *a*, as schematically shown in Fig. 1.8. Note that it is possible to assume the top and bottom areas are equal because in a dipole approximation a flux tube cross-section changes from $h_1 \approx 100$ km to $h_2 \approx 300$ km by less than 10 per cent. Assume that the FACs $j_\parallel$ and the sheet currents $\mathbf{J}$ are associated with the cylinder, as shown in Fig. 1.8.

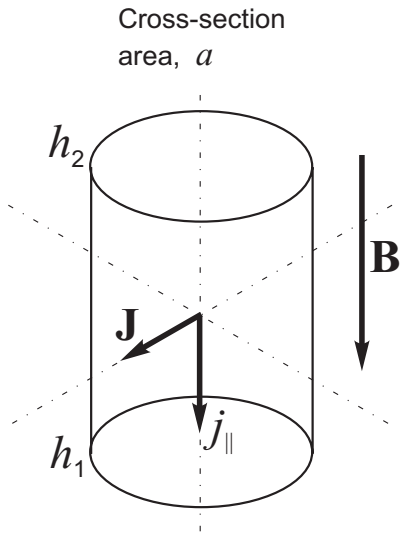

Figure 1.8. Decomposition of the ionospheric currents into the horizontal component **J** and the incident, field-aligned component $\mathbf{j}_{||}$, in a thin cylindrical flux tube located between the heights h_1 and h_2, having the cross-sectional area a. **B** is the geomagnetic field.

We start from the current continuity equation

$$\frac{\partial \rho}{\partial t} + \nabla \cdot \mathbf{j} = 0\,, \tag{1.4}$$

where **j** is the current density and ρ is the charge density. In the steady-state approximation due to the charge conservation principle $\frac{\partial \rho}{\partial t} = 0$, and hence

$$\nabla \cdot \mathbf{j} = 0\,. \tag{1.5}$$

We represent the currents flowing inside as a superposition of the field-aligned currents $\mathbf{j}_{||}$ and perpendicular to the geomagnetic field currents $\mathbf{j}_{\perp}$. In Cartesian coordinates *XYZ*, with the Z axis pointing upward, they are expressed as $\mathbf{j}_{||} = \begin{pmatrix} 0 \\ 0 \\ j_z \end{pmatrix}$ and $\mathbf{j}_{\perp} = \begin{pmatrix} j_x \\ j_y \\ 0 \end{pmatrix}$. Assuming (1.5), one gets

$$\nabla \cdot \mathbf{j}_{||} = -\nabla \cdot \mathbf{j}_{\perp}\,. \tag{1.6}$$

Integrating over the cylindrical volume V gives

$$\iiint_V \nabla \cdot \mathbf{j}_{||} dv = -\iiint_V \nabla \cdot \mathbf{j}_{\perp} dv\,. \tag{1.7}$$

By the Gauss theorem a volume integral of divergence can be converted into a surface integral. Applying the Gauss theorem to the left hand side of (1.7) yields a surface integral over the surface *S* consisting of the top, bottom, and side surfaces of the flux tube:

$$\iiint_V \nabla \cdot \mathbf{j}_\parallel dv = \iint_S \mathbf{j}_\parallel \cdot d\mathbf{a} = a j_\parallel . \tag{1.8}$$

The surface integral in (1.8) can be rendered in the simple form of $aj_\parallel$ because the FAC $\mathbf{j}_\parallel$ flows only through the top and bottom of the cylinder and does not flow through the side surface. Here the $j_\parallel$ is just j_z, a scalar field-aligned current density in A m^{-2}. The right hand side of (1.7) may also be simplified. Since the cross-section area *a* is constant along the altitude, the volume integral can be replaced by a 1-dimensional integration. Also, the divergence operator $\nabla\cdot$ can be carried outside the integral because for the horizontal currents $\mathbf{j}_\perp$ its $\partial/\partial z$ term is zero:

$$-\iiint_V \nabla \cdot \mathbf{j}_\perp dv = -\int_{h_1}^{h_2} \nabla \cdot \mathbf{j}_\perp a dz = -a\nabla \cdot \int_{h_1}^{h_2} \mathbf{j}_\perp dz . \tag{1.9}$$

Using (1.8) and (1.9) and cancelling *a* on both sides, the continuity equation can be written as follows:

$$j_\parallel = \nabla \cdot \int_{h_1}^{h_2} \mathbf{j}_\perp dz . \tag{1.10}$$

The integral on the right hand side is the height-integrated, perpendicular to field 2-dimensional current density **J**, which has the dimensionality of A m^{-1}:

$$\mathbf{J} = \int_{h_1}^{h_2} \mathbf{j}_\perp dz . \tag{1.11}$$

With the notation (1.11) we finally arrive to the equation relating scalar FACs $j_\parallel$ in A m^{-2} and horizontal ionospheric sheet currents **J**:

$$j_\parallel = -\nabla \cdot \mathbf{J} . \tag{1.12}$$

We should note that in our reasoning $j_{||}$ is considered positive if it flows *out* of the ionospheric elementary volume. Conversely, an incident FAC is considered positive if it flows *into* the ionosphere. Therefore, the sign of the right hand side of equation (1.12) should be changed, and that finally yields:

$$j_\parallel = \nabla \cdot \mathbf{J} . \tag{1.13}$$

Note that here the incident FACs $j_{\parallel}$ are considered positive if they flow *into* the ionosphere. The equation (1.13) is actually a current continuity condition. It plays the basic role in the analysis of three-dimensional current systems in the earth ionosphere and magnetosphere because it allows reduction of 3-D problems down to 2-D problems, as will be shown later.

1.5.3 Ohm's law

Ohm's law establishes the relationship between the current and the electric field through the conductivity. It may take various forms depending on assumptions and applications. Under the approximation of charge neutrality, $n^+ = n^-$, where n is positive and negative charge number density, and under steady-state conditions, Ohm's law is

$$\mathbf{j} = \hat{\sigma}\,\mathbf{E}, \tag{1.14}$$

where $\mathbf{j}$ is the three-dimensional current density in A m^{-2} and $\mathbf{E}$ is the electric field in V m^{-1}. The coefficient $\hat{\sigma}$ is the tensor of conductivity measured in S m^{-1}. Generally, the ionospheric conductivity is determined by the electron number densities together with the collision frequencies. The ionospheric conductivity is anisotropic, i.e. it must be presented as a (3 x 3)-component tensor $\hat{\sigma}$. The conductivity tensor components are linear combinations of the Pedersen conductivity σ_P, the Hall conductivity σ_H, and the direct or longitudinal conductivity $\sigma_{\parallel}$. In a conventional coordinate system with the *Z* axis directed along the magnetic field the conductivity tensor takes the form

$$\hat{\sigma} = \begin{pmatrix} \sigma_P & \sigma_H & 0 \\ -\sigma_H & \sigma_P & 0 \\ 0 & 0 & \sigma_{\parallel} \end{pmatrix}. \tag{1.15}$$

The Pedersen conductivity σ_P determines the current along the electric field, whereas the Hall σ_H conductivity determines the current across the electric field. The ionosphere has the Hall conductivity due to the $\mathbf{E} \times \mathbf{B}$ drift motion of charges. The longitudinal conductivity $\sigma_{\parallel}$ exists because the magnetized electrons and ions tend to move in spiral trajectories along the magnetic field lines if there is a potential drop along the field line. Therefore the $\sigma_{\parallel}$ determines the current along the magnetic field.

All the three conductivities are obtained from the equation of motion. They are presented as

$$\sigma_P = \frac{Ne}{B}\left[\frac{\omega_e \nu_{en}}{\omega_e^2 + \nu_{en}^2} + \frac{\omega_i \nu_{in}}{\omega_i^2 + \nu_{in}^2}\right], \tag{1.16a}$$

$$\sigma_H = \frac{Ne}{B}\left[\frac{\omega_e^2}{\omega_e^2 + \nu_{en}^2} + \frac{\omega_i^2}{\omega_i^2 + \nu_{in}^2}\right], \tag{1.16b}$$

$$\sigma_\parallel = Ne^2\left[\frac{1}{m_e \nu_{en}} + \frac{1}{m_i \nu_{in}}\right], \tag{1.16c}$$

where $N = N_e = N_i$ is the charge number density for electrons or ions, ω_e and ω_i are the electron and ion gyrofrequencies, ν_{en} and ν_{in} are the electron-neutral and ion-neutral collision frequencies, and m_e and m_i are the electron and ion masses, respectively.

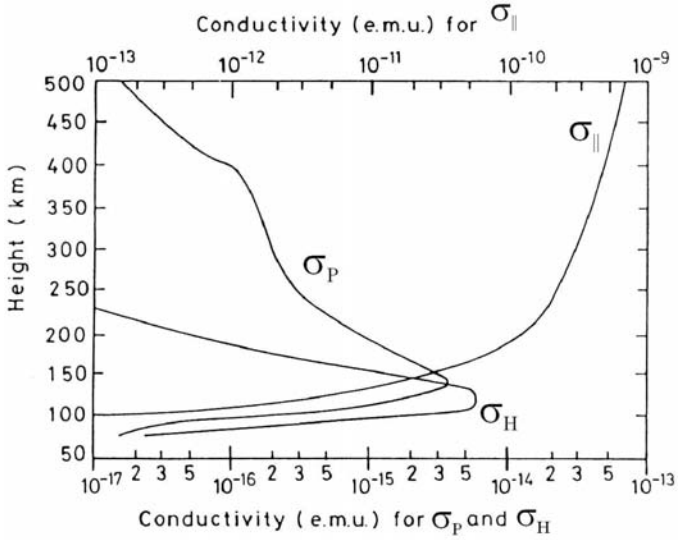

Figure 1.9. Ionospheric conductivity profiles calculated for middle latitude at noon. (After *S.-I. Akasofu and S. Chapman* [1972])

The gyrofrequencies are determined as $\omega_e = eB/m_e$ for electrons and $\omega_i = eB/m_i$ for ions. For collisional frequencies in the D, E, and F regions refer to Table 1.1. Fig. 1.9 shows the altitudinal profiles for the three conductivity components.

Notice the four-orders of magnitude scale difference between the σ_P, σ_H, and the $\sigma_\parallel$. The Pedersen and Hall conductivities grow from D to E region because the collision frequencies for electrons and ions decrease. However, at the altitude of ~ 130 km (well within the E region)

the Hall conductance reaches its maximum and then falls off with height rapidly because the drift motion at decreasing collision rates does not lead to charge separation anymore. The Pedersen conductivity first increases with the height due to decreasing collision frequency. It reaches its maximum at somewhat higher altitude, ~ 150 km, and then gradually falls off because in absence of enough collisions the charge motion assumes almost purely drift character. The direct conductivity $\sigma_{\parallel}$, increases with the altitude, because the decreasing collision rates do not hamper the free charge motion under the electric field force.

To study currents in the magnetosphere-ionosphere system, it is convenient to consider a 2-D ionosphere with the height-integrated Hall and Pedersen conductivities Σ_H and Σ_P. Ohm's law (1.14) written in the Cartesian coordinates

$$\begin{pmatrix} j_x \\ j_y \\ j_z \end{pmatrix} = \begin{pmatrix} \sigma_P & \sigma_H & 0 \\ -\sigma_H & \sigma_P & 0 \\ 0 & 0 & \sigma_{\parallel} \end{pmatrix} \cdot \begin{pmatrix} E_x \\ E_y \\ E_z \end{pmatrix} \tag{1.17}$$

can be decomposed into two independent equations using the block structure of the $\hat{\sigma}$ matrix:

$$\mathbf{j}_{\perp} = \begin{pmatrix} j_x \\ j_y \end{pmatrix} = \begin{pmatrix} \sigma_P & \sigma_H \\ -\sigma_H & \sigma_P \end{pmatrix} \cdot \begin{pmatrix} E_x \\ E_y \end{pmatrix}, \tag{1.18a}$$

$$j_z = \sigma_{\parallel} E_z . \tag{1.18b}$$

The expression for $\mathbf{j}_{\perp}$ in equation (1.18a) is a 2-D horizontal component of the total 3-D current **j**. Substituting (1.18a) into the integral (1.11) gives the relation between the 2-D ionospheric sheet current **J** and the horizontal electric field $\mathbf{E}_{\perp}$:

$$\mathbf{J} = \int_{h_1}^{h_2} \begin{pmatrix} \sigma_P & \sigma_H \\ -\sigma_H & \sigma_P \end{pmatrix} \cdot \begin{pmatrix} E_x \\ E_y \end{pmatrix} dz = \left[\int_{h_1}^{h_2} \begin{pmatrix} \sigma_P & \sigma_H \\ -\sigma_H & \sigma_P \end{pmatrix} dz \right] \mathbf{E}_{\perp} . \tag{1.19}$$

The electric field is carried outside the integral because it is assumed to be either height-independent or height-averaged. The integral in square brackets in (1.19) is called the *conductance* tensor $\hat{\Sigma}$. It has the structure

$$\hat{\Sigma} = \begin{pmatrix} \Sigma_P & \Sigma_H \\ -\Sigma_H & \Sigma_P \end{pmatrix} \tag{1.20}$$

and its components are the height-integrated Pedersen and Hall conductivities called Pedersen and Hall conductances, determined respectively as

$$\Sigma_P = \int_{h_1}^{h_2} \sigma_P dz \ , \tag{1.21a}$$

$$\Sigma_H = \int_{h_1}^{h_2} \sigma_H dz \ , \tag{1.21a}$$

where h_1 and h_2 are the lowest and highest altitudes in the region of interest. The conductances have the dimensionality of S (Siemens, or mho, as the reverse of Ohm). Hence, the two-dimensional Ohm's law (1.19) is written as

$$\mathbf{J} = \hat{\Sigma}\mathbf{E}. \tag{1.22}$$

It is also convenient to write the 2-D Ohm's law in the form

$$\mathbf{J} = \Sigma_P \mathbf{E} - \Sigma_H \left(\hat{\mathbf{e}}_z \times \mathbf{E}\right), \tag{1.23}$$

where $\hat{\mathbf{e}}_z$ is the unit vector along the *Z* axis. The $\hat{\mathbf{e}}_z$ vector can be also expressed using the geomagnetic field direction, $\hat{\mathbf{e}}_z = -\mathbf{B}/B$, and in these terms Ohm's law takes the form

$$\mathbf{J} = \Sigma_P \mathbf{E} - \Sigma_H \left(\frac{\mathbf{E} \times \mathbf{B}}{B}\right), \tag{1.24}$$

thus associating the current, electric, and magnetic field in one equation. In this thesis we predominantly use Ohm's law in the form (1.22).

1.6 Birkeland field-aligned currents

As we have seen, the conductivity along the geomagnetic field far exceeds that across the field. This means that even small electric fields applied along the magnetic field should lead to a strong field-aligned currents. *K. Birkeland* (1908) proposed that besides the horizontal ionospheric currents, vertical currents also flow from space into the high-latitude ionosphere. Later these currents were detected with the use of satellites and they received the name Birkeland field-aligned currents. We should note that Birkeland (vertical) currents are difficult to detect at the ground level with magnetometers because according to the Fukushima's theorem (Chapter 5, Section 5.2.1) their magnetic effect is compensated by the magnetic effect of the Pedersen currents.

Typical distributions of FACs are shown in Fig. 1.10. The FACs are nearly always present at a magnitude of about 10^{-8} - 10^{-7} $\mathrm{A\,m^{-2}}$ [*Hargreaves*, 1992]. Two zones are evident;

these are related to the auroral oval. The poleward FACs regardless of the current polarity (inward or outward) form “region 1” and the equatorward FACs

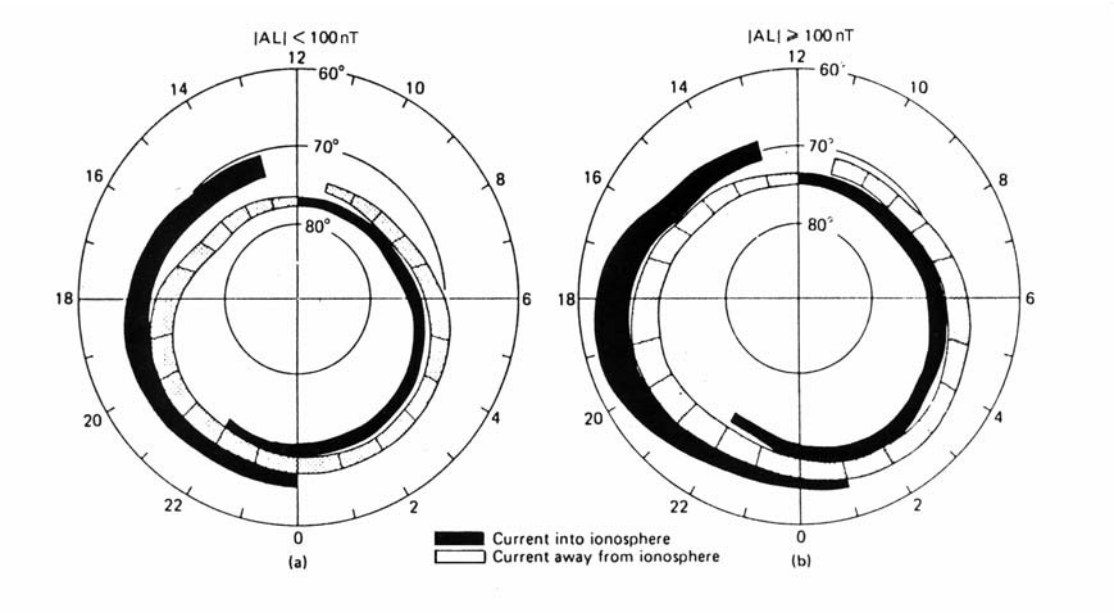

Figure 1.10. Distribution of Birkeland field-aligned currents during (a) weak and (b) active disturbances. (T. Iijima and T. A. Potemra, *J. Geophys. Res.* **83**, 599, 1978)

form “region 2” currents. On the earth’s dayside, region 1 is always dominant while around midnight the regions have approximately equal strength. At midnight the flow occurs in three regions, downward-upward-downward. In terms of electrojets, this reversal region is known as the Harang discontinuity. The magnetic activity index K_p is a good indicator of the FACs intensity, because the current density and the K_p index are linearly related. The total current in the Birkeland system is 10^6 to 10^7 A [*Hargreaves*, 1992]. Measurements have shown that the total Birkeland currents into is approximately equal to the total of the currents out of the ionosphere. An increase in disturbance level results in equatorward expansion of the Birkeland FAC zones.

The Birkeland FACs originate in the magnetotail via charge separation. It is known that in any force field, whose lines cross a magnetic field, charged particles undergo drift motion in the direction perpendicular to the force and to the magnetic field. The electric field force is the only one that causes both positive and negative charges to drift in the same direction, normal to the magnetic field. Any other forces (for example, gravitational, frictional, or inertial) make the charges drift in opposite directions, leading to charge separation and to electric current formation.

In the course of tail reconnection the magnetic potential energy is converted into kinetic energy of the particles moving earthward. The particles moving in the non-uniform earth's field undergo several kinds of charge-separating drifts due to their inertia, the pressure gradient, the magnetic field gradient and curvature. A combination of these drift charge separators leads to the formation of several current filaments closing via the earth's ionosphere. The ionospheric footprints of these currents make the pattern of Birkeland FACs.

A detailed summary on the magnetospheric source regions for the Birkeland currents is given by *Potemra* [1994]. The region 2 Birkeland current system (except its midnight part) is directly connected to the ring current. The region 2 is the divergence of the ring current. It is caused by the magnetospheric plasma pressure gradients [*Liu et al*., 1987]. The dayside (except at noon) region 1 is mapped up to the LLBL region. According to the viscous interaction model, the LLBL forms a generator supplying the current of opposite polarities on the either side of region 1. To explain the region 1 variations due to the B_Z, *Lundin et al*. [1991] suggested that the LLBL becomes thinner as B_Z becomes more negative, which leads to region 1 currents intensification. *Siscoe et al*. [1991] introduced a voltage generator in the HBL (high-latitude boundary layer), which in combination with the LLBL current generator provide region 1 source for a partially closed and open magnetosphere. The nightside region 1 currents, except at midnight, are connected to the plasma sheet region. The midnight Birkeland currents are due to the inner magnetosphere processes associated with the substorm activity to be briefly introduced in Section 1.8 and considered in Chapter 4.

1.7 Transient phenomena

The magnetosphere-ionospheric system is not stationary. First, it is exposed to the IMF changes in intensity and direction. The solar wind velocity, particle number density, and composition are also variable. These changes in the interplanetary environment cause variations in the solar energy input to the magnetosphere. Second, the magnetosphere and ionosphere constitute a complex, non-linear system capable of transitions from one quasi-stable state to another. Therefore, the solar wind impact on the magnetosphere may lead to restructuring of the magnetosphere-ionosphere (MI) system in a variety of ways.

Both changes in the SW and MI own state are manifested as ionospheric and magnetospheric transient events observable with the use of vast instrumentation, including

magnetometers, radars, riometers, all-sky cameras, satellites and many other devices. Examples of the transients that will be addressed in this thesis are global magnetic storms, substorms, poleward-propagating magnetic perturbations (PPMPs, see [*Stauning et al*., 1994]), and travelling convection vortices (TCVs).

1.8 Objectives of the research

The purpose of the research carried out in this thesis is to investigate the role of ionospheric conductance and conductance gradients in a number of high-latitude magnetosphere-ionosphere phenomena. The instrumentation utilised comprises the Super Dual Auroral Radar Network (SuperDARN) HF radars, ground-based magnetometers, and satellite instruments.

The ionospheric conductance is an important ionospheric parameter. It is determined by the charge carrier number density. In this thesis the conductance is shown to take part in the broad spectrum of the processes related to the magnetosphere-ionospheric coupling. Unfortunately, the conductance is difficult (sometimes impossible) to measure. The most reliable sources for local ionospheric conductance data are the expensive measurements involving powerful incoherent-scatter radars. Satellite instruments measuring particle precipitation flux may be also used. In our study we use the ionospheric conductance models.

We believe that many high-latitude phenomena can be controlled or at least strongly affected by the ionospheric conductance and its gradients. Here we briefly describe these phenomena and state the problems we are going to tackle.

1. The auroral substorm is the phenomenon of a sharp increase in the auroral luminosity and geomagnetic disturbance at ~65° of the magnetic latitude in the midnight sector. An intense research on the nature of substorms has been going since the concept was introduced in 1960s. The aspect that is addressed in this thesis is their seasonal and diurnal periodicity. Our goal is to describe these periodicities and make an attempt to relate those with variations of the overall conductance in conjugate ionospheres.

2. Storm sudden commencements (SSCs) are global-scale magnetic perturbations observed at the beginning of some geomagnetic storms. The perturbations are triggered by a shock structure arriving from the sun with the solar wind. The global geomagnetic storm is characterized by a simultaneous global decrease in the horizontal geomagnetic field intensity, which slowly recovers for several hours or days. It has been widely believed that the SSCs are

random and have no seasonal and diurnal periodicity. We decided to investigate periodicities in the SSC occurrence and explore a possibility that those periodicities originate from the conductance variations in conjugate hemispheres.

3. Radar aurora is a phenomenon of weak signal return from the ionosphere at radiation frequency well above the critical frequency of reflection from the ionosphere. The phenomenon is widely used for ionospheric plasma convection studies (SuperDARN experiment and alike) because, as it turns out, the velocity of irregularities producing the backscattered signal is proportional to the plasma convection velocity at F-region heights. It has been reported in the past that the SuperDARN echo occurrence rate changes over season and solar cycle. Our goal is to investigate these changes for various radars (versus a single radar considered in the past) and compare the variability for conjugate radars. Since mechanisms of irregularity production involve effects of the conducting ionosphere, we attempt to assess the potential relationship between the occurrence of the F-region echoes and the ionospheric conductance.

4. The magnetic equivalent convection (MEC) is a name given to the ionospheric plasma convection velocity derived from ground-based magnetometer measurements. The MEC has been used extensively in the past and it is an estimate of the convection rather than a direct measurement, for example, the direct SuperDARN convection measurement. The MEC is still in use, though not as widely as in the past. One of the reasons is that magnetic perturbation depends strongly on the conductance magnitude. Also, conductance gradients can significantly affect the magnetometer signal. Our goal is to investigate statistically how different the MEC convection and the real convection as measured simultaneously by SuperDARN radars. We also consider the effects of the gradients by splitting the data into sets for strongly inhomogeneous and more or less uniform conductances.

5. The interhemispheric currents (IHCs) is a relatively new phenomenon of the field-aligned current redistribution between the conjugate regions of the northern and southern ionospheres. These currents flow along the closed geomagnetic field lines. In this thesis, our goal is to estimate the intensity of IHCs for realistic conductances of the high-latitude ionosphere and study their seasonal variations. This is a theoretical work. Our additional goal is to investigate possibilities of IHCs detection through a variety of ways, as the experimental confirmation of IHCs existence is still an open question.

6. Traveling convection vortices (TCVs) is a transient phenomenon characterized by emergence of vortical patterns in magnetic equivalent convection on a scale of one-two thousand kilometres, travelling azimuthally away from noon at a speed of several $km\,s^{-1}$. There are several hypotheses on the TCV nature as well as several related issues to be resolved. We study theoretically the TCV appearance in a case of TCV occurrence near the solar terminator, the region of strong conductance gradient. We also attempt to prove that TCVs indeed occur because of circular motion of the ionospheric plasma. For this, we consider direct SuperDARN convection measurements.

1.9 Thesis outline

The outline of the thesis is as follows. In Chapter 2 we describe the instruments used for the work. Then in Chapter 3 we consider theoretically the high-latitude electrodynamics for the case of two conducting hemispheres with one of these having a strong conductance gradient. This configuration is favourable to the formation of the interhemispheric currents. Chapter 4 presents the investigation of the role of total ionospheric conductance in substorms, SSCs, and radar auroras. In Chapter 5 we compare magnetic equivalent convection and SuperDARN true convection. We also investigate the effect of a conductance gradient in magnetometer measurements, propose a method of magnetometer data correction and compare with SuperDARN convection data again. The results of TCV study in SuperDARN and magnetometer data are discussed in Chapter 6. The conclusions and suggestions for further research are given in Chapter 7.

CHAPTER 2

RESEARCH INSTRUMENTS

This Chapter is devoted to description of the instruments used in this thesis. We consider principles of the SuperDARN radars operation, then give basics of magnetometer measurements, describe used magnetometer networks, and finally provide information on satellite measurements of solar wind parameters and IMF components.

2.1 SuperDARN HF radars

The Super Dual Auroral Radar Network (SuperDARN) is an international network of high-frequency (HF) coherent scatter radars designed to study the plasma convection, electric fields, and field-aligned currents (FACs) in the high-latitude ionosphere. The radars work in cycles of transmission-reception. During the transmission phase the antenna radiates a polarised wave pulse with the (incident) wave vector $\mathbf{k}_i$. During the reception phase the radar's receiver "listens" to the echo. The radiation is received because of the presence of a large number of small-scale ionospheric irregularities along the path of the wave. The ionospheric irregularities result from the plasma instabilities of several kinds. The irregularities are spatial layered structures stretched along the earth's magnetic field. In the case the distance between the layers is half of the incident wavelength, $\lambda_i / 2$, the weak reflections from individual layers are in phase and therefore can create an echo of sufficient power to be detected by a radar. This process is

called *coherent scatter*. If the coherent scatter wave vector is denoted by $\mathbf{k}_s$, the plasma irregularities favourable for coherent scatter have wave vectors $\mathbf{k}_{irr}$ given by,

$$\mathbf{k}_{irr} = \mathbf{k}_s - \mathbf{k}_i . \tag{2.1}$$

For a monostatic radar, $\mathbf{k}_s = -\mathbf{k}_i$, and equation (2.1) implies $\lambda_{irr} = \lambda_i / 2$. For a radar frequency of 10 MHz this means that the irregularity scale is 15 m (decameter scale).

For a coherent echo to occur, the radar wave should propagate perpendicular to the irregularity plane / the geomagnetic field line direction. The angle of radiowave incidence is called *aspect angle*, and the radar aurora has substantial aspect sensitivity. The advantage of HF radars is the fact that the HF radiowaves undergo significant refraction in the ionosphere, which makes it easier to reach the irregularity wavefronts at the right angle.

Table 2.1. SuperDARN radar sites and their boresight directions.

Radar Station	Geo. Lat (^{o}N)	Geo. Lon (^{o}E)	CGM Lat (^{o}N)	CGM Lon (^{o}E)	Boresight Direction
Saskatoon	52.16	-106.53	61.34	-45.26	+23.1
Kapuskasing	49.39	-82.32	60.06	-9.22	-12.0
Prince George	53.98	-122.59	59.88	-65.67	-5.0
Goose Bay	53.32	-60.46	61.94	23.02	+5.0
Stokkseyri	63.86	-22.02	65.04	67.33	-59.0
Kodiak	57.60	-152.20	57.17	-96.28	+30.0
King Salmon	58.68	-156.65	57.43	-100.51	-20.0
Þykkvibær	63.86	-19.20	64.59	64.65	+30.0
Hankasalmi	62.32	26.61	59.78	105.53	-12.0
Sanae	-71.68	-2.85	-61.52	43.18	+173.2
Syowa East	-69.01	39.61	-55.25	22.98	+106.5
Syowa South	-69.00	39.58	-55.25	23.00	+165.0
Kergulen	-49.35	70.26	-58.73	122.14	+168.0
Halley	-75.52	-26.63	-61.68	28.92	+165.0
Tiger	-43.38	147.23	-55.31	-133.36	+180.0
Unwin	-46.51	168.38	-54.86	-106.50	+227.9

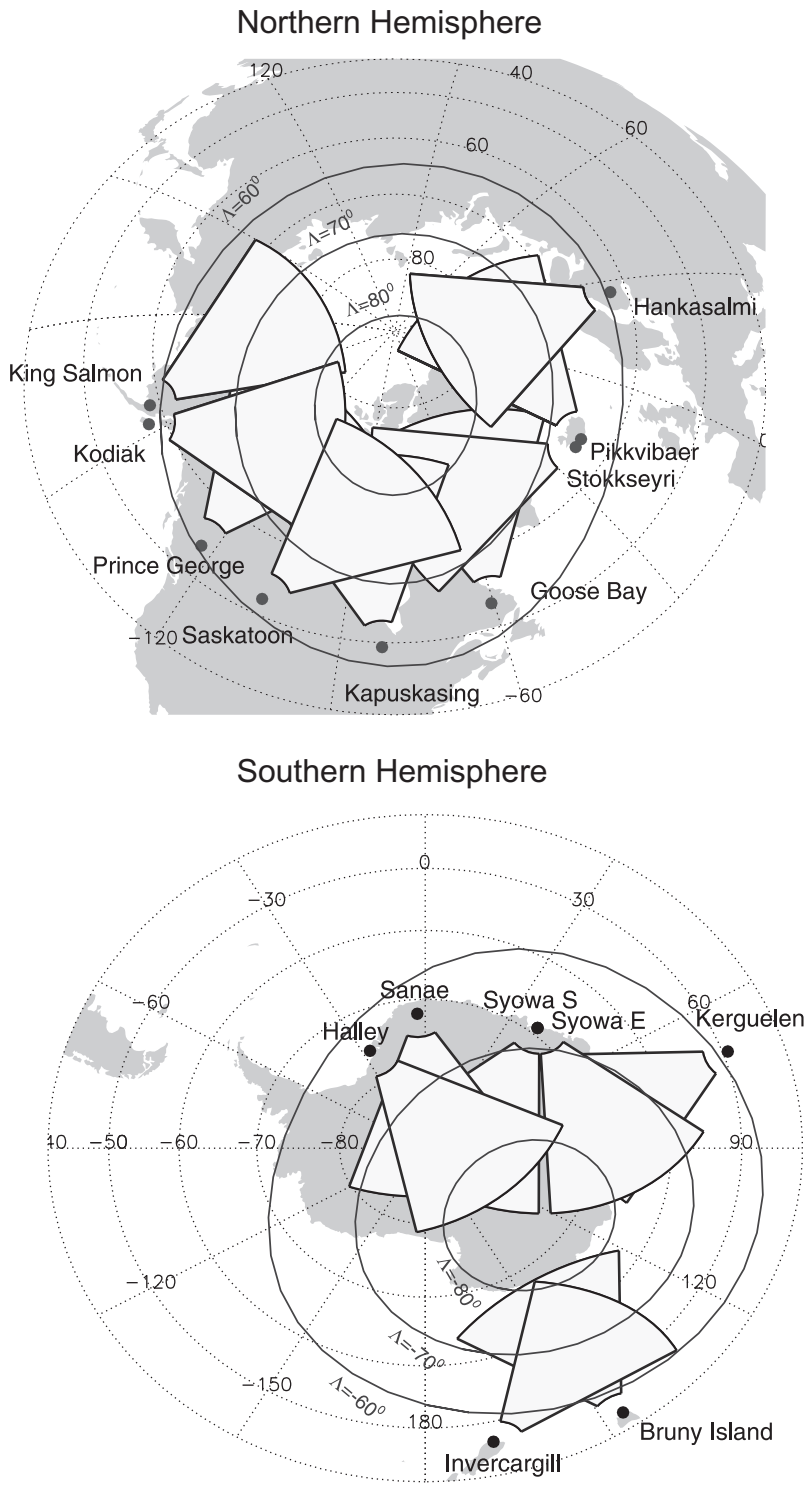

Figure 2.1. Locations of currently operating SuperDARN radars and their fields of view. The geographical coordinate grid is given by thin dotted lines. The CGM parallels are drawn by solid lines.

The SuperDARN radars are designed to measure several parameters of decametre scale ionospheric irregularities. The radars are organized in geographically separated pairs so that two

velocities obtained from the same scattering volume can be merged to produce the two-dimensional vector of the plasma convection. Multiple crossings of the beams allow the radar to cover significant portion of the high-latitude ionosphere.

The first SuperDARN radar was set up in Goose Bay [*Greenwald et al.*, 1985]. At present there are 16 radars, nine of which are in the northern hemisphere and seven in the southern hemisphere, as shown in Fig. 2.1. Table 2.1 lists the locations of the radars and their boresight directions. The radars probe the ionosphere in 16 alternating directions, each ~ 3.24° apart. Each beam is kept in the same direction for 7 seconds during normal-scan operation, or for 3 seconds for fast-scan operation. The direction of a beam is switched electronically so that a full scan is completed in 2 minutes for the normal-scan common mode or in 1 minute for the fast-scan common mode. The radar operating frequency can be chosen at any value from 8 to 20 MHz. In practice, the frequency is selected by the following criteria: (i) there is no interference from other HF sources; (ii) there are ample backscatter echoes.

Normally, the transmitted pulse length is 300 μs, corresponding to a range resolution of ~ 45 km. The total of 70 range gates is sampled along each beam. The closest range gate is set at 180 km. The maximum range is 180+70*45=3330 km. The large range interval makes it possible to monitor both the *E* and *F* ionospheric regions. The pulses are irregularly separated in time with a unit pulse separation of 2.4 ms. Each pulse is a 300 μs sinusoidal wave train at the carrier frequency f_T. The receiver samples the incoming echo radiation near the carrier frequency f_T continuously, with the exception of the intervals when the transmitter is on. The measured voltage is presented in the form of a complex number. The real and imaginary parts of a sample are the result of coherent mixing of the received waveform with in-phase and the quadrature reference signals, respectively, averaged over 300 μs. Thus each complex sample contains information on both the magnitude and phase of the received signal.

The streaming sequence of the complex samples x_k is processed into complex *autocorrelation functions* (ACFs) of the returned signals. An individual ACF is retrieved for each 45 km range gate, and each ACF is calculated at several lags using the following scheme. Consider a multi-pulse sequence of *N* pulses as a set of $N(N-1)/2$ pulse pairs. Each pulse pair separated by the time τ_{lag} determines one point of the ACF at that lag. An appropriately designed pulse sequence should contain almost all of the possible lags and as little ambiguity as possible in

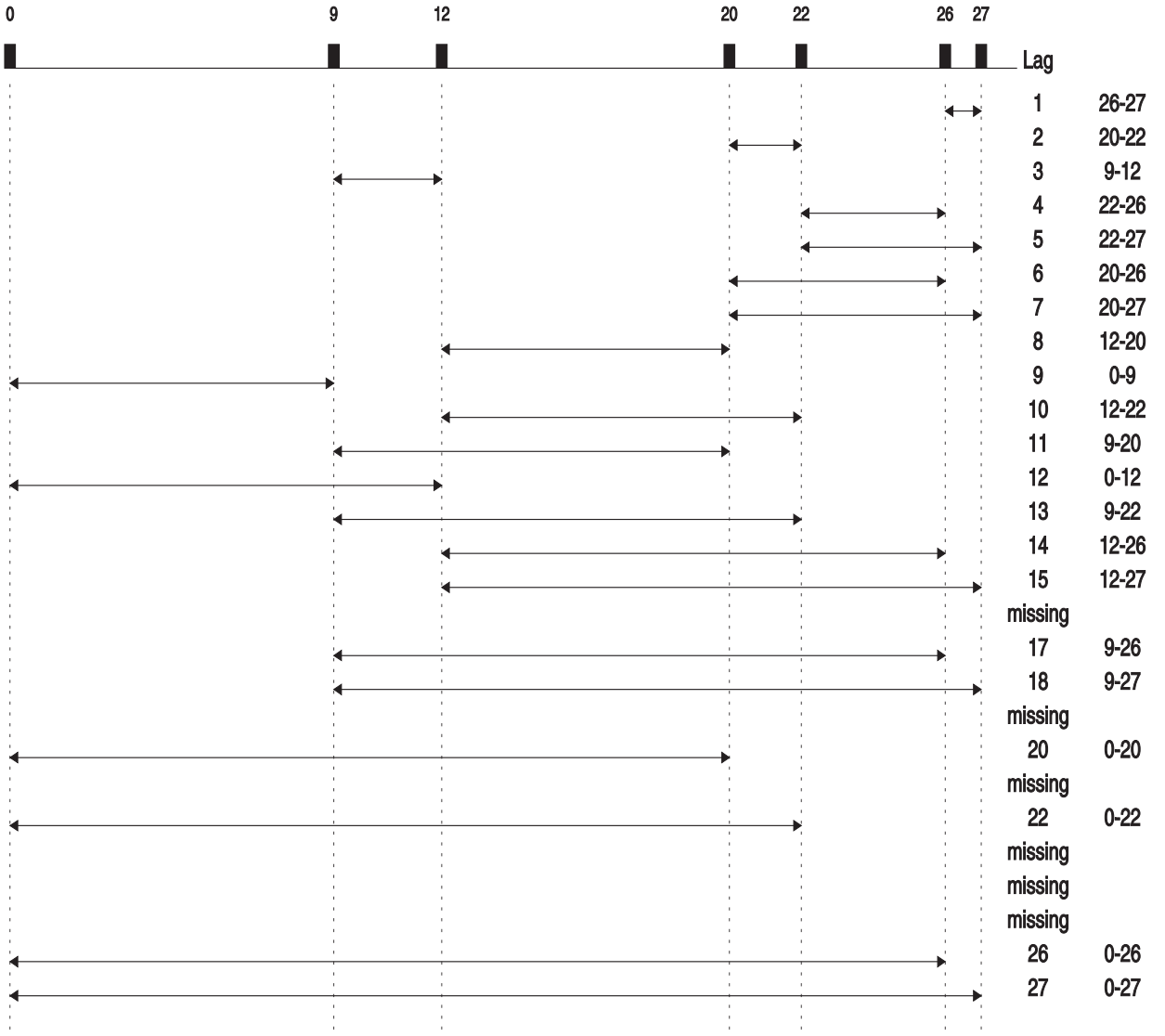

Figure 2.2 The 7-pulse sequence in use by the SuperDARN radars. The pulses are 300 μs long and they are separated by integral multiples of the unit separation (lag) time which is normally set to 2.4 ms. A total of 22 usable lags is achieved to calculate the ACF. (Courtesy of K. McWilliams)

determination of the range gate responsible for a given lag. Unfortunately, not all of the possible $N(N-1)/2$ lags can be used. There are several "bad" lags because the echo from some range gates reaches the SuperDARN radar at the time it is transmitting and therefore cannot be received. Such echoes have to be ignored. At present, the sequence used in normal operation mode consists of 7 pulses, as shown in Fig. 2.2 [*Schiffler*, 1996]. Out of the 6 lag intervals of 21.6 ms, 7.2 ms, 19.2 ms, 4.8 ms, 9.6 ms, and 2.4 ms, twenty two usable lags are obtained to retrieve the ACF. Note that the zero lag is also taken into account. The correlation of a pulse with itself, a

zero lag ACF, equals the power of received signal. Newer pulse sequences, 8-pulse and 9-pulse ones, are being designed and tested to become operational in the near future [*McWilliams*, 2003].

The autocorrelation function of a complex number sequence x_k at the lag *m* can be calculated using the formula

$$R_m = \frac{1}{N} \sum_{k=0}^{N-m-1} x_k^* x_{k+m}, \quad k = 0,...,N-1, \tag{2.2}$$

where x_k^* is the complex conjugate of x_k. Generally, any of the 70 range gates may be responsible for a received sample x_k, therefore for each range gate the x_k is treated as an echo of a pulse transmitted at the moment determined by this range gate distance from the transmitter. Because there is almost a complete set of discrete lags between the pulses it is possible (in some duration) to estimate the complex ACF at every lag for every range gate. In order to decrease the effects of noise, the multi-pulse sequences are repeated 70 times in the common scan mode and 30 times in the fast scan mode. The ACF is obtained via averaging over 70 or 30 multi-pulse sequences at each lag.

An example of the ACF analysis [*Villain et al.,* 1987] is shown in Fig. 2.3. The real and imaginary parts of the complex ACF $R(\tau) = R_m$, where the lag τ takes discrete values according to the lag number *m*, are plotted as two curves in (a).

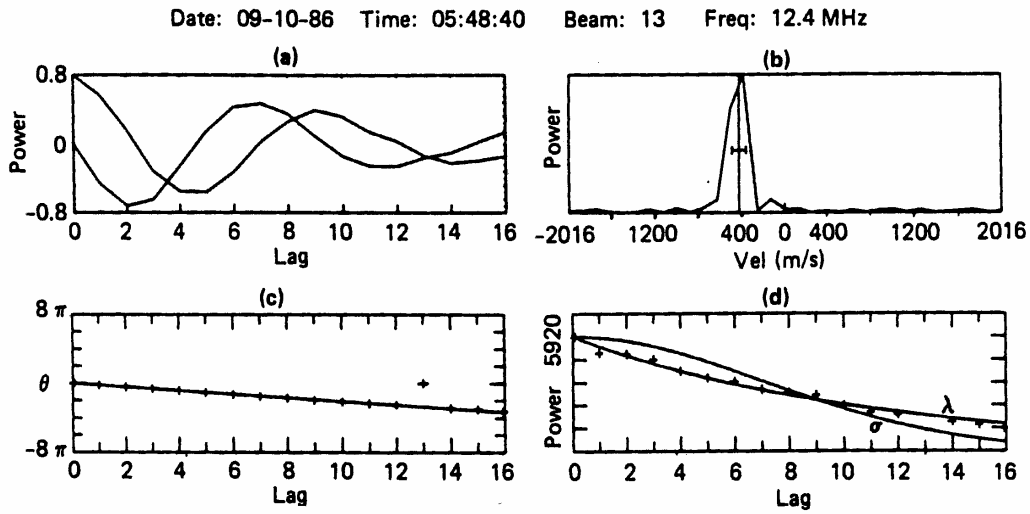

Figure 2.3. An example of the radar signal processing techniques. (a) Real and imaginary part of the ACF. (b) Doppler spectrum obtained through FFT of the ACF. (c) Phase angle as a function of lag and its linear squares fit. (d) Power variation of the ACF as a function of lag with exponential (λ) and Gaussian (σ) least squares fits. (From *Villain et al.,* [1987])

The imaginary part of ACF equals zero at the zero lag, while the real part at the zero lag has the maximum value, which is the signal intensity. The standard method of ACF processing, the FITACF, allows determination of the echo power $P_0 = P(0)$ (zero-lag value of the ACF), the Doppler velocity V_D, and the spectral width W (b). The Doppler frequency is determined by a straight-line fit to the ACF phase angle variation $\omega\tau$, shown in Fig. 2.3c. The FITACF technique assumes that the velocity spectrum (b) is single-peaked. The spectral width is determined by the best fit of the ACF power variation with lag to either an exponential or Gaussian function, as shown in (d).

To determine the echo parameters the obtained ACF data points need to be approximated by a mathematical model. In the framework of FITACF approach two models of the ACF $R(\tau)$ are assumed:

$$R_\lambda(\tau) = P_0\, e^{-\lambda\tau}\, e^{i\omega\tau} \quad \text{(“lambda” model),} \tag{2.3a}$$

$$R_\sigma(\tau) = P_0\, e^{-\sigma^2\tau^2}\, e^{i\omega\tau} \quad \text{(“sigma” model),} \tag{2.3b}$$

where λ and σ are called decorrelation coefficients. Lambda model (2.3a) describes exponential decay of the ACF while in the sigma model (2.3b) the ACF decay is Gaussian. The ACF power function $P(\tau)$ equals the ACF magnitude, $P(\tau) = |R(\tau)|$, and it is in the lambda and sigma models, respectively:

$$P_\lambda(\tau) = P_0\, e^{-\lambda\tau}, \tag{2.4a}$$

$$P_\sigma(\tau) = P_0\, e^{-\sigma^2\tau^2}\ . \tag{2.4b}$$

Examples for both functions are plotted in (d). The phase angle variation versus lag, $\omega\tau$, is obtained from the relationship

$$\tan(\omega\tau) = \mathrm{Im}\big[R(\tau)\big] \big/ \mathrm{Re}\big[R(\tau)\big]. \tag{2.5}$$

It is interesting to note that the power and the phase are completely independent functions. The phase variation is assumed to be a straight line, the slope of which gives the Doppler shift frequency ω_D. Then the Doppler line-of-sight velocity (VLOS) V_D is related to the ω_D and the radio frequency of the radar transmitter f_T by the equation

$$V_D = \frac{c}{4\pi\, f_T}\omega_D\,. \tag{2.6}$$

The measured Doppler velocity V_D may be considered as the phase velocity of the plasma wave irregularity. For the F region altitudes, this phase velocity is close to the component of the plasma $\mathbf{E}\times\mathbf{B}$ drift in the direction of incident radio wave vector [*Xu*, 2003].

The spectral width W may be presented in the frequency domain and in the velocity domain. In the frequency domain, the spectral widths for lambda and sigma models are

$$W_\lambda = 2\lambda\,, \tag{2.7a}$$

$$W_\sigma = 4\sigma\sqrt{\ln 2}\,. \tag{2.7b}$$

These spectral widths are expressed in the frequency units, s^{-1} and may be converted into the velocity domain via multiplying by the factor from (2.6):

$$W_\lambda = \frac{c}{4\pi\, f_T}\left(2\lambda\right) = \frac{c\lambda}{2\pi\, f_T}\,, \tag{2.8a}$$

$$W_\sigma = \frac{c}{4\pi\, f_T}\left(4\sigma\sqrt{\ln 2}\right) = \frac{c\sigma\sqrt{\ln 2}}{\pi\, f_T}\,. \tag{2.8b}$$

There are alternative to FITACF methods of obtaining the parameters described above. The Fast Fourier Transform (FFT) approach is based on the convolution theorem, according to which the Fourier transform of the ACF is the power spectrum of the signal. Another spectral method is the Burg algorithm for the Maximum Entropy method [*Burg*, 1975]. The Burg algorithm also can be used to study multiple-peak spectra [*Schiffler*, 1996; *Huber and Sofko*, 2000; *Danskin et al.*, 2004].

In the original SuperDARN approach, the LOS velocities are merged to derive the 2-D vector of plasma convection. This method, being physically correct, has a significant deficiency; if one of the radars in a pair does not have an echo, the convection prediction is impossible. To overcome this and other problems of the "merge" approach, a new method has been developed. It is called the FIT method [*Ruohoniemi and Baker*, 1998].

Currently the FIT technique is a standard method of obtaining the two-dimensional convection velocities. In this method a potential function in the form of spherical harmonic expansion is fitted to all of the radar measurements over the entire high-latitude ionospheric area. The developed "map potential" procedure utilizes both actual data and a statistically-based global electric potential model [*Ruohoniemi and Greenwald*, 1996; *Ruohoniemi and Baker*, 1998]. The standard form of spherical harmonics expansion for electrostatic potential is assumed:

$$\Phi(\theta,\varphi) = \sum_{l=0}^{L} \sum_{m=-M}^{M} A_{lm} Y_{lm}(\theta,\varphi), \tag{2.9}$$

where the A_{lm} are the coefficients at the spherical functions Y_{lm} of the order l and the degree m, $m \le l$. After the scan, a data set is formed of the N LOS velocity values W_i and their uncertainties σ_i (i =1,2,…N), and the coefficients are determined in a weighted least-square procedure, which minimizes the chi-squared value in the form

$$\chi^2 = \sum_{i=1}^{N} \frac{1}{\sigma_i^2} [\mathbf{V}_i \cdot \mathbf{K}_i - W_i]^2, \tag{2.10}$$

where N is the number of grid points, $\mathbf{V}_i$ is the fitted velocity vector at the i-th grid cell, and $\mathbf{K}_i$ is the unit vector along the line-of-sight. The dot product $\mathbf{V}_i \cdot \mathbf{K}_i$ is a projection of the velocity vector onto the line-of-sight direction. The χ^2 value is used as a criterion of the model-to-observation fit quality.

In terms of the area coverage and smoothness, the FIT technique has advantages over the merge technique. However, the FIT technique is based on the filtering process which tends to smooth out some smaller-scale plasma flow structures. There is another significant drawback to the FIT technique. The plasma flow in this model is represented by a potential function, which implies that the flow is purely vortical and divergence-free. This is not always true [*André et al.*, 2000].

2.2 Magnetometers and magnetometer arrays

Magnetometers are instruments for mesurements of the magnetic field intensity and direction. Currently several different types of magnetometers are used: fluxgate, fluxset, proton precession, and others.

The fluxgate magnetometer is based on the properties of the magnetization curves of a highly magnetically permeable material. Two bars of this material are oriented in such a way that, in the absence of a magnetic field, the magnetization curves of the two bars are equal and opposite. In the presence of a magnetic field, the magnetization of the two bars is different and the difference is measured as a voltage in an output coil. This type of magnetometer has an accuracy of 0.1 – 2.0 nT and produces a continuous analogue output. The output voltage is digitized for processing. It records either the total magnetic intensity or one of its three vector

components. A three-axis fluxgate magnetometer is the most common type of magnetometers used in the ground-based magnetic observatories.

The fluxset magnetometers are somewhat similar to the fluxgate magnetometers. The external magnetic field to be measured influences the time necessary to produce the reversal magnetization of a ferromagnetic core under periodic magnetic excitation. The core and excitation field are designed so that the time shift depends only on the sign and value of the given external magnetic field component H_x, H_y, and H_z (which is parallel with the core). Therefore in fluxset magnetometers the measurement of the magnetic field amplitude is replaced by the duration measurement at high accuracy. While the fluxgate method is based on *amplitude* modulation (the amplitude of the 2nd harmonic is propotional to the measured magnetic field), the fluxset method carries out *pulse width* modulation (PWM). The PWM is more robust with respect to thermal noise and other disturbances.

The proton precession magnetometer is based on a property of the atomic nucleus. If the electrons spinning about the nucleus are deflected from the direction of the earth's field, the distorted spin axis will precess back to the direction of the earth's field. The precession frequency *f*, called the Larmor frequency, is related to the magnitude of the magnetic field *F* by $f = A \cdot F$, where and *A* is the atomic constant for the element in use. The sensor consists simply of a bottle of material, such as water or a hydrocarbon, containing hydrogen nuclei, with an induction coil of wire, wound around the bottle. A cyclical microvolt signal is generated in the coil whose frequency, the Larmor frequency, can be measured. For accurate total field measurements (0.1 nT to 1 nT) the frequency must be measured to 1 part in 100,000 to 1,000,000. Because of the necessity to continually deflect the electronic spin vectors, the measurements are not continuous. This type of magnetometer has an accuracy of 0.1 – 1.0 nT and produces an intermittent (digital) sample in intervals from 0.5 s to 1 s. It records the total magnetic intensity and has a limited dynamic range.

In this thesis the data from a number of magnetometer networks have been used. These networks and arrays cover a vast high-latitude region from Alaska through Canada and Greenland to England and Scandinavia. The names of magnetometer networks used (ordered from west to east) are:

GIMA (Geophysical Institute Magnetometer Array);

CANOPUS (Canadian Auroral Network for the OPEN Program Unified Study) array;

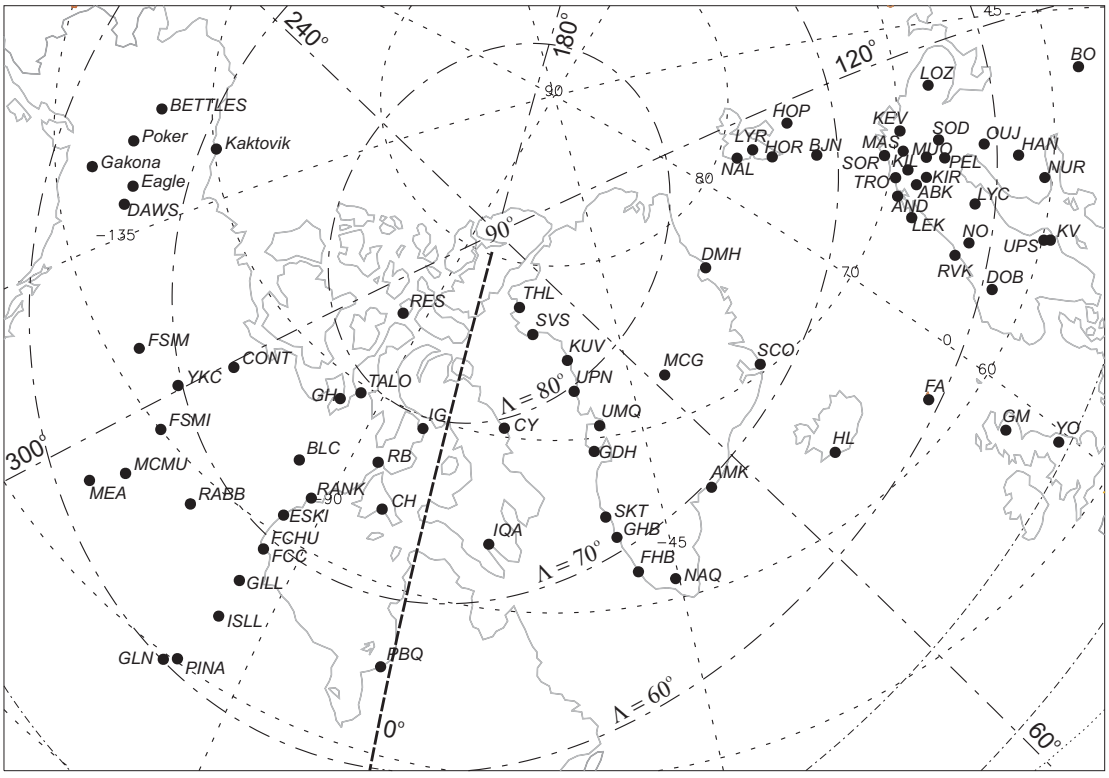

Figure 2.4. Locations of GIMA, CANOPUS, GSC, MACCS, SAMNET, and IMAGE magnetometer stations. Geomagnetic (CGM) coordinate grid is shown using dash-and-dot lines. The geographical coordinate grid is given in dotted lines. The zero CGM meridian is plotted as a thicker dashed line.

GSC (Geological Survey of Canada) array;

MACCS (Magnetometer Array for Cusp and Cleft Studies) array;

DMI (Danish Meteorological Institute) array on Greenland;

SAMNET (Lancaster University, UK);

IMAGE (International Monitor for Auroral Geomagnetic Effects, Finland).

In a number of cases when the data from some of the sources were not readily accessible, the global magnetometer network (INTERMAGNET) data were used. Fig. 2.4 shows the geographical locations for most of the magnetometer stations used in this thesis.

The Geophysical Institute of the University of Alaska, Fairbanks operates the GIMA magnetometer sites located in Alaska and Western Canada. Originally it was established as the Alaska Meridian Chain. Since then the number of sites has increased. Currently it supports the Geophysical Institute rocket program carried out at the Poker Flat Rocket Range. The GIMA

magnetometer data are available online at the high resolution of 1 s. Table 2.2 provides the GIMA magnetometer locations.

Table 2.2. Location of GIMA magnetometer stations.

Station Name	Code	Geo. Lat (^{0}N)	Geo. Lon. (^{0}E)	CGM Lat. (^{0}N)	CGM Lon. (^{0}N)
Village	Arctic	68.118	214.44	68.610	59.067
Bettles	Bettles	66.901	208.45	66.461	255.265
College International	CIGO	64.873	212.14	65.304	260.764
Eagle	Eagle	64.780	218.838	66.444	267.157
Fort Yukon	FtYukon	66.560	214.78	67.297	261.329
Gakona	Gakona	62.393	214.87	63.542	265.689
Kaktovik	Kaktovik	70.135	216.35	70.693	257.814
Poker Flat	Poker	65.119	212.57	65.604	260.904

CANOPUS was designed as an integral part of the Global Geospace Science Mission (GGS) organized by NASA as part of the International Solar-Terrestrial Physics Program (ISTP). Currently the CANOPUS magnetometer array comprises 13 stations whose locations are listed in Table 2.3. 3-component fluxgate magnetometers of the ring-core type are employed at each station. The data are available at the sample rate of one point per 5 s.

Table 2.3 Location of CANOPUS magnetometer stations.

Station Name	Code	Geo. Lat (^{0}N)	Geo. Lon. (^{0}E)	CGM Lat. (^{0}N)	CGM Lon. (^{0}N)
Contwoyto Lake	CONT	65.75	248.75	73.24	-57.44
Dawson	DAWS	64.05	220.89	65.98	-87.80
Eskimo Point	ESKI	61.11	265.95	71.21	-28.22
Fort Churchill	FCHU	58.76	265.92	69.01	-27.75
Fort McMurray	MCMU	56.66	248.79	64.60	-52.41
Fort Simpson	FSIM	61.76	238.77	67.51	-67.60
Fort Smith	FSMI	60.02	248.05	67.71	-54.90
Gillam	GILL	56.38	265.36	66.71	-28.20
Island Lake	ISLL	53.86	265.34	64.29	-27.83
Pinawa	PINA	50.20	263.96	60.59	-29.41
Rabbit Lake	RABB	58.22	256.32	67.39	-42.48
Rankin Inlet	RANK	62.82	267.89	72.91	-25.34
Taloyoak	TALO	69.54	266.45	78.95	-31.05

The Geophysical Survey of Canada (GSC) is a branch of Natural Resources Canada (NRCAN). GSC runs a network of 14 Magnetic Observatories across Canada, the locations of which are given in Table 2.4. Modern CANMOS (CANadian Magnetic Observatory System) instrumentation is set up at twelve of these observatories. The data are available at the sample rate of 1 point each 5 s.

Table 2.4. Location of NRCAN/GSC magnetometer stations.

Station Name	Code	Geo. Lat (^{0}N)	Geo. Lon. (^{0}E)	CGM Lat. (^{0}N)	CGM Lon. (^{0}N)
Alert	ALE	82.50	297.65	87.06	99.74
Baker Lake	BLC	64.32	263.99	74.00	-32.54
Cambridge Bay	CBB	69.12	254.97	77.31	-51.27
Fort Churchill	FCC	58.76	265.91	69.01	-27.76
Glenlea	GLN	49.65	262.88	59.93	-30.92
Iqaluit	IQA	63.75	291.48	72.84	14.82
Meanook	MEA	54.62	246.65	62.17	-54.39
Mould Bay	MBC	76.31	240.64	81.03	-86.62
Ottawa	OTT	45.40	284.45	56.08	1.10
P-de-la-Baleine	PBQ	55.28	282.26	65.79	-1.25
Resolute Bay	RES	74.69	265.11	83.37	-40.54
St. John's	STJ	47.59	307.32	53.75	31.33
Victoria	VIC	48.52	236.58	53.90	-64.01
Yellowknife	YKC	62.48	245.52	69.57	-59.64

The MACCS magnetometer array is a result of cooperation between Boston University and Augsburg College with assistance from the GSC and CANOPUS. MACCS magnetometers are located at high latitudes, 74^o-84^o CGM, as seen from Table 2.5. The MACCS data are intended for the study of processes at the magnetospheric cusp and cleft. Four of the GSC magnetometer stations, marked by '*' in Table 2.5, are also a part of the MACCS array. The MACCS and CANOPUS employ the same ring-core fluxgate magnetometers. The MACCS magnetometer data are provided at the sample rate of 1 point per 5 seconds.

Table 2.5. Location of MACCS magnetometer stations.

Station Name	Code	Geo. Lat (^{0}N)	Geo. Lon. (^{0}E)	CGM Lat. (^{0}N)	CGM Lon. (^{0}N)
Pangnirtung	PG	66.1	294.2	74.69	19.98
Clyde River	CY	70.5	291.4	79.12	18.50
Iqaluit (*)	IQ	63.8	291.5	72.88	14.86
Cape Dorset	CD	64.2	283.4	74.07	1.65
Iglooik	IG	69.3	278.2	79.01	-7.33
Coral Harbour	CH	64.1	276.8	74.27	-9.91
Repulse Bay	RB	66.5	273.8	76.49	-15.62
Pelly Bay	PB	68.5	270.3	78.23	-22.90
Baker Lake (*)	BK	64.3	264.0	73.99	-32.51
Gjoa Haven	GH	68.6	264.1	77.92	-34.81
Cambridge Bay (*)	CB	69.1	255.0	77.29	-51.19
Resolute Bay (*)	RE	74.7	265.0	83.37	-40.81

The Danish Meteorological Institute (DMI) has performed the Greenland coastal magnetometer data acquisition in digital form since 1981. The DMI stations are listed in Table 2.6. From 1981 to 1990 the sampling rate was 1 point per minute. After a modification completed by 1991 all the stations run at a rate 1 sample each 20 s. Since 1999 the DMI data acquisition system has been capable to record at the rate 1 sample per second. Most of the sensors now are three-axes linear-core fluxgate magnetometers.

Table 2.6. Location of DMI (Greenland) magnetometer stations.

Station Name	Code	Geo. Lat (^{0}N)	Geo. Lon. (^{0}E)	CGM Lat. (^{0}N)	CGM Lon. (^{0}N)
Thule (Qaanaaq)	THL	77.47	290.77	85.39	33.32
Savissivik	SVS	76.02	294.90	83.64	35.91
Kullorsuaq	KUV	74.57	302.82	81.22	44.51
Upernavik	UPN	72.78	303.85	79.49	42.02
Uummannaq (Umanaq)	UMQ	70.68	307.87	76.90	43.93
Godhavn (Qeqertarsuaq)	GDH	69.25	306.47	75.80	40.39
Attu	ATU	67.93	306.43	74.56	39.00
Sondre Stromfjord (Kangerlussuaq)	STF	67.02	309.28	73.16	41.74
Sukkertoppen (Maniitsoq)	SKT	65.42	307.10	71.99	37.97
Godthab (Nuuk)	GHB	64.17	308.27	70.56	38.53
Frederikshab (Paamiut)	FHB	62.00	310.32	68.01	39.65
Narsarsuaq	NAQ	61.16	314.56	66.31	43.91
Nord	NRD	81.60	343.33	80.93	105.80
Danmarkshavn	DMH	76.77	341.37	77.24	87.10

Daneborg	DNB	74.30	339.78	75.16	80.47
Scoresbysund (Ittoqqortoormiit)	SCO	70.48	338.03	71.60	73.23
Ammassalik (Tasiilaq)	AMK	65.60	322.37	69.29	54.63

The SAMNET magnetometer network is operated by the Ionosphere and Radio Propagation Group (RPG) in the Department of Communication Systems at the Lancaster University. It operates several stations equipped with fluxgate magnetometers. SAMNET began operation in October, 1987. It has stations in the UK, the Faroe Islands, and Iceland. The SAMNET station names and coordinates are listed in Table 2.7. The sampling interval was one sample in 5 s before November 1995. Now the stations are recording at 1 sample per second rate. The SAMNET data are available online for bona-fide research purposes.

Table 2.7. Location of SAMNET magnetometer stations. The IMAGE stations are not listed (see Table 2.8 for IMAGE).

Station Name	Code	Geo. Lat (^{0}N)	Geo. Lon. (^{0}E)	CGM Lat. (^{0}N)	CGM Lon. (^{0}N)
Eskdalemuir, UK	ESK	55.32	-3.200	52.892	77.756
Faroes	FAR	62.050	-7.020	60.745	78.085
Glenmore Lodge, UK	GML	57.16	-3.68	55.018	78.167
Hartland, UK	HAD	50.99	-4.48	47.907	75.136
Hella, Iceland	HLL	63.77	-20.56	64.486	68.465
Lerwick, UK	LER	60.13	-1.18	58.027	81.565
York, UK	YOR	53.95	-1.05	51.113	78.919

The IMAGE magnetometer network consists of 29 magnetometer stations run by 10 institutes from Estonia, Finland, Germany, Norway, Poland, Russia and Sweden. The IMAGE station names and locations are listed in Table 2.8. The geographic latitude coverage from 58° to 79° is especially suitable for electrojet studies. IMAGE is a result of development of the EISCAT magnetometer cross, started in 1982. The IMAGE network benefits for its high density and evenness. The IMAGE data archives are available online at the sampling rate of 10 s.

Table 2.8. Location of IMAGE magnetometer stations.

Station Name	Code	Geo. Lat (^{0}N)	Geo. Lon. (^{0}E)	CGM Lat. (^{0}N)	CGM Lon. (^{0}N)
Ny Ålesund	NAL	78.92	11.95	75.25	112.08
Longyearbyen	LYR	78.20	15.82	75.12	113.00
Hornsund	HOR	77.00	15.60	74.13	109.59
Hopen Island	HOP	76.51	25.01	73.06	115.10
Bear Island	BJN	74.50	19.20	71.45	108.07
Sørøya	SOR	70.54	22.22	67.34	106.17
Alta	ALT	69.86	22.96	66.41	106.70
Kevo	KEV	69.76	27.01	66.32	109.24
Tromsø	TRO	69.66	18.94	66.64	102.90
Masi	MAS	69.46	23.70	66.18	106.42
Andenes	AND	69.30	16.03	66.45	100.37
Kilpisjärvi	KIL	69.02	20.79	65.88	103.79
Kautokeino	KAU	69.02	23.05	65.55	106.08
Ivalo	IVA	68.56	27.29	65.10	108.57
Abisko	ABK	68.35	18.82	65.30	101.75
Leknes	LEK	68.13	13.54	65.40	97.50
Muonio	MUO	68.02	23.53	64.72	105.22
Lovozero	LOZ	67.97	35.08	64.23	114.49
Kiruna	KIR	67.84	20.42	64.69	102.64
Sodankylä	SOD	67.37	26.63	63.92	107.26
Pello	PEL	66.90	24.08	63.55	104.92
Rørvik	RVK	64.94	10.98	62.23	93.31
Lycksele	LYC	64.61	18.75	61.44	99.29
Oulujärvi	OUJ	64.52	27.23	60.99	106.14
Mekrijärvi	MEK	62.77	30.97	59.10	108.45
Hankasalmi	HAN	62.30	26.65	58.71	104.61
Dombås	DOB	62.07	9.11	59.29	90.20
Nurmijärvi	NUR	60.50	24.65	56.89	102.18
Uppsala	UPS	59.90	17.35	56.51	95.84
Karmøy	KAR	59.21	5.24	56.46	86.15
Tartu	TAR	58.26	26.46	54.47	102.89

In this thesis we also used the 1-minute data provided by the INTERMAGNET global network. INTERMAGNET is comprised of the geomagnetic observatories placed all over the world. All the INTERMAGNET stations belong to various magnetometer networks. The INTERMAGNET data are provided in a uniform format at the 1 sample per minute rate. We only used the data from the northern high-latitude magnetometers. In Table 2.9 are listed only the

stations whose data we occasionally used when they were not available directly from the networks described above.

Table 2.9. Location of INTERMAGNET magnetometer stations.

Station Name	Code	Geo. Lat (^{0}N)	Geo. Lon. (^{0}E)	CGM Lat. (^{0}N)	CGM Lon. (^{0}N)
Baker Lake	BLC	64.33	263.97	74.31	-33.85
Barrow	BRW	71.32	203.38	70.07	-109.91
Cambridge Bay	CBB	69.12	254.97	77.48	-53.06
College	CMO	64.87	212.14	65.12	-96.97
Fort Churchill	FCC	58.79	265.91	69.31	-28.64
Godhavn	GDH	69.25	306.47	75.98	40.74
Iqualuit	IQA	63.75	291.48	73.21	14.91
Lerwick	LER	60.13	358.82	58.03	81.57
Meanook	MEA	54.62	246.65	62.26	-55.05
Narsarsuaq	NAQ	61.17	314.57	66.47	43.93
Newport	NEW	48.27	242.88	55.05	-57.30
Nurmijarvi	NUR	60.51	24.66	56.75	102.48
Ottawa	OTT	45.4	284.45	56.32	0.75
Resolute Bay	RES	74.69	265.11	83.57	-43.50
Sodankyla	SOD	67.37	26.63	63.70	107.68
Thule	THL	77.47	290.77	85.63	33.34
Yellowknife	YKC	62.49	245.51	69.72	-60.62

2.3 Spaceborne instruments

For this thesis, information on the solar wind (SW) and interplanetary magnetic field (IMF) parameters was required. These data were obtained from the instruments onboard two satellites: WIND and ACE.

The WIND spacecraft is the first of two missions of the Global Geospace Science (GGS) initiative. This initiative was a United States contribution into the worldwide collaboration in the International Solar-Terrestrial Physics (ISTP) program. WIND was launched on November 1, 1994. For the first two years of operation WIND was positioned in a sunward, multiple double-lunar-swing-by orbit with a maximum apogee of 250 R_E. Afterwards, it was put into a halo orbit at the earth-sun L1 Lagrangian point. The Lagrangian point is defined as the location where the gravitational and centrifugal pull of the sun and earth cancel each other. Such a point exists on the earth-sun line at the distance ~ 230 R_E from the earth. In October 1998 WIND was

repositioned into a petal orbit, which has an angle of 60^o from the earth's ecliptic plane, ~ 10 R_E from the earth in perigee, and ~ 80 R_E in apogee.

The data from two onboard instruments were used in the thesis: the Solar Wind Experiment (SWE) and the Magnetic Fields Investigation (MFI). The SWE (Solar Wind Experiment) instrument includes two Faraday cup ion detectors that provide measurements of the solar wind protons and alpha particles at energies up to 8 keV. The basic MFI configuration consists of dual, wide range (±0.001 to ±65536 nT) triaxial fluxgate magnetometers mounted remote from the spacecraft body on a deployed boom, a 12-bit resolution A/D converter system and a microprocessor controlled data processing and control unit.

The Advanced Composition Explorer (ACE) spacecraft is an Explorer mission managed by the Office of Space Science Mission and Payload Development Division of the NASA. ACE was launched on August 25, 1997. ACE is located at the L1 point and stays at a relatively constant position with respect to the earth during its revolutions round the sun.

Two of the ACE onboard instruments data were used in this thesis: the Solar Wind Electron Proton Alpha Monitor (SWEPAM) and the magnetometer (MAG) instruments. SWEPAM measures the solar wind plasma electron and ion fluxes as functions of their direction and energy at the rate of one measurement per minute. The SWEPAM also provides real-time solar wind observations continiously transmitted to the ground. Two separate sensors are provided for the electron and ion measurements. The ion sensor measures particle energies in the range from 0.26 to 36 KeV. The electron sensor measures in the energy range between 1 and 1350 eV. The sensors utilize electrostatic analyzers with fan-shaped fields-of-view to measure the energy per charge of each particle by bending their flight paths through the system. The rotation of the satellite allows sweepeng across all the field-of-view directions. The MAG instrument measures the direction and magnitude of local interplanetary magnetic field at the rates of 3, 4 or 6 samples per second. It also provides the 24 vectors/s Fast Fourier Transform (FFT) on board. The MAG is based on a twin triaxial fluxgate magnetometer system. Two identical sensors are mounted on booms. The instrument's dynamic range of measurements is from ± 4 nT up to ± 65,536 nT per axis in eight discrete ranges.

CHAPTER 3

FORMATION OF INTER-HEMISPHERIC CURRENTS

The global-scale field-aligned currents described in Section 1.6 are responsible for average patterns in the distribution of the electric field and currents in the high-latitude ionosphere. As the solar wind and IMF conditions change, significant departures from the average patterns have been reported [e.g., *Ruohoniemi and Greenwald*, 1996]. These occur because of more localized properties of the magnetospheric sources governing the field-aligned currents. For example, the IMF B_y conditions control the location of the front-side merging area and the flow configuration in the prenoon/afternoon sector of the magnetosphere [*Ruohoniemi and Greenwlad*, 1996].

In this Chapter we study one important effect that can lead to significant modification of the average field-aligned current distribution and convection pattern. It arises under the condition of differing ionospheric conductances between the conjugate hemispheres, for example due to the difference in the solar illumination between the sunlit and dark ionospheres. Such conductance gradients can lead to the development of *interhemispheric currents* (IHCs) flowing between conjugate ionospheric areas. The IHCs are different from the Birkeland currents in the sense that they are (a) transient and (b) tied not to a magnetic latitude but to an area of the conductance gradient. The goals of this Chapter are to estimate the intensity of IHCs and investigate their variability with changing conditions in the ionosphere. The results presented in this Chapter have been published by *Benkevitch et al*. [2000] and *Benkevich and Lyatsky* [2000].

3.1 Previous studies

Formation of the interhemispheric field-aligned currents is not an absolutely new effect. In the past, it was reported that IHCs can arise due to differences in sources of ionospheric currents (related, for instance, to the effect of the interplanetary magnetic field B_y component or to the dynamo action of neutral winds) or different ionospheric conductivities in the northern and southern hemispheres [*Lyatsky*, 1978; *Richmond and Roble*, 1987; *Lu et al*., 1995; *Gasda and Richmond*, 1998]. The generation of interhemispheric field-aligned currents by the dynamo action of thermospheric winds was investigated by *Richmond and Roble* [1987], who showed that such currents are substantial even at equinoxes, with about 290 kA of total current. The dynamo effect is especially significant at low and middle latitudes where the role of other sources is relatively small.

At high latitudes, interhemispheric field-aligned currents can be generated through several processes. The formation of interhemispheric currents associated with the IMF B_y component was considered by *Leontyev and Lyatsky* [1974], *Lyatsky* [1978], and *Kivelson et al.* [1996], who attributed the IHCs to the potential difference between the northern and southern polar caps. Interhemispheric currents can also appear when the electric potential generated in one polar cap is transferred along magnetic field lines at the polar cap boundary into the opposite hemisphere [*Maltsev and Lyatsky*, 1982a]. Because of this, the magnetic pulsations, generated in one polar cap on open field lines, can be observed in the opposite polar cap.

IHCs can also be generated by symmetric sources in both hemispheres if there is a difference between ionospheric conductances in the northern and southern hemispheres, which is especially evident for summer/winter conditions. The role of the interhemispheric conductance asymmetry in the generation of interhemispheric currents was discussed by *Richmond and Roble* [1987], *Lu et al*. [1995, 1996], *Gasda and Richmond* [1998], and *Lyatsky et al.* [1999b]. Such interhemispheric currents are concentrated in a region with a large gradient of conductance, for instance, near the solar terminator. The appearance of a polarization electric field and field-aligned currents at the terminator has been studied earlier by *Atkinson and Hutchinson* [1978] and *Maltsev and Lyatsky* [1982b]. The total magnitude of interhemispheric currents in this case is approximately equal to that of the ionospheric currents entering the terminator position (or its projection in the summer ionosphere), and it can be roughly estimated as $I_{\parallel} = x\Sigma_H E$, where E is the ionospheric electric field along the terminator and x is the distance between the ionospheric

footprints of these current sources. For typical magnitudes of Σ_H in the winter ionosphere equatorward of the terminator ~6 S [*Hardy et al.*, 1987], E = 30 mV/m, and x = 2000 km, one obtains $I_{||} = 2\times10^5$A. This magnitude is comparable with that of the R1 field-aligned currents [*Potemra*, 1994], and it is more than the magnitude of field-aligned currents produced by neutral winds in the high-latitude ionosphere [*Richmond and Roble*, 1987].

3.2 Interhemispheric currents as redistribution of existing FACs

Field-aligned currents from magnetospheric sources $j_{||}$ along with the ionospheric conductance $\hat{\Sigma}$ determine the distribution of ionospheric electric potential Φ. Due to the conjugacy, the potentials in the conjugate regions in either hemisphere have the same patterns. However, even though the potentials in the northern and southern hemispheres are equal at every point, the conductance distributions in the conjugate regions are usually not the same due to differences in solar illumination or particle precipitation conditions. These differences in the conductance, specifically in the conductance gradients, force the redistribution of FACs between the hemispheres, as schematically shown in Fig. 3.1.

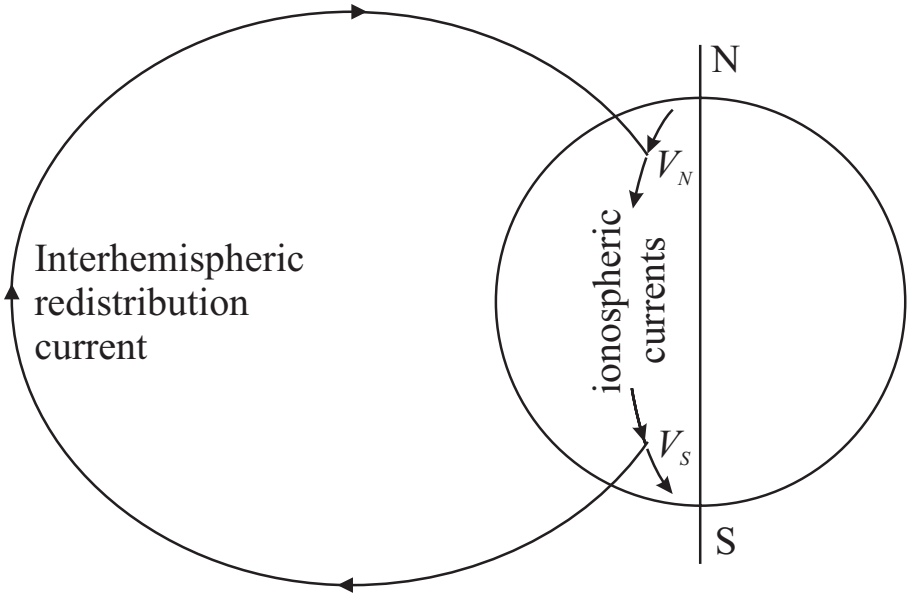

Figure 3.1. A schematic diagram showing the interhemispheric redistribution currents flowing along a closed geomagnetic field tube connecting the conjugate points V_N and V_S.

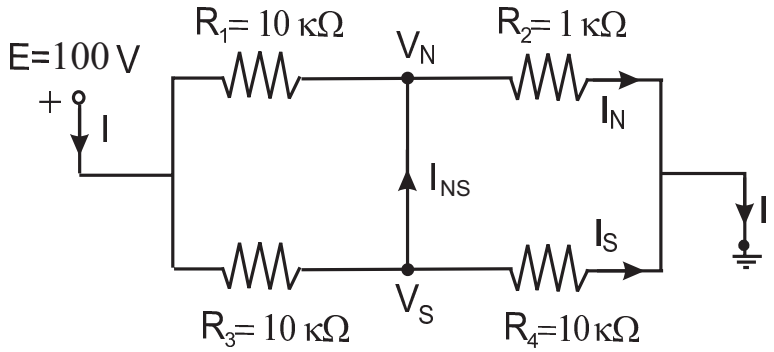

Figure 3.2. An electric circuit explaining why the interhemispheric current (here I_{NS}) must appear in a case of conductance asymmetry between the hemispheres.

A simple electric circuit model can illustrate the emergence of the redistribution currents between the hemispheres. In Fig. 3.2 the resistors R_1 and R_2 denote a non-uniform northern conductance along a meridian, whereas R_3 and R_4 stand for uniformly distributed southern conductance along the conjugate meridian. V_N and V_S are the conjugate points where the nothern conductance has a disruption, for example, due to the transition from dark to sunlit region.

The potentials at the points V_N and V_S are equal. For the specified values of the resistances and voltages, the current drawn from the voltage source is $I = E/(R_1 \| R_3 + R_2 \| R_4) = 100\,V/(5k + 0.909k) = 16.923 mA$, the voltage at the NS wire is $V_{NS} = V_N = V_S = I(R_2 \| R_4) = 15.385\,V$, the northern current is $I_N = V_{NS}/R_2 = 15.385\,mA$, and the southern current is $I_S = V_{NS}/R_4 = 1.539\,mA$. The "interhemispheric" redistribution current then is $I_{NS} = (I_N - I_S)/2 = 6.923\,mA$. Note that the redistribution current flows between the points N and S with *zero* potential difference between them. This model shows that the conductance drop of an order of magnitude leads to the current drain to another hemisphere through the highly conducting field lines, and this drain is of the same order of magnitude as that of the sheet current in one of the hemispheres. In a real 3-D case, the interhemispheric FACs may thus have similar magnitude ratio with the ionospheric sheet currents.

A more detailed schematic explaining the generation of interhemispheric field-aligned currents is shown in Fig. 3.3. During winter months, part of the dayside northern ionosphere is dark (as shown by the shaded region). This is the region of low ionospheric conductance. Original field-aligned currents flowing into the dawn sectors and out of the dusk sectors of the southern (S)

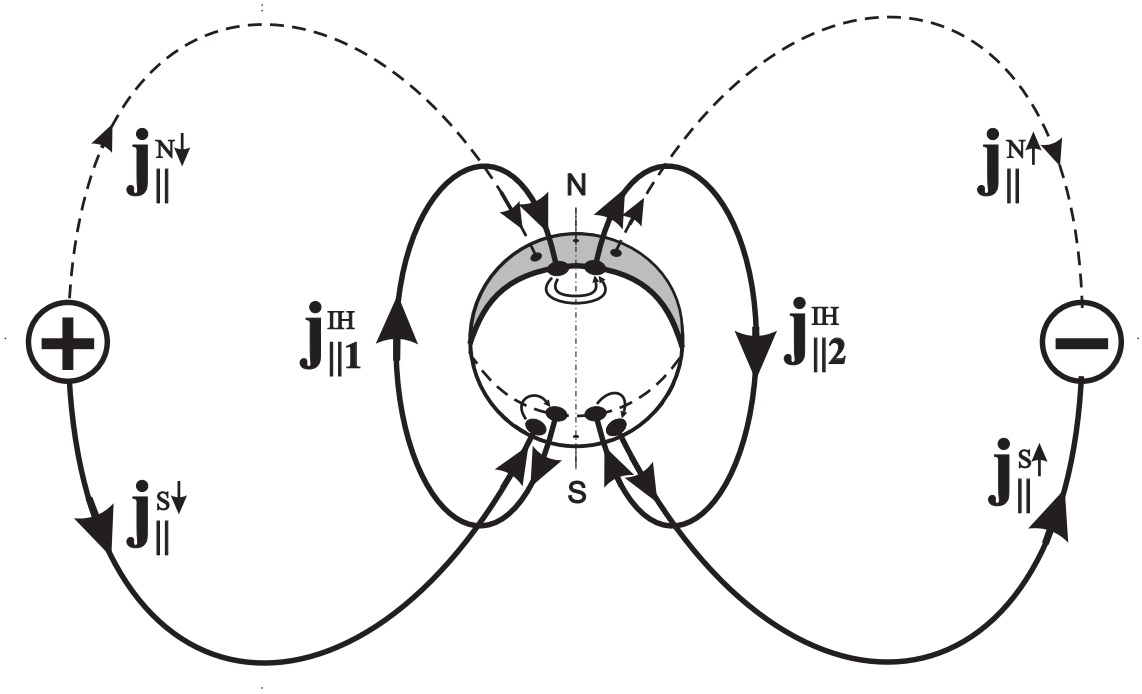

Figure 3.3. A scheme illustrating the generation of interhemispheric field-aligned currents in the northern hemisphere for winter conditions. The earth's ionosphere is shown as viewed from a subsolar point in the earth's magnetic equatorial plane. The shaded region shows the dark ionosphere in the northern hemisphere. The downward field-aligned currents (from magnetospheric generators) flowing into the northern and southern high-latitude ionospheres are denoted by $j_{\parallel}^{N\downarrow}$ and $j_{\parallel}^{S\downarrow}$ while the out-flowing FACs are denoted $j_{\parallel}^{N\uparrow}$ and $j_{\parallel}^{S\uparrow}$, respectively. The interhemispheric redistribution currents, denoted as $j_{\parallel 1}^{IH}$ and $j_{\parallel 2}^{IH}$, are flowing along magnetic field lines tied to the terminator position in the northern ionosphere and to the conjugate terminator projection in the southern ionosphere.

and northern (N) high-latitude ionospheres are shown by $\mathbf{j}_{\parallel}^{S\downarrow}$, $\mathbf{j}_{\parallel}^{N\downarrow}$, $\mathbf{j}_{\parallel}^{S\uparrow}$, and $\mathbf{j}_{\parallel}^{N\uparrow}$, respectively. The field-aligned currents are closed through the ionospheric sheet currents. Because of the low conductance in the dark northern ionosphere, no significant ionospheric currents flow there. However, since the northern and southern ionospheres are connected by highly conductive magnetic field lines, some interhemispheric field-aligned currents, $\mathbf{j}_{\parallel 1}^{IH}$ and $\mathbf{j}_{\parallel 2}^{IH}$, close the ionospheric sheet currents in a lower-latitude sunlit part of the northern ionosphere. These interhemispheric currents are attached to the region of strong gradient of the ionospheric conductance in the winter ionosphere. This region is related to the terminator position in the northern ionosphere and to the conjugate mapping of the terminator in the southern ionosphere.

3.3 Analytical description of interhemispheric currents

To create an analytical model for the interhemispheric currents, we apply the method of complex analysis proposed by *Lyatsk*y [1978]. The convenience of the complex number analysis is in the possibility of representation of vector values in the form of non-vector complex numbers. In addition, scalars can also be represented as complex values. The solution is usually obtained as an algebraic formula convenient for further analysis and calculations.

In *Lyatsky's* [1978] approach, the ionosphere is associated with the complex plane. The conductance, electric field, and currents are represented as complex-valued functions. The potential and the currents are united in one function of the complex potential as will be shown later.

3.3.1 Methods of complex analysis for two-dimensional vector fields

Let us illustrate how *Lyatsky's* [1978] method works for solving ionospheric electrodynamics problems. A complex coordinate is denoted as $z = x + iy$, where $i = \sqrt{-1}$, and x and y are coordinates on the complex plane. We denote the operation of complex conjugation with the asterisk, so that $z^* = x - iy$. The tensor of conductance is a complex function whose real part is the Pedersen conductance and the imaginary part is the Hall conductance

$$\Sigma = \Sigma_P - i\Sigma_H . \tag{3.1}$$

The complex potential $F(z)$ is an analytical function whose real part is the electric potential Φ:

$$\Phi = \mathrm{Re}\, F . \tag{3.2}$$

The currents flowing within the plane are specified via the current function $\Psi(z)$ which is defined by the equation

$$\mathbf{J} = \hat{e}_z \times \nabla\Psi , \tag{3.3}$$

where $\mathbf{J}$ is the sheet current field. To express the current function using the complex potential F one can use the Ohm's law

$$\mathbf{J} = -\hat{\Sigma}\nabla\Phi = -\begin{Vmatrix} \Sigma_P & \Sigma_H \\ -\Sigma_H & \Sigma_P \end{Vmatrix} \cdot \begin{Vmatrix} \dfrac{\partial\Phi}{\partial x} \\ \dfrac{\partial\Phi}{\partial y} \end{Vmatrix} = -\begin{Vmatrix} \Sigma_P \dfrac{\partial\Phi}{\partial x} + \Sigma_H \dfrac{\partial\Phi}{\partial y} \\ -\Sigma_H \dfrac{\partial\Phi}{\partial x} + \Sigma_P \dfrac{\partial\Phi}{\partial y} \end{Vmatrix} . \tag{3.4}$$

So, in vector notation the Ohm's law is

$$\mathbf{J} = -\Sigma_P \nabla\Phi + \Sigma_H \left(\hat{e}_z \times \nabla\Phi\right). \tag{3.5}$$

As an analytical function, the complex potential satisfies the Cauchy-Riemann equations

$$\begin{cases} \dfrac{\partial \operatorname{Re} F}{\partial x} = \dfrac{\partial \operatorname{Im} F}{\partial y} \\ \dfrac{\partial \operatorname{Re} F}{\partial y} = -\dfrac{\partial \operatorname{Im} F}{\partial x} \end{cases}, \tag{3.6}$$

or in vector notation

$$\nabla \operatorname{Re} F = -\hat{e}_z \times \nabla \operatorname{Im} F\,. \tag{3.7}$$

Combining (3.2) and (3.7), we get

$$\mathbf{J} = \hat{e}_z \times \nabla\left(\Sigma_P \operatorname{Im} F + \Sigma_H \operatorname{Re} F\right). \tag{3.8}$$

Note that the expression in parentheses is the imaginary part of the product

$$\begin{aligned} \Sigma^* F &= \left(\Sigma_P + i\Sigma_H\right)\left(\operatorname{Re} F + i \operatorname{Im} F\right) \\ &= \left(\Sigma_P \operatorname{Re} F - \Sigma_H \operatorname{Im} F\right) + i\left(\Sigma_H \operatorname{Re} F + \Sigma_P \operatorname{Im} F\right) \end{aligned}. \tag{3.9}$$

Therefore, we can write

$$\mathbf{J} = \hat{e}_z \times \nabla\left(\Sigma^* F\right) = \hat{e}_z \times \nabla\Psi\,, \tag{3.10}$$

and eventually express the current function as

$$\Psi = \operatorname{Im}\left(\Sigma^* F\right). \tag{3.11}$$

The electric field is also a complex-valued function. Using the Cauchy-Riemann equations (3.6) we get

$$E = -\nabla\Phi = -\frac{\partial \operatorname{Re} F}{\partial x} - i\frac{\partial \operatorname{Re} F}{\partial y} = -\frac{\partial \operatorname{Re} F}{\partial x} + i\frac{\partial \operatorname{Im} F}{\partial x}, \tag{3.12}$$

or

$$E = -\left[\frac{\mathrm{d}F}{\mathrm{d}z}\right]^*, \tag{3.13}$$

where the z is a complex variable $x + iy$. The vector current field $\mathbf{J}$ is rendered in the form of a scalar field $J(z)$ via the Ohm's law for the complex plane

$$J = \Sigma E\,. \tag{3.14}$$

Note again that in the complex-plane method both vector and scalar entities are similarly presented as complex functions.

3.3.2 Analytical model of interhemispheric currents for a sharp conductance gradient

Consider two conjugate ionospheric rectangular segments. Introduce complex coordinates in both hemispheres such that the real axis would be aligned with the parallels and the imaginary axis would be aligned with the meridians, as shown in Fig. 3.4. Although the voltage sources are actually far away in the magnetosphere (see Fig. 3.3), in our simplified model they are placed between the ionospheric rectangles to supply incident currents at the right angles to them. The imaginary axes point at the poles, at the north pole in the northern hemisphere and at the south pole at the southern hemisphere. We have four semiplanes with different complex conductances: $\Sigma_{N1} = \Sigma_{N1P} - i\Sigma_{N1H}$ and $\Sigma_{N2} = \Sigma_{N2P} - i\Sigma_{N2H}$ in the northern hemisphere and $\Sigma_{S1} = \Sigma_{S1P} - i\Sigma_{S1H}$ and $\Sigma_{S2} = \Sigma_{S2P} - i\Sigma_{S2H}$ in the southern hemisphere. Two magnetospheric sources of opposite polarity supply field-aligned currents incident on both hemispheres at two different points located

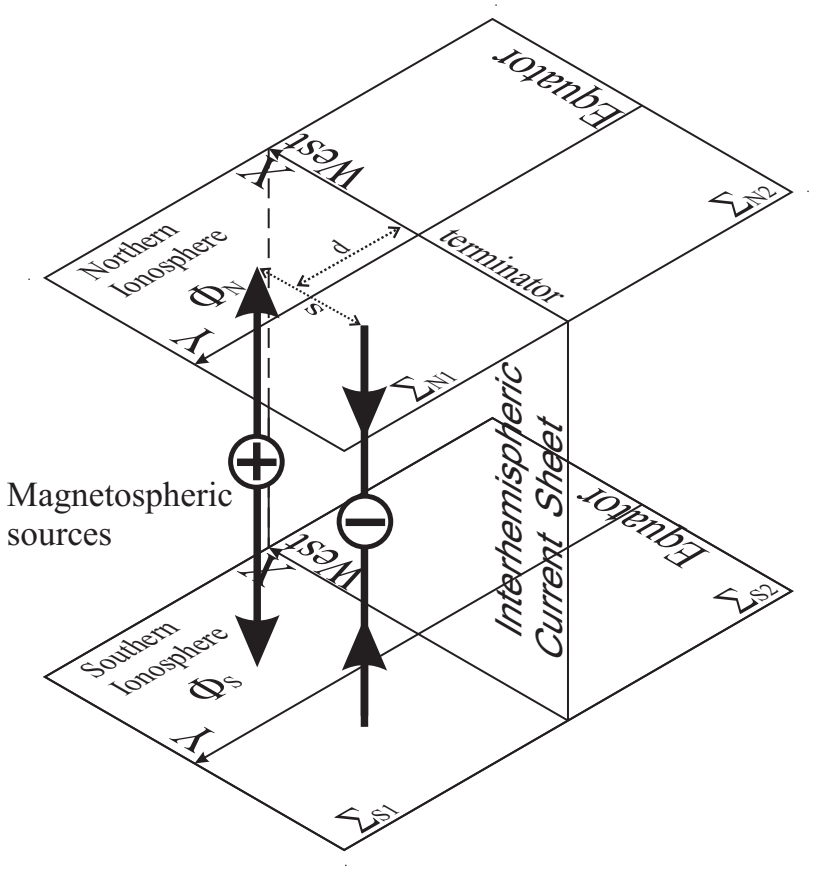

Figure 3.4. Model used for analytical description of the interhemispheric currents. The terminator is modeled as a conductance change between Σ_{N1} in the dark part of the northern ionosphere and Σ_{N2} in its sunlit part. The conductance of the southern hemisphere is uniform ($\Sigma_{S1} = \Sigma_{S2}$) and large because this ionosphere is sunlit. All the redistribution currents flow inside of a plane denoted as the interhemispheric current sheet.

at the distance *d* from a conductance discontinuity line (which models the terminator). The sources are at some specified distance *s* from each other. It is required to find the distributions of electric potential in either hemisphere and field-aligned currents between the hemispheres.

The problem can be decomposed into two similar tasks of finding the required distributions first for the positive source and, second, for the negative one, each mapped at the point $z_1 = id$. The final solution is a simple superposition of the potentials and field-aligned currents found for the both sources shifted by *s*/2 on either side of the imaginary axis. Therefore, below we show the method of solution for only one source. Due to the high conductivity of the magnetospheric field lines connecting the conjugate points of the segments, their conjugate points can be considered identical having the sum conductances. In other words, the ionospheric segments may be thought "overlapped". This notion can be justified by considering a simplified, one-dimensional case of a linear circuit consisting of a chain of resistances connected in parallel pairs, as shown in Fig. 3.5. The upper chain stands for a northern magnetic meridian at the ionospheric altitude, while the lower chain stands for its conjugate in the southern hemisphere. In each pair the conductances are added up. Thus, the poleward overlapped semiplane has the conductance $\Sigma_1 = \Sigma_{N1} + \Sigma_{S1}$ while the equatorward overlapped semiplane has the

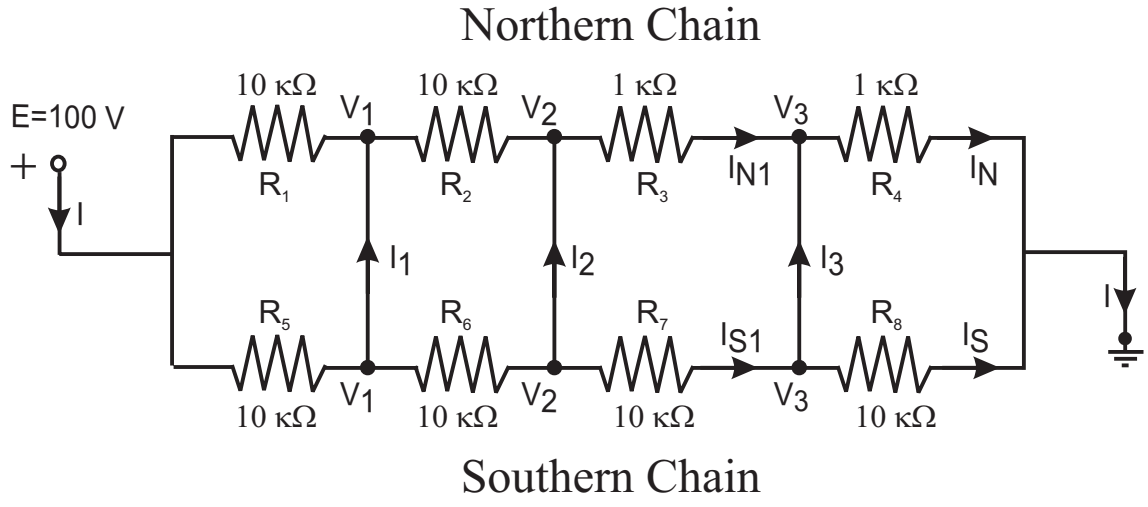

Figure 3.5. A model circuit explaining two properties of electrically connected conjugate ionospheres: 1. The conductances of the areas connected in parallel (conjugate) pairs are added up for each pair; 2. Interhemispheric current I_2 flows only between the hemispheres with the parallel conductance drop; The current I_1 between the hemispheres with equal conductance is zero (just out of symmetry). The current I_3 between the hemispheres with different but constant conductances is zero, too.

conductance $\Sigma_2 = \Sigma_{N2} + \Sigma_{S2}$. These conductances have the Pedersen and Hall components

$$\Sigma_1 = \Sigma_{1P} - i\Sigma_{1H} = \left(\Sigma_{N1P} + \Sigma_{S1P}\right) - i\left(\Sigma_{N1H} + \Sigma_{S1H}\right), \tag{3.15}$$

$$\Sigma_2 = \Sigma_{2P} - i\Sigma_{2H} = \left(\Sigma_{N2P} + \Sigma_{S2P}\right) - i\left(\Sigma_{N2H} + \Sigma_{S2H}\right). \tag{3.16}$$

In the case with the sharp conductance change across the imaginary axis in the overlapped plane, i.e. from Σ_1 to Σ_2, we know ahead that all the interhemispheric, redistribution currents will be concentrated within the plane containing both real axes coincident with the terminator and its conjugate projection (see Fig. 3.4). In order to explain why this is the case, consider Fig. 3.5 in more detail. Note that the resistances placed along the northern meridian have a drop in their values at the point V_2 from 10 kΩ down to 1 kΩ while the resistances along the southern meridian are the same. We shall show that the interhemispheric currents flow at the conductance drops only. The interhemispheric current I_1 is zero because of the obvious resistance symmetry: $R_1 = R_5 = R_2 = R_6$. The I_2 is nonzero and northward for the reasons shown in Section 3.2 (see Fig. 3.2). The I_3 is a current between the resistive circuits with different but uniform resistance,

$$R_3 = R_4 \text{ and } R_7 = R_8. \tag{3.17}$$

To calculate the I_3, i.e. the current between conjugate points of the hemispheres with different but uniform conductances, we start from calculation of the total current as $I = E/\left(R_1 \| R_5 + R_2 \| R_6 + R_3 \| R_7 + R_4 \| R_8\right)$. The potentials at the points V_2 and V_3 are $V_2 = I\left(R_3 \| R_7 + R_4 \| R_8\right)$ and $V_3 = I\left(R_4 \| R_8\right)$, respectively. The currents into the node V_3 in the north and in the south are, respectively, $I_{N1} = \left(V_2 - V_3\right)/R_3 = I(R_3 \| R_7 + R_4 \| R_8 - R_4 \| R_8)/R_3 = I\left(R_3 \| R_7\right)/R_3$ and $I_{S1} = \left(V_2 - V_3\right)/R_7 = I(R_3 \| R_7 + R_4 \| R_8 - R_4 \| R_8)/R_7 = I\left(R_3 \| R_7\right)/R_7$. The currents from the node V_3, I_N and I_S, are $I_N = V_3/R_4 = I\left(R_4 \| R_8\right)/R_4$ and $I_S = V_3/R_8 = I\left(R_4 \| R_8\right)/R_8$, respectively. Now recalling conditions (3.17) and substituting $R_3 \to R_4$ and $R_7 \to R_8$ into the expressions for I_{N1} and I_{S1} one can see that $I_{N1} = I_N$ and $I_{S1} = I_S$. Therefore, no current branches into the "interhemispheric shunt" at the point V_3 and the interhemispheric current I_3 is zero.

Since the ionospheric segments are connected with the highly conducting field lines, the potential distribution is the same in both of them. This becomes obvious if one notes that each

pair of conjugate points is electrically shunted by the field line, hence both points are at the same potential.

The idea behind the method of solution is in representing a problem for stationary currents in the form of an electrostatic problem. In electrostatics, problems of the electric field distribution in a medium with a boundary surface at which the dielectric permittivity ε undergoes a finite discontinuity are solved with the use of so called "reflected charge method" [see e.g. *Jackson*, 1975]. The electric field due to a charge q is distorted in a medium with the discontinuous permittivity. In this method, the discontinuity surface is ignored, and the distortion of field introduced by the discontinuity is ascribed to a dummy charge q' placed behind the boundary surface at the location of the "mirror image" for the charge q (as though the discontinuity surface were a mirror). The magnitude of q' is calculated from the problem geometry and the permittivity ratios.

In the problems for electric current distribution in the tenuous ionospheric plasma, the dielectric permittivity is considered constant everywhere and equal to that of a vacuum, ε_0. The distribution of the ionospheric electric field due to a FAC I is distorted due to discontinuity in the conductance Σ (e.g. at the solar terminator line). Acting in a way similar to that in electrostatics, we can attribute the electric field distortion to a dummy FAC I' thus ignoring the conductance discontinuity. The FAC I' is located at the point of the mirror image of the FAC I. The magnitude of I' is calculated from the problem geometry and the conductance ratios.

In order to derive the expression for the complex potential due to a point FAC I we replace the FAC by a charge that produces the electric field equivalent to that of the FAC. Note that we work in 2-D and the electric field due to the FAC falls off inversely proportional to the distance from its footprint. The electric field due to a point charge q falls off inversely proportional to the *squared* distance from its location. Therefore, the FAC can only be replaced by an infinite, uniformly charged thread, with the linear charge density τ (in the units of $C m^{-1}$). The electric field due to this abstract object, if it is fixed at the FAC location perpendicular to the ionospheric plane, is exactly the same as that due to the FAC. For simplicity, we shall call it "a charge τ", keeping in mind that it is actually a linearly distributed charge density. In order to find what value of τ produces the same electric field as the FAC I does, consider the Ohm's law (1.21) in a scalar, 2-D form for the Pedersen currents J_P and Pedersen conductance Σ_P:

$$J_P = \Sigma_P E \,. \tag{3.18}$$

Since the FAC's I footprint is a single point, the field E and the current J_P are radially divergent and circularly symmetric. At any point of the plane at the distance r from the I footprint, the Pedersen current J_P is associated with the FAC as

$$J_P = \frac{I}{2\pi r} \,. \tag{3.19}$$

The electric field due to an infinite, charged thread at the distance r from it is known as

$$E = \frac{\tau}{2\pi\,\varepsilon_0 r}, \tag{3.20}$$

where ε_0 is the permittivity of free space [*Jackson*, 1975]. After substitution of (3.19) and (3.20) into (3.18), one can get the relationship between the τ and the I

$$\tau = \frac{\varepsilon_0}{\Sigma_P} I = \frac{\varepsilon_0}{\Sigma_{N1P} + \Sigma_{S1P}} I \;. \tag{3.21}$$

One can propose that the electric field pattern is distorted not due to the conductance discontinuity across the real axis but due to a reflected charge τ' on the other side of the discontinuity line (terminator). This dummy charge is located equatorward from the terminator at the point $z_2 = -id$. It can be shown that because of the Hall conductance, the τ' has a complex value. Note that the reflection of the dummy charge τ' must be taken into consideration, too. Fig. 3.6 shows positions of all the three charges. We denote the complex potential due to the charge τ throughout the plane as F_0, the potential due to the reflected charge τ' in the poleward semiplane as F_1', and the potential in the equatorward semiplane due to the reflection of complex conjugate of τ' as F_2'. From electrostatics we know that the potential Φ due to a uniformly charged thread is proportional to negative logarithm of the distance r from the thread:

$$\Phi = -\frac{\tau}{2\pi\,\varepsilon_0} \ln r \,. \tag{3.22}$$

In (3.22) it is assumed that the Φ is zero at the unity distance from the thread. Converting the polar coordinates into those in the complex plane, we get three potentials due to the aforementioned charges:

$$F_0 = -\frac{\tau}{2\pi\,\varepsilon_0}\ln(z - z_1)\ , \tag{3.23a}$$

$$F_1^{/} = -\frac{\tau^{/}}{2\pi\,\varepsilon_0}\ln(z - z_2)\ , \tag{3.23b}$$

$$F_2^{/} = -\frac{\left(\tau^{/}\right)^{*}}{2\pi\,\varepsilon_0}\ln(z - z_1)\ . \tag{3.23c}$$

As seen from Fig. 3.6, only the equatorward parts of the F_0 (a) and $F_1^{/}$ (b) are used to represent the resultant potential F_1 in the poleward semiplane. The equatorward potential F_2 is in turn a superposition of F_0 (c) and $F_2^{/}$ (d) in the equatorward semiplane only. The complex potential thus consists of two parts, F_1 and F_2, different in the poleward and equatorward semiplanes and

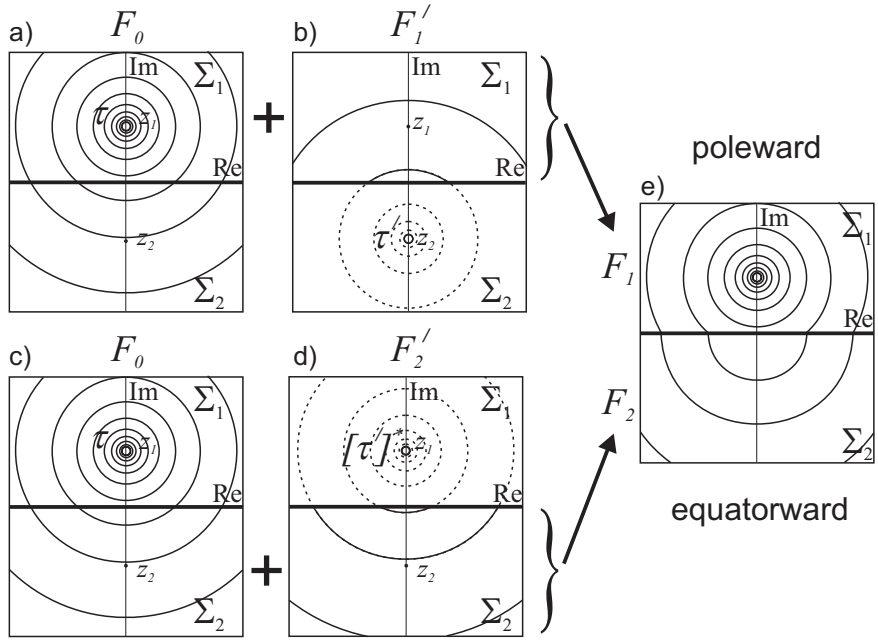

Figure 3.6. A schematic explaining solution to the problem of finding a potential function in a plane separated by a singular line (Re axis) into two semiplanes with different conductances, Σ_1 and Σ_2. a) and c) Potential F_0 due to a charge τ equivalent to the incident FAC I in a plane with the uniform Σ_1. b) Potential $F_1^{/}$ due to the reflected charge $\tau^{/}$ in a plane with the uniform Σ_2. d) Potential $F_2^{/}$ due to the complex conjugate of the $\tau^{/}$ reflection, $\left[\tau^{/}\right]^{*}$. e) The resultant potential consists of two parts, F_1 in the poleward semiplane and F_2 in the equatorward semiplane merged across the conductance discontinuity line along the Re axis.

merged along the real axis (i.e., the terminator)

$$F_1 = F_0 + F_1^{/} \qquad \textit{poleward}\,, \tag{3.24a}$$

$$F_2 = F_0 + F_2^{/} \qquad \textit{equatorward}\,. \tag{3.24b}$$

These expressions essentially mean that the background potential F_0 (Fig. 3.6a, c) due to the real FAC I (or, which is the same, due to the charge τ) is distorted in both poleward and equatorward semiplanes, but it is distorted by different dummy charges. The poleward distortion is introduced by the potential $F_1^{/}$ due to the reflected charge $\tau^{/}$ (Fig. 3.6b). The equatorward potential distortion is caused by the reflection of the charge $\tau^{/}$ (Fig. 3.6d).

To determine the mirror charge $\tau^{/}$, we note that the currents and the current stream function (3.11) are continuous at the boundary between the two semiplanes with different conductances, or at the real axis in our case. The reflected charge can be found from the continuity condition

$$\mathrm{Im}\left(J_1 - J_2\right) = \mathrm{Im}\left(\Sigma_1 E_1 - \Sigma_2 E_2\right) = 0\,, \tag{3.25}$$

and from the fact that *at the real axis*

$$z - z_1 = \left(z - z_2\right)^*. \tag{3.26}$$

Then the continuity of the currents at the real axis is expressed as

$$\mathrm{Im}\left(\left(\Sigma_1 - \Sigma_2\right)\left[\frac{2\tau}{z - z_1}\right]^* + \Sigma_1 \frac{2\left(\tau^{/}\right)^*}{z - z_1} - \Sigma_2 \frac{2\tau^{/}}{\left[z - z_1\right]^*} \right) = 0\,. \tag{3.27}$$

Using the identity $\mathrm{Im}\left(U\right) = \dfrac{1}{2i}\left(U - U^*\right)$ yields the mirror charge:

$$\tau^{/} = \frac{\Sigma_1 - \Sigma_2}{\Sigma_1^* + \Sigma_2}\tau^*, \tag{3.28}$$

where the '*' in τ^* is left out of the generality considerations. The charge τ is real, and $\tau^* = \tau$.

The real currents flowing in both semiplanes are:

$$\Psi_1 = \mathrm{Im}\left(\Sigma_1^* F_1\right)\,, \tag{3.29a}$$

$$\Psi_2 = \mathrm{Im}\left(\Sigma_2^* F_2\right). \tag{3.29b}$$

The fact that some current escapes one of the hemispheres and contributes to the other one along the real axis means that the current functions in both hemispheres have discontinuities across this

line. We make use of this fact. The current between the hemispheres at the discontinuity line $y = 0$ must be equal to the "drop" between the poleward and the equatorward current functions, calculated as (3.11):

$$\Psi_1^{\parallel}|_{y=0} = \frac{1}{2}\mathrm{Im}\left[\Sigma_2^* F_2 - \Sigma_1^* F_1\right]_{y=0}\ , \tag{3.30a}$$

$$\Psi_2^{\parallel}|_{y=0} = \frac{1}{2}\mathrm{Im}\left[\Sigma_1^* F_1 - \Sigma_2^* F_2\right]_{y=0} = -\Psi_1^{\parallel}|_{y=0}\,. \tag{3.30b}$$

Due to discontinuous character of the conductance distribution the interhemispheric currents flow within the plane connecting the "terminator" in the north ionosphere and its conjugate projection in the south ionosphere.

Consider a sample problem to evaluate equations (3.30). Assume that the conductance in the north is $\Sigma_{N1P} = 0.88\ S$, $\Sigma_{N1H} = 1.50\ S$, $\Sigma_{N2P} = 8.8\ S$, $\Sigma_{N2H} = 15.0\ S$, and in the south it is $\Sigma_{S1P} = \Sigma_{S2P} = 8.8\ S$ and $\Sigma_{S1H} = \Sigma_{S2H} = 15.0\ S$. Thus the conductance at the terminator undergoes a sharp change by a factor of ten. Assume that the magnetospheric current sources generate the currents $I^{\downarrow} = 1000\ A$ and $I^{\uparrow} = -1000\ A$, whose footprints are located at the distance d = 810 km poleward from the terminator and *s* = 2000 km from each other. The distances and currents are chosen arbitrarily. The sketch in Fig. 3.7 explains the positions of the incident currents with respect to the terminator.

Using equations (3.30), we obtain the interhemispheric field-aligned current distribution along the terminator and show it in Fig. 3.8. Notice the current density bump from ~ -1700 km to 900 km with the maximum slightly eastward from the positive source line. This bump indicates existence of an interhemispheric current jet flowing from the southern hemisphere into the northern hemisphere, incident on the terminator. There are also the interhemispheric current jets beyond ~ -1700 km and 900 km flowing back to the southern hemisphere. Fig. 3.7 clarifies why there are three interhemispheric FAC filaments. The strongest one in the middle is a continuation of the currents flowing equatorward between the FAC sources. The interhemispheric FACs on the sides have the opposite polarity because they follow the ionospheric current vortices on the sides. Also, note the westward shift of the ionospheric flows and interhemispheric FAC positions. This effect is caused by the Hall conductance.

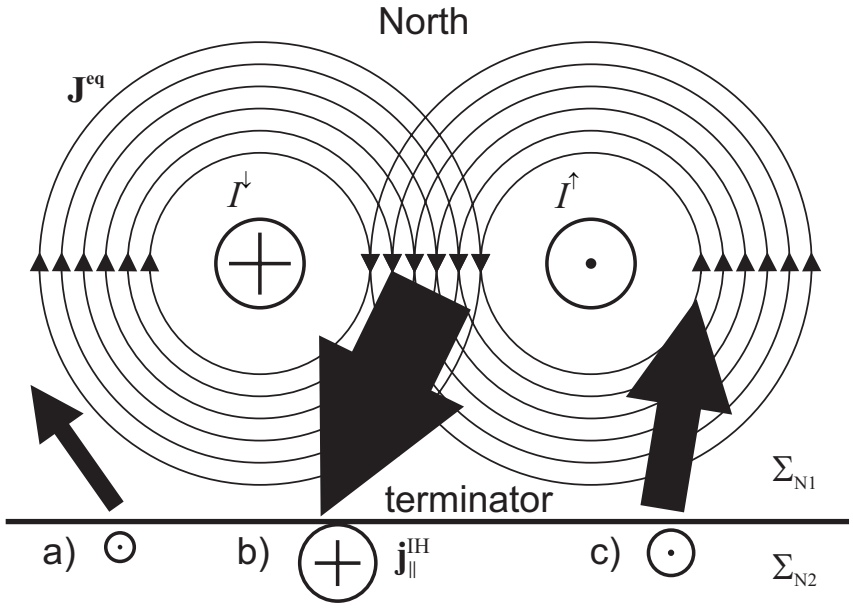

Figure 3.7. Schematic showing the mutual position of incident FACs $I^{\downarrow}$ and $I^{\uparrow}$ with respect to terminator, the induced ionospheric equivalent currents $\mathbf{J}^{eq}$, and the interhemispheric currents incident on the terminator $\mathbf{j}_{\parallel}^{IH}$. The ionospheric conductance has sharp jump at the terminator changing from Σ_{N1} to Σ_{N2}. The $\mathbf{j}_{\parallel}^{IH}$ have three filaments (a, b, and c) due to the equivalent current flow structure.

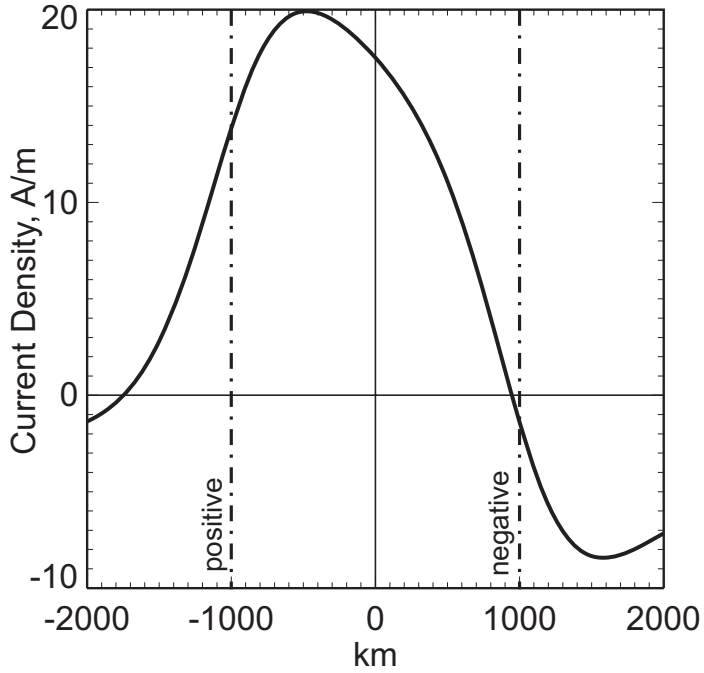

Figure 3.8. Analytically obtained interhemispheric current distribution. The dash-and-dot lines show source current footprint positions for positive and negative sources. The current has three filaments, two negative and one positive between them.

The method of complex analysis presented here is useful not only for interhemispheric current calculations but also for obtaining the ionospheric sheet current distributions (3.29). The complex analysis applications for the ionospheric equivalent current studies will be given in more detail in Chapters 5 and 6 of this thesis.

3.3.3 On a possibility of interhemispheric currents estimates from SuperDARN convection data

Generally, the ionospheric conductance distribution cannot be considered as uniform with a discontinuity line at the terminator. Also, the spherical geometry of the ionosphere has to be taken into account. In order to calculate realistic field-aligned current distributions the numerical methods other than the simple analytical modeling described in the previous section should be employed. Here we derive the relationship between the FACs, potential and conductance for a general case of their arbitrary distributions. Using this relationship, the FACs can be calculated from the SuperDARN potential maps and given conductance distribution. Conversely, the obtained relationship can be solved numerically as the Poisson equation with respect to the potential Φ, for given FACs $j_{\parallel}$ and conductance distribution $\hat{\Sigma}$.

The electric field **E** in the Ohm's law (1.22) can be presented as the negative gradient of the potential, $-\nabla\Phi$, so that

$$\mathbf{J} = -\hat{\Sigma}\nabla\Phi, \tag{3.31}$$

where **J** is the ionospheric sheet current density, **E** is the electric field, and $\hat{\Sigma}$ is the tensor of ionospheric conductance (1.20). The FACs $j_{\parallel}$ appear at the points with non-zero divergence of the ionospheric currents according to the continuity condition (1.13), which after substitution of the sheet currents **J** from (3.31) takes the form

$$j_{\parallel} = -\nabla\cdot(\hat{\Sigma}\nabla\Phi). \tag{3.32}$$

In the Cartesian coordinates XYZ, where the Z axis points upward (i.e. against the geomagnetic field **B** in the northern hemisphere, or $\mathbf{e}_z = -\mathbf{b}$), and the X and Y axes are horizontal, this equation can be rewritten as

$$-j_{\parallel} = \begin{pmatrix} \frac{\partial}{\partial x} & \frac{\partial}{\partial y} \end{pmatrix} \cdot \left(\begin{pmatrix} \Sigma_P & \Sigma_H \\ -\Sigma_H & \Sigma_P \end{pmatrix} \cdot \begin{pmatrix} \frac{\partial\Phi}{\partial x} \\ \frac{\partial\Phi}{\partial y} \end{pmatrix} \right). \tag{3.33}$$

Further expansions yield:

$$-j_{\parallel} = \frac{\partial}{\partial x}\left(\Sigma_P \frac{\partial \Phi}{\partial x}\right) + \frac{\partial}{\partial x}\left(\Sigma_H \frac{\partial \Phi}{\partial y}\right) - \frac{\partial}{\partial y}\left(\Sigma_H \frac{\partial \Phi}{\partial x}\right) + \frac{\partial}{\partial y}\left(\Sigma_P \frac{\partial \Phi}{\partial y}\right); \tag{3.34}$$

$$-j_{\parallel} = \frac{\partial \Sigma_P}{\partial x}\frac{\partial \Phi}{\partial x} + \Sigma_P \frac{\partial^2 \Phi}{\partial x^2} + \frac{\partial \Sigma_H}{\partial x}\frac{\partial \Phi}{\partial y} + \Sigma_H \frac{\partial^2 \Phi}{\partial x \partial y}$$

$$- \frac{\partial \Sigma_H}{\partial y}\frac{\partial \Phi}{\partial x} - \Sigma_H \frac{\partial^2 \Phi}{\partial x \partial y} + \frac{\partial \Sigma_P}{\partial y}\frac{\partial \Phi}{\partial y} + \Sigma_P \frac{\partial^2 \Phi}{\partial y^2} \ . \tag{3.35}$$

After regrouping, we get

$$-j_{\parallel} = \Sigma_P\left(\frac{\partial^2 \Phi}{\partial x^2} + \frac{\partial^2 \Phi}{\partial y^2}\right) + \left(\frac{\partial \Sigma_P}{\partial x}\frac{\partial \Phi}{\partial x} + \frac{\partial \Sigma_P}{\partial y}\frac{\partial \Phi}{\partial y}\right) + \left(\frac{\partial \Sigma_H}{\partial x}\frac{\partial \Phi}{\partial y} - \frac{\partial \Sigma_H}{\partial y}\frac{\partial \Phi}{\partial x}\right); \tag{3.36}$$

$$-j_{\parallel} = \Sigma_P\left(\frac{\partial^2 \Phi}{\partial x^2} + \frac{\partial^2 \Phi}{\partial y^2}\right) + \begin{pmatrix} \frac{\partial \Sigma_P}{\partial x} & \frac{\partial \Sigma_P}{\partial y} \end{pmatrix} \cdot \begin{pmatrix} \frac{\partial \Phi}{\partial x} \\ \frac{\partial \Phi}{\partial y} \end{pmatrix} + \det\begin{pmatrix} \frac{\partial \Sigma_H}{\partial x} & \frac{\partial \Sigma_H}{\partial y} \\ \frac{\partial \Phi}{\partial x} & \frac{\partial \Phi}{\partial y} \end{pmatrix} \cdot \mathbf{e}_z , \tag{3.37}$$

where $\mathbf{e}_z$ is the unit vector pointing along the *Z* axis. Finally, using the vector operations and differential symbols we can obtain an expression relating the FACs $j_{\parallel}$, potential Φ, and conductances Σ_P and Σ_H :

$$-j_{\parallel} = \Sigma_P \nabla^2 \Phi + (\nabla \Sigma_P) \cdot (\nabla \Phi) + [(\nabla \Sigma_H) \times (\nabla \Phi)] \cdot \mathbf{e}_z \ . \tag{3.38}$$

Equation (3.38) shows that not only the Laplacian of potential distribution itself but also the conductance gradients can give rise to the field-aligned currents. Note that the FACs appear where the electric field vector $-\nabla\Phi$ and the Pedersen conductance $\nabla\Sigma_P$ gradient are close to *collinearity*. And, conversely, the FACs appear where the electric field vector $-\nabla\Phi$ and the Hall conductance gradient $\nabla\Sigma_H$ are close to *normality*.

The derived equation (3.38) can be used for finding the potential distribution in the high-latitude ionosphere through its numerical solution. We describe one possible approach to achieve this goal in Appendix A. We shall go along this path later in Chapter 6. We should mention that similar efforts have been undertaken in a number of other studies, e.g. [*Untiedt and Baumjohann*, 1993; *Haines and Torta*, 1994; *Amm*, 1995]. In this section, however, we are interested in field-aligned currents, and for this reason we consider equation (3.38) in a different way. Namely, we assume that the right-hand part of it can be computed from experimental data and thus the global

distribution of FACs can be found. The numerical method for solving this problem is also described in Appendix A.

More specifically, the FACs distribution is sought for a given electric potential map from the SuperDARN radar observations, as shown in Fig. 3.9a. We assume the solar photoconductance distribution in the northern hemisphere according to the *Moen and Brekke* [1993] model (see Appendix C).

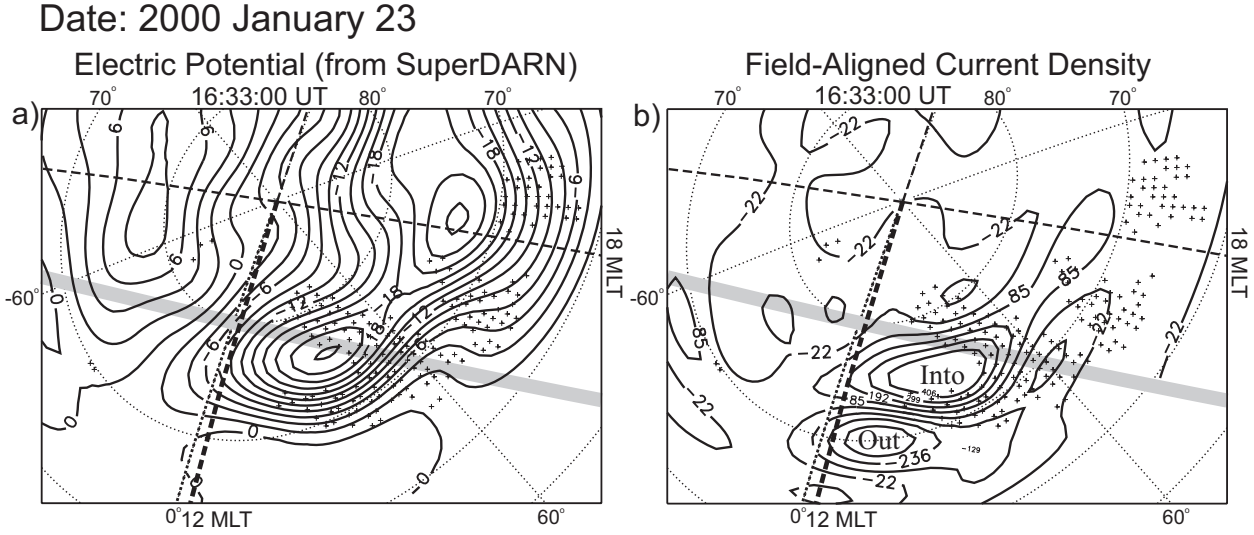

Figure 3.9. a) SuperDARN potential map, kV, in northern hemisphere. b) Interhemispheric field-aligned current distribution, nA/m^2, obtained from (a). The "+" signs indicate the radar echo locations where the plasma velocity data are available. The thick grey line stands for the terminator position.

The derived FACs distribution is shown in Fig. 3.9b. One can notice that the FAC maximum is ~0.5 $\mu A\,m^{-2}$. It is achieved in the equatorward vicinity of the terminator in the area where the conductance gradients reach their maximum (equatorward from the terminator). This current density is comparable by magnitude with that of region 1 and region 2 FACs during weakly disturbed periods, which is ~ 0.5-1.5 $\mu A\,m^{-2}$ [*Potemra,* 1994].

3.4 Interhemispheric currents for a smooth conductance gradient: Numerical simulation

More realistic estimates of IHCs for smooth conductance gradients are performed in this section. We also study two effects: seasonal variation of IHCs and their dependence on the current source location with respect to the region of maximum conductance gradient.

3.4.1 Seasonal variation in the intensity of IHCs

To study the seasonal variation of the IHCs we use equation (3.38) and solve it for the potential Φ by assuming that the FAC distribution $j_{\parallel}$ and the Pedersen and Hall conductance distributions Σ_P and Σ_H are known. Here is a list of other assumptions.

1. The ionospheric conductance is assumed to be constant poleward of the terminator and varying as a function of the solar zenith angle equatorward of the terminator in accordance with the model by *Robinson and Vondrak* [1984] and *Robinson et al.* [1987]. The effect of particle precipitation on the ionospheric conductance is ignored. Therefore, the results obtained reflect relatively quiet conditions. The models of ionospheric conductance are described in more detail in Appendix C.

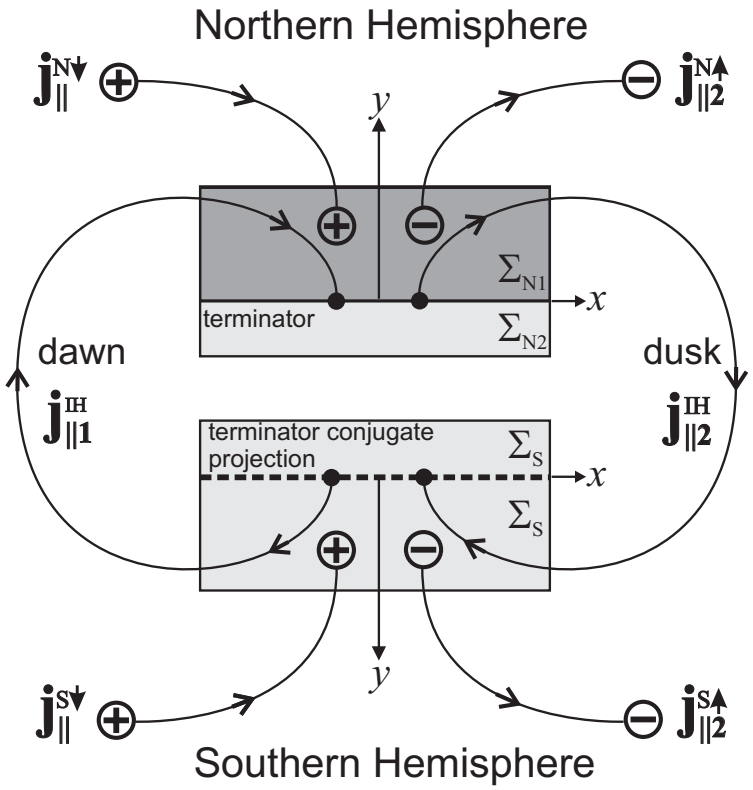

Figure 3.10. The model chosen for the study. The ionosphere is assumed to be a plane having the conductance Σ. Poleward of the terminator, the conductance of the winter northern ionosphere Σ_{N1} is assumed to be constant. Equatorward of the terminator, the ionospheric conductance Σ_{N2} is assumed to vary as a function of the solar zenith angle. The dashed line in the southern ionosphere denotes the projection of the terminator onto the southern ionosphere. Interhemispheric currents arising around the terminator are denoted by $j_{\parallel 1}^{IH}$ and $j_{\parallel 2}^{IH}$. Because of a very low conductance Σ_{N1} the source currents $j_{\parallel}^{N\downarrow}$ and $j_{\parallel}^{N\uparrow}$ are much weaker than $j_{\parallel}^{S\downarrow}$ and $j_{\parallel}^{S\uparrow}$.

2. Sources of the electric field (i.e. field-aligned current's ionospheric footprints) are assumed to be located around noon at 78° of geomagnetic latitude. The sources appear in the dark winter hemisphere and in the sunlit summer hemisphere. The sources for each hemisphere are a pair of field-aligned currents separated in the azimuthal direction. They have a bell-like distribution over circular areas of the ionosphere. The potential drop between the currents is assumed to be the same in both hemispheres.

3. The geomagnetic field lines are assumed to be closed. This implies that the boundary of the open magnetic field lines is poleward of the terminator position, which is typical for dayside winter conditions. The conjugate ionospheres are assumed to be connected by highly conducting magnetic field lines.

Fig. 3.10 schematically shows the model of ionosphere-magnetospheric currents used in the simulation. Since the sources of the electric field in the northern winter hemisphere are located in the dark region with a low ionospheric conductance, they produce weak ionospheric currents, so that the currents in both ionospheres are produced mainly by sources in the southern hemisphere only. This implies that ionospheric currents in the southern summer hemisphere, while approaching the projection of the northern terminator, are divided into two parts: one part is closed in the southern ionosphere and the other part flows (as field-aligned currents) to the northern ionosphere and is closed there, equatorward of the terminator.

The distributions of the electric potential and field-aligned currents have been obtained via a numerical solving of equation (3.38).The simulations were conducted on a numeric domain grid containing 95×129 nodes. The domains were thought to be located at the conjugate regions of the ionosphere and at high latitudes, so that the terminator and the centers of source FACs were at equal distances from the middle line of the grid. Daily solar energy flux S_a at 10.7 cm affects the value of the FACs so we performed the simulations for two values of S_a, 60 (minimum) and 240 (maximum). Because of the linear character of the problem, the resulting currents and potential patterns are linearly scalable, so we did all the simulations in relative units. There were two distributed magnetospheric voltage sources producing two incident current filaments, positive $\mathbf{j}_{\parallel}^{\downarrow}$ and negative $\mathbf{j}_{\parallel}^{\uparrow}$. For the $\mathbf{j}_{\parallel}^{\downarrow}$ and $\mathbf{j}_{\parallel}^{\uparrow}$ a simple, smooth two-dimensional distribution was selected

$$\boldsymbol{j}_{\parallel}^{\downarrow} = 0.0796 \exp[-0.25(x^2 + y^2)] \tag{3.39}$$

and $\boldsymbol{j}_{\parallel}^{\uparrow} = -\boldsymbol{j}_{\parallel}^{\downarrow}$, with a unity integral flow each, i.e.,

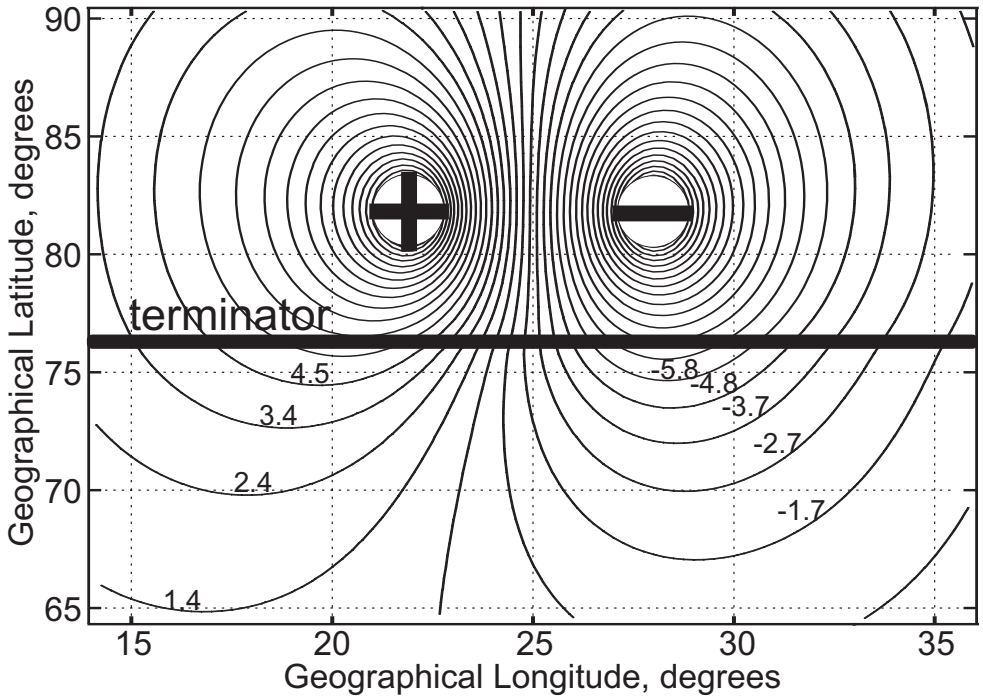

Figure 3.11. Calculated electric potential distribution, kV, in the Southern and Northern Hemispheres. The bold line shows the terminator position. The Hall and Pedersen conductances used for calculations are shown in Fig. 3.13, which are related to the conductance distribution at noon at the Sodankyla meridian (geographic longitude about 25°) on February 14. The ratio of the distance between field-aligned current to the distance between these currents and the terminator is 3.

$$I_0^{\downarrow} = \int_S \mathbf{j}_{\parallel}^{\downarrow} ds = 1 \text{ and } I_0^{\uparrow} = \int_S \mathbf{j}_{\parallel}^{\uparrow} ds = 1. \tag{3.40}$$

As mentioned earlier, for the regions of closed field lines, the electric potential distribution in the conjugate hemispheres is the same because of highly conducting magnetic field lines. In a region of open magnetic field lines the potential distribution is also approximately the same because the sources are assumed to be located just at the boundary of the regions with open field lines, and no other sources are assumed to be inside these regions.In this case, the electric potential in those regions must satisfy the Laplace equation, which has a unique solution for given boundary conditions. Since the boundary conditions for the potential at the boundary of open field line regions are the same in both hemispheres, the solution to the potential distribution in these regions is also the same. Fig. 3.11 shows a typical calculated potential distribution. The field-aligned currents between the hemispheres can be derived by applying the differential operator on the right-hand side of the Poisson equation (3.38) to the

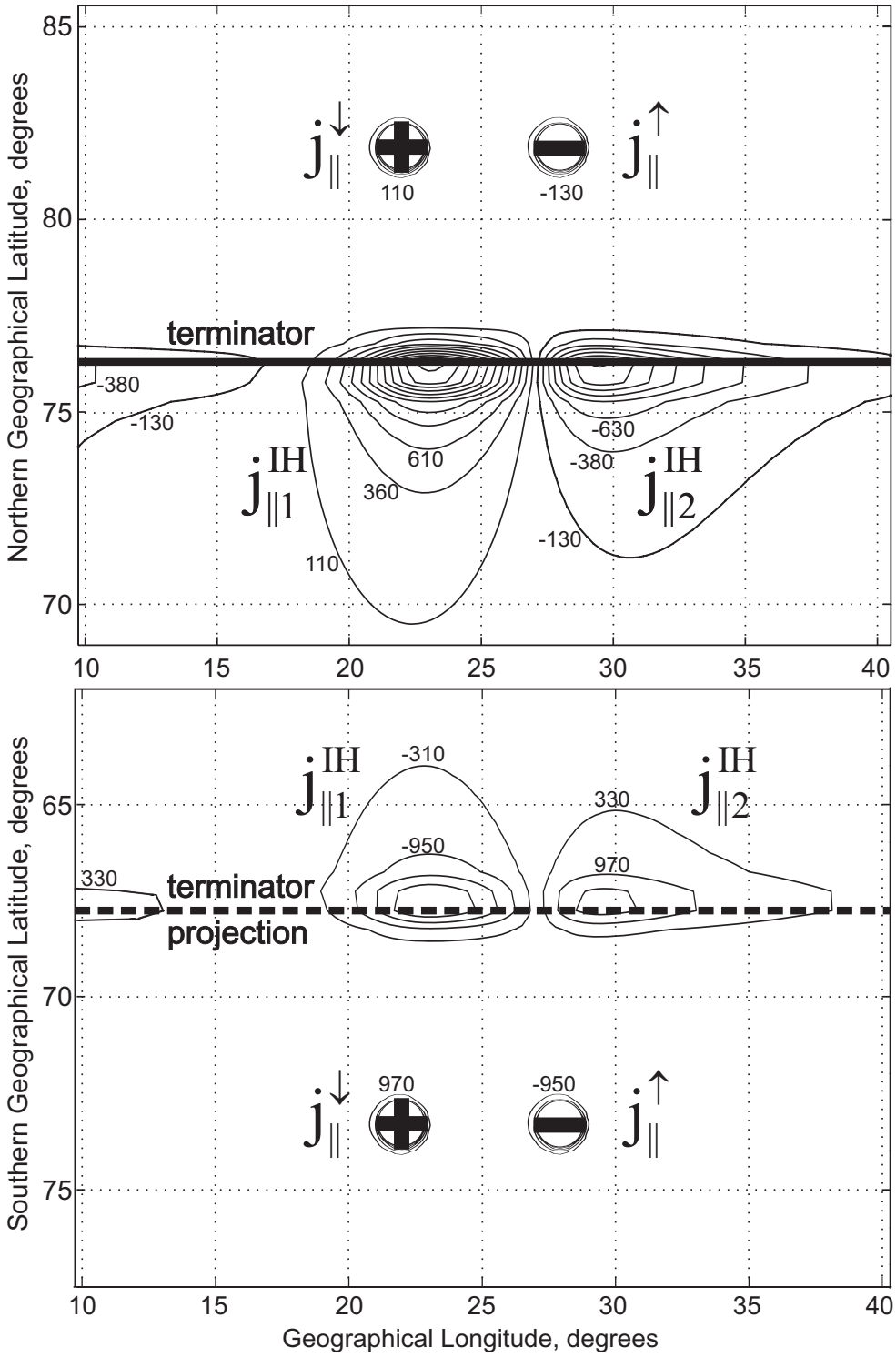

Figure 3.12. Calculated distribution of the field-aligned currents, $\mu A \cdot m^{-2}$, in the northern (a) and southern (b) ionospheres for February 14. Noon is at the Sodankyla meridian (geographic longitude about 25°). Contours show the lines of an equal current density. The source field-aligned currents $\mathbf{j}_{\|0}{}^{\downarrow}$ and $\mathbf{j}_{\|0}{}^{\uparrow}$ are marked by plus and minus signs. The maxima of the interhemispheric currents $\mathbf{j}_{\|2}{}^{\downarrow}$ and $\mathbf{j}_{\|2}{}^{\uparrow}$ arising around the terminator are shifted eastward with respect to the maxima of the source field-aligned currents.

potential distribution. For this, instead of the total conductance components Σ_P and Σ_H, one should use either their northern (Σ_P^N and Σ_H^N) or southern (Σ_P^S and Σ_H^S) parts.

Thus the potential distribution in Fig. 3.11 is the same for both southern and northern hemispheres (if viewed from the northern pole). The thick solid line in Fig. 3.11 shows the terminator position. Note that the potential distribution in Fig. 3.11 may be related both to stationary sources of the magnetospheric convection and to non-stationary events such as the traveling convection vortices if their sources are located poleward of the terminator [*Lyatsky et al.*, 1999b].

The field-aligned currents emerging at the terminator are obtained numerically by applying the right-hand side operator of (3.38) to the potential distribution. Fig. 3.12 shows typical FAC distributions for the latitudinal conductance profiles plotted in Fig. 3.13. Like the original FACs, the secondary currents flowing between northern and southern hemispheres along closed geomagnetic field lines also form two major filaments: the positive $\mathbf{j}_{\|1}^{IH}$ and the negative $\mathbf{j}_{\|2}^{IH}$ (if viewed from the north pole region). However, unlike the original FACs, whose magnitude depends on the ionospheric conductance, the secondary field-aligned currents in every pair of conjugate points have equal absolute values and opposite signs. Their magnitude reaches maximum at the terminator. The maxima of $\mathbf{j}_{\|1}^{IH}$ and $\mathbf{j}_{\|2}^{IH}$ are substantially displaced eastward. This displacement is a result of the Hall conductance effect. For the case of pure Pedersen conductance, the maximum of the interhemispheric FACs would be located under the original FAC footprint at the perpendicular to the terminator. The Hall currents, forming circular motions around the FAC footprint, contribute, however, to the interhemispheric currents, forming some eastward shift of $\mathbf{j}_{\|1}^{IH}$ and $\mathbf{j}_{\|2}^{IH}$ maxima. The simulation has been performed for three locations: (1) the Canadian sector, (2) the Greenland sector, and (3) the Scandinavian sector. As mentioned above, the FAC sources were placed at 78° of geomagnetic latitude around local noon, while the terminator geographic latitude changed with time lapse from the winter solstice, December 22, through the vernal equinox, March 21, towards the summer solstice, June 21. The meridians in both sectors were chosen close to observatories available there: Fort Churchill in Canada, Sondre Stromfjord in Greenland and Sodankyla in Scandinavia.

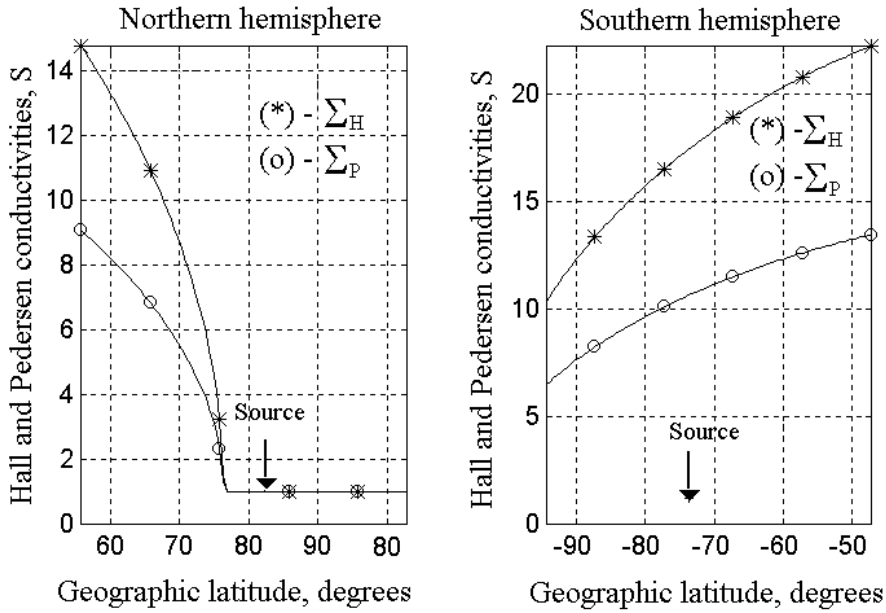

Figure 3.13. Latitudinal distribution of the Pedersen (marked with open circles) and Hall (marked with asterisks) conductances in the northern and southern ionospheres. Arrows show the positions of the source field-aligned currents. The figure is obtained using the Robinson-Vondrak model (see Appendix C). The conductance of 1 S is related to the dark ionosphere.

Table 3.1. Coordinates for the centers of source field-aligned currents for the 1999 epoch.

	Corrected Geomagnetic		Geocentric	
Observatory	λ^o	φ°	λ^o	φ°
Fort Churchill	78	328.59	68.40	265.90
Sondre Stromfjord	78	47.92	72.13	309.30
Sodankyla	78	129.31	82.25	26.63

The geocentric and corrected geomagnetic coordinates for the centers of source FACs for 1999 epoch, where λ is latitude and φ is longitude, are shown in Table 3.1.

We calculated the ratio $\delta I_N^{IH} = I_N^{IH} / I_{N0}^{\downarrow}$, i.e. the fraction of the source FACs, $I_{N0}^{\downarrow}$, branching into interhemispheric FACs, I_{N1}^{IH} and I_{N2}^{IH}, where I denotes the integral values of the respective FACs. Figs. 3.14, 3.15, and 3.16 present plots of the calculated variations of the ratio δI_N^{IH} over the season as well as the positions of the terminator and the source FACs. Each ratio plot consists of two curves. The curve marked with asterisks is related to solar minimum, while

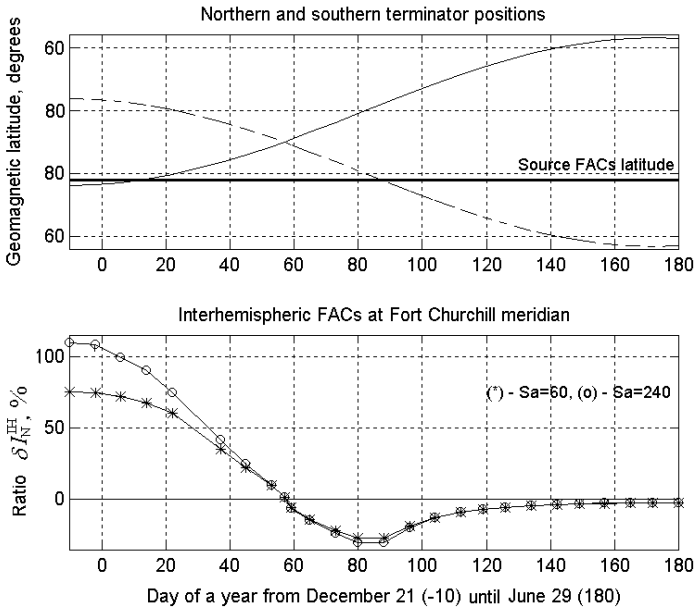

Figure 3.14. Variation of the ratio of the interhemispheric and source field-aligned currents at the Churchill meridian (Canadian sector) over half a year, from winter to summer solstices. The upper panel shows positions of the terminator and source FACs versus the geomagnetic latitude. The solid curve shows the position of the northern terminator. The dashed curve shows the projection of the southern terminator onto the northern ionosphere. The bold solid line shows the position of the source FACs. The lower panel shows the ratio of the interhemispheric currents to the source currents. The curve marked with asterisks is for low solar activity, S_a=60, and the curve marked with circles is for high activity, S_a=240. The calculations are made for the downward source FACs and related interhemispheric FACs.

that marked with circles is related to solar maximum. At the winter solstice, there is a pronounced asymmetry in the conductance between the hemispheres. However, the ratio factor is quite moderate because the sources are far from the terminator. As the distance decreases, the branching enlarges to attain 100-200% of the source FACs. The curves have their maxima at the moments that the sources are about to cross the terminator. After crossing the terminator, the ionospheric footprints of source FACs in both the northern and southern hemispheres appear in the sunlit region, and the ratio factor quickly decreases to zero at the moment of utter symmetry in the source FACs position with respect to the terminators. It is interesting to note that this does not occur at the equinoxes but some time earlier or later. For example, at Fort Churchill such a “magnetic equinox” comes on February 26, at Sondre Stromfjord it comes on March 8, and at Sodankyla it comes on April 2, while the usual “geographical equinox” is March 21. The reason for this is the difference in positions of the geomagnetic and geographic poles. Because of that, the sun appears at the plane of the geomagnetic equator at different times for different earth’s sectors.

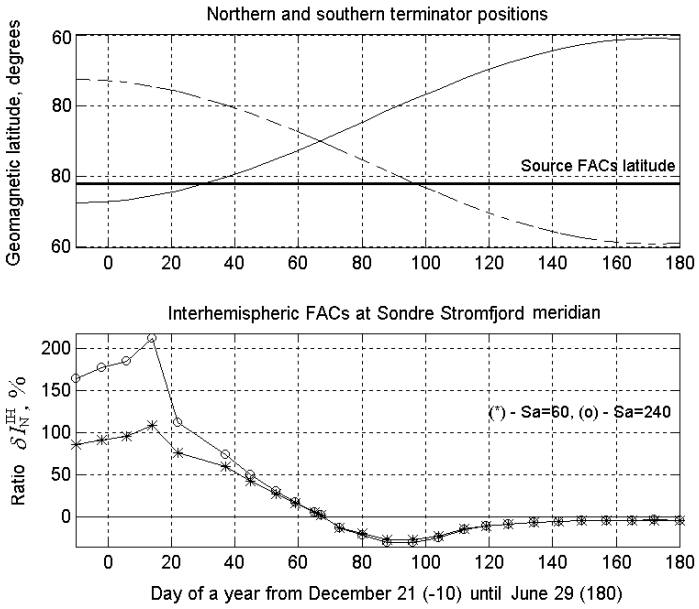

Figure 3.15. Variation of the ratio of the interhemispheric and source FACs at the Sondre Stromfjord meridian (Greenland sector) from the winter to summer solstices (similar to Fig. 3.14). However, the ratio factor is maximum not at the winter solstice but shortly before the source FAC crossing of the northern terminator.

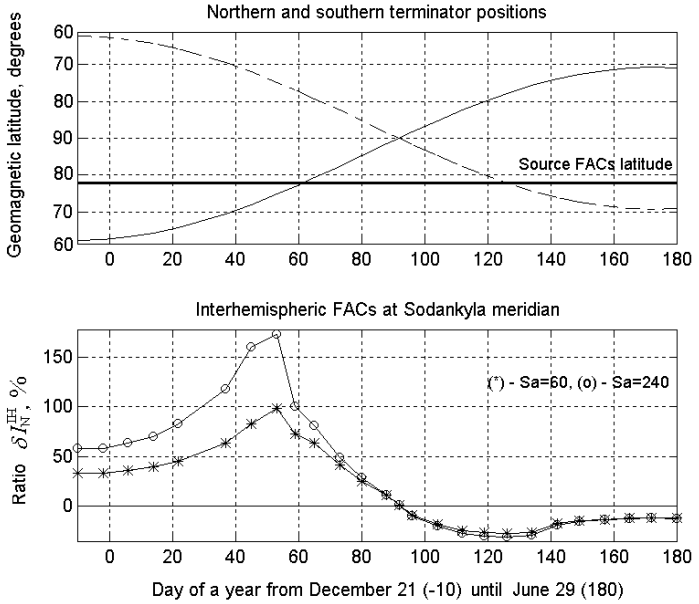

Figure 3.16. Variation of the ratio of the interhemispheric and source FACs at the Sodankyla meridian (Scandinavian sector) over half a year from the winter to summer solstices (similar to Fig. 3.14).
It is interesting to note that this does not occur at the equinoxes but some time earlier or later. For

After passing this symmetry point, the role of the northern terminator in the branching of FACs becomes insignificant. Toward the northern summer, the currents begin to flow over out of

the northern hemisphere into the southern hemisphere. So after the zero points the interhemispheric FACs alter the sign. However, the ratio factor $\delta I_{\mathrm{N}}^{\mathrm{IH}}$ for this period never exceeds 30% because the source FACs have a large value due to the high conductance of the sunlit ionosphere.

3.4.2 Dependence of field-aligned current magnitude on distance between sources and their location with respect to the terminator

In order to find out how the fraction of the total southern FACs branched out into the secondary field-aligned currents depends on the relative distance between sources, we conducted simulations under the following conditions. The Earth's axis inclination angle α was 23.45°, and the highest terminator latitude χ was 66.55°, which corresponds to the winter solstice. We chose the distance between the centers of primary current sources and the terminator *s* to be equal to 330 km (about 3° along the meridian), and varied *d*, the distance between the sources. The dependence of the ratio factor $\delta I_{\mathrm{N}}^{\mathrm{IH}} = I_{\mathrm{N}}^{\mathrm{IH}} / I_{\mathrm{N0}}^{\downarrow}$, i.e., the fraction of downward secondary currents relative to the downward original currents, on the ratio *d/s* is shown in Fig. 3.17.

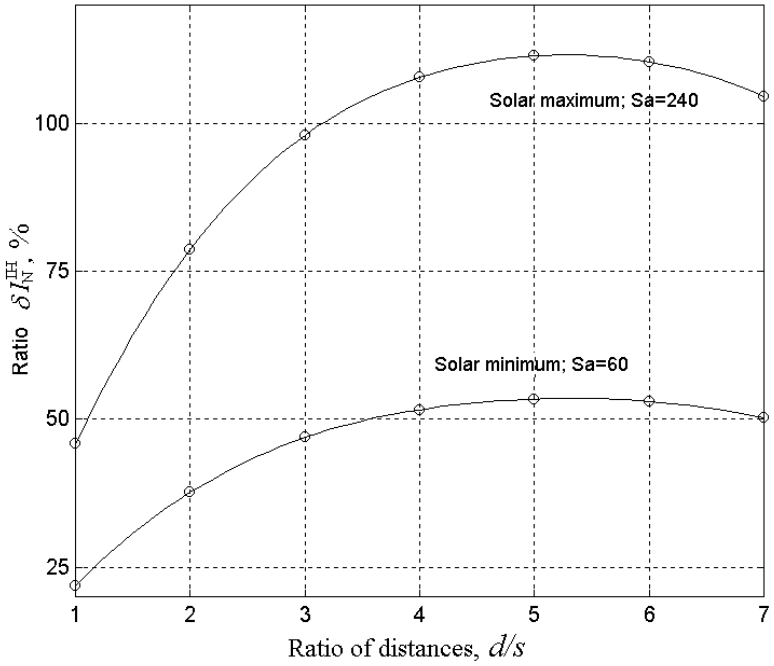

Figure 3.17. Calculated ratio of the interhemispheric to source FACs dependent on the distance between the sources and the terminator. The ratio *d/s* is the ratio of the distance between centers of the source FAC to the distance from these currents to the terminator. The curves are related to minimum (S_a = 60) and maximum (S_a = 240) of solar activity.

The two curves are drawn for the minimum and maximum of solar activity. Fig. 3.17 shows that the field-aligned current drain to the opposite hemisphere is dependent on the relative distance between current sources with respect to their distance from the terminator. Very close sources (ratio 1) “feed” each other and supply only a small fraction of their currents to the interhemispheric FACs. A large distance between the sources also results in decrease of the interhemispheric FAC generation. The optimum is reached for the distance ratio ~5.

3.5. Conclusions

In this Chapter we showed that seasonal conductance asymmetry due to the solar radiation can lead to the emergence of interhemispheric field-aligned currents between the conjugate hemispheres. Interhemispheric currents appear along the magnetic field lines going out of the regions with strong conductance gradients, associated with the solar terminator. These currents close a part of ionospheric currents in the summer high-latitude ionosphere through the conjugate winter ionosphere of the opposite hemisphere. Using the complex analysis technique, we developed an analytical method for the interhemispheric currents’ estimations under simplified conditions. To make further advance in understanding the interhemispheric currents we applied numerical solution of appropriate equations for a smooth conductance gradient around the solar terminator line. The total magnitude of interhemispheric currents was found to be close to one half of that of ionospheric currents crossing the terminator projection in the sunlit ionosphere. We showed that although the interhemispheric currents are stronger for summer/winter conditions, they are significant for equinoctial conditions as well because of a diurnal change of the terminator position with respect to the geomagnetic poles. We described quantitatively the relative values of these currents for various geographical sectors and seasons. Although we do not have decisive experimental data pertaining to the phenomenon so far, we proposed a method of calculation of field-aligned currents from the known potential (SuperDARN observations) and conductance (model or other observations) and the obtained values that reasonably agree with the body of the data on field-aligned currents.

An interesting implication of the model considered in this section is that the upward directed interhemispheric currents may lead to the generation of auroras near the terminator [*Lyons*, 1981; *Kozlovsky and Lyatsky*, 1999; *Stenbaek-Nielsen and Otto*, 1997]. The observations of the auroras around the terminator might be possible from the satellite based UV images.

Another interesting consequence of the interhemispheric currents is that no correlation but rather anti-correlation between auroral events associated with these currents must occur in opposite hemispheres. Although there are yet no direct observations supporting this prediction, poor conjugacy of some auroras [e.g., *Stenbaek-Nielsen and Otto*, 1997] may possibly be considered as an indirect indication of the effect.

CHAPTER 4

IONOSPHERIC CONDUCTANCE EFFECTS IN OCCURRENCE OF SUBSTORMS, GLOBAL STORMS, AND RADAR AURORAS

For the magnetospheric sources maintaining FACs of certain intensity, equation (3.38) clearly indicates that the electric field intensity in the ionosphere depends strongly on the conductance. We have shown in the previous section that the conductance distribution in both hemispheres has to be considered to describe the electric potential/convection pattern in each of the hemispheres. The ionospheric conductance depends strongly on the sun's radiation that experiences well-defined seasonal and solar cycle variations. Because of these variations, one would expect seasonal and perhaps solar cycle control of many phenomena occurring in the high-latitude ionosphere.

This chapter is focused on studies of several phenomena whose occurrence is ultimately related to the ionospheric conductance in conjugate areas of both hemispheres, the total conductance of the earth's ionosphere. These are the substorms, storm sudden commencements and HF radar echo occurrence. We argue that the diurnal and annual variations in the photoconductance of the ionosphere play important if not key role in these phenomena. This implies that they are not random because there is a common factor involved. This is important for practical applications, for example for the successful prediction of strong storms and substorms as these can be harmful for various technological systems on the ground and in space. Most of the results presented in this Chapter have been published by *Benkevitch et al*. [2002], *Koustov et al*. [2004], and *Khachikyan et al*. [2005].

4.1 Cycles in geomagnetic activity and their reasons

The geomagnetic activity has long been known to be highly variable in time. One of the earliest variations distinguished in the geomagnetic activity was its semiannual variation. Two major mechanisms were suggested to explain this variation: the axial mechanism and the equinoctial mechanism. The axial mechanism [*Cortie,* 1912] is based on the 7.2° tilt of the solar rotation axis with respect to the ecliptic plane. Due to this tilt the earth reaches the highest northern and southern heliographic latitude on September 6 and March 5, respectively. Near these dates the earth is more in line with the sunspot zones as suggested by *Cortie* [1912], or with midlatitude coronal holes as suggested by *Bohlin* [1977]. The axial mechanism can explain the seasonal modulation of geomagnetic activity, but it can not explain its diurnal modulation.

The equinoctial mechanism [*Bartels*, 1925; 1932; *McIntosh*, 1959] was suggested to explains both seasonal and diurnal modulations of the geomagnetic activity. The equinoctial hypothesis states that the variation of angle ψ between the sun-earth line (which is close to the solar wind flow direction) and the earth's dipole axis is the controlling parameter in the variation of geomagnetic activity. It assumes that the coupling efficiency of the solar wind with the magnetosphere is maximim at the equinoxes, when the ψ becomes close to 90º, and it is reduced beyond the equinoxes, when the ψ sharpens. The angle ψ varies seasonally because of the 23.45° tilt of the earth's rotation axis with respect to the ecliptic plane, and it varies diurnally due to ~11.5° inclination of the dipole axis to the earth's rotation axis. Its full range is from ~55° to ~125°; the range of the acute angle between the earth-sun line and the dipole axis, ψ, is ~55° to 90°. At the equinoxes, ψ varies between ~78.5° and 90°, but at the solstices it varies between ~55° and ~78.5°; therefore, at the equinoxes the resulting diurnal variation is relatively weak compared to that at the solstices. Despite the observational support, the way the equinoctial mechanism works has remained unknown [*Cliver et al.,* 2000]. *Boller and Stolov* [1970] suggested a theoretical explanation of the equinoctial effect in terms of the Kelvin-Helmholtz's instability. They proposed that annual and diurnal variations of the angle of attack of the earth's dipole to the solar wind cause modulations of the conditions favorable for the development of Kelvin-Helmholtz's instability at the flanks of the magnetosphere. This proposal could explain both diurnal and semiannual variations of geomagnetic activity. However, *Russell and McPherron* [1973] mentioned that *in situ* measurements of the solar wind-magnetosphere interaction indicated that this instability is not responsible for geomagnetic activity.

The results of *in situ* measurements of the solar wind-magnetosphere interaction lead to another approach in explanation of diurnal and seasonal variations of geomagnetic activity. Taking into account that geomagnetic activity at the ground level is caused by substorms and that magnitude of the IMF southward component has been shown to control substorm activity, *Russell and McPherron* [1973] suggested a model of UT/seasonal variations of geomagnetic activity (further referred as the RM model) based on the assumption that the substorm activity reaches its maximum when the earth magnetic dipole is in line with the most probable southward direction of the IMF. This dipole orientation is most favorable for the merging process and hence for the solar wind energy input to the magnetosphere. The direction of the SW flow in the Parker spiral is assumed to be the most probable direction about which the IMF fluctuates. Therefore the controlling parameter is the angle φ between the *Z* axis of the *GSM* coordinate system and the solar equatorial plane [*Russell and McPherron*, 1973]. This angle varies over a range from about 52° at equinoxes to 90^0 at solstice. When the angle φ reaches minimum value of 52°, which occurs on April 5 at 2230 UT and on October 8 at 1030 UT, the geomagnetic activity is expected to be at its maximum, because at these times the solar wind magnetic field lying entirely in the sun's equatorial plane has its maximum projection on the *Z* axis of the GSM coordinate system. The *Russell and McPherron* [1973] model predicts both seasonal and diurnal variations of geomagnetic activity and suggests that the spring maximum in activity is associated on average with the IMF directed toward the sun and the fall maximum with IMF directed away from the sun. As the IMF polarity varies with the 22-year magnetic solar cycle, the RM mechanism predicts stronger spring maximum for one 11-year solar cycle and stronger fall maximum for another 11-year solar cycle. The RM mechanism is dependent on both tilt of the sun's rotation axis and earth's dipole axis with respect to the ecliptic plane and may be considered as a combination of the axial and the equinoctial mechanisms.

Fig. 4.1 shows a) the plot of the ψ angle, the controlling parameter in the equinoctial model, and b) the φ angle, the controlling parameter in the RM model as functions of months and UT hours (from *Cliver et al.* [2000]). It is evident that both models predict the increase in geomagnetic activity near equinoxes for daily averaged data.

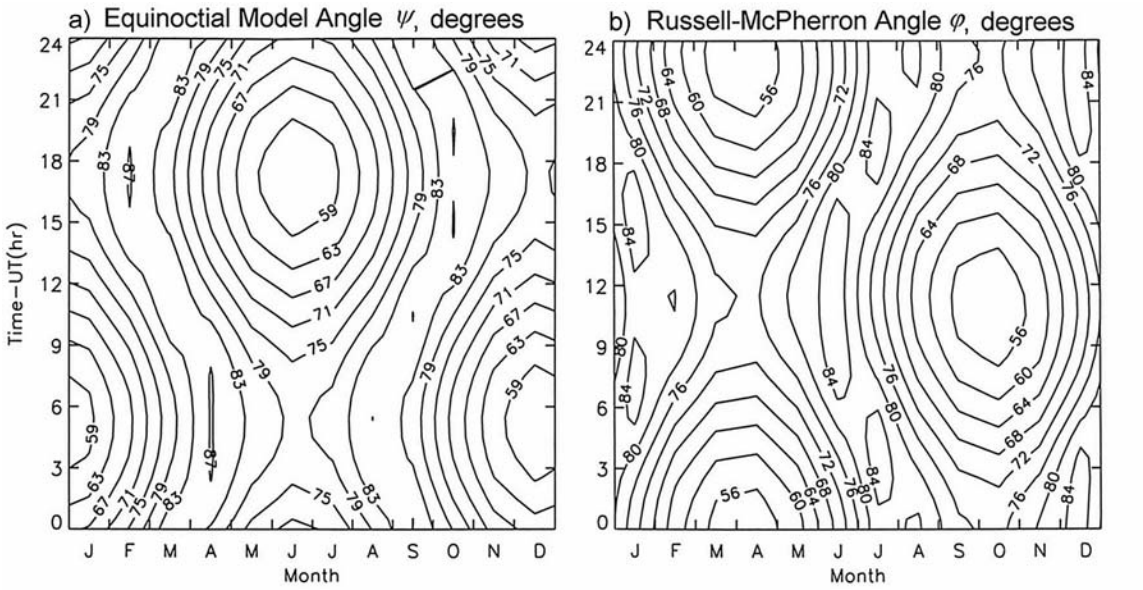

Figure 4.1. A contour plot in degrees of the seasonal and diurnal variations of the controlling parameters in a) equinoctial model and b) Russell-McPherron model. [from *Cliver et al.,* 2000]

The equinoctial model (a) predicts maxima of the geomagnetic activity near the largest ψ [*McIntosh*, 1959]; this occurs at equinoxes. The RM model predicts maxima of the geomagnetic activity near the smallest φ [*Russell and McPherron*, 1973]. The equinoctial model (a) predicts larger UT variation at solstices, but the RM model (b) predicts larger UT variation at equinoxes. The equinoctial model (a) predicts maxima of geomagnetic activity for monthly averages at 1100 and 2300 UT (when ψ is the largest). The RM model predicts maxima of geomagnetic activity for monthly averages also at 1100 and 2300 UT when the φ angle is the smallest.

The UT variation predicted by the RM model (Fig. 4.1b) has a phase lag of about 6 hours as compared to prediction by the equinoctial model (Fig. 4.1a). The reasons for this phase lag have been discussed in detail by *Russell and McPherron* [1973]. The UT variations of both angles depend on seasons.

At present there are no doubts that equinoctial and the RM mechanisms are both responsible for UT/seasonal modulation of geomagnetic activity [Cliver et al., 2000; Lyatsky et al., 2001; Clua de Gonzalez et al., 2001 and references therein]. Cliver et al. [2000] have found that equinoctial mechanism could be responsible for about 65% of semiannual modulation, whereas axial and RM mechanisms are responsible for the other 35%. At the same time, no such estimations are made for the case of UT modulation of geomagnetic activity.

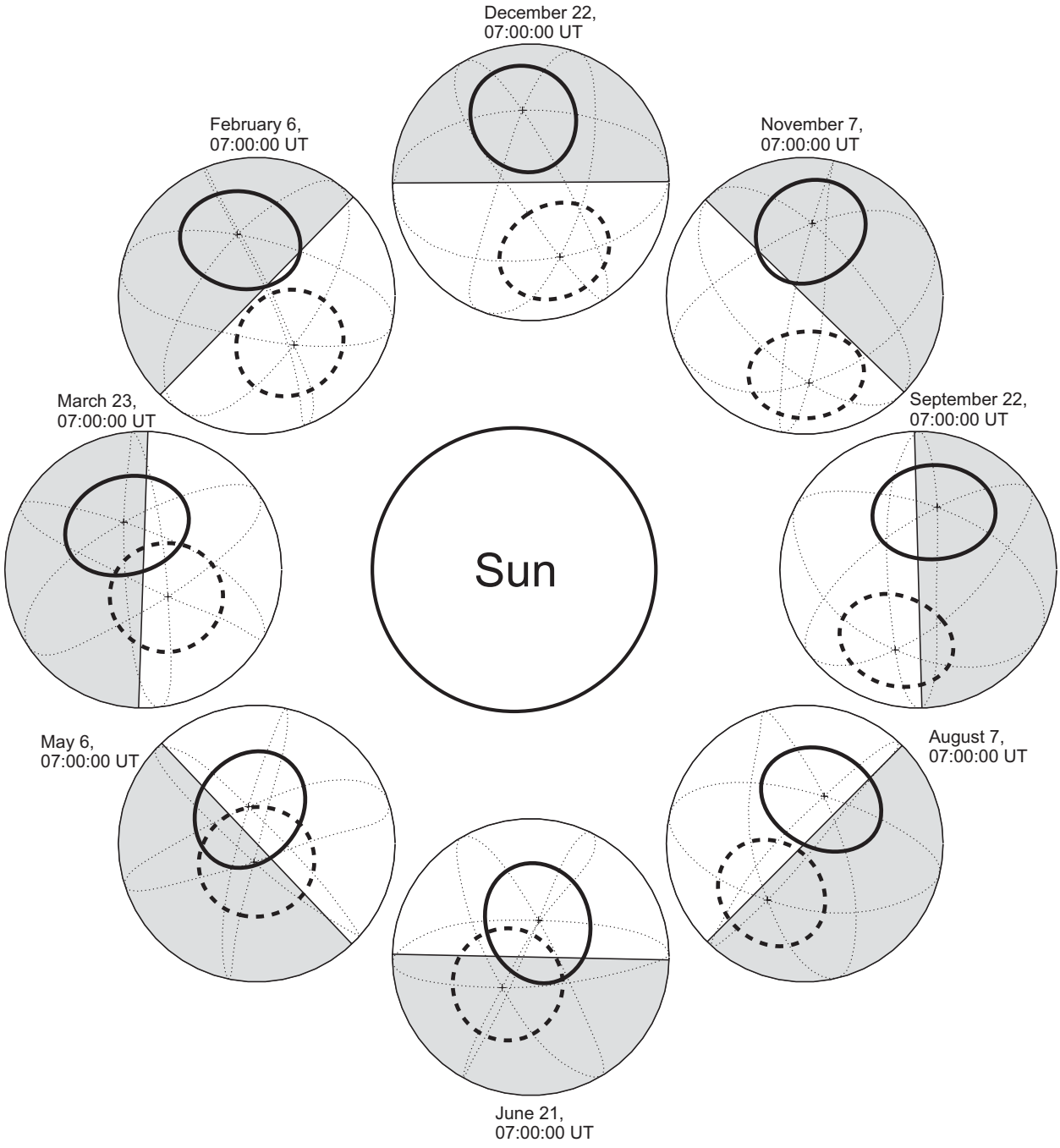

Figure 4.2. A scheme showing positions of the ±66° AACGM latitude ovals with respect to the darkside ionosphere at 0700 UT for eight evenly distributed days of a year. The earth projections on the ecliptic plane are given for the days close to solstices (December 22 and June 21), equinoxes (March 23 and September 22), and for the intermediate days. The shaded halves denote the dark sides. The magnetic parallel at +66° AACGM in the northern hemisphere is shown as a thick solid oval line. The -66° AACGM parallel in the southern hemisphere is shown as a thick dashed oval line. The thin dotted lines are for the AACGM meridians.

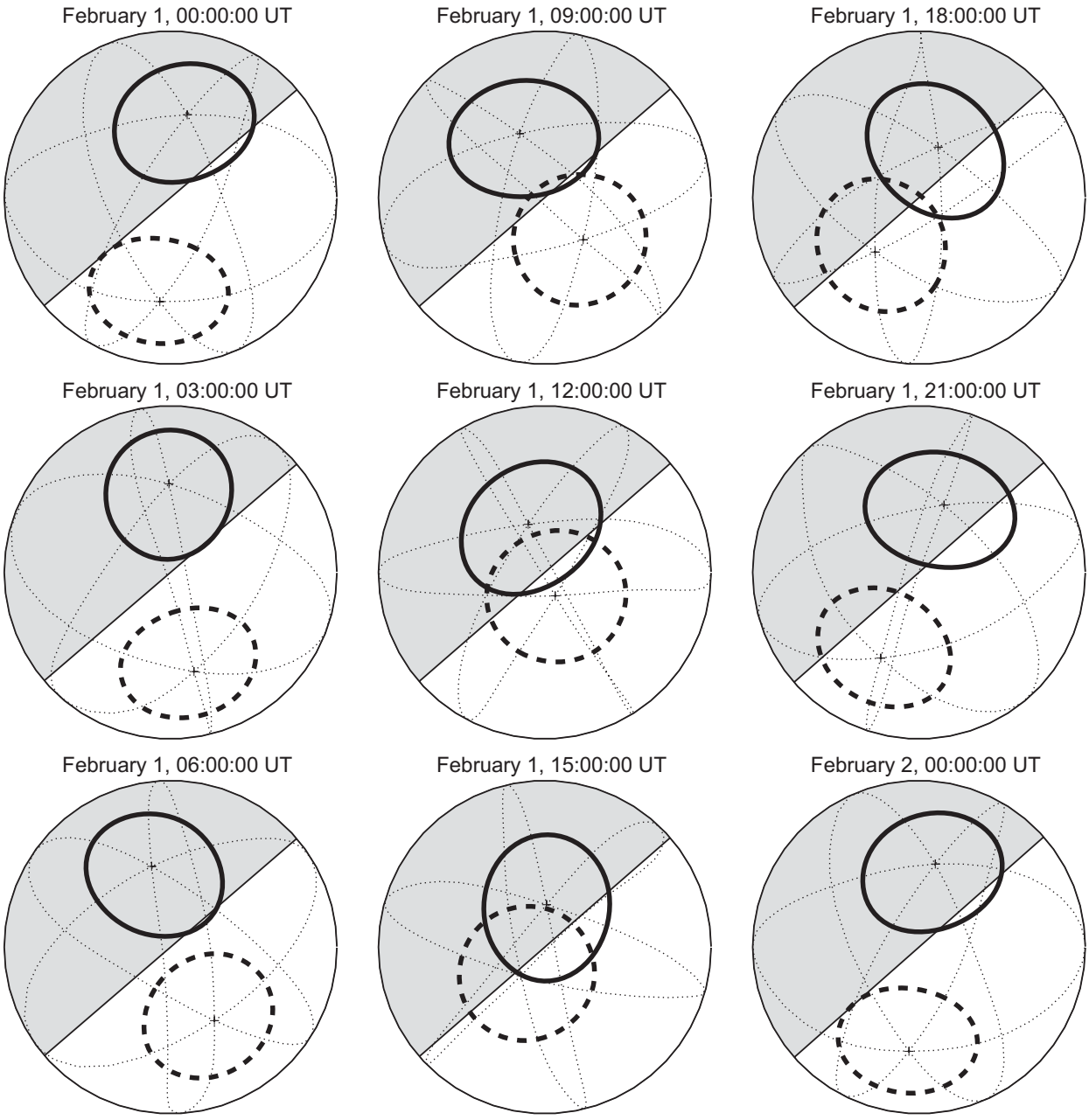

Figure 4.3. The same as Fig. 4.2 but the earth ecliptic projections shown here are three hours apart within the same day, February 1.

Recently, a new theoretical explanation of the equinoctial effect was suggested by *Lyatsky et al.* [2001], who assumed that geomagnetic activity depends on solar illumination of the nightside auroral oval, with the maximum activity when neither hemisphere is sunlit and minimum activity when the nightside oval of either hemisphere is sunlit. *Lyatsky et al.* [2001]

argued that the total ionospheric conductance is a major factor for global magnetospheric events. *Kan* [1993], *Lysak* [1991] and *Lyatsky and Hamza* [2001] showed theoretically the significance of ionospheric conductance for the geomagnetic and auroral activity. *Newell et al*. [1996], *Ahn et al*. [2000] and *Petrinec et al*. [2000] provided observational evidence confirming the importance of ionospheric conductance in determining the extent of geomagnetic and auroral disturbances. The important role of the low total ionospheric conductance in complex features of sudden commencements, particularly in middle latitudes in winter, was mentioned recently by *Kikuchi et al.* [2001].

In order to better understand the explanation of equinoctial mechanism by *Lyatsky et al.* [2001] one should note that on its yearly path around the sun and due to its axial rotation the earth takes various positions with respect to the sunlight direction. Therefore, conjugate areas of the earth's geomagnetic coordinate grid at the high-latitude ionospheric level can take several positions with respect to the terminator line. Since in the conjugate areas the geomagnetic field lines are closed, the conductance distributions within these areas must be added up to make "total conductance". At different moments any two conjugate points can be a) both sunlit with high total conductance; b) both in the darkside with low total conductance; c) northern point sunlit and southern point in darkness with total conductance like that at the northern point; d) southern point sunlit and northern point in darkness with total conductance like that at the southern point. Fig. 4.2 illustrates this idea by showing the earth in its projection on the ecliptic plane for several seasons of a year at the same time of 0700 UT. One can see that during the interval from March 22 to September 22 at 0700 UT both ovals (±66° AACGM) have their nightsides in the darkness, and, hence, the total conductance is low. From November 7 to February 6 at 0700 UT one of the 66° ovals (the southern one) is entirely exposed to the sunlight. Therefore, its nightside segment has relatively high conductance, and the total conductance is high, too. Fig. 4.3 shows a number of similar ecliptic earth projections but for several moments over one day, February 1. One can conclude that both northern and southern ovals (66° AACGM) have their nightside segments in darkness and hence low-conducting from 0900 UT to 2100 UT. To describe the total conductance quantitatively, we computed the sum of the conductances at the conjugate ionospheric ends of high-latitude flux tube as envisaged by *Lyatsky et al.* [2001] and *Newell et al.* [2002].

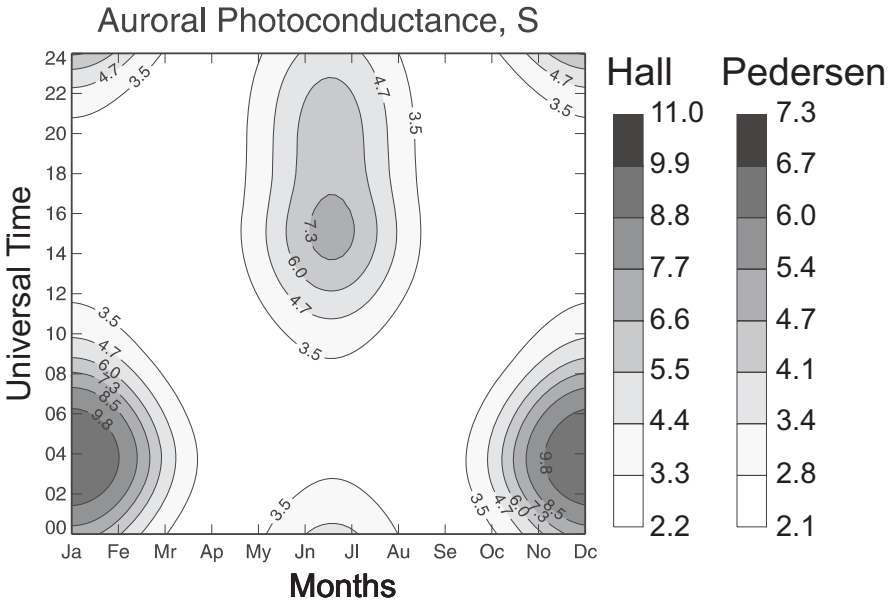

Figure 4.4. Seasonal/UT distribution of the total (northern plus southern) ionospheric Hall and Pedersen photo-conductances at magnetic local midnight for the 66^o magnetic latitude.

The AACGM coordinate system (described by *Baker and Wing* [1989]) was used to find conjugate points at 66^o magnetic latitude and at the midnight meridian. We calculated the solar zenith angle χ at each of the conjugate points at 15-min intervals throughout the day and then computed the height integrated Hall and Pedersen ionospheric photoconductances in Siemens (S) as proposed by *Robinson and Vondrak* [1984], but with smooth Gaussian decay on the nightside (see Appendix C). A moderate solar activity was assumed, S_a=140×10^{-2} W/m^2 (note that in the *Robinson and Vondrak* [1984] formulae S_a=140 was substituted). Also, a background nocturnal conductance of 1.0 S was included.

Fig. 4.4 shows the computed total conductance distribution in the coordinates "universal time-month". Near winter solstice, there is a strong peak centered near 0400 UT and a drop between 12 and 20 UT. Near summer solstice there is a broad maximum centered at ~ 16 UT and a somewhat narrower minimum from about 04 to 08 UT.

Thus there are three different models for the geomagnetic activity variation: (1) axial hypothesis, (2) equinoctial hypothesis, and (3) RM effect. The way the axial and RM models work is fundamentally different from that of the equinoctial model. While the mechanisms (1) and (3) explain the semiannual variation by the variation in the properties of the solar wind, the mechanism (2) reduces the coupling efficiency near the solstices. *Cliver et al.* [2000] suggested a beautiful metaphor characterizing the aforementioned models: "…while the axial and RM

mechanisms work by “building mountains” at the equinoxes, the equinoctial hypothesis “digs valleys” at the solstices”. Note that although the mechanism suggested by *Lyatsky et al.* [2001] is in the framework of the equinoctial model, it reduces not the coupling efficiency itself, but rather the magnetosphere’s ability to accumulate energy in the tail particle populations due to its dissipation in the highly conductive sunlit ionosphere. In the subsequent sections we show how the idea of *Lyatsky et al.* [2001] works for substorms, SSCs, and radar aurora occurrence.

4.2 Substorm onsets and ionospheric conductance

The concept of a substorm was introduced by *Akasofu* [1964] who described the evolution of auroral arcs during a typical cycle of auroral activity involving three phases: the growth phase, the expansion phase, and the recovery phase. The expansion phase of a substorm is characterized by sudden increases in luminosity and geomagnetic activity beginning at ~66° magnetic latitude and covering width of ~70° longitude around midnight. Accompanying geomagnetic perturbations in the auroral zone are usually referred to as a magnetic substorm. These ionospheric signatures of a substorm are caused by the processes occurring deep in the magnetosphere [*Rostoker*, 1999]. The addition of energy to the magnetotail through the reconnection results in a thinning of the plasma sheet. This eventually leads to the start of reconnection at a point closer to the earth. A large blob of plasma called plasmoid then is disconnected from the earth magnetic field and starts moving downtail at high speed.

The variations in many other magnetospheric and ionospheric phenomena during substorms have been studied extensively over the last several decades [*Rostoker et al*., 1980; *Rostoker*, 2002].

4.2.1 Magnetic perturbations associated with a substorm

There are several discernible phases of the magnetic substorm. In the midnight sector, high-latitude magnetograms of the *H*-component form “negative bays”: sudden decrease down to (typically) –100 to –300 nT within ~5-10 minutes, then slow return within 1-2 hours. A typical substorm magnetogram is shown in Fig. 4.5. During the periods of negative IMF B_Z, the high-latitude ionospheric current system can take two major patterns, called DP2 and DP1. These two patterns are shown schematically in Fig. 4.6. The DP2, shown in Fig. 4.6a, reflects the two-cell convection flow. The substorm expansion phase is characterized by sudden building up of the

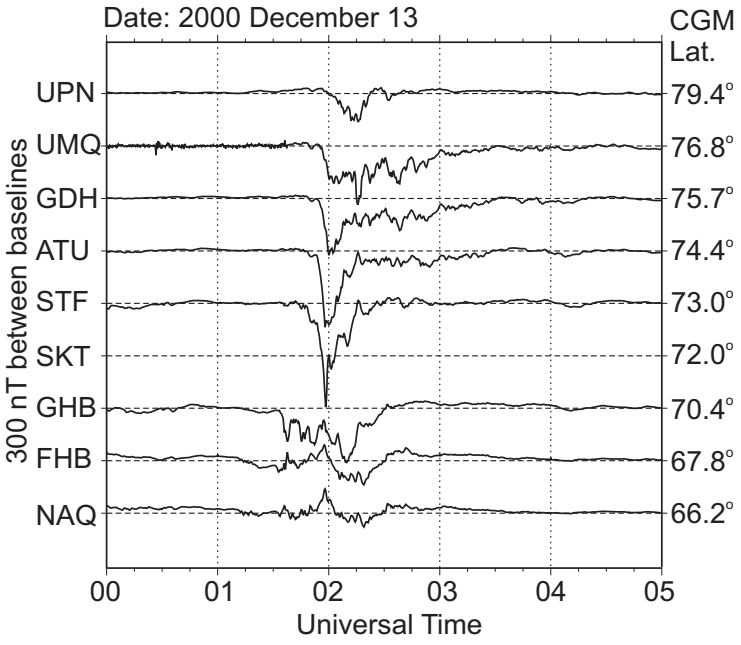

Figure 4.5. Magnetic traces of *H*-component from a set of magnetometers from the Greenland west coast magnetometer chain. A negative bay is clearly seen at STF, ATU and GDH stations, which indicates substorm onset time prior to 0200 UT.

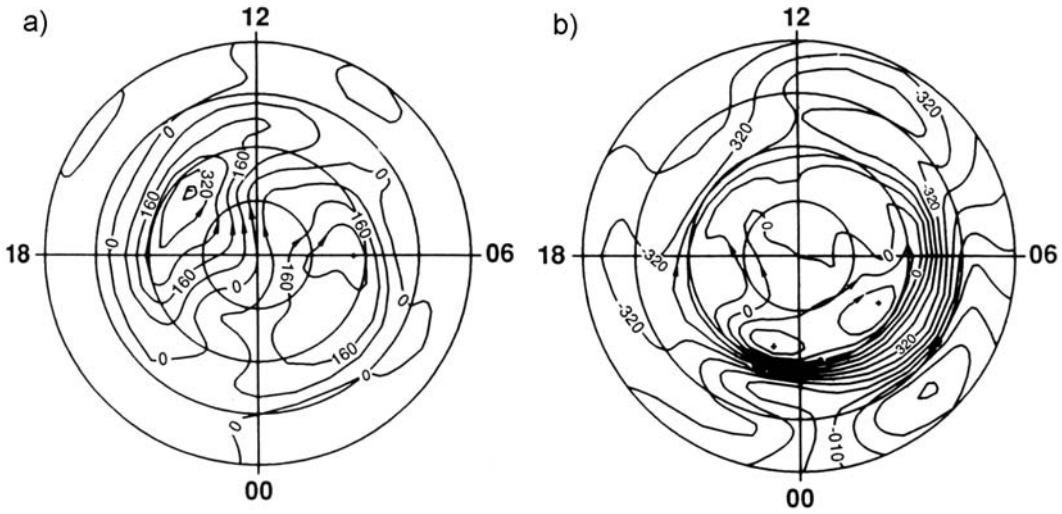

Figure 4.6. Examples of high latitude ionospheric current systems. a) The two-cell DP-2 current system is established during the substorm growth phase, corresponding to periods of negative IMP B_z. b) The single-cell DP-1 current system dominates during the substorm expansion phase. (From *Clauer and Kamide* [1985]).

westward substorm (or auroral) electrojet, which is a part of the DP1 current system, shown in Fig. 4.6b. The magnetic effect of the westward electrojet prevails over that of the 2-cell DP2 current system (Fig. 4.6a), which typically exists prior to the substorm expansion.

4.2.2 The auroral electrojet indices AL, AU, AE, and AO

The auroral electrojet indices were defined by *Davis and Sigiura* [1966] as a measure of the global auroral electrojet activity relatively uncontaminated by the effect of the ring current. They suggested using the magnetic traces of *H*-component from several magnetometer stations uniformly placed around the pole at the electrojet latitude, about 70° CGM. The stations are listed in Table 4.1 and their locations are shown in Fig. 4.7. The AU and AL indices are introduced as the upper and lower envelopes of the magnetograms from all the pre-selected stations. The AU an AL have been available as one-hour values since 1957. The technique is illustrated in Fig. 4.8. There is some evidence that the AU index variations may be related to the DP2 magnetic disturbances driven by the variations of the solar wind electric field while the AL index is more related to substorm activity and the DP1 current system [e.g., *Nishida*, 1968]. The AE and AO indices are derived from the AU and AL indices using the equations AE = AU–AL and AO = ½(AU+AL) [*Mayaud*, 1980]. An example of all the four index variations is given in Fig. 4.9a,b. Note the indications on possible substorms at 0800 and at 1400 UT. The ring current contribution to the AU and AL is considered approximately equal and is cancelled in the AE index through the subtraction. Therefore, AE only responds to the strengthening of the auroral electrojets (see Fig. 4.9b).

Table 4.1. Geomagnetic observatories used for preparing AL, AU, AE, and AO index data.

Observatory	Code	Geographic Coord.		CGM Coord.	
		Lat, deg.	Lon., deg	Lat., deg.	Lon., deg
Abisko	ABK	68.36	18.82	65.12	102.08
Dixon Island	DIK	73.55	80.57	68.39	156.01
Cape Chelyuskin	CCS	77.72	104.28	71.75	175.55
Tixie Bay	TIK	71.58	129.00	65.75	-162.94
Cape Wellen	CWE	66.17	190.17	62.85	-114.88
Barrow	BRW	71.30	203.25	70.03	-109.98
College	CMO	64.87	212.17	65.12	-96.95
Yellowknife	YKC	62.40	245.60	69.65	-60.44
Fort Churchill	FCC	58.80	265.90	69.31	-28.66
Poste-de-la-Baleine	PBQ	55.27	282.22	66.10	-1.65
Narssarssuaq	NAQ	61.20	314.16	66.59	43.51
Leirvogur	LRV	64.18	338.30	65.10	67.82

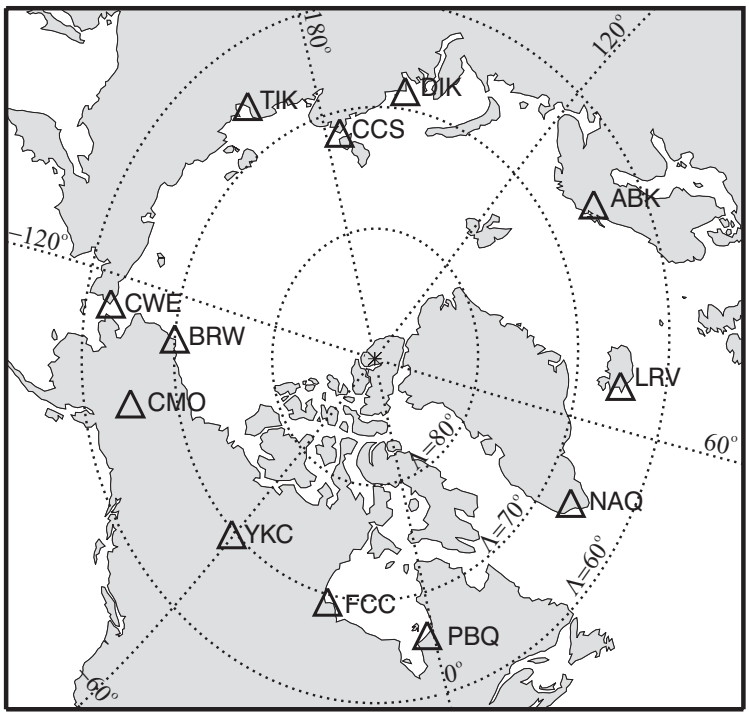

Figure 4.7. Locations of the magnetic stations whose data are used for computing the AE index. AACGM geomagnetic latitudes (70°, 75° and 80°) and longitude (every 60°) are shown by thin dotted lines.

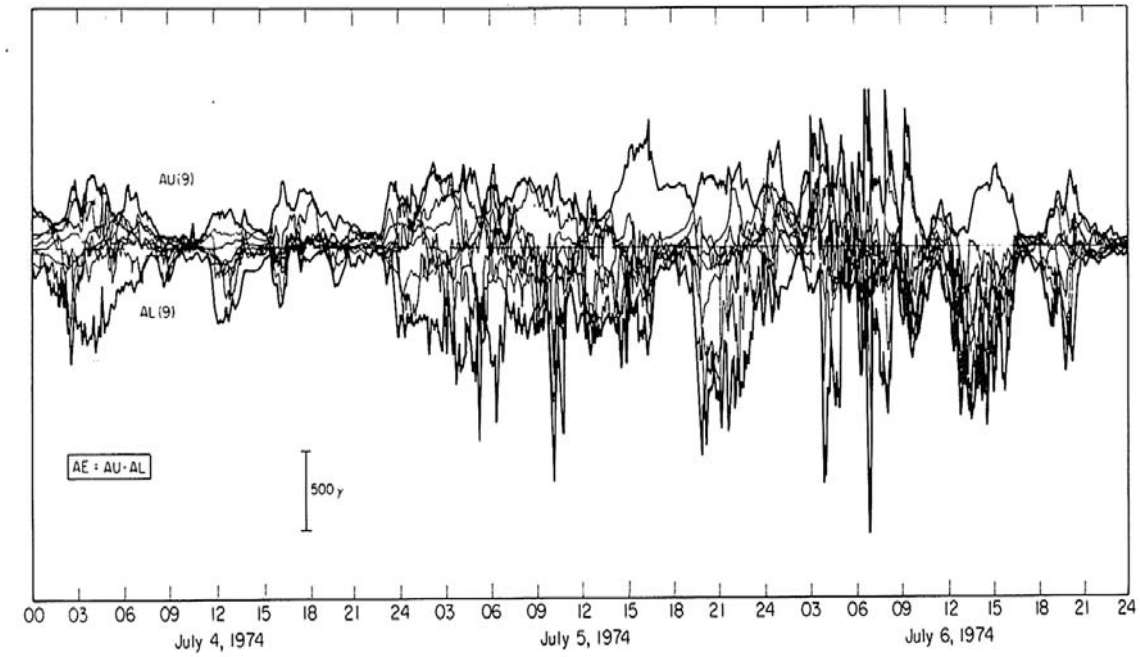

Figure 4.8. Illustration of the method for obtaining AL and AU. Traces of the H-records at the 12 stations are superimposed. The resulting upper and lower envelopes are the AL and AU indices. (after *Allen et al*. [1976])

The relation of the AE index to substorm onsets is not so straightforward because shortly after the interplanetary magnetic field (IMF) turns southward, the DP2 current system is usually established [*Nishida*, 1968]. The DP2 current system contributes to the values of the AU and AL indices in the evening and morning sectors, respectively.

In general, enhanced convection leads to increased eastward electrojet (increased AU) and westward electrojet (decreased AL) activity so the AE index can increase substantially even without substorms. Also, motions of the electrojets relative to the ground stations rather than a change in current intensity (at the substorm onset) might lead to some AE index change.

For substorm onset identification, the AO index was suggested [e.g., *Mayaud*, 1980] as a better indicator. Indeed, in the absence of substorm activity, enhanced convection can lead to a DP2 current system that produces westward and eastward electrojets of approximately the same intensity. This leads to an increase in AU, an equal decrease in AL, and therefore a substantial AE increase, whereas the AO index will remain close to zero. During a substorm, the strong intensification of westward electrojet in the midnight sector causes a strong increase in the AL index, leading to increases in both the AE and AO indices.

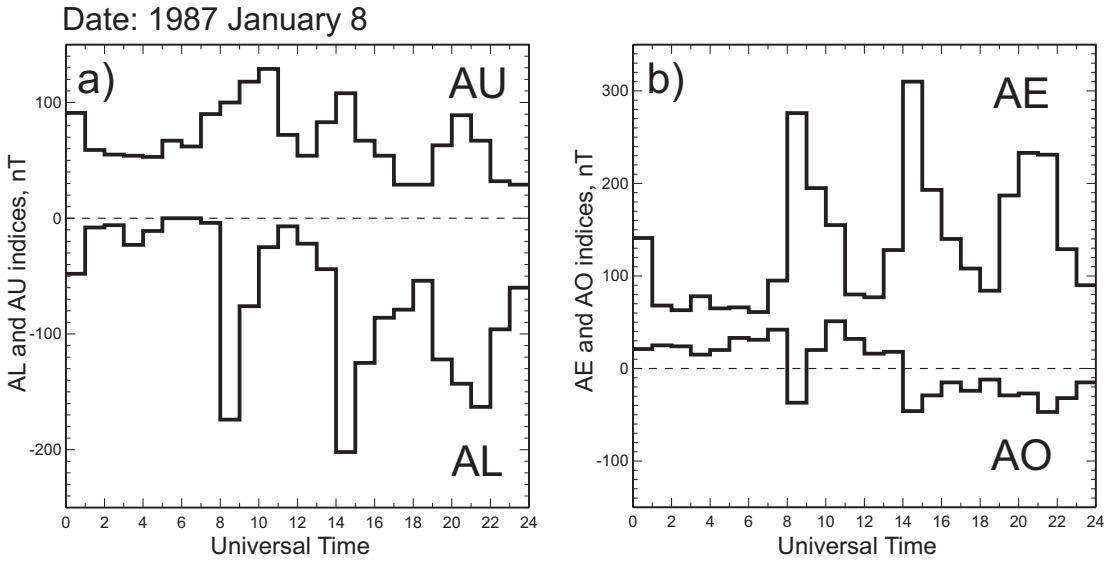

Figure 4.9. a) Variations of the AL and AU magnetic indices over 24-hour period. b) Variations of the AE and AO indices for the same period as in a).

The current systems during the growth and expansion phases result from increases in both the electric field and the conductivity. The dawn-to-dusk electric field increase is not confined just to the midnight sector, and the resulting general increase in both the eastward and westward

electrojets results in an increase in AE but almost no change in AO. On the other hand, the upward field-aligned current (FAC) in the substorm current wedge sector at substorm onset leads to a large localized conductivity increase that affects both AO and AE. Therefore, AE responds to both the general electric field increase and localized conductivity increase while AO responds mainly to the latter, and should be a better indicator of localized substorm onset activity.

4.2.3 Derivatives of AO and AE and their seasonal/UT variations

Although the AU, AL, AO and AE indices reflect substorm activity, the time for a substorm onset cannot be identified precisely, especially with hourly averaged indices (available for long-term studies) since substorm activity can last from tens of minutes to many hours. In this chapter we postulate that the derivatives dAO and dAE of the AO and AE indices are more reliable identifiers of substorm onsets. Negative dAO values indicate the strengthening of the westward electrojet during substorm onset as do positive AE values, so we consider here only positive dAE and negative dAO values. For the analysis we used the AE hourly data for 1957-1988 and the AO hourly data for 1968-1988 except for two years (1976 and 1977) for which these indices are not available. The data were taken from the Kyoto World Data Center WEB site. The AE and AO data are available for more recent years; however, we found these to be quite noisy which can be explained by missing original magnetometer records from key stations for these newer data.

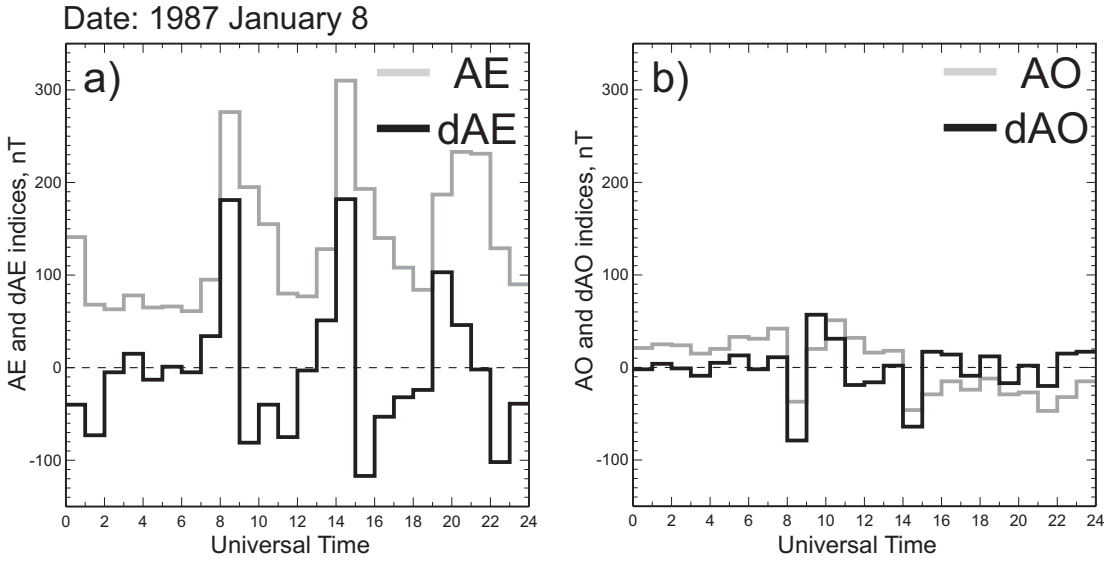

Figure 4.10. a) Variations of the AE index and dAE parameter for a 24-hour period. b) Variations of the AO index and dAO parameter for the same period as in a).

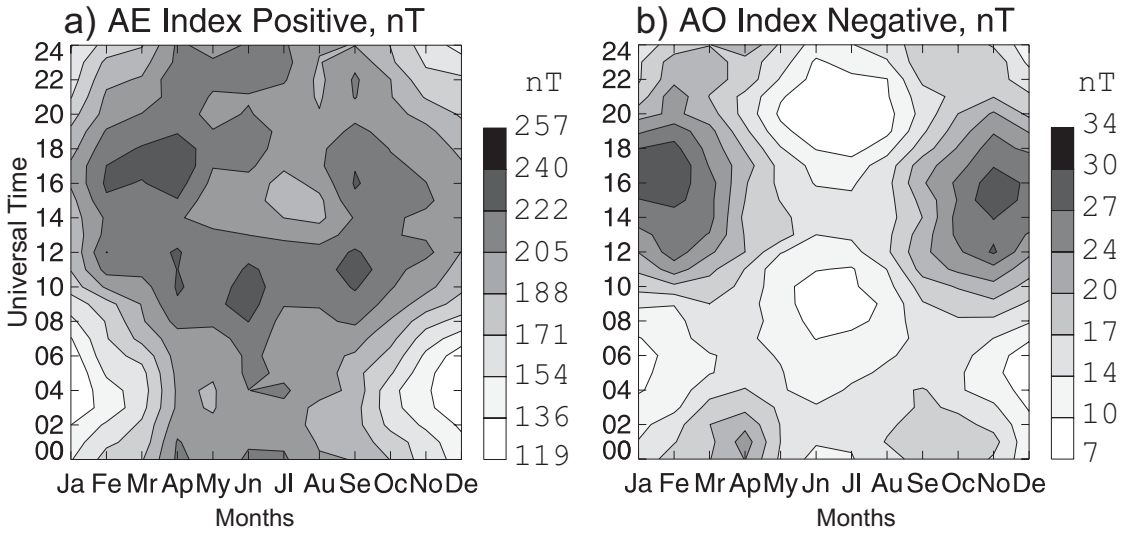

Figure 4.11. Seasonal/UT distributions of the AE (a) and AO (b) geomagnetic indices. AE index data are for 1958-1988 and AO index data are for 1966-1988.

To find the derivatives of the AE and AO indices we used the difference of these indices taken for the current and succeeding hour: $dAE_t = AE_{t+1} - AE_t$ and $dAO_t = AO_{t+1} - AO_t$. We note that for most of the years (but not for all), the index average value was assigned to the beginning of each 1-hour interval. Therefore the derivatives that we introduce here would be better to assign to 0.5-hour or even 1 full hour later time. However, this would be incorrect for every record, and for this reason we assign derivatives to the same time as for original AE and AO. An example of dAE and dAO variations compared to the respective variations of AE and AO are shown in Fig. 4.10. Before proceeding with dAE and dAO, we show first in Fig. 4.11 the 32-year (1957-1988) averaged seasonal/UT variations of the AE index and 23-year (1966-1988) averaged values of the AO index. Since our ultimate goal is to investigate periods of substorm activity, only negative AO values were used in creating Fig. 4.11. The distributions in Figs. 4.11a and 4.11b are very similar to those obtained earlier by *Cliver et al.* [2001] and *Lyatsky et al.* [2001] for the AE index and *Lyatsky and Hamza* [2001] for the AO index. We note that the plots of the AE and AO indices are significantly different. The AO plot shows only two main peaks, about a month before and after winter solstice at around 16-18 UT, whereas the AE index exhibits equinoctial peaks in the 10-18 UT interval. However, the most obvious difference is that there is virtually no AO activity near the summer solstice (June) whereas AE activity is quite pronounced. Notice that here and below all seasons are mentioned with respect to the northern hemisphere for which the AO and AE magnetic indices were derived.

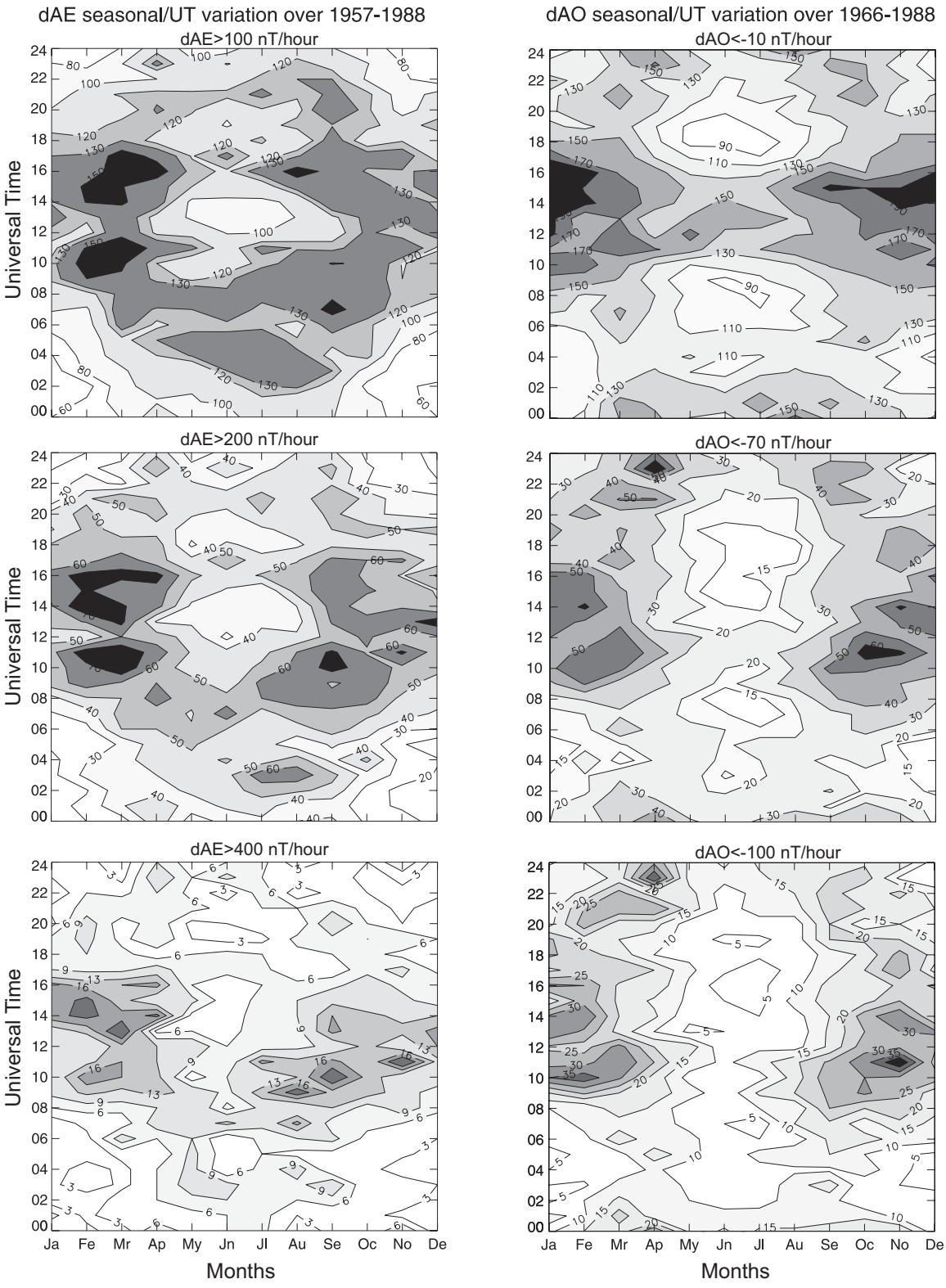

Figure 4.12. Seasonal/UT distributions for the number of occurrences of dAE (left column) and dAO (right column) assuming various thresholds. The thresholds for indices were selected as 100, 200, and 400 nT/hour for dAE and -10, -70, and -100 nT/hour for dAO. Each panel has its own color scale.

Fig. 4.12 shows seasonal/UT distributions for the occurrence of dAE (left column) and dAO (right column) for various thresholds from weak (top panels) to moderate (middle panels) to strong (bottom panels). Each panel has its own scale. We note that the distribution of dAO remains approximately the same for different thresholds while for dAE the distributions change with increasing threshold. For the highest thresholds (bottom panels) the distribution of the dAE is similar to that of dAO. We note also a clear shift in the position of peaks for dAO to 9-16 UT in Fig. 4.12 as compared with the position of the similar peaks in the AO index in Fig. 4.11b where they are located around 16-18 UT. A similar shift in the position of the winter peaks to earlier UT hours is also seen on diagrams for dAE.

To characterize quantitatively the degree of agreement between the AE-AO distributions and between the dAE-dAO distributions, we computed the correlation coefficients R between original AE and AO indices and between their derivatives. We found that R(AE, AO)= 0.29 (Fig. 4.11, a and b) while R(dAE,dAO) is 0.45 for dAE>100 nT/hour and dAO<-10 nT/hour (two top panels in Fig. 4.12), 0.59 for dAE>200 nT/hour and dAO<-70 nT/hour (two middle panels in Fig. 4.12), and 0.59 for dAE>400 nT/hour and dAO<-100 nT/hour (two bottom panels in Fig. 4.12). Thus, in spite of significant difference in the seasonal/UT distribution of the AO and AE indices, the seasonal/UT distributions of their derivatives show much more similarity.

All diagrams in Fig. 4.12 indicate enhanced occurrence of large absolute values of the dAO and dAE for winter months starting from September all the way to April. Local peaks fall on October-November and February-March. These are slightly away from the equinoxes. We state that these peaks correspond to the preferred interval for substorm onsets.

4.2.4 Preferred periods of substorm onsets and total ionospheric conductance

Several studies have attributed geomagnetic activity enhancements to the effect of the conductance in conjugate high-latitude ionospheres [*Lyatsky et al*., 2001; *Lyatsky and Hamza*, 2001; *Newell et al*., 2002]. The idea is that the nightside conductance in both hemispheres is important for the current flow between the ionosphere and magnetosphere, because the conjugate points in northern and southern hemispheres are electrically closed via the highly-conducting geomagnetic field lines. Fig. 4.13 illustrates this idea as applied to the substorms.

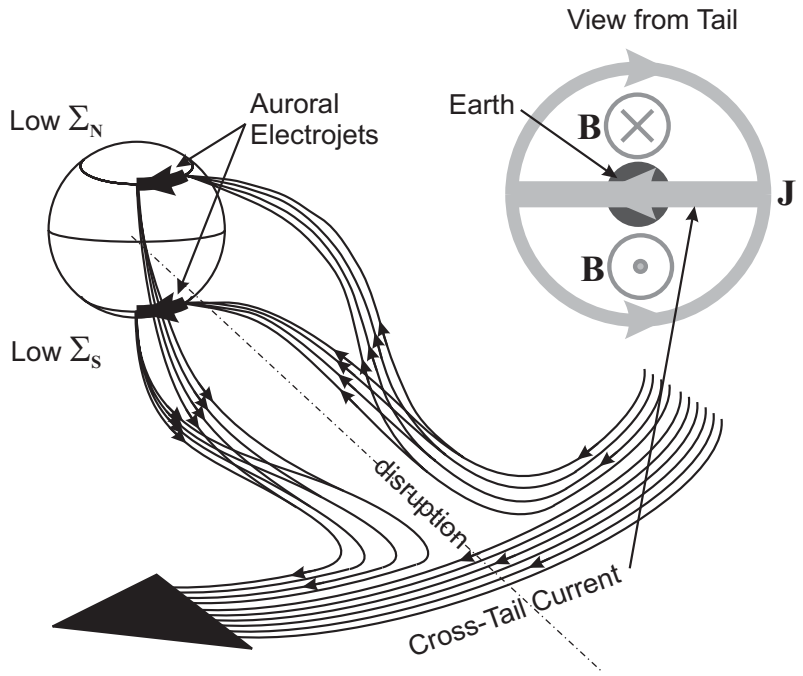

Figure 4.13. A scheme explaining how the low conductances in the midnight auroral zones in both northern and southern hemisphere create favourable conditions for building up high potential drop across the current paths, energetic particle acceleration, and subsequent substorm.

A disruption of the cross-tail current followed by formation of the substorm current wedge closed via the high-latitude ionospheres in both hemispheres is a necessary condition for a substorm onset. This process is schematically shown in Fig. 4.13. With high conductance in at least one of the hemispheres the energy of the cross-tail current will dissipate in either or both ionospheres in the form of Joule heating without any burst-like features. However, if the conductance is low in both hemispheres (i.e. both midnight auroral segments are in the dark region), the cross-tail current generator causes rapid build-up of voltage drop along the current path, most of which falls over its ionospheric closure portion. Charged particles are accelerated by the high potential drop along the substorm current wedge filaments. The high-energy particles precipitate in the auroral zone to form the auroral breakup. The local conductance enhancement due to ionization lets the cross-tail current work its way through a relatively thin ionospheric path in a burst-like manner, which is observed as the auroral substorm. This phenomenon is called the magnetosphere-ionospheric feedback instability, and its development requires low conductance in both hemispheres' midnight auroral segments [*Lysak*, 1991]. Therefore, in order that the feedback instability and subsequent substorm could develop, the northern and southern 66° CGM ovals must be both partially on the dark side.

If one compares the dAE and dAO parameter distribution in Fig. 4.12 with the distribution of the total conductance (i.e. the sum of conductances at the conjugate ionospheric ends of a high-latitude flux tube) shown in Fig. 4.4, the agreement between intervals of low conductance in Fig. 4.4 and of large values of dAO and dAE in Fig. 4.12 is evident. For example, the broad summer maximum at ~1200-2000 UT in Fig. 4.4 corresponds to the position of the minimum in dAO for the stronger cases (lower panels) in Fig. 4.12.

In order to evaluate the degree of agreement between the distributions of dAO/dAE parameters and conductances (Figs. 4.12 and 4.4), we computed correlation coefficients R between the parameters and the values of $1/\Sigma_H$ (see Table 4.2) by considering over-the-year sequence of each parameter. The coefficients R(dAO, $1/\Sigma_H$) vary in between 0.50 and 0.63 with larger values for the intermediate level of the dAO threshold (-70 nT/hour). Coefficients R(dAE, $1/\Sigma_H$) are better, in between 0.53 and 0.68, again with the best correlation for the intermediate threshold of 200 nT/hour. The correlation coefficients improve but not more than by 10% if one shifts values of dAE/dAO forward by 0.5-2 hours. This might be due to the way dAO and dAE were introduced, see Section 4.2.2. The presented parameters allow us to conclude that low solar illumination of conjugate auroral zones (low conductance) plays a significant role in substorm generation.

The distribution of dAO and dAE in Fig. 4.12 shows that for the winter months the peak in substorm onset occurrence is observed between 0900 and 1600 UT, when local midnight is located in the Alaskan and East Siberian sectors. For the summer months, the diurnal variation for dAO is not as pronounced. Similar conclusions were drawn by *Hajkowicz* [1998] from the analysis of the AE index; he reported, however, that interval of the strongest substorm occurrence is between 1300 and 1600 UT, corresponding to midnight in the Japanese and East Siberian sectors. Our analysis for substorms also agrees with the conclusions by *Hajkowicz* [1998], *Cliver et al.* [2000] and *Lyatsky et al.* [2001] that the period 0300-0600 UT for winter months is the most unfavorable for magnetic activity.

One can argue that longitudinal variations in magnetic indices are due to uneven longitudinal distribution of the magnetometer sites. This issue was considered by *Hajkowicz* [1998]. He concluded that the overall longitudinal maximum in AE is not an artifact. There are longitudinal variations in particle precipitation; in particular, stronger particle fluxes are observed over Alaska than over Scandinavia.

Table 4.2. The correlation coefficients, R, characterizing the agreement between the dAE/dAO parameters and the reciprocal of the Hall auroral conductance Σ_H.

Index lag, hours†	R(dAO, $1/\Sigma_H$) at thresholds, nT/h*			R(dAE, $1/\Sigma_H$) at thresholds, nT/h*		
	-10	*-70*	*-100*	*100*	*200*	*400*
0	.50	.63	.61	.65	.68	.53
0.5	.49	.63	.61	.63	.67	.53
1.0	.51	.64	.62	.67	.70	.54
1.5	.53	.64	.62	.72	.73	.55

* Each column contains the correlations for the parameters with different thresholds

† The lines differ by the temporal forward shift of the index data series that results in the index lag.

Besides, the *am* magnetic index (derived from a more uniform set of magnetic stations) indicates maxima reminiscent the ones we obtained for dAE and dAO, see Fig. 1 in *Cliver et al*. [2000].

4.2.5 Summary

In this study of preferred periods for substorm onsets, we have considered two new parameters, dAE and dAO, which are the derivatives of standard AE and AO over 1-hour intervals. dAE and dAO are better measurers of the sharp decreases in the geomagnetic field *H*-component at substorm onsets.

We found that seasonal/UT distributions of dAO and dAE are similar to those of the standard AO index. Clear peaks in dAE, dAO and in AO are centered near winter solstice at 9-16 UT with maxima in February-March and October-November. There is a pronounced minimum near summer solstice. The 9-16 UT sector corresponds to the time when magnetic midnight is in the Alaskan and East-Siberian sectors. Substorms are rare at all UT times in summer and between 0 and 6 UT in winter. We have thus confirmed and expanded previous findings by *Hajkowicz* [1998], *Cliver et al*. [2000], and *Lyatsky et al.* [2001].

The obtained distributions of substorm onsets have been compared with seasonal/UT variations in the total conductance of the high-latitude ionosphere in the midnight sector. Only the conductance due to the solar illumination was examined, and both northern and southern hemispheres were considered since the magnetic field lines electrically connect the ionospheric auroral zones. We found that, at solstice, substorm onsets occur primarily in the hemisphere for

which the midnight auroral oval is in darkness. On the other hand, substorm onsets occur in both hemispheres at equinox because both conjugate midnight auroral zones are in darkness. Periods of the strongest substorm occurrence are only slightly shifted from the equinoxes toward the winter solstice. These results suggest that the magnetosphere-ionosphere feedback instability might be a factor in triggering substorms since this mechanism requires low ionospheric conductance.

4.3 Storm sudden commencements and the ionospheric conductance

The geomagnetic storm is characterized by a simultaneous global decrease of the horizontal magnetic field intensity and its subsequent recovery [e.g. *Chapman and Bartles*, 1940]. The magnetogram traces of the *H* component at the storm time show a "negative bay" similar to that of a substorm. However, unlike substorms the magnetic storms are not confined to the nightside but have global character and usually last from hours to one day and even longer. The magnetic field depression is now known to be due to an enhancement of the trapped magnetospheric particle population and therefore increase of the global westward ring current. *Sigiura and Chapman* [1960] undertook a comprehensive study of storm morphology. Later *Sigiura* [1964] introduced a *Dst* index as the average of the *H* component variations among several evenly spaced low-latitude geomagnetic observatories. The *Dst* index represents the hourly average of *H* components stripped of the variations not related to the ring current [*Mayaud*, 1980]. The global storm intensities vary from weak with -30 nT < Dst < -50 nT to great (or intense) with Dst < -100 nT. At some great storms the *Dst* dropped down to -600 nT [e.g. *Gonzalez et al.*, 1994].

When a sudden increase in solar wind dynamic pressure reaches the earth, the magnetosphere is compressed, the magnetopause moves closer to the earth, and the magnetopause current intensifies. If a geomagnetic storm follows, this phenomenon is called a sudden storm commencement or SSC [*Kivelson and Russell*, 1996]. We argue that the high-latitude nightside ionospheric conductance exerts a considerable influence upon development of SSCs because the ring current is partially closed through the ionosphere via the evening and morning segments of the Birkeland region 2 FACs [*Tsyganenko*, 2000]. After the event of the SW shock structure arrival, high conductance in either nightside sector causes dumping of the ring current energy through Joule heating, which hampers further ring current intensification.

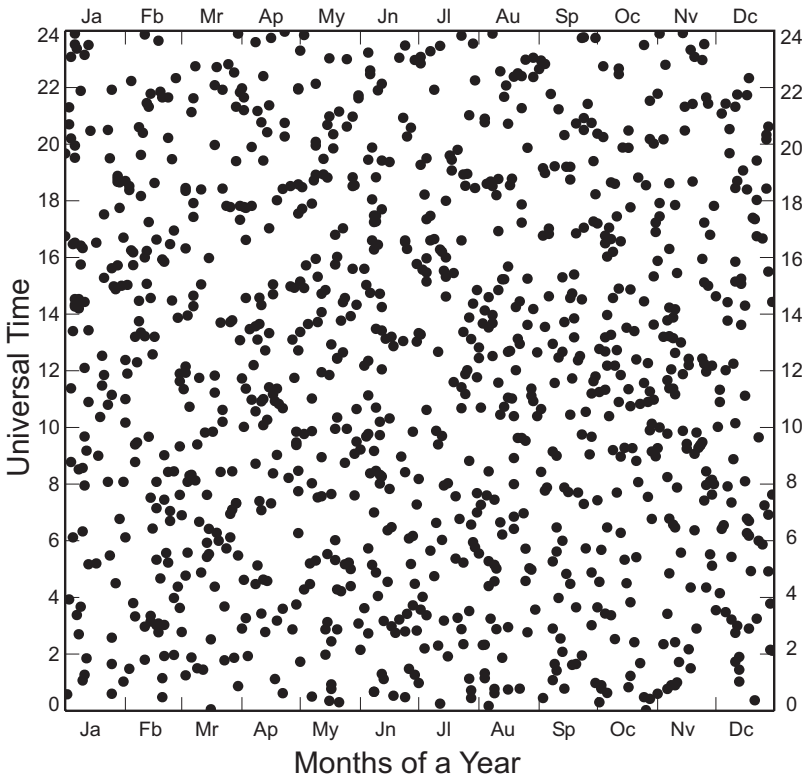

Figure 4.14. Seasonal/UT distribution of the 1066 SSC events from March 1968 to October 2001. Each individual event is shown as a dot.

Starting from 1968 more than forty observatories worldwide have been involved in the SSC monitoring [*Mayaud*, 1973]. A list of SSCs containing the data from 1968 year to the present can be found on the website of the National Geophysical Data Centre http://www.ngdc.noaa.gov/stp/GEOMAG/geomag1.html. In this section we consider the SSC data from May 1968 to September 2001 amounting 1066 events to explore a possibility of conductance control of the SSC occurrence. This study has been conducted in collaboration with *Khachikyan* [2005]. Therefore, SSCs have to be less frequent during the periods when one or both nightside auroral sectors are sunlit. Conversely, low conductance in the night sectors in both hemispheres prevents the ring current from energy losses and, hence, it is favourable for a sudden storm commencement. Fig. 4.14 shows the seasonal/UT distribution of the 1066 SSC events. The raw SSC data demonstrate their dependence on the 11-year and 22-year solar cycle, which is not a subject of this research (data are not presented here). However, in the global storm and SSC studies so far there have been made no attempts to remove in the SSC time series the upper frequencies to consider only the annual, semiannual, diurnal, and semidiurnal harmonics. These

harmonics are chosen because for most of the phenomena related to the geomagnetic activity they have been detected reliably and discussed for the most kinds of phenomena. It will be shown that the seasonal/UT distribution of the SSC data after such a "low-pass" filtering shows reasonable agreement with both *Russell and McPherron* [1973] and *Lyatsky et al*. [2001] models.

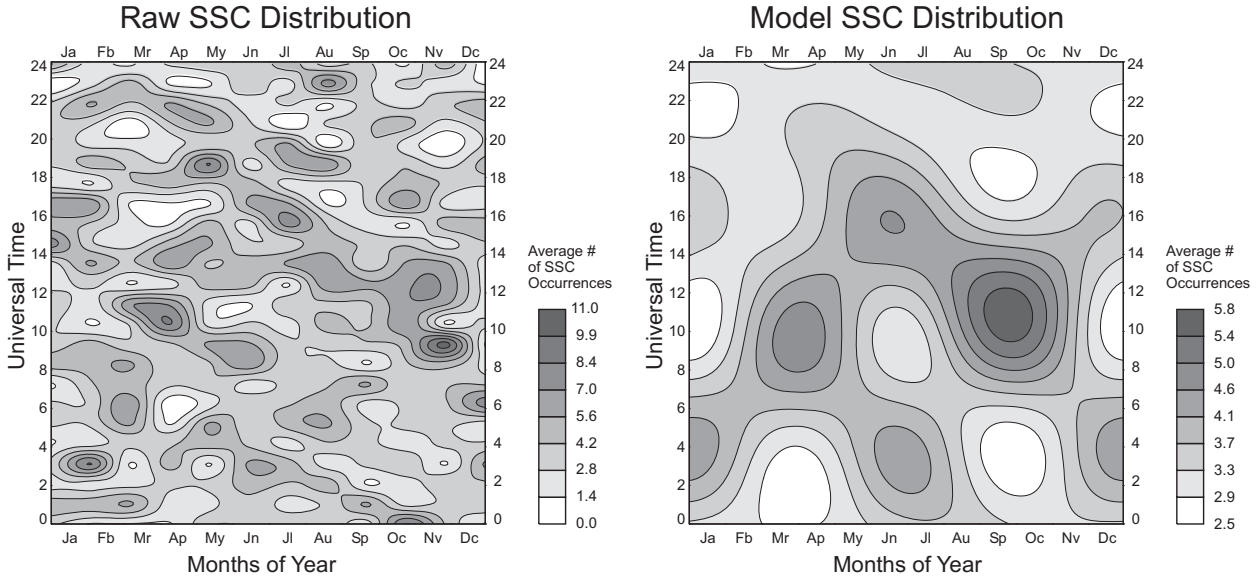

Figure 4.15. Contour plots of seasonal/UT distribution of the 1066 SSC events shown in Fig. 4.14 after processing. a) The UT vs months domain is divided into 1 hour by 1 month bins and the raw data are averaged within each bin. b) The binned data from (a) are fitted to a model containing annual and semiannual modes along the Month scale and diurnal and semidiurnal harmonics along the UT scale.

Unlike substorms, the SSCs onsets do not show obvious seasonal or diurnal modulations. In order to test if the features in Fig. 4.14 have seasonal and UT dependence the total number of 1066 SSC occurrences has been divided into 1 hour × 1 month bins, for the intervals from 0000-0100 to 2300-0000 and for all the months. The pattern in Fig. 4.15a shows the result of the binning. The pattern is still irregular, but it is not as random as that in Fig. 4.14. One can discern the equinoctial maxima between 0900 and 1500 UT from March to May and between 0800 and 1400 UT from September to November. Another broad maximum is observed in summer between 1300 and 2000 UT. Generally, the pattern shows a hatch-like facture revealing periodicity in both dimensions.

As a next step, the raw data in Fig. 4.14 have been fitted to a model, which is a two-dimensional harmonic function with annual and semiannual modes in one dimension and diurnal

and semidiurnal modes in the other dimension. The procedure is equivalent to the extraction of the two-dimensional modes mentioned above. Fig. 4.15b shows the result of the model calculations. The pattern has an absolute fall maximum at ~1100 UT. Also, the pattern of UT variation changes with season and the pattern of seasonal variation changes with UT. Fig. 4.16 shows the plot of averaged data against the model averages. In the yearly average plot on panel a) the occurrence rate has maximum near 1100-1200 UT.

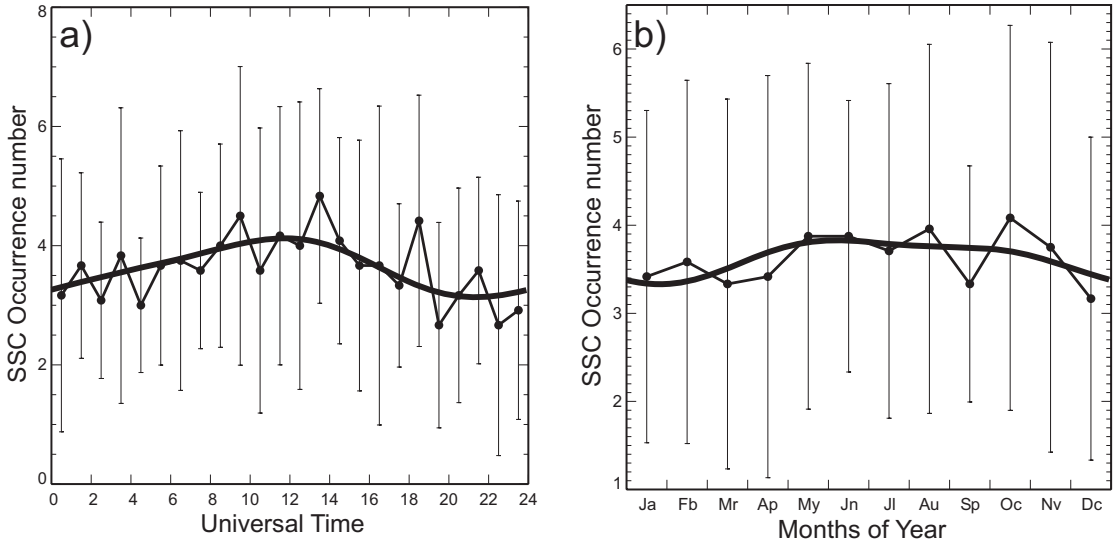

Figure 4.16. Plots of the SSC data averaged over a) years and b) days. The thicker smooth lines are produced by a model containing only diurnal, semidiurnal, annual, and semiannual variations. The vertical bars show standard deviations.

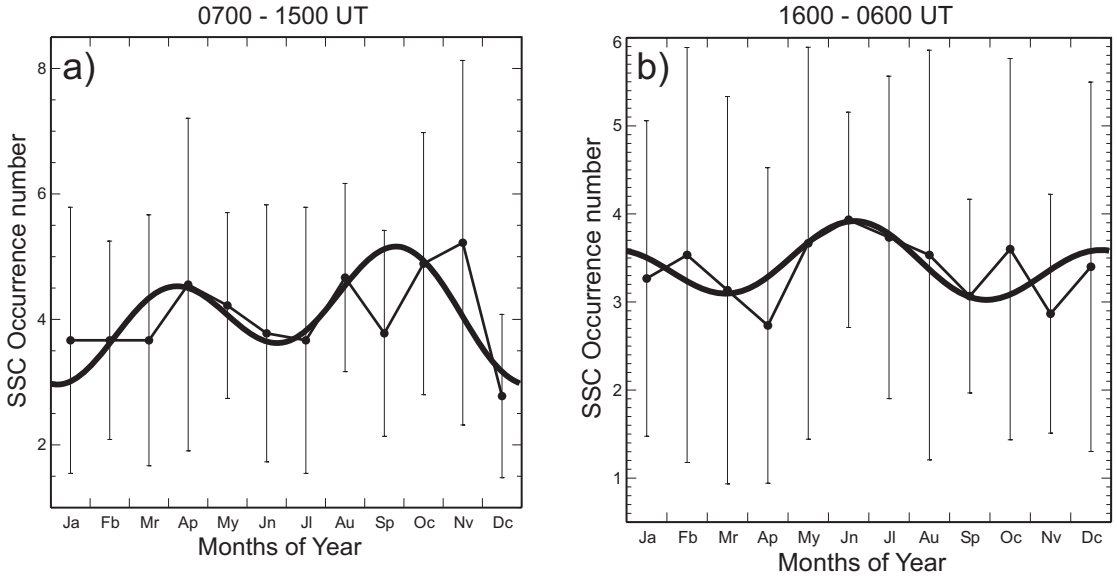

Figure 4.17. Plots of the SSC data averaged over years for parts of a day: a) 0700 – 1500 UT and b) 1600 – 0600 UT. The thicker smooth lines are produced by the model as in Fig. 4.16.

In the daily average plot in Fig. 4.16b the occurrence rate shows no obvious maxima or minima. However, a separate consideration of the data for the intervals 0700 – 1500 UT and 1600 – 0600 UT reveals of the annual variations. In Fig. 4.17 a) for 0700 – 1500 UT the occurrence number has a variation of the "classical" type with two equinoctial maxima. Fig. 4.17b shows a "non-classical" type of variation with the maxima in solstices. The "non-classical" peak of geomagnetic activity in July has already been found by *Clua de Gonzalez et al*. [1993, 2001] and attributed to the offsets in non-centered dipole of the earth magnetic field.

The interpretation of the diagram in Fig. 4.15b may be performed with the use of both *Russell and McPherron* [1973] and *Lyatsky et al*. [2001] models. The SSC peak at 1100 UT ±4 hours is in agreement with the *Russell and McPherron* [1973] model (see Fig. 4.1b). At the same time this model cannot explain the spring maximum between 0800 – 1200 UT and the summer maximum between 0200 – 0500 UT. However, these can be explained in the framework of total conductance model. In Fig. 4.4 the diagram has a "valley" where the total conductance reaches minimum just for the three mentioned SSC maxima. Moreover, the intensity of the fall 1100 UT maximum in Fig. 4.12b can be explained by the superimposition of the RM and the (equinoctial) total conductance effects. The SSC spring maximum between 0800 – 1200 UT and the summer maximum between 0200 – 0500 UT can be attributed solely to the work of total conductance mechanism.

4.4 Ionospheric conductance effects in occurrence of midnight F region echoes

In this section the long-term data (1996-2001) for a number of SuperDARN HF radars in both northern and southern hemisphere are considered to study the midnight F-region echo occurrence with the focus on the equinoctial effect and the nightside total conductance variation. According to the data the echo occurrence rate increases towards the solar cycle maximum for all radars considered and has a clear winter maximum for some of them [*Koustov et al.*, 2004]. The echo occurrence rate also experiences clear equinoctial maxima for many radar locations, especially at higher latitudes and in Antarctica. We shall show here that the equinoctial maxima are likely to be controlled by the electric field increase due both to the Russell-McPherron effect and to differences in conjugate ionospheric conductances controlled by the tilt of the earth's axis.

The occurrence of F-region coherent HF echoes depends upon both electric field and electron density distributions in the ionosphere because the gradient-drift (GD) instability (the

most commonly invoked mechanism of F-region irregularity formation) depends on the magnitude of plasma flow [e.g., *Tsunoda*, 1988] whereas the electron density controls the ionospheric refraction needed for radio waves to reach perpendicularity with the earth's magnetic field lines and thus to detect the irregularities [e.g., *Danskin et al.*, 2002]. Both these ionospheric parameters experience seasonal change, and one would expect some sort of seasonal variation in echo occurrence. Further, the F-region echo occurrence is controlled by additional factors such as the presence of strong plasma density gradients (which are unfortunately difficult to monitor) and radio wave absorption in the D region.

Many of the SuperDARN radars were operational from 1996 to 2001, i.e. from the solar cycle minimum to maximum. *Ruohoniemi and Greenwald* [1997] considered long-term (1988-1993) trends for the Goose Bay radar and concluded that the auroral zone echoes occurred more frequently at solar cycle maximum and during winter. The lack of echoes during the summer was interpreted as the result of solar radiation (for the sunlit ionosphere) smoothing out the plasma gradients necessary for the production of irregularities. Higher echo occurrence during winter was also reported by *Milan et al.* [1997] who investigated 20 months of data from the CUTLASS HF radar in Finland. They concluded that the ionospheric electron density profile controls the appearance of echoes at a specific range because refraction is a key factor determining the preferential time sectors and radar ranges for echo detection. *Ballatore et al*. [2001] found that there is a statistically significant correlation between northern hemisphere radar echo occurrence and negative IMF B_Z values, independent of season. More recently, *Parkinson et al*. [2003] considered one year (1999-2000) of echo statistics for the Australian SuperDARN radar and noticed a March (autumn) maximum, though the overall seasonal variation was apparently not significant.

It is possible that a combination of factors controls the echo occurrence and greatly diminishes the seasonal variation. Due to many other factors involved, the equinoctial maxima may not be prevalent even though they are generally expected to occur. In this study, we consider only the seasonal variation in F-region echo occurrence. We concentrate on midnight sector observations in the auroral zone where ionospheric echoes are more frequent and where they can be received via the direct propagation (half-hop) mode in which radio waves reach the F-region irregularities on a direct path determined by ionospheric refraction.

4.4.1 Data selection and processing

Fig. 2.1 (Chapter 2) shows the locations and fields of view of the SuperDARN HF radars in the northern and southern hemispheres. The PACE geomagnetic latitudes [*Baker and Wing*, 1989] 60^0, 70^0 and 80^0 are indicated. The echoes are monitored from ~65^0-80^0 MLAT. In this section, data for the following radars are discussed: Hankasalmi, Pikkvibaer, Saskatoon and Kodiak in the northern hemisphere and Halley and Syowa East in the southern hemisphere. These radars were chosen to investigate longitudinal variations as well as the effects of different offsets between the geomagnetic and geographic poles. For the selected radars, we used data only from the beams nearly perpendicular to the contours of equal PACE latitude. These meridionally-oriented beams were chosen to reduce the variability in echo occurrence due to different orientation of the beams with respect to the average convection pattern. To have a uniform data set, only observations in the standard operating mode (2-min or 1-min sequential 16-beam scans) were considered. In practice, there were usually at least 15 days of measurements for each month.

For the northern hemisphere, Fig. 2.1, one can notice that the chosen radars have similar geomagnetic coverage. There are, however, noticeable differences in their geographical coverage; the Hankasalmi and Pikkvibaer viewing zones are about 4^0 poleward of the Kodiak radar field-of-view (FoV) and ~10^0 poleward of the Saskatoon radar FoV. The southern hemisphere radars cover about the same magnetic latitudes as the northern hemisphere radars but they monitor much higher geographic latitudes. The radar selection was also based on a desire to examine conjugate effects seen by the radars at Pikkvibaer and Syowa. We limit our discussion to observations at magnetic latitudes around 70.5^0, typical latitudes at which the SuperDARN echoes can be received through the direct mode. At farther ranges, the signals are strongly affected by the propagation conditions that are difficult to monitor, so the far-ranges observations are not considered here.

For each of the radars, the echo occurrence rate was computed as a ratio of the number of registered echoes in every individual radar gate to the total number of observations in this gate for all selected beams over each month. A similar approach was undertaken by *Ballatore et al*. [2001]. Only ionospheric echoes stronger than 3 dB were counted. Ratios were averaged for each 10 minutes of observations and in 1^0 magnetic latitude bins. We should warn the reader that *Ruohoniemi and Greenwald* [1997] used a different method for counting the echoes; echo occurrence was assigned to a specific latitude irrespective of its longitude. This resulted in higher

echo occurrence rates as compared to the ones reported in this study. Though Ruohoniemi and Greenwald's approach is useful for assessing the data availability for convection studies, our method of counting is more suitable for studying echo occurrence. The echo occurrence rates reported in this paper are consistent with the data reported by others [*Hosokawa et al*., 2001; *Villain et al.*, 2002; *Parkinson et al*., 2003].

4.4.2 Seasonal variations of the F region echo occurrence and total nightside conductance

In order to see if there is anticorrelation between the midnight F region echo occurrence rates and the midnight conductances in both hemispheres their annual variation plots have been superimposed. In Fig. 4.18 we show the midnight echo occurrence rates at geomagnetic latitude 70^0 and the photoconductance of the ionosphere at this latitude. We also include data from the Kodiak radar from the northern hemisphere for two reasons. First, we demonstrate that this radar shows seasonal variations similar to the Hankasalmi radar, with minima during summer, local maxima during equinoxes, and overall enhanced occurrence during winter. The second reason is to show that the echo occurrence–conductance relationship is similar to other radars where magnetic midnight occurs in a different UT sector. In Fig. 4.18, the horizontal axis for the Halley and Syowa data starts from January. The procedure for computation of the photoconductance was described by *Benkevitch et al.* [2002]. The largest contribution to the photoconductances comes from the E region, with little contribution from the rest of the ionosphere. The sum of the conductances of both hemispheres (or the total conductance) is shown in Fig. 4.18 by the solid line, while the northern (southern) hemisphere conductance is shown by the dotted (dash-dotted) line. Note that the solid lines of total conductance are actually horizontal cross-sections of the diagram in Fig. 4.4 at the UTs corresponding to the midnight positions of the radars. One can see that for Hankasalmi there is an obvious anti-correlation between the seasonal changes of the total conductance and echo occurrence rate. For Halley the overall summer echo decrease correlates well with the conductance increase of the southern hemisphere (dash-dot line), with the "bite out" of echo occurrence in May-August correlating with the enhanced conductance of the northern hemisphere (dotted line). One can infer from the data that the two minima in the total conductance coincide with the equinoctial maxima in echo occurrence and an enhancement of the total conductance in June matches with the minimum in echo occurrence.

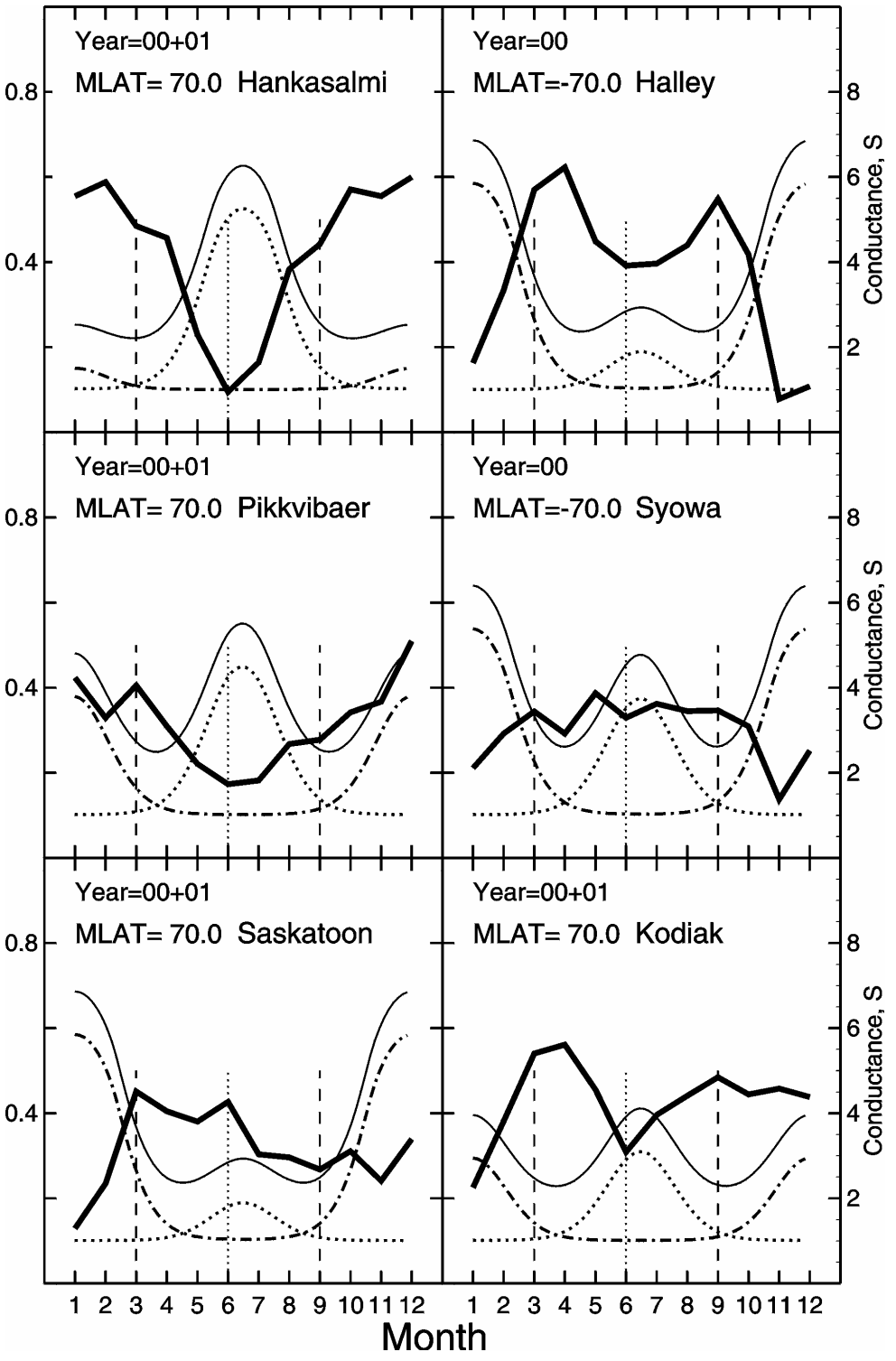

Figure 4.18. Midnight echo occurrence rates (thick solid line) between 2300 and 0100 MLT versus month for various radars in 2000-2001 (Syowa and Halley for 2000 only) at $\Lambda=70.5^0$. The thin solid line is the total photoconductance of the northern and southern hemispheres at $\Lambda=70^0$ and 0000 MLT for various months. The dotted (dash-doted) line represents conductance of the northern (southern) hemispheres as a function of month. The photoconductance calculations were described by *Benkevitch et al*. [2002] and in Appendix C of this thesis.

Observations at Pikkvibaer and Syowa (middle panels) show different behaviour. Both data sets indicate clear echo occurrence minima during local summer for the respective hemisphere with some barely recognizable equinoctial maxima. These variations seem to agree with the conductance change for the case of a one-hemisphere contribution and do not agree with the conductance variations for the case in which both hemispheres are considered.

Observations in Saskatoon (bottom left column) seem to agree with the hypothesis that echoes show up more frequently when the total conductance of the both hemispheres is low. The echo occurrence rise from January to May corresponds to the fall of southern conductance. This conclusion holds for Kodiak (the bottom right column). One can see some anticorrelation between echo occurrence and the total conductance of both hemispheres for June-July.

Overall, one can conclude that in a number of cases the local conductance is probably more important than the conductance in the opposite hemisphere since the Pikkvibaer and Syowa data are not very sensitive to the conductance of the opposite hemisphere. However, the observed variability of echo occurrence for the Hankasalmi and Halley radars is best explained by the total conductance curves. The data for the Kodiak, Pikkvibaer, Syowa and Saskatoon show some features that are consistent with the seasonal variations of the total conductance, for example the Pikkvibaer spring maximum correlates well with the decrease in the total conductance.

4.4.3 Summary

In this section we studied the seasonal variations of midnight echo occurrence for F-region HF SuperDARN observations at magnetic latitudes of $70.5^0 \pm 1^0$, both in northern and southern hemispheres. Data for 2000-2001 were considered. The observations are summarized below.

There is a seasonal variation in the midnight echo occurrence for most of the radars, and the character of this variation depends on the radar's geographic location. For the most poleward-located radars such as Halley, Syowa and Pikkvibaer, there is a clear tendency for a maximum during local winter. There are additional equinoctial maxima, especially in Antarctica, that are often even stronger than the winter maxima. For the lowest geographically located radar, namely Saskatoon, the seasonal variation in echo occurrence is less pronounced and there is an enhancement during summer.

It follows from the analysis that the seasonal variations in the F-region HF echo occurrence are controlled by a combination of the irregularity production factors and the

propagation conditions for the radio waves. The increases of echo occurrence detected by many of the radars during equinoxes are the result of more frequent occurrence of enhanced electric fields and perhaps a more irregular ionosphere. The more frequent occurrence of the electric field enhancements should be attributed to combination of the equinoctial effect of total conductance decrease *Lyatsky et al*. [2001] and the *Russell and McPherron* [1973] effect of seasonal change of the earth dipole orientation with respect to the solar wind flow. The lack of echoes during local summer for most of the radars is related to the irregularity absence caused by the lack of strong gradients. This occurs due to the smoothing effect of the relatively uniform photoionization. Summer propagation conditions are satisfactory most of the time.

4.5 Conclusions

In this Chapter we investigated natural cycles of three phenomena: substorms, SSCs, and HF radar auroras. For each of these we looked at seasonal and diurnal variations and showed that they depend on the conditions for the solar wind interaction with the magnetosphere, the *Russell and McPherron* [1973] mechanism, and on the magnetosphere's ability to respond to the enhanced reconnection rates by having appropriate conductances in the northern and southern hemispheres, as suggested by *Lyatsky et al*. [2001]. We found evidence that the total conductance of the ionosphere (northern plus southern) is important for occurrence of all the three phenomena.

CHAPTER 5

MAGNETOMETER EQUIVALENT CONVECTION AND PLASMA CONVECTION OBSERVED BY THE SUPERDARN RADARS

When various aspects of the high-latitude electrodynamics are studied experimentally, it is very important to keep in mind that conductance of the high-latitude ionosphere is an extremely important factor that controls the distribution of the electric potential and the plasma flow patterns. This chapter considers conductance effects in magnetometer data and the potential impact of uncertainties in magnetometer-inferred convection patterns on convection studies. More specifically, we compare true ionospheric convection data (SuperDARN) with magnetometer-defined equivalent convection direction. We also propose a generalized formulation and strict proof of Fukushima theorem and, building upon the theoretical developments, propose a method that improves magnetometer convection direction estimates. The other focus of the study is on the effect of the regular conductance gradients (associated with the sun's illumination) on the high-latitude magnetic perturbations. The results of this Chapter have been reported at the 2004 Annual SuperDARN Workshop [*Benkevitch and Koustov*, 2004], 2004 AGU Fall Meeting [*Liang et al.*, 2005] and 2005 Annual DASP Meeting [*Benkevitch et al.*, 2005].

5.1 Introduction

Ground-based magnetic observations have been widely used in space physics [*Birkeland*, 1908; *Cortie*, 1912; *McIntosh*, 1959; *Axford and Hines*, 1961; *Dungey*, 1961; *Akasofu*, 1964; *Davis and Sigiura*, 1966; *Nishida*, 1968; *Fukushima*, 1969, 1976a, 1976b; *Harang*, 1946; *Maltsev*, 1973; *Russell and McPherron*, 1973; *Leontyev and Lyatsky*, 1974; *Olson and Rostoker*, 1975; *Iijima and Potemra*, 1978; *Vasyliunas*, 1979; *Lyons et al.*, 1979; *Mayaud*, 1980; *Kamide et al.*, 1981; *Baumjohann et al.*, 1981]. Among other areas, the magnetometer measurements have contributed significantly to understanding of the plasma convection in the earth's ionosphere and magnetosphere. Comprehensive reviews on the topic were provided by *Untiedt and Baumjohann* [1993] and, earlier, by *Glassmeier* [1987]. Several methods have been developed to infer the plasma flow parameters from magnetometer observations. In the simplest approach, the plasma convection is estimated by relating it to the so-called magnetic equivalent convection (MEC), the vector obtained by simple rotation of the horizontal magnetic perturbation vector by 90º anticlockwise. A more reliable convection estimate can be obtained by applying the *Kamide-Richmond-Matsushita* (KRM) algorithm [*Kamide et al.*, 1981] which takes into consideration the conductance distribution over the globe. In other studies, the magnetometer data were combined with incoherent scatter radar measurements of the ionospheric electron densities [*Baumjohann et al.*, 1981; *Untiedt and Baumjohann*, 1993; *Amm*, 1998]. The most advanced method, the AMIE technique, combines the ground magnetic measurements and other data sources such as auroral imagers and satellites for the conductance estimates and satellite drift meters and coherent/incoherent radar data for the electric field estimates [*Richmond and Kamide*, 1988; *Richmond*, 1992]. In this approach, the magnetometer data are a part of the combined data set used for the global assessment of the high-latitude electrodynamics.

The deployment of the SuperDARN coherent HF radars [*Greenwald et al.*, 1995] covering the high-latitude ionosphere in both hemispheres marked a new stage in the convection studies. The SuperDARN radars provide convection maps on a global scale with a temporal resolution of 1-2 min. Importantly, these radars monitor the ionosphere not only over the land but also over the seas where it is impossible to perform regular magnetic measurements. The advantage of the radars is also in their ability to provide a direct measurement of the Doppler velocity of the scatterer, which in the F region should be a good estimate of the plasma velocity, whereas the magnetometer estimates are indirect as the magnetic perturbation depends, besides

the plasma drift, on other factors, particularly the conductance and current distributions for several hundred kilometers around the magnetometer site.

Magnetometers are sensitive to the electric currents flowing mostly at the E-region heights (around 110 km). These currents are proportional to the plasma convection velocity but they also depend on the ionospheric conductance. Quite often, an assumption is made that the conductance distribution in the ionosphere is spatially uniform and temporally constant. Then the convection velocity estimates can be done because according to the Fukushima theorem [*Fukushima,* 1976a] the magnetic effect on the ground due the vertical field-aligned currents is cancelled by the magnetic effect due to the Pedersen currents (flowing perpendicular to the magnetic field along the electric field direction). This means that the perturbation detected by a ground-based magnetometer is completely determined by the Hall current. The convection estimate based on the above assumptions is called the magnetic equivalent convection (MEC). The absolute value of the MEC vector depends on the conductance of the ionosphere, and because it is typically not known, one can simply express the MEC in units of the magnetic perturbations, nanoTeslas (nT).

Although the MEC can be obtained for any magnetometer at each instant of time, the relationship of the inferred MEC and the true plasma convection is more complicated than simple proportionality. The reason is that there are several additional factors that influence the magnetic perturbations. In the context of this work, the most important factor is the non-homogeneity of the conductance distribution in the high-latitude ionosphere. For such conditions, the traditionally formulated Fukushima theorem is not valid.

Despite difficulties with interpretation of the ground-based magnetometer data, they are widely used in the convection studies in a simple approach by equating the MEC and true convection [e.g., *Huang et al.,* 2000]. It is often believed that errors in such estimates are insignificant, especially for the sunlit ionosphere for which spatial variations of the ionospheric (Hall) conductance are not significant. However, the validity of this approach is an issue for every specific event.

In the past, several attempts have been made to compare the MEC and true convection [e.g., *Lyatsky et al.,* 1999a; *Huang et al.,* 2000]. *Lyatsky et al.* [1999a] considered several vortex events in the SuperDARN convection and associated equivalent currents and showed that the MEC patterns were displaced equatorward with respect to the SuperDARN-observed patterns.

For the dayside winter ionosphere this shift was attributed to the effect of the conductance gradient near the terminator. *Huang et al*. [2000] studied the agreement between the magnetometer- and SuperDARN-inferred convection for various MLT sectors. They showed that the patterns have rather good agreement between 1200-1500 MLT, but the agreement worsens around 1800 MLT. This was explained by the presence of large conductance gradients near the day-night transition region.

The previous studies have utilized only small numbers of individual magnetometers to compare with SuperDARN. In this Chapter we perform more comprehensive analysis by involving all recently operational northern hemisphere magnetometers and all SuperDARN radars.

5.2 Ionospheric convection and ground-based magnetometer measurements

The use of the ground-based magnetometers for prediction of the ionospheric plasma velocity is based on the assumption that the horizontal geomagnetic field variation $\mathbf{B}_\perp$ is completely due to the ionospheric sheet currents $\mathbf{J}$. The relationship between them can be derived from the boundary conditions for the magnetic field of the sheet current (see, for example, *Granzow* [1983], equation 7)

$$\mathbf{J} = \frac{1}{\mu_0}\hat{\mathbf{e}}_z \times \left(\mathbf{B}^e - \mathbf{B}^i\right), \tag{5.1}$$

where $\mathbf{B}^e$ is the external field variation above the current sheet and $\mathbf{B}^i$ is the internal field variation below the ionosphere. The vertical field component $B_\parallel$ is continuous in the vicinity of the surface, $B_\parallel^i = B_\parallel^e$, and the horizontal field components on both sides of the sheet currents, $\mathbf{B}_\perp^e$ above and $\mathbf{B}_\perp^i$ beneath, have equal magnitudes and opposite signs, whence

$$\mathbf{B}^e - \mathbf{B}^i = \mathbf{B}_\perp^e - \mathbf{B}_\perp^i = -2\mathbf{B}_\perp^i . \tag{5.2}$$

It is assumed that the ionospheric current sheet is within the conducting layer of the ionosphere at the altitude of ~110 km. For the ionospheric current patterns having the scales of hundreds of kilometers, the ground-based magnetometers located 110 km below may be considered to be in the "close vicinity" of the current sheet. This fact justifies the assumption that the horizontal field component $\mathbf{B}_\perp$, measured at the ground level, is actually the internal field component near the

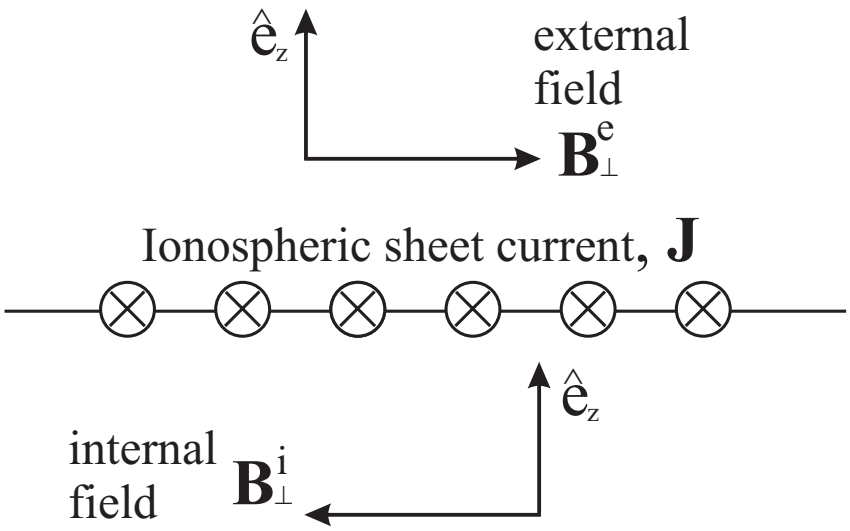

Figure 5.1. A schematic diagram explaining why the ground magnetic effect is only one half of that of the ionospheric current sheet.

current sheet $\mathbf{B}_{\perp}^{i}$, as shown in Fig. 5.1. This reasoning yields the equation associating the ionospheric sheet currents with the horizontal field variation measured at the ground level:

$$\mathbf{J} = -\frac{2}{\mu_0}\hat{\mathbf{e}}_z \times \mathbf{B}_{\perp}. \tag{5.3}$$

If one assumes that the measured field variation $\mathbf{B}_{\perp}$ (in nT) is due to the ionospheric sheet currents only, the azimuth and magnitude of the sheet currents $\mathbf{J}$ (in mA/m) can be estimated simply by rotating the $\mathbf{B}_{\perp}$ anticlockwise and scaling it by a factor $2\times10^{6}/\mu_0$:

$$J\left[\mathrm{mA}\cdot\mathrm{m}^{-1}\right] = \left(1.592\ \mathrm{mA}\cdot\mathrm{m}^{-1}\cdot\mathrm{nT}^{-1}\right) B_{\perp}\left[\mathrm{nT}\right]. \tag{5.4}$$

To what extent the above estimate is true depends on many factors. First, the E-region ionospheric currents are not the only source of the magnetic field at the ground level. Second, the earth has the underground conducting layer where the "reflected" or "mirror" currents are generated (this effect is considered in classical electrodynamics classes: any wire with current placed near a conducting surface generates its mirror image with a countercurrent [*Jackson*, 1975]). These currents introduce some error in the magnetic measurements, which is difficult to account for. For example casual rains can sharply increase the ground conductance and create temporary mirror currents. In addition, the magnitude of the E-region currents depends on the charge carrier's number density, which in turn is not uniform in space and constant in time. For

this reason the estimate of the ionospheric plasma velocity based on the magnetic equivalent currents is not perfect in most cases.

One more reason for discrepancies between the magnetometer estimates for the horizontal plasma velocities and measurements by other methods is the fact that the information is obtained from different ionospheric heights. For example, SuperDARN radars measure convection in the F region (altitude 160-500 km) while the magnetometers get the magnetic field variations from rather a thin layer with maximum conductance within the E region at the altitude ~110 km. The motion of electrons and ions are qualitatively different in these regions. In the F region the plasma is almost collisionless, both ions and electrons are magnetized, they drift with the same velocity, and therefore no drift-associated electric current is produced. In the E region the electrons are still magnetized, and the ions are not, due to the frequent ion-neutral collisions. The electrons undergo the $\mathbf{E}\times\mathbf{B}$-drift motion, but the ion drift is so heavily slowed down that it makes it possible to consider the ion drift velocity $\mathbf{V}_{0i}$ to be zero (as compared to the electron drift velocity $\mathbf{V}_{0e}$). Hence, the E-region plasma drift motion results in the ionospheric currents flowing in the direction roughly opposite to the direction of the electron flow:

$$\mathbf{j} = en\left(\mathbf{V}_{0i} - \mathbf{V}_{0e}\right) \approx -en\mathbf{V}_{0e}, \tag{5.5}$$

where e is the charge of an electron and n is the electron number density. Although (5.5) is a good approximation, ground-based magnetometers are still sensitive to the magnetic effect of the relative electron-ion drift while SuperDARN F-region measurements are based on the assumption that $\mathbf{V}_{0i} = \mathbf{V}_{0e}$ and that $\mathbf{j} = 0$.

Let us find how the ionospheric plasma velocity is related to the equivalent sheet currents $\mathbf{J}$. Combining the Ohm's law (1.22) and the drift velocity equation (1.2) yields

$$\mathbf{v} = \frac{\hat{\Sigma}^{-1}\mathbf{J}\times\mathbf{B}}{B^2}, \tag{5.6}$$

where $\hat{\Sigma}^{-1} = \frac{1}{\Sigma_P^2 + \Sigma_H^2}\begin{pmatrix} \Sigma_P & -\Sigma_H \\ \Sigma_H & \Sigma_P \end{pmatrix}$. However, the ground magnetic measurements only provide the information on the rotational component of the ionospheric sheet current field by the Fukushima theorem, to be formulated in the next Section. If we assume that the ionospheric conductance $\hat{\Sigma}$ is homogeneous, then the equivalent currents are exactly the Hall currents. Considering the Pedersen conductance equals zero means that all of the sheet current are the Hall

currents only, $\mathbf{J} = \mathbf{J}_H$, whence

$$\hat{\Sigma}^{-1}\mathbf{J}_H \times \mathbf{B} = \frac{1}{\Sigma_H^2}\begin{pmatrix} 0 & -\Sigma_H \\ \Sigma_H & 0 \end{pmatrix}\mathbf{J}_H \times \mathbf{B} = \frac{1}{\Sigma_H}\hat{\mathbf{e}}_z \times \mathbf{J}_H \times \mathbf{B} = \frac{1}{\Sigma_H}\mathbf{J}_H\left(\hat{\mathbf{e}}_z \cdot \mathbf{B}\right) = \frac{\mathbf{J}_H|\mathbf{B}|}{\Sigma_H}\ , \qquad (5.7)$$

which yields the equation for the Hall drift velocity

$$\mathbf{v}_H = \frac{\mathbf{J}_H|\mathbf{B}|}{\Sigma_H B^2}. \qquad (5.8)$$

This relationship between the Hall current and the plasma velocity can be rewritten in the absolute vector values as

$$v_H = \frac{1}{\Sigma_H B} J_H. \qquad (5.9)$$

To obtain the approximate relationship between the ground horizontal magnetic field and the ionospheric plasma velocity, we combine (5.9) with (5.4) and get

$$v_H = \frac{1.592 \times 10^6}{\Sigma_H B} B_\perp, \qquad (5.10)$$

where both horizontal magnetic variation $B_\perp$ and the geomagnetic field B are measured in nT. The proportionality coefficient $1.592 \times 10^6 \left(\Sigma_H B\right)^{-1}$ is highly variable; it can be as low as $1\,\mathrm{m \cdot s^{-1} \cdot nT^{-1}}$ for the sunlit ionosphere and as high as $30\,\mathrm{m \cdot s^{-1} \cdot nT^{-1}}$ for the dark ionosphere.

We see that convection velocity estimates performed with the use of the ground-based magnetometers are very sensitive to the value of the conductance (which is often not known) so that only for conductance distributions close to homogeneous the magnetometer measurements can provide a qualitative pattern of the convection. The ionospheric conductance is generally inhomogeneous. On a global scale it is controlled by the solar radiation: the conductance of the sunlit region can be one or two orders of magnitude higher than that of the dark region, in absence of the particle precipitations. The conductance gradients significantly change the equivalent current patterns so that the equivalent current streamlines can depart from the true plasma velocity streamlines to almost any extent. Practical calculations of the equivalent current systems taking into account the variations of conductance and conductance gradients require a strict mathematical criterion that would allow distinguishing the equivalent currents amongst the total sheet current field. This criterion is a generalized Fukushima theorem, which we formulate and prove in the following sections.

5.2.1 Generalized Fukushima theorem and equivalent currents

In the high-latitude regions (above 70° degrees of magnetic latitude) the earth magnetic field is almost vertical. Therefore the FACs are almost perpendicular to the ionosphere. Consider a FAC flowing into the ionosphere through a thin flux tube. The FAC is associated with a divergent electric field that drags electric charges out of the inflow point, creating the Pedersen current in the E region. Since the earth's magnetic field is orthogonal to the electric field, the electrons drift in the direction perpendicular to that of the electric field. In the E region of the ionosphere this drift causes vortical Hall currents with the centre at the FAC footprint. Each of the three current components, FACs, Pedersen and Hall currents, generate magnetic field measurable at the ground level.

In the 1960s, *Fukushima* showed that the ground magnetic effect due to the FACs and Pedersen currents could not be measured because the ionospheric Pedersen currents and the associated FACs produce equal but opposite magnetic effect and therefore cancel each other. This idea led to the notion that what we measure using the ground-based magnetometers is mostly the effect of the ionospheric Hall currents only. It has been referred to as the "Fukushima theorem". However, the ionospheric conductance inhomogeneities can introduce significant distortions to the magnetometer measurements of the Hall currents, therefore the magnetically measurable part of the total ionospheric currents was termed the "equivalent currents".

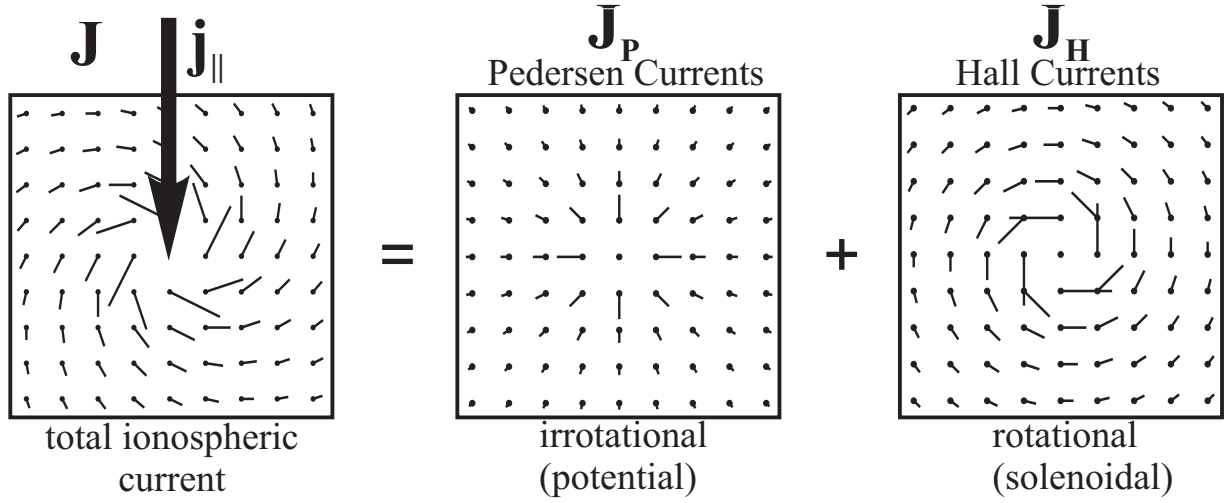

Figure 5.2. Decomposition of the total ionospheric sheet currents $\mathbf{J}$ into the Pedersen $\mathbf{J}_P$ and Hall $\mathbf{J}_H$ components. For uniform ionospheric conductance this decomposition coincides with decomposition into irrotational $\mathbf{J}^{irr}$ and rotational $\mathbf{J}^{rot}$ components.

For a uniform conductance distribution, the decomposition of currents into the Pedersen and Hall components is equivalent to its decomposition into the irrotational and rotational components, as schematically shown in Fig. 5.2. If the ionospheric conductance is uniform, the Pedersen currents form the divergent component of all the ionospheric currents. In a uniformly conducting ionosphere the Hall currents are exactly the equivalent currents, which means that what is measured with the ground-based magnetometers is the effect of the Hall currents overhead. However, the ionospheric conductance is non-uniform, especially in the regions close to the solar terminator and at a case of particle precipitations. The latter produce strong local ionization and, hence, conductance enhancement. Below we show that the measurable magnetic effect is due to the rotational (or solenoidal, or vortical) component of the ionospheric sheet current field, which is not identical to the Hall currents under a non-uniform ionospheric conductance.

The strict formulation of the Fukushima theorem and its proof clarifies which part of the ionospheric currents cancels the arbitrarily distributed FACs' magnetic effect.

Generalized Fukushima Theorem. The magnetic fields due to vertical incident field-aligned current $j_{\parallel}$ and due to ionospheric curl-free sheet current $\mathbf{J}^{irr}$ cancel each other and therefore produce zero magnetic field variation at the ground level.

To prove it in this general form we first need to prove it for a simplest case.

Lemma 5.1. A system of a line current vertically incident on a conducting plane with uniform Pedersen conductance and the associated symmetrically divergent sheet currents inside of the plane produces zero magnetic effect.

Proof. The current system is shown in Fig. 5.3. Draw on the ground plane a circle *C* of an arbitrary radius *R* with the centre at the vertical projection of the FAC $j_{\parallel}$. The total current *I* flowing through the circle *C* equals to the surface integral of the curl of magnetic field **B** over the C interior. Applying the Stokes theorem, one can convert the area integration of the curl into the magnetic field circulation integral along the C circumference:

$$I = \frac{1}{\mu_0}\iint_S \nabla \times \mathbf{B} da = \frac{1}{\mu_0}\int_C \mathbf{B}\cdot d\mathbf{l}\,, \tag{5.11}$$

where *S* is the area of *C*, and *d***l** is an element of the circle. Because of symmetry of the problem, the magnetic field must be the same at each point of the circle, i.e. $|\mathbf{B}| = B$.

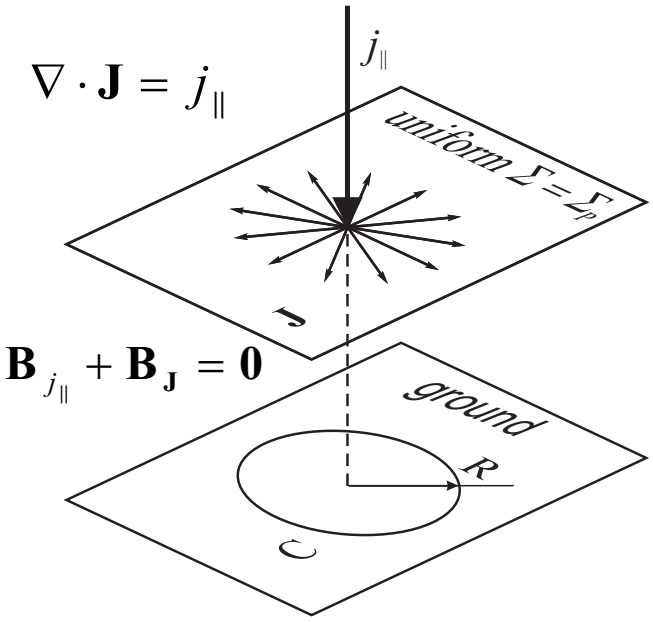

Figure 5.3. An illustration to the proof that the incident current $j_{\parallel}$ and its uniform divergent sheet currents **J** produce zero total magnetic effect at the ground level.

Also, the vector **B** can be horizontal *only*. And third, it must be tangential to *C*. Hence, its circulation in (5.11) is expressed in a simple form:

$$\mu_0 I = \int_C \mathbf{B} \cdot d\mathbf{l} = 2\pi RB \ . \tag{5.12}$$

Note that no current flows through the circle *C* on the ground, therefore $I = 0$ and $2\pi RB = 0$, whence $B = 0$ and $\mathbf{B} = 0$ at the ground. Lemma 5.1 has been proven. This proof belongs to *Fukushima* [1987].

We also need to determine some properties of the relationship between an incident line FAC $I_{\parallel}$ and the resulting Pedersen currents **J** for the uniform conductance. Note, that a 2-dimensional, curl-free vector field **J**, having zero divergence everywhere but at a single point, is circularly symmetric with respect to this single point. In short,

$$\left.\begin{array}{l} \nabla \times \mathbf{J} \equiv 0 \\ \nabla \cdot \mathbf{J} = I_{\parallel} \delta_{\perp}(\mathbf{r}) \end{array}\right\} \Rightarrow \mathbf{J} \text{ is circularly symmetric}. \tag{5.13}$$

Here $I_{\parallel}$ is a scalar coefficient, $\delta_{\perp}(\mathbf{r})$ is the two-dimensional Dirac delta-function at the location $\mathbf{r}$ within the 2-D plane. The condition $\nabla \times \mathbf{J} \equiv 0$ immediately implies the existence of a scalar potential function Ξ (a Greek letter Xi) such that

$$\mathbf{J} = -\nabla \Xi \ . \tag{5.14}$$

Taking the divergence of both parts of (5.14) and combining with (5.13) yields $-\nabla \cdot \mathbf{J} = \nabla \cdot \nabla \Xi = \nabla^2 \Xi = -I_{\parallel} \delta(\mathbf{r})$, hence the Poisson equation

$$\nabla^2 \Xi = -I_{\parallel} \delta(\mathbf{r}) . \tag{5.15}$$

Due to the circular symmetry of the equation, (5.15) can be represented in the polar coordinates (r,φ) through the one-dimensional delta-function $\delta(r)$ [*Bracewell* 1999, p. 85] as

$$\nabla^2 \Xi = -I_{\parallel} \frac{\delta(r)}{\pi r} . \tag{5.16}$$

The solution to (5.16) is

$$\Xi(r) = \frac{I_{\parallel}}{2\pi} \ln \frac{r_0}{r}, \quad \text{where} \quad \Xi(r_0) = 0 . \tag{5.17}$$

The field **J** is explicitly expressed by (5.14) as the negative gradient of Ξ, or

$$\mathbf{J} = \frac{I_{\parallel}}{2\pi r} . \tag{5.18}$$

Both potential Ξ and vector field **J** are obviously circularly symmetric. Note, that if the scalar $I_{\parallel}$ is treated as an incident point FAC, then the $\mathbf{J}$ in (5.18) is the Pedersen current in a uniformly conducting plane, associated with the FAC $I_{\parallel}$.

Now the generalized Fukushima theorem may be easily proven.

Proof to the generalized Fukushima theorem: The Helmholtz theorem states that a vector field **J** may be decomposed into a sum of two vector fields, rotational and irrotational. Therefore for the vector field of overall ionospheric sheet currents

$$\mathbf{J} = \mathbf{J}^{rot} + \mathbf{J}^{irr} , \tag{5.19}$$

the rotational being the field with zero divergence and irrotational being with zero curl:

$$\nabla \cdot \mathbf{J}^{rot} = 0 , \tag{5.20a}$$

$$\nabla \times \mathbf{J}^{irr} = 0. \tag{5.20b}$$

Note that the Helmholtz decomposition is generally not unique. Indeed, any vector field $\mathbf{A}$ that satisfies both (5.20a) and (5.20b) conditions can be added to $\mathbf{J}^{rot}$ and subtracted from $\mathbf{J}^{irr}$ in (5.19) leaving the total field $\mathbf{J}$ the same:

$$\mathbf{J} = \left(\mathbf{J}^{rot} + \mathbf{A} \right) + \left(\mathbf{J}^{irr} - \mathbf{A} \right) . \tag{5.21}$$

The vector field $\mathbf{A}$ is also determined as the gradient of a harmonic function, i.e. any function satisfying the Laplace equation. However, later we shall show how to specify $\mathbf{J}^{rot}$ and $\mathbf{J}^{irr}$ without ambiguity.

A field-aligned current $j_{\parallel}$ incident on the ionosphere equals to the divergence of the ionospheric sheet current density by the current continuity condition

$$j_{\parallel} = \nabla \cdot \mathbf{J}\,, \tag{5.22}$$

which, after substitution of (5.19) yields

$$j_{\parallel} = \nabla \cdot \mathbf{J} = \nabla \cdot \left(\mathbf{J}^{irr} + \mathbf{J}^{rot} \right) = \nabla \cdot \mathbf{J}^{irr} + \nabla \cdot \mathbf{J}^{rot}\,. \tag{5.23}$$

Due to condition (5.20a) only the irrotational component of the ionospheric sheet currents is associated with the FACs $j_{\parallel}$:

$$j_{\parallel} = \nabla \cdot \mathbf{J}^{irr}\,. \tag{5.24}$$

However, so far we cannot state that all irrotational ionospheric currents $\mathbf{J}^{irr}$ are due to FACs. Any irrotational ionospheric currents *not* associated with FACs would produce their own magnetic field, which would not be cancelled by that of the associated FACs, therefore these irrotational currents would be a part of equivalent currents, while we are proving just the opposite. The following reasoning is intended to prove that the ionosphere cannot contain any irrotational sheet currents except those invoked by FACs.

We decompose the (generally distributed) FACs $j_{\parallel}$ into an infinite sum of elementary, infinitesimal vertical line currents $\alpha_i^{\parallel}$ and assume that the ionospheric sheet current system formed by the *i*-th of these FACs is β_i. Then the total ionospheric sheet current system **J** is a sum of infinite number of the infinitesimal currents β_i. For an *i*-th elemental current the Helmholtz decomposition (5.19) is

$$\beta_i = \beta_i^{irr} + \beta_i^{rot}\,, \tag{5.25}$$

and according to (5.24),

$$\alpha_i^{\parallel} = \nabla \cdot \beta_i^{irr}\,. \tag{5.26}$$

The $\alpha_i^{\parallel}$ is a line FAC, hence, the β_i^{irr} is a curl-free sheet current whose divergence is zero everywhere except at the point of the $\alpha_i^{\parallel}$ incidence. Otherwise, β_i^{irr} would have some other than

$\alpha_i^{\parallel}$ source. As we have shown in (5.13 and further), a sheet current like β_i^{irr} must be circularly symmetric with respect to this point of incidence. Note that the association $\alpha^{\parallel} \leftrightarrow \beta^{irr}$ is bijective, i.e. the set of β_i^{irr} exhausts all the $\alpha_i^{\parallel}$, composing the finite FAC $j_{\parallel}$. Should we find a β_k^{irr} not associated with any FAC from the $\alpha^{\parallel}$ set, it will immediately imply existence of an $\alpha_k^{\parallel}$ which does not belong to $\alpha^{\parallel}$. However, this would contradict the assumption that the set of $\alpha_i^{\parallel}$ covers all elements of $j_{\parallel}$. According to Lemma 5.1 we conclude that the magnetic effects due to $\alpha_{\parallel}^{i}$ and β_k^{irr} cancel each other, and only the magnetic field due to β_i^{rot} is measurable at the ground. Finally, when we make a superposition of all the infinitesimal currents $\alpha_i^{\parallel}$, β_i^{irr}, and β_i^{rot} back into $j_{\parallel}$, $\mathbf{J}^{irr}$, and $\mathbf{J}^{rot}$ respectively, we can see that the magnetic field due to both $j_{\parallel}$ and $\mathbf{J}^{irr}$ is zero.

In order to eliminate the arbitrariness in the Helmholtz decomposition (5.19) we observe that the total irrotational component $\mathbf{J}^{irr}$ consists of the infinitesimal irrotational currents β_i^{irr} in the explicit form (5.18) only, i.e.

$$\beta_i^{irr} = \frac{\alpha_i^{\parallel}}{2\pi r}, \tag{5.27}$$

therefore both $\mathbf{J}^{irr}$ and $\mathbf{J}^{rot}$ are specified unambiguously. The $\mathbf{J}^{rot}$ is determined as difference between the total currents $\mathbf{J}$ and the irrotational currents $\mathbf{J}^{irr}$. The generalized Fukushima theorem is thus proven. It has an important implication.

Corollary: The ionospheric equivalent currents $\mathbf{J}^{eq}$ is exactly the divergence-free, rotational component $\mathbf{J}^{rot}$ of total ionospheric sheet currents $\mathbf{J}$, i.e.

$$\mathbf{J}^{eq} = \mathbf{J}^{rot}. \tag{5.28}$$

Indeed, if the magnetic effect due to irrotational currents is completely cancelled by that of the FACs, then the ground magnetic effect of the ionospheric currents is only due to the rotational component $\mathbf{J}^{rot}$ of the ionospheric sheet currents. Relationship (5.28) may be referred to as the generalized Fukushima theorem as well. In other words, the equivalent currents are those and only those whose divergence is zero.

5.2.2 Equivalent current function calculation from known electric potential and conductance

According to the generalized Fukushima theorem (5.28) the ionospheric equivalent currents constitute the purely rotational component of all the ionospheric sheet currents. A purely rotational field is conveniently representable in the form of a current stream function denoted by Ψ. This is very similar to the presentation of an irrotational field by its potential. Both potential and stream functions are scalars, and the vector fields they represent are their partial derivatives. The definition for the equivalent current stream function is

$$\mathbf{e}_z \times \nabla\Psi = \mathbf{J}^{eq}, \tag{5.29}$$

where $\mathbf{e}_z \times$ operator means that the components of gradient of the "potential", $\nabla\Psi$, are rotated by 90° to make up a rotational current field. The convenience of current function is that its contour lines are streamlines of the current it represents. The current function is expressed in the current units, Amperes in SI. One should be aware that the value of current function at a specific point has no physical meaning. Adding any constant to the current function does not change its gradient and hence leaves the current vector field the same. However, the difference between the current function values at any two points equals to the magnitude of all the sheet currents flowing between these two points.

Here we derive the Poisson equation for the current function Ψ. Applying the curl operator $\nabla\times$ to both sides of the (5.29) yields:

$$\nabla \times \left(\mathbf{e}_z \times \nabla\Psi \right) = \nabla \times \mathbf{J}^{eq}. \tag{5.30}$$

Expanding the left hand side with the vector identity $\mathbf{A}\times(\mathbf{B}\times\mathbf{C}) = \mathbf{B}(\mathbf{A}\cdot\mathbf{C}) - \mathbf{C}(\mathbf{A}\cdot\mathbf{B})$ results in

$$\mathbf{e}_z \cdot \nabla^2\Psi = \nabla \times \mathbf{J}^{eq}, \tag{5.31}$$

which is identical to

$$\nabla^2\Psi = \left(\nabla \times \mathbf{J}^{eq} \right)_z. \tag{5.32}$$

The Poisson equation (5.32) can be solved for the equivalent current stream function Ψ. However, (5.32) requires that the equivalent currents be already known in the vector form $\mathbf{J}^{eq}$, which gives no benefit. To present (5.32) in a more practical form, note that the right hand side of (5.32) is a vorticity of the equivalent currents. Knowing that due to the Fukushima theorem (5.28) the equivalent currents are exactly the rotational component of the entire currents, that the curl of an

irrotational field is zero everywhere, and using the Helmholtz decomposition (5.19) we can find that the vorticity of equivalent currents equals to the vorticity of the entire ionospheric sheet currents **J**:

$$\nabla \times \mathbf{J} = \nabla \times (\mathbf{J}^{eq} + \mathbf{J}^{pot}) = \nabla \times \mathbf{J}^{eq}. \tag{5.33}$$

Thus we arrive to the Poisson equation

$$\nabla^2 \Psi = \left(\nabla \times \mathbf{J}\right)_z, \tag{5.34}$$

which allows calculation of the equivalent currents in the form of Ψ, provided the entire sheet current system **J** is known. Unfortunately, we usually do not know **J**, so the right hand side of (5.34) needs further transformations.

Using Ohm's law (1.22) one can express the **J** in (5.34) through the electric field as

$$\nabla \times \mathbf{J} = \nabla \times \left(\hat{\Sigma}\mathbf{E}\right). \tag{5.35}$$

Expanding $\hat{\Sigma}\mathbf{E}$ in Cartesian coordinates yields

$$\nabla \times \mathbf{J} = \nabla \times \left(\begin{pmatrix} \Sigma_P & \Sigma_H \\ -\Sigma_H & \Sigma_P \end{pmatrix} \cdot \mathbf{E} \right) = \nabla \times \begin{pmatrix} \Sigma_P E_x + \Sigma_H E_y \\ -\Sigma_H E_x + \Sigma_P E_y \end{pmatrix}, \tag{5.36}$$

where Σ_H and Σ_P are the Hall and Pedersen conductances, and after expanding the curl we get

$$\begin{aligned} \left(\nabla \times \mathbf{J}\right)_z &= \frac{\partial}{\partial x}\left(-\Sigma_H E_x + \Sigma_P E_y\right) - \frac{\partial}{\partial y}\left(\Sigma_P E_x + \Sigma_H E_y\right) \\ &= -\Sigma_H \left(\frac{\partial E_x}{\partial x} + \frac{\partial E_y}{\partial y} \right) + \Sigma_P \left(\frac{\partial E_y}{\partial x} - \frac{\partial E_x}{\partial y} \right) \\ &\quad - \left(\frac{\partial \Sigma_H}{\partial x} E_x + \frac{\partial \Sigma_H}{\partial y} E_y \right) + \left(\frac{\partial \Sigma_P}{\partial x} E_y - \frac{\partial \Sigma_P}{\partial y} E_x \right). \end{aligned} \tag{5.37}$$

Under the magnetostatic condition $\nabla \times \mathbf{E} \equiv 0$, so

$$\Sigma_P \left(\frac{\partial E_y}{\partial x} - \frac{\partial E_x}{\partial y} \right) = \Sigma_P \left(\nabla \times \mathbf{E}\right) \cdot \mathbf{e}_z \equiv 0. \tag{5.38}$$

After the substitutions

$$\Sigma_H \left(\frac{\partial E_x}{\partial x} + \frac{\partial E_y}{\partial y} \right) = \Sigma_H \nabla \cdot \mathbf{E}, \tag{5.39a}$$

$$\left(\frac{\partial \Sigma_H}{\partial x} E_x + \frac{\partial \Sigma_H}{\partial y} E_y \right) = \left(\nabla \Sigma_H\right) \cdot \mathbf{E}, \text{ and} \tag{5.39b}$$

$$\left(\frac{\partial \Sigma_P}{\partial x} E_y - \frac{\partial \Sigma_P}{\partial y} E_x\right) = \left[\left(\nabla \Sigma_P\right) \times \mathbf{E}\right]_z, \tag{5.39c}$$

into (5.37) the expression for vorticity can be simplified to

$$\left(\nabla \times \mathbf{J}^{eq}\right)_z = -\Sigma_H \left(\nabla \cdot \mathbf{E}\right) - \left(\nabla \Sigma_H\right) \cdot \mathbf{E} + \left[\left(\nabla \Sigma_P\right) \times \mathbf{E}\right]_z. \tag{5.40}$$

In order to eventually impart the form of a general Laplace operator to the vorticity expression in (5.34) we replace the electric field by the negative gradient of potential, $\mathbf{E} \equiv -\nabla \Phi$, to get the expression

$$\left(\nabla \times \mathbf{J}\right)_z = \Sigma_H \nabla^2 \Phi + \left(\nabla \Sigma_H\right) \cdot \left(\nabla \Phi\right) - \left[\left(\nabla \Sigma_P\right) \times \left(\nabla \Phi\right)\right]_z. \tag{5.41}$$

Having the current vorticity in the form (5.41) we can substitute it into (5.34) to obtain the Poisson equation for the equivalent current stream function Ψ:

$$\nabla^2 \Psi = \Sigma_H \nabla^2 \Phi + \left(\nabla \Sigma_H\right) \cdot \left(\nabla \Phi\right) - \left[\left(\nabla \Sigma_P\right) \times \left(\nabla \Phi\right)\right]_z. \tag{5.42}$$

Equation (5.42) shows that not only the potential distribution itself but also the conductance gradients can lead to emerging equivalent current vortices. Note that the $\mathbf{J}^{eq}$ vortex can appear where the electric field vector $-\nabla \Phi$ and the Hall conductance gradient $\nabla \Sigma_H$ are close to *collinearity*. And, conversely, the $\mathbf{J}^{eq}$ vortex appears where the electric field vector $-\nabla \Phi$ and the Pedersen conductance $\nabla \Sigma_P$ gradient are close to *normality*. Equation (5.42) is used in this Chapter for the numerical calculation of the equivalent current patterns based on the SuperDARN-provided electric potential maps and the Moen-Brekke solar photoconductance model. Using of (5.42) allows one to take into account the conductance gradients near the terminator and thus substantially improve agreement between the magnetic estimates of true plasma velocity estimations.

Another interesting implication of equation (5.42) is the fact that even though the ionospheric conductance were purely Pedersen but non-uniform, vortical structures in equivalent currents are still possible in the areas with conductance gradients. Indeed, assuming $\Sigma_H = 0$ in (5.42) one gets

$$\nabla^2 \Psi = -\left[\left(\nabla \Sigma_P\right) \times \left(\nabla \Phi\right)\right]_z. \tag{5.43}$$

The latter means that the equivalent current vortices can occur just due to the Pedersen conductance gradients.

The equivalent current stream function Ψ can also be obtained from the direct magnetometer measurements provided the magnetometer network is dense enough. The horizontal component of magnetic field at the ground level and the ionospheric sheet currents are directly proportional, as seen from equation (5.3). Therefore it seems feasible to retrieve the ionospheric sheet current patterns at the scales greater than ~100 km (E-region altitudes) through the interpolation of the measured horizontal magnetic variation. In principle, this method provides fairly good results. Fig. 5.4a shows an example of linear interpolation. The actual horizontal magnetic vectors are rotated 90° counterclockwise and plotted at the locations of ground-based magnetometer stations as thick arrows.

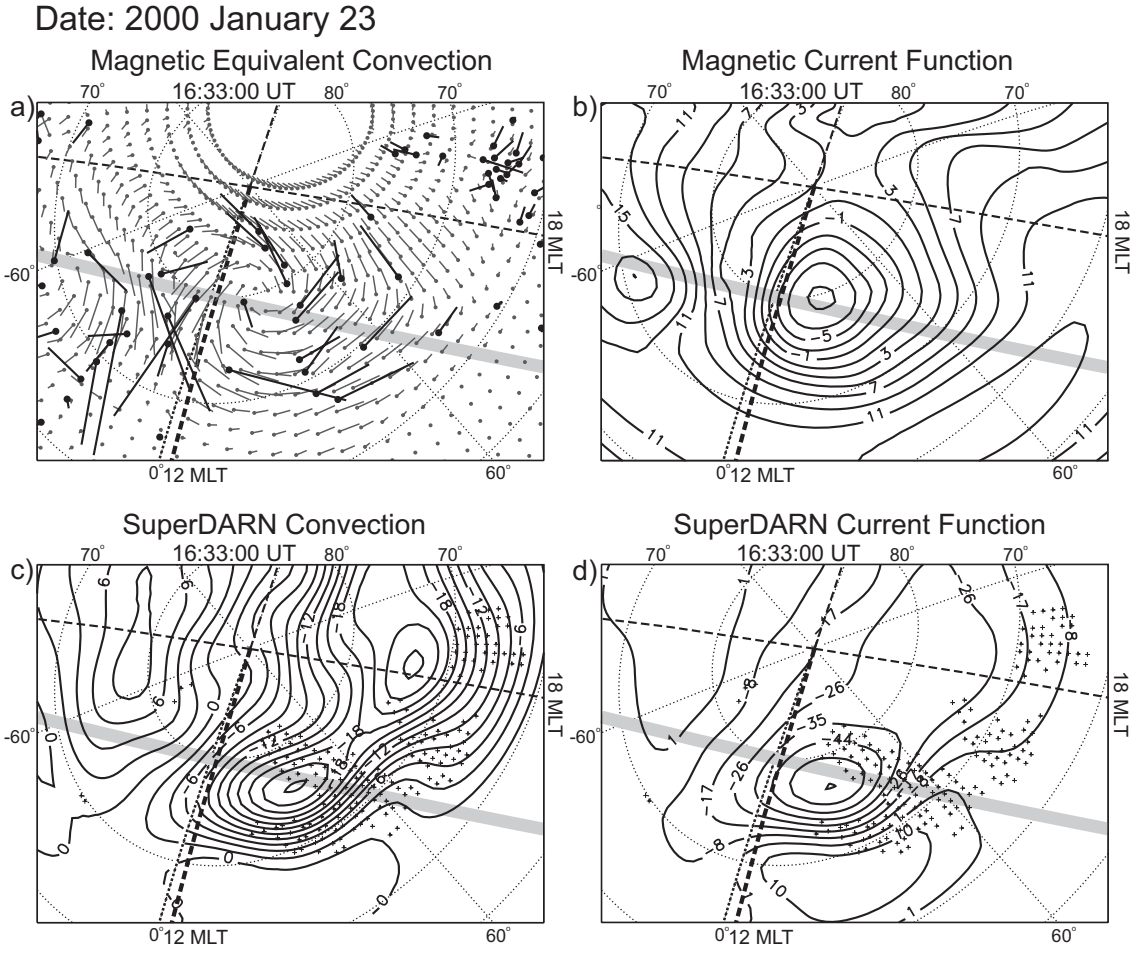

Figure 5.4. Ionospheric equivalent current functions retrieved from ground magnetic measurements and from SuperDARN data for the event on 200, January 23, at 16:33 UT. (a) magnetic equivalent convection vectors (thick line segments) and result of their interpolation on a spherical grid (quiver of thin line segments at grid nodes); (b) the equivalent current function obtained from the interpolation, A; (c) SuperDARN potential map, kV; (d) the equivalent current function obtained from the SuperDARN potential map. The legend is the same as in Fig. 3.9.

The interpolation is performed with the use of spherical triangulation and subsequent linear interpolation algorithms developed by *Renka* [1984, 1997]. Each of the two components of the horizontal geomagnetic field, B_E and B_N, are interpolated individually so that the interpolation results in couples of values, B_N^{ij} and B_E^{ij}, for each (*ij*)-th grid node. The retrieved pattern of the ionospheric sheet currents at the nodes of a smooth spherical grid is shown as quiver of thin arrows.

However, this method is not satisfactory in a number of cases, because the direct linear interpolation does not guarantee conservation of the fundamental property of equivalent currents, their divergence-free condition as stated in (5.20a) and (5.28).

The resultant vector pattern can contain points with non-zero divergence, which is unphysical because by the Fukushima theorem the equivalent currents are purely rotational. Such a distortion of equivalent current patterns can arise from the lack of information due to the irregularity of the geographical locations of the magnetometer stations as well as their scarcity. Therefore it would be desirable to remove the irrotational component from the interpolated equivalent current field to leave only its rotational component. This problem can be solved through extraction of the current stream function from the interpolated magnetic equivalent convection field as described below.

Denote the on-grid interpolated sheet current field as $\mathbf{J}^{ij}$. Its value is known at each (*ij*) grid node. One can obtain the grid values of current function Ψ^{ij} via numerical solving the Dirichlet's problem for the Poisson equation (5.26) in the geometry of a spherical cap with the angular radius θ_0:

$$\begin{aligned} &\nabla^2\Psi = \left(\nabla\times\mathbf{J}\right)_z \\ &\Psi\big|_\Gamma = \Psi_0 \end{aligned}. \qquad (5.44)$$

Here Ψ_0 is a boundary condition at the edge of the spherical cap. Without much loss of generality we may assume $\Psi_0 = 0$ A at the boundary, which means that the current through the boundary is zero. The result is shown in Fig. 5.4b. The contour lines of the calculated current stream function in kA show the current streamlines retrieved from the magnetic measurements shown in panel (a).

For comparison we also show the SuperDARN potential map and the current stream function calculated from it over the same region at the same time in Figs. 5.4c and 5.4d. This equivalent current streamlines are calculated as a solution to equation (5.42). One can notice

reasonable agreement between the ionospheric equivalent current patterns derived from the ground-based magnetometer measurements in panel (b) and from the SuperDARN measurements in panel (d).

5.3 Assessment of plasma convection estimates from magnetometer data using SuperDARN

In this section a statistical comparison between the ground-based magnetometer data and the SuperDARN measurements is undertaken. The goals of this study are, first, to check how good the magnetometer convection estimates under various conditions are and, second, to test the developed method of the magnetometer estimates correction.

5.3.1 Approach to the data grouping: sunlit, dark, and transition ionospheres

As previous comparisons showed, the ionospheric conductance distribution affects significantly the relationship between the MEC and true convection. On a global scale, the conductance is controlled by the solar radiation; the conductance of the sunlit ionosphere can be one order of magnitude higher than that of the dark ionosphere.

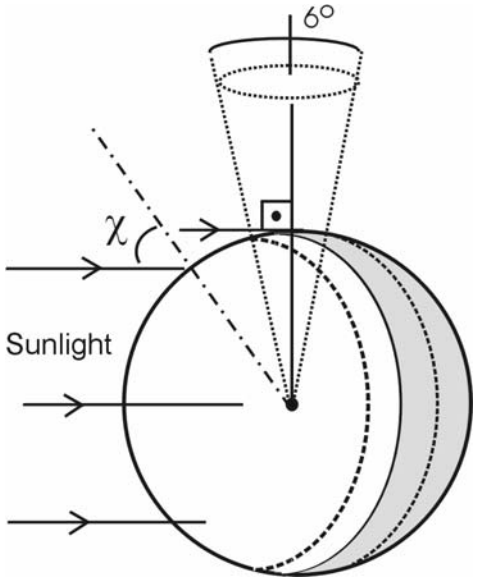

Figure 5.5. A scheme illustrating the criteria for assigning the measurements to the sunlit, transition and dark ionospheres in terms of the sun's zenith angle χ. The shaded half of the sphere corresponds to the geometrically dark ionosphere. At the edge of this region, the terminator, $\chi = 90°$. The transition region between the dark and sunlit ionospheres is introduced as a 6°-wide part of the sphere evenly located on the either side of the terminator.

At high-latitudes, the conductance is also affected by the particle precipitations, but estimations of this factor are always complicated. In this study, we consider relatively quiet events for which we can make a supplementary assumption that the effects of particle precipitations were not very strong.

For the statistical analysis, we split our observations into three major groups: observations in the sunlit, dark and transition ionospheres, as illustrated in Fig. 5.5. To refer an original data point to a specific region, we computed for it the solar zenith angle χ , the angle between the vector directed to the sun and the radius vector normal to the spherical ionosphere. We assigned an individual point to the sunlit, transition and dark ionospheres if its solar zenith angle was $\chi < 87°$, $87° < \chi < 93°$, and $\chi > 93°$, respectively.

We also anticipate that the degree of the MEC and true convection agreement depends on the season of a year. During winter, most of the high-latitude ionosphere is in the darkness over the day. In absence of precipitation, one would expect no significant conductance gradients. Certainly, any local precipitation can provide conductance non-homogeneity and this may affect the MEC, but for relatively quiet events this should not be a great effect. During summer, the ionosphere is predominantly sunlit, and the solar photoconductance is only slightly and smoothly changing with the latitude. For the transition region ionosphere, for any season, large conductance gradients exist all the time and we expect that within this region the MEC and true convection agreement would be the worst.

There is one seasonal effect that needs to be kept in mind, namely the north-south hemisphere conductance asymmetry due to the difference in the solar illumination. These conductance differences cause the interhemispheric currents in the transition region. Magnetic effects of such currents may distort the equivalent current patterns , see next section. Near equinoxes, the north-south hemisphere conductance asymmetry is minimal; therefore the interhemispheric currents' effect should not be observed. The aforementioned seasonal effects are somewhat confusing in terms of expectations, and one of the goals of this study is to detect any seasonal features in the radar and magnetometer data.

We also expect the magnetic local time effects. We consider four different MLT sectors: nightside (2100-0300 MLT), dawn (0300-0900 MLT), dayside (0900-1500 MLT) and dusk (1500-2100 MLT). It is reasonable to expect the best agreement around the noon because of more uniform conductance there. The worst agreement should be in the midnight sector due strong

effects of particle precipitations. The two other sectors, dawn and dusk, are expected to demonstrate approximately equal degree of agreement. Due to the frequent occurrence of the transition region in these sectors, the degree of agreement should be intermediate. However, some dawn-dusk asymmetry may be observed because of the differences in the Birkeland FACs and their ionospheric footprint locations. In the dusk sector, the downward FACs are located equatorward and the upward FACs are poleward with respect to (approximately) 70° AACGM. In the dawn sector the picture is just the opposite. The upward FACs increases the ionospheric conductance due to the associated electron precipitations, whereas the downward FACs remove the electrons from the ionosphere, causing a local electron number density depletion and, hence, reduction of the conductance [*Lyatsky et al*., 1999a].

Finally, we expect the magnetic latitude effects. For relatively quiet conditions, one would expect some enhanced conductance in the area of the auroral oval; the associated conductance gradients would lead to differences between the MEC and true convection.

5.3.2 Approach to the comparison

For the analysis, data from all existing magnetometers and all SuperDARN radars in the northern hemisphere were considered. The instrument locations are shown in Fig. 5.6. To describe the level of magnetic activity in various sectors, we present the data from three magnetometer networks: GIMA (Alaska), DMI (Greenland), and IMAGE (Scandinavia). For these networks, the magnetometers are located along about the same magnetic meridian, and the three meridians cover almost completely the combined FoV of the SuperDARN radars (roughly, half of the globe).

The MEC was determined by rotating the measured magnetic horizontal disturbance vector by 90° counterclockwise. We only consider the veracity of the MEC and true convection patterns in terms of the direction; for the magnitude comparison, information on the ionospheric conductance is required, and it was not available. We express the MEC is units of magnetic field measurements, nanoTeslas (nT).

For computations of the magnetic perturbations δB_x and δB_y, the baselines were selected as the daily averages. We note that, generally, the ionospheric plasma convection is associated with all the modes of daily magnetic variation, including S_q variation. Averaging over the day saves all the modes of the horizontal magnetic field variations.

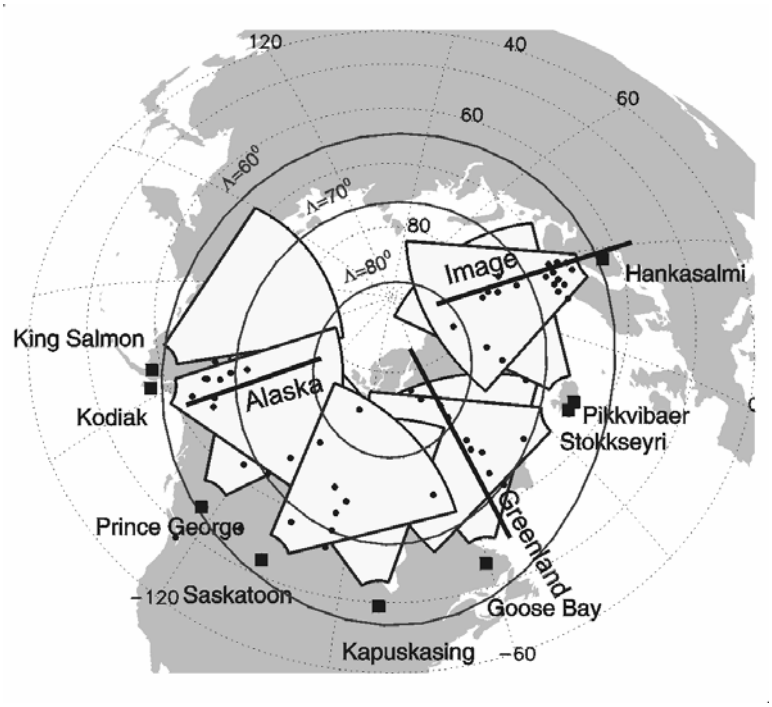

Figure 5.6. A map showing the northern hemisphere SuperDARN radar locations (bold squares), their FoVs (circular sectors), and the magnetometer locations (solid dots). The solid lines are the approximate locations of the magnetic meridians for the GIMA (Alaska), DMI (Greenland), and Image (Scandinavia) magnetometer arrays.

Fig. 5.7a gives an example of the SuperDARN convection map (the contours of electrostatic potential) and the MEC vectors obtained for the same period of time. The potential is shown in dashed contours for positive values and in solid contours for negative values. The plus signs indicate the locations of SuperDARN echoes. The radar-magnetometer comparison can be made for all magnetometer locations, but the radar convection data are only reliable in those parts of the ionosphere where the echoes did exist. Below, the comparison was performed for only those magnetometers for which there was at least one radar measurement within a circular vicinity of a magnetometer station of the radius of 160 km (roughly, the azimuthal size of the radar cell). In Fig. 5.7a, for the areas with common data, the MEC vectors are well aligned with the SuperDARN convection direction. We will characterize the difference between the above vectors by the angle $\Delta\theta$. One should realize that the MEC vectors can be rotated clockwise or anticlockwise with respect to the SuperDARN potential contours. To distinguish these two situations, the following rule for $\Delta\theta$ counting was adopted, Fig. 5.7b. For the MEC vector rotated CW (CCW) from the SuperDARN convection contour, the value of $\Delta\theta$ was counted as positive (negative).

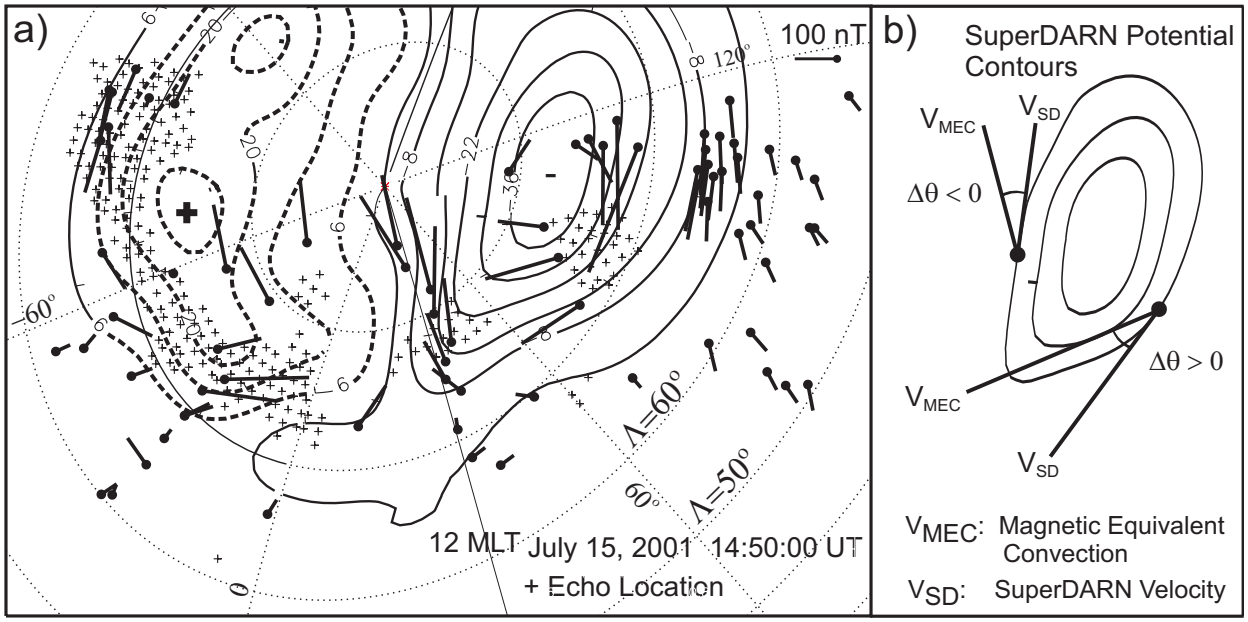

Figure 5.7. a) A SuperDARN contour map of the electrostatic potential (kV) and the equivalent convection vectors (lines with large dots at their origin) expressed in nT. The ACCGM coordinate system is used (dotted lines). The "+" sign indicates the radar echo location. b) A scheme illustrating the mutual orientation of the SuperDARN velocity vector V_{SD} and equivalent convection vector V_{MEC} for positive and negative values of the azimuth difference angle $\Delta\theta$. Notice that the V_{SD} vector at any point is tangential to the potential contour line.

We also considered only those radar (magnetometer) measurements for which the radar velocity (magnetic perturbation) was over 100 m/s (>5 nT). These limitations were introduced to exclude potential effects of ground scatter contribution to the SD velocities (effectively reducing the true convection velocity) and uncertainty in the baseline determination for the magnetometers. Overall, five events were considered, each lasting 24 hours. These are February 9, 2001, July 15, 2001, December 13, 2001, January 25, 2001, and March 20, 2001. The first three events were selected for studying the seasonal effects. For the comparisons in terms of the MLT and magnetic latitude, data for all five events were merged into a single data base. For all the above events the SuperDARN coverage was larger than for other days of the respective month/season.

5.3.3 SuperDARN-magnetometer comparison for the equinox conditions

We first consider the event near the vernal equinox, February 9, 2001. During this day, the SuperDARN provided (on average) 700 vectors for each 1-min frame. The convection vectors were available in all three considered regions of the ionosphere. In terms of the magnetic activity, this was a relatively quiet day; the planetary *Kp* index was between 1 and 2 with an average value

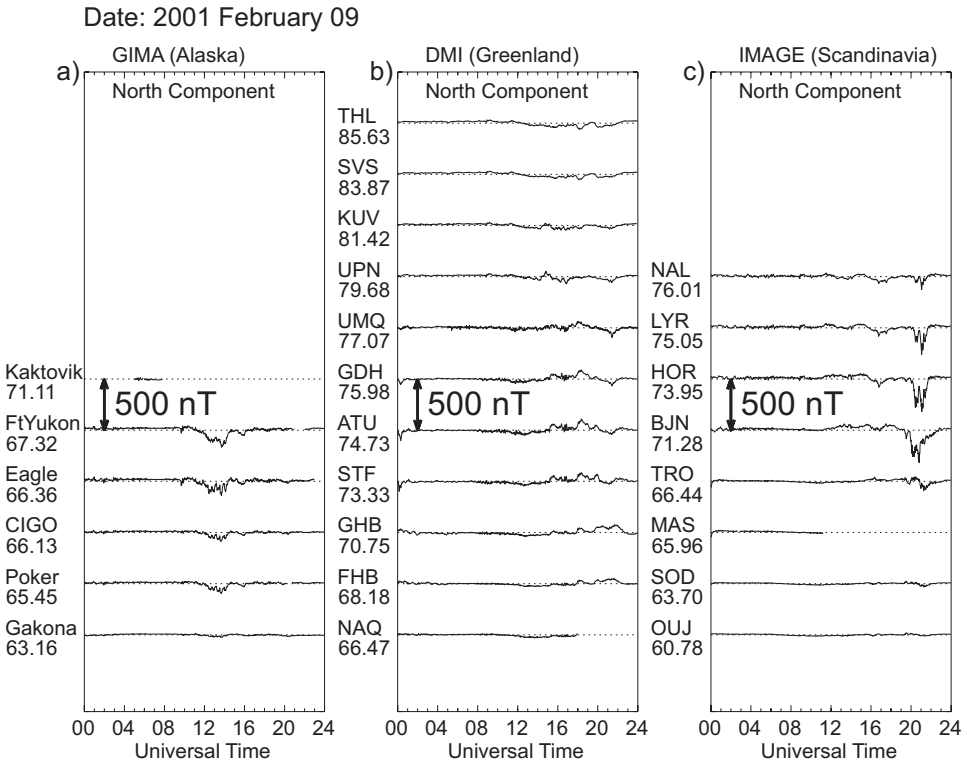

Figure 5.8. Stackplots of magnetometer H-component perturbations for February 9, 2001 in a) Alaskan, b) Greenland, and c) Scandinavian sectors. The names of magnetometer stations and respective AACGM latitudes are given on the left hand side of each plot.

of ~1.5. Consistently, the SuperDARN cross-cap potential was not high, around 40 kV on average. To characterize magnetic activity in various MLT sectors, we present in Fig. 5.8 the earth's magnetic field perturbations in the north-south component recorded in the Alaskan, Greenland and European sectors. One can see that maximum perturbations were of the order of 200 nT; they were lasting for less than 2 hours in each sector.

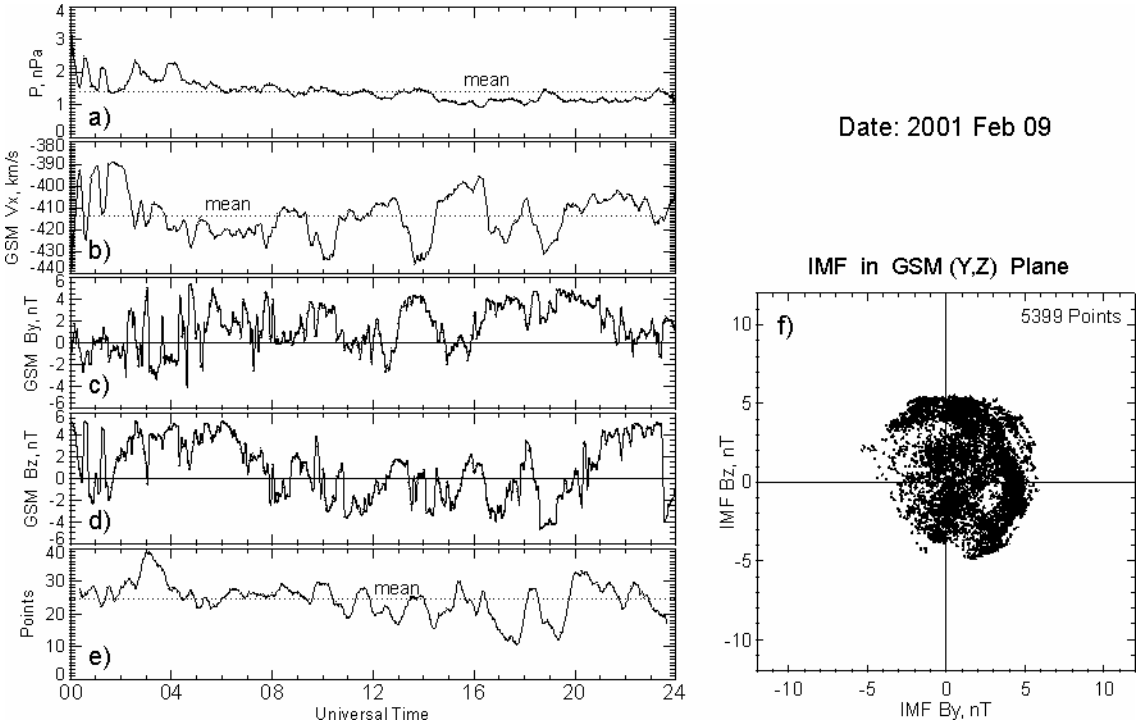

Figure 5.9. ACE data for February 9, 2001: a) The solar wind dynamic pressure in nPa, b) The solar wind earthward velocity in km/s, c) The IMF By component intensity (GSM) in nT, and d) The IMF Bz component intensity (GSM) in nT. Panel e) shows the total number of magnetometers in whose vicinity the SuperDARN observations were available. Panel f) is the scatter plot for the IMF vector orientations in the *Y-Z* (GSM) plane. The IMF data sampling rate was 16 s. The ACE satellite was ~ 238.5 R_E away from the earth sunward. The time delay for the disturbance propagation to the earth's ionosphere was ~ 61 min.

Fig. 5.9 presents the ACE satellite observations of the IMF and the solar wind parameters on February 9, 2001. One can see that the magnetic activations occurred when the IMF B_z component was predominantly negative, Fig 5.9d. In terms of the IMF orientation in the Y-Z plane, there were no preferential conditions for the whole day, Fig. 5.9f, which is a very fortunate feature since it provides an opportunity to perform a comparison for all possible IMF orientations. Fig. 5.9e shows that on average, about 25 points are available for the magnetometer-radar comparison for every SD convection map. This number is significantly lower than the total number of SuperDARN measurements available (~700) since the number of magnetometers within SD FoV is limited to about 50.

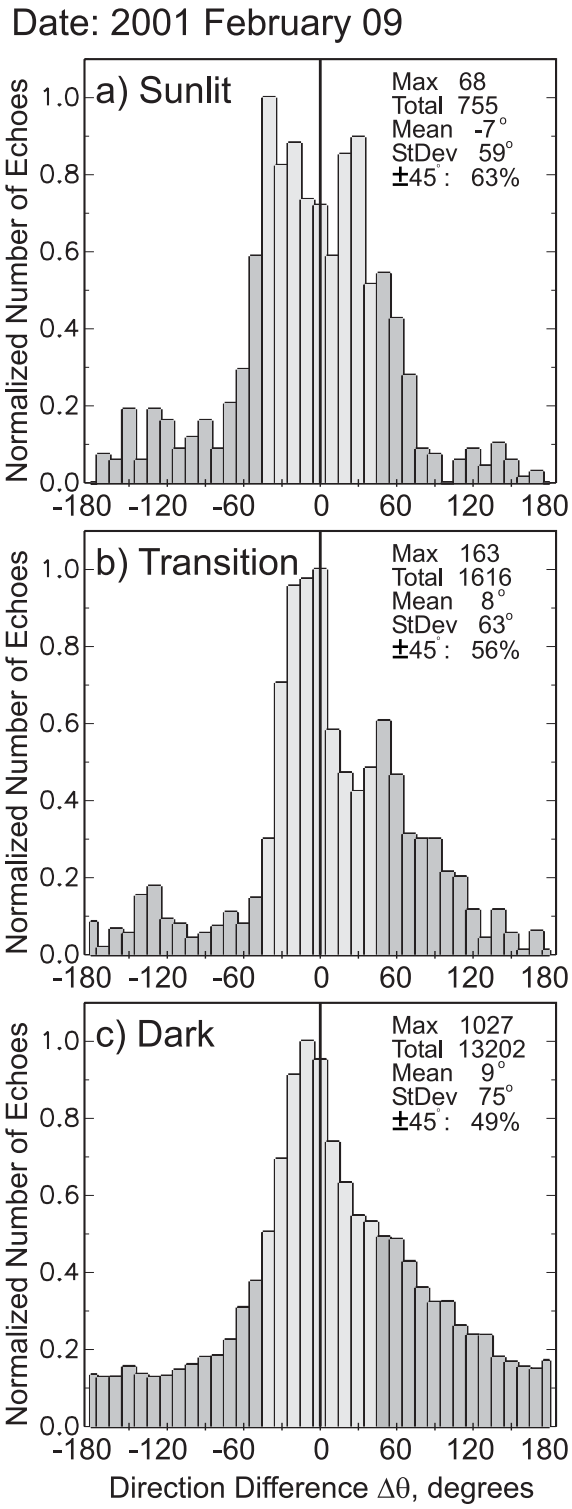

Figure 5.10. Statistical distributions for the angle Δθ (the azimuth difference between the SuperDARN velocity and the equivalent convection) on February 9, 2001 (near vernal equinox). The comparison is performed for the a) sunlit, b) transition, and c) dark ionospheric regions. 10° bins of $\Delta\theta$ are used. The histograms are normalized to one. The maximum value for each distribution as well as the total number of points, the mean value and the standard deviation (StDev) of the distributions (in degrees) are given in the right top corner of each panel.

Fig. 5.10 presents the results of the comparison. Here three plots (sunlit, transition and dark ionospheres) are the histogram distributions for the difference in the azimuth of the MEC and the SuperDARN convection ($\Delta\theta$). The number of available points is significant, with especially good statistics for the dark ionosphere. All three distributions have one major peak, though for the sunlit ionosphere data the distribution is double-peaked having two components around zero (±30°). The mean values for the distributions are around zero indicating an overall tendency for the MEC to be close to the radar convection. In all diagrams, there are some points of strong disagreement, up to 180°. This is especially true for the dark ionosphere where the "tails" in the distribution are very strong. In terms of the distribution width, the sunlit comparison shows the smallest width. For the majority of points in all the three diagrams the direction difference $\Delta\theta$ is less than ±45°. We show this "critical" value of the difference by the different coloring in all panels for the reader's convenience and we will consider all points within these gates as points of reasonable/good agreement. One can see that there are 63%, 56%, and 49% of good points for the dayside, transition and dark ionospheres.

5.3.4 SuperDARN-magnetometer comparison for the winter conditions

Now we consider the winter event of December 13, 2001. During this day, the SuperDARN provided (on average) 650 vectors for each 1-min frame but those were mostly within the transition and dark regions of the ionosphere. In terms of the magnetic activity, this was even quieter day; the planetary *Kp* index was between 0 and 2 with an average value of ~1. Consistently, the SuperDARN cross-cap potential averaged to smaller value of ~35 kV. The earth's magnetic field perturbations in the north-south component recorded in the Alaskan, Greenland and European sectors show only minor activity (<150 nT) between 00 to 05 UT, Fig. 5.11. The magnetic activity correlates well with the period of negative IMF Bz , Fig. 5.12d. In terms of the IMF orientation in the Y-Z plane, Fig. 5.12f , besides the interval of strong negative Bz at the beginning of the day, there was no preferential orientation. For this event, on average, there were also about 25 points for the magnetometer-radar comparison for every SD convection map. However, there were very few data points for the sunlit region, and these data are not presented here.

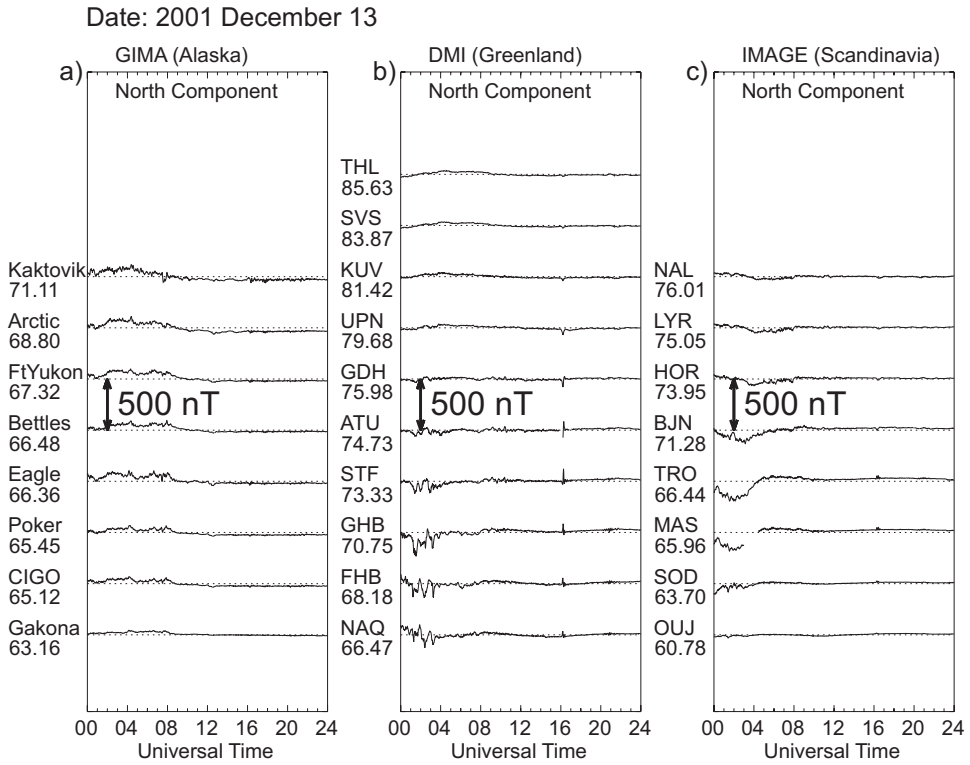

Figure 5.11. The same as in Fig. 5.8 but for December 13, 2001.

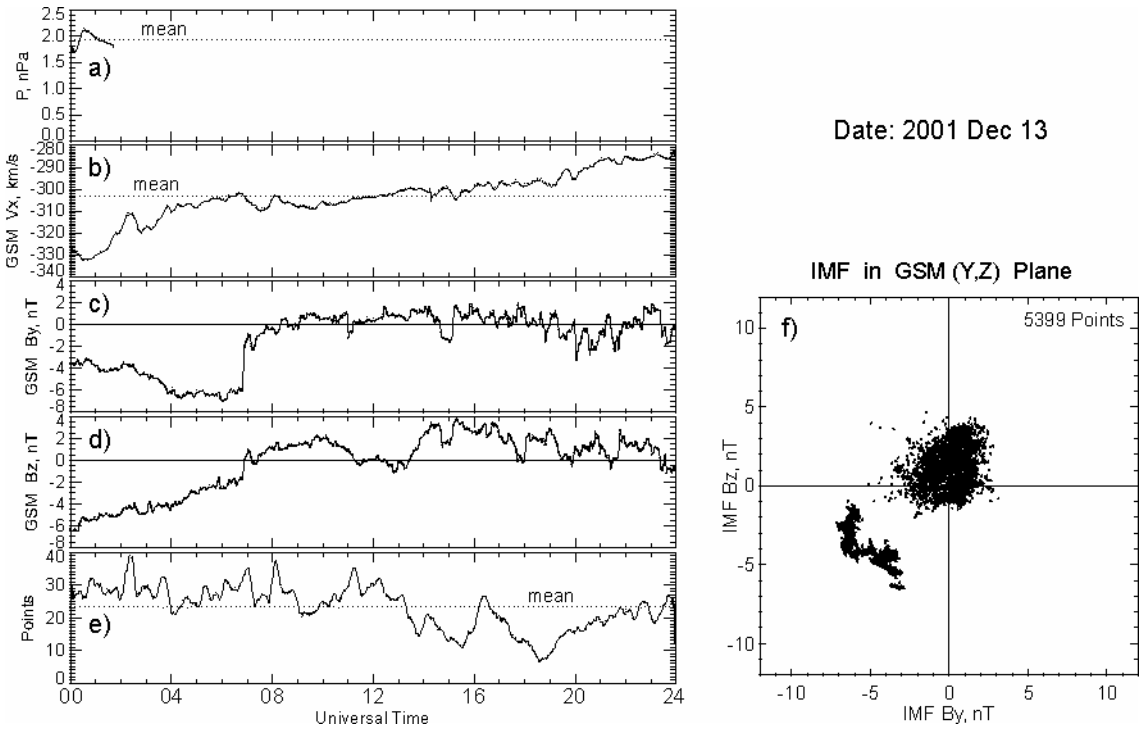

Figure 5.12. The same as in Fig. 5.9 but for December 13, 2001. The ACE satellite was ~ 238.1 R_E away from the earth sunward. The time delay for the disturbance propagation to the earth's ionosphere was ~83 min.

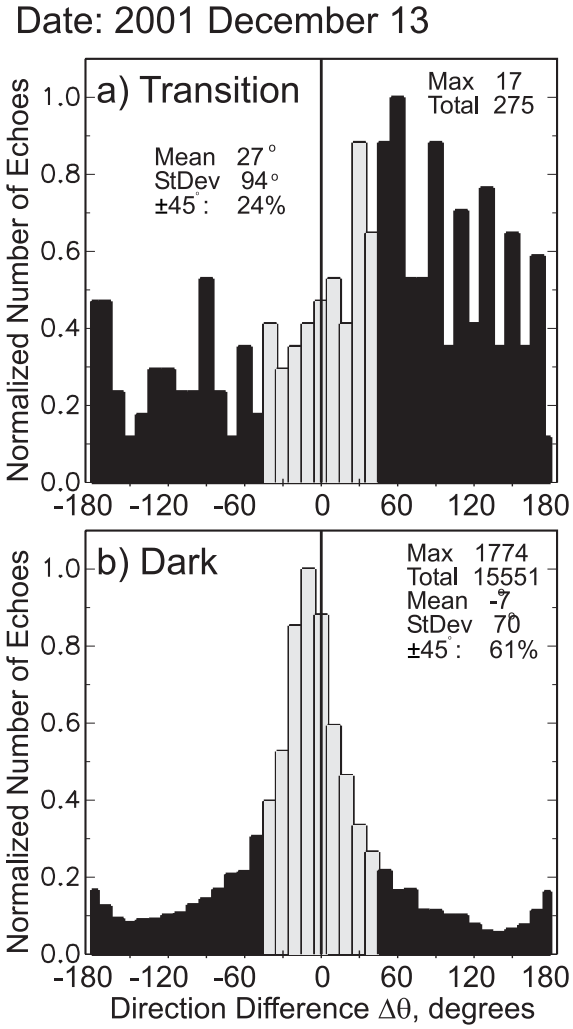

Figure 5.13. The same as in Fig. 5.10 but for December 13, 2001. The number of points for the sunlit ionosphere was insignificant and corresponding data are not shown.

Fig. 5.13 presents statistics for the angle $\Delta\theta$ for the transition and the dark ionospheres. The dark ionosphere data show clear maximum with a small mean shift of 7°. The width of the distribution is slightly smaller than that for the equinox event. For the majority of points (61%) the dark region histogram shows the direction difference less than 45°. The distribution for the transition region is not well defined. Perhaps, small amount of points involved (275) is one of the reasons. One can say for sure that the whole distribution is shifted toward positive values of $\Delta\theta$ with quite frequent occurrence of large positive values of $\Delta\theta$.

5.3.5 SuperDARN-magnetometer comparison for summer conditions

Finally, we consider the summer event, July 15, 2001. This day was more magnetically active. The *Kp* index was between 1 and 4 with the average value of 2. Magnetic perturbations were especially strong (>500 nT) in the Alaskan sector (Fig. 5.14) during the second half of the day. The IMF Bz component was longer negative than positive, and the IMF By component was mostly positive so that, for this event, there were preferential IMF conditions, namely Bz<0 and By>0. The cross-cap potential was stronger, ~ 60 kV. The SuperDARN provided smaller number of vectors, 200 on average, which translated to about 15 points of joint SD-magnetometer data.

Fig. 5.16 shows the data for the angle $\Delta\theta$ for all three regions. The number of data points is especially large for the sunlit ionosphere, Fig. 5.16a, for which the distribution is only slightly shifted from the zero and the tails are not significant. For the case of the transition ionosphere the distribution has also only one peak but the tails are significant, leading to large width of the distribution. For the dark ionosphere, the whole distribution is non-symmetric and shifted toward positive values of $\Delta\theta$. There are two peaks; the smaller one is centered at 0° and the stronger one is centered at ~60°. There are 69%, 51%, and 38% of good points for the dayside, transition and dark ionospheres. We would like to point out that there is a systematic pattern in distribution shifts: mean $\Delta\theta$ is negative for the sunlit ionosphere, slightly positive for the transition ionosphere and stronger positive for the dark ionosphere. It is interesting to note that the same tendency was observed for the equinoctial event.

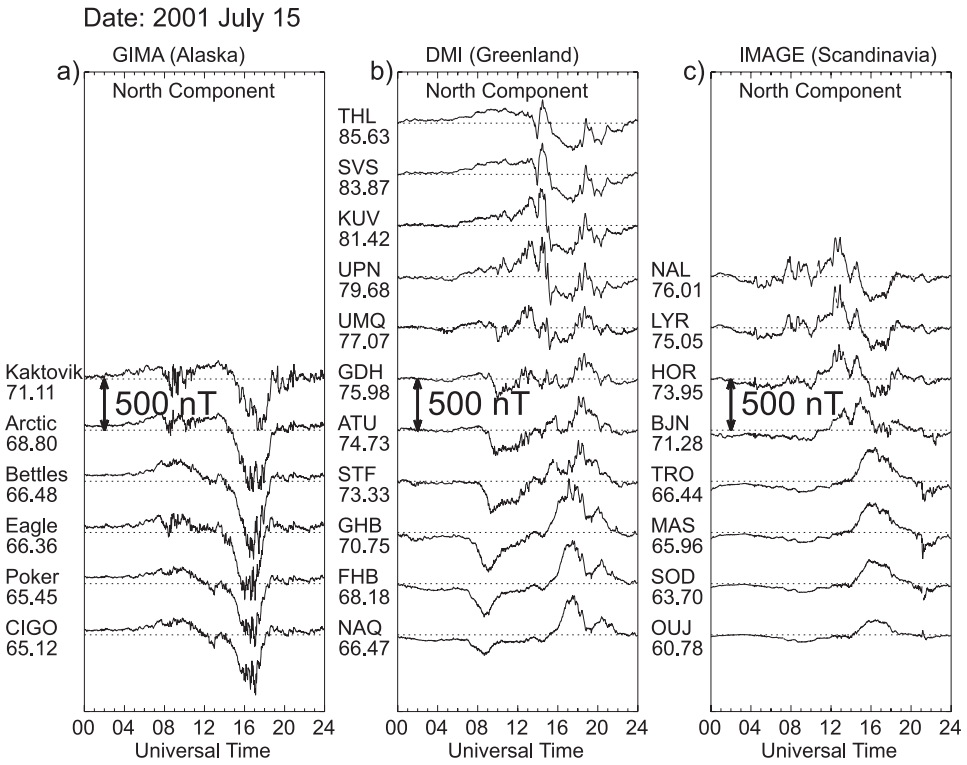

Figure 5.14. The same as in Fig. 5.8 but for July 15, 2001.

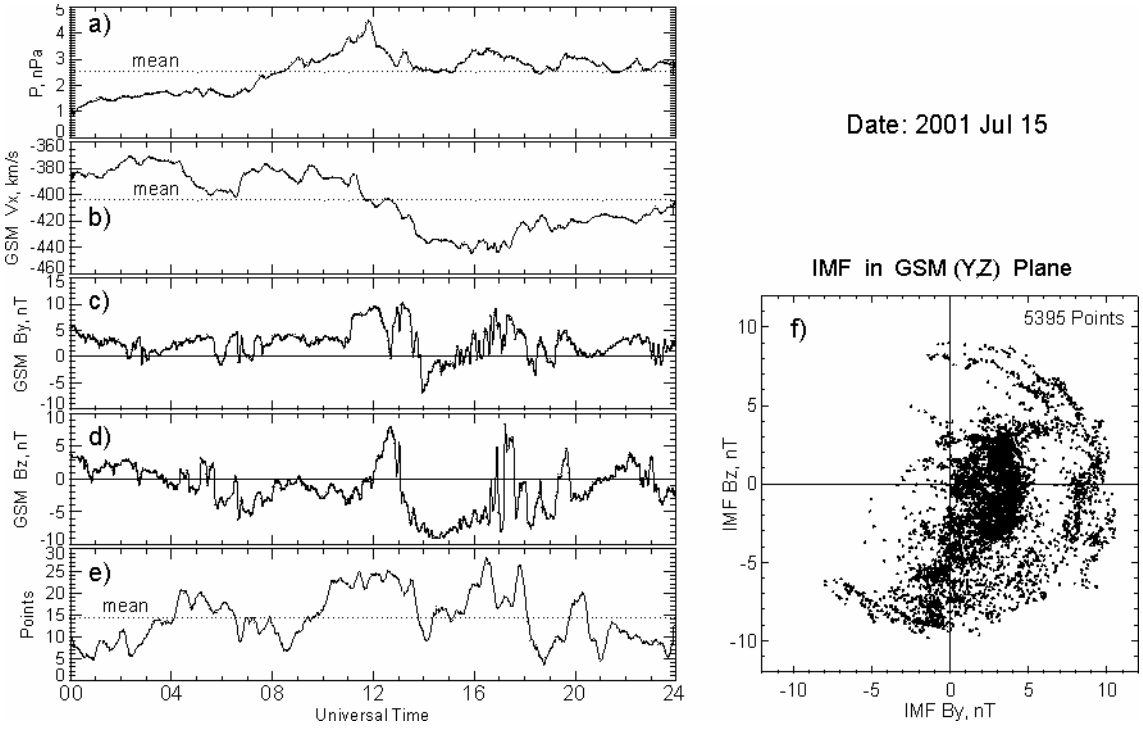

Figure 5.15. The same as in Fig. 5.9 but for July 15, 2001. The ACE satellite was ~ 250.1 R_E away from the earth sunward. The time delay for the disturbance propagation to the earth's ionosphere was ~66 min.

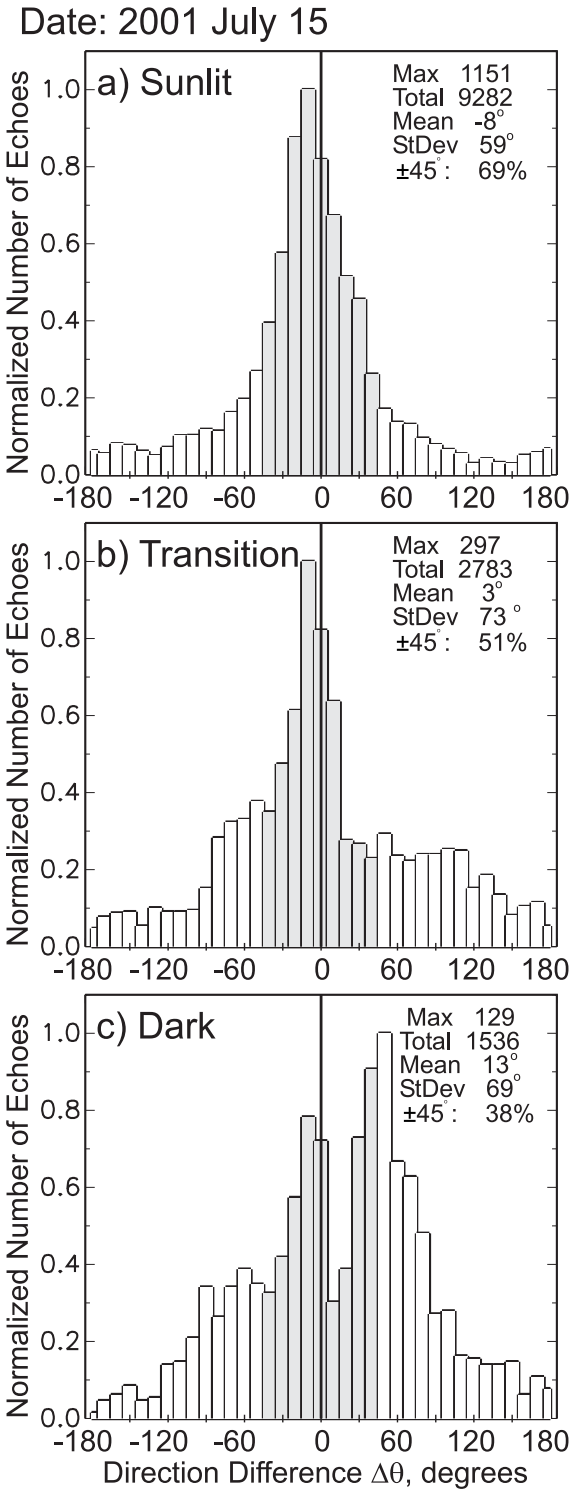

Figure 5.16. The same as in Fig. 5.10 but for July 15, 2001.

5.3.6 SuperDARN-magnetometer comparison for various MLT sectors

We now compare the MEC and SD convection in various MLT sectors. To increase data statistics, we consider all the five days. There should not be a concern for the merging data since we illustrated that although there are some differences in the histograms for $\Delta\theta$ for various seasons, the differences were not drastic indicating that the seasonal effect is not a strong factor controlling $\Delta\theta$.

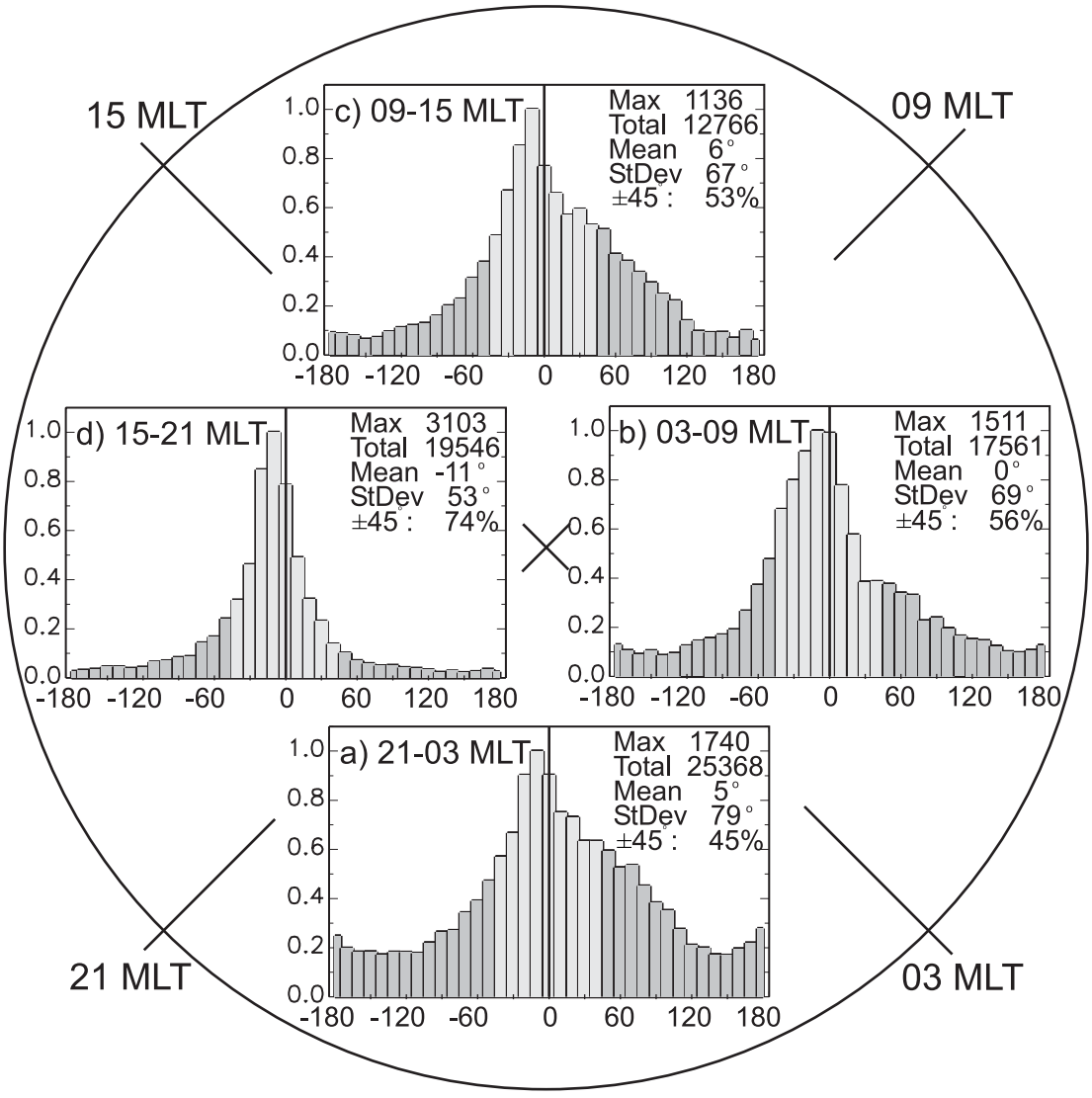

Figure 5.17. Statistical distributions for the angle $\Delta\theta$ for four magnetic local time sectors: nightside (2100-0300), dawn (0300-0900), dayside (0900-1500) and dusk (1500-2100). Data for all magnetic latitudes and for five days from various seasons of 2001 were used. The histograms are normalized to one. The maximum value in the distribution as well as the total number of points, the mean value, the standard deviation of the distribution (in degrees), and the percentage of data points within ±45° are given in the right top corner of each diagram.

Now we consider data over five days from different seasons that we split into four MLT groups: nightside (2100-0300), dawn (0300-0900), dayside (0900-1500), and dusk (1500-2100). The resultant histograms are presented in Fig. 5.17 in the form of a circle divided into four sectors, each of which contains a $\Delta\theta$ histogram for the respective MLT sector. All the distributions in Fig 5.17 are single-peaked with the peaks near zero. All the distributions are only slightly asymmetric with most narrow (minimal tails) distribution for the dusk sector observations. The mean shift of the distribution is largest in the dusk sector.

5.3.7 SuperDARN-magnetometer comparison for various MLT sectors and magnetic latitudes

To expand the comparison, we now consider partitioning the data set according to eight MLT sectors and 5° magnetic latitude gates within each sector. The only reason for such data segmentation was that there is reasonable amount of data for each segment. Instead of considering all histograms, we present below information on the mean, standard deviation, and percentage of the data points within ±45° of the distributions only, to simplify the data analysis. The standard deviation is considered as the distribution width.

Fig. 5.18 shows a circular diagram where the circle is divided into segments to represent the partitioning of the high latitude ionosphere. Each segment covers 5° of AACGM latitude and 3 hours of MLT. The statistical comparison of the MEC and SD convection direction has been performed for each individual segment and the results, the mean and standard deviation, are shown in each segment as two lining parameters. The lining tilt with respect to the vertical equals to the distribution mean in degrees. The lining shade of gray characterizes the width of each distribution. For convenience, all the numerical data for the histogram are presented in Table 5.1 and Table 5.2, respectively. Consider first the mean shifts of the histograms characterized by the slopes of the linings in Fig. 5.18. The strongest deviations are observed at low latitudes of 60°-70° deg in the pre noon sector and at high latitudes of 80°-85° in all time sectors. The mean shifts are as large as 90°.

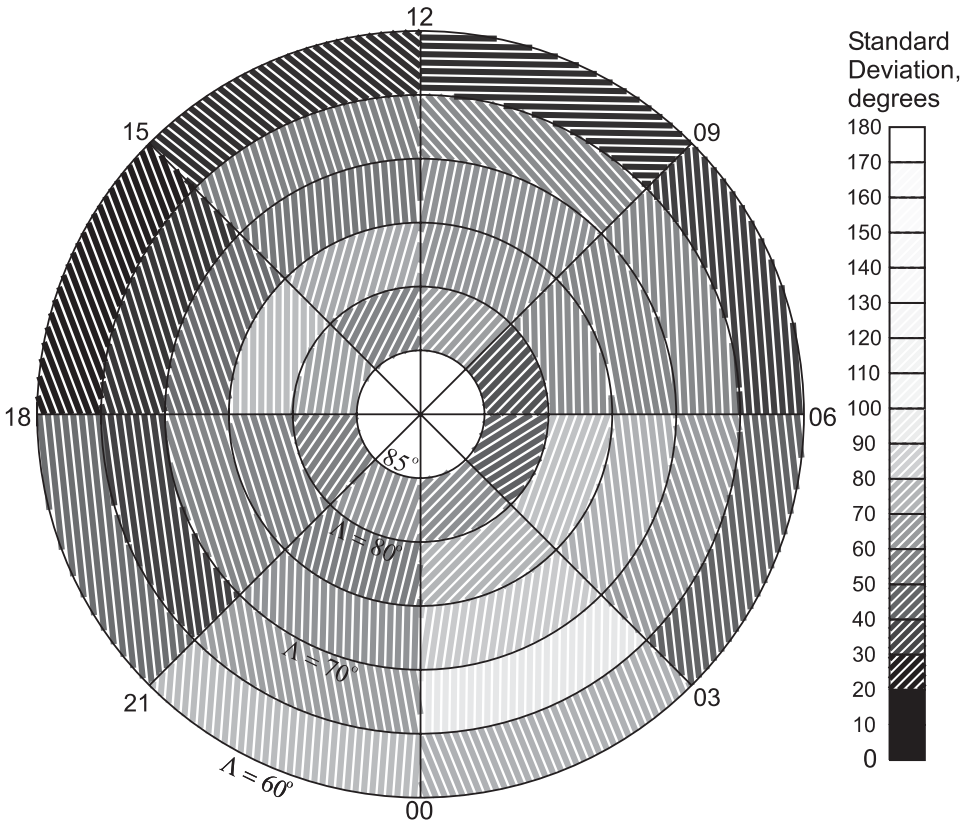

Figure 5.18. The mean value and standard deviation of the distributions for the angle $\Delta\theta$ in eight magnetic local time sectors and various magnetic latitudes. 5° step in the AACGM latitude (between 60° to 85°) was used. The mean value of $\Delta\theta$ is shown by the slope of the lining with respect to the vertical (in degrees) within each segment of the data. The standard deviation of the distribution is shown by the shade of gray of the lining. Data for five days in various seasons of 2001 were used.

Table 5.1. SDC/MEC direction difference histogram means, degrees.

MLT Λ	00-03	03-06	06-09	09-12	12-15	15-18	18-21	21-00
60°-65°	-22.1	-6.3	-4.4	-89.0	-51.3	-20.9	-5.9	4.3
65°-70°	0.8	-18.4	-2.7	-41.9	-17.8	-17.4	-7.8	-9.9
70°-75°	8.3	-6.8	-10.0	11.5	-4.5	-19.1	-17.8	1.4
75°-80°	44.6	20.0	-1.1	15.6	15.9	0.3	-17.6	13.9
80°-85°	44.3	58.0	44.1	42.0	26.8	8.7	34.3	19.9

Table 5.2. SDC/MEC direction difference histogram standard deviations, degrees.

MLT / Λ	00-03	03-06	06-09	09-12	12-15	15-18	18-21	21-00
60°-65°	77.4	47.4	35.4	31.3	32.0	27.6	50.8	80.8
65°-70°	97.2	69.2	61.1	62.3	58.5	32.8	36.3	69.7
70°-75°	86.2	76.9	60.1	64.8	54.7	50.5	59.8	65.3
75°-80°	78.9	83.3	62.3	66.1	73.7	81.6	59.4	56.7
80°-85°	64.0	46.2	42.1	70.4	59.4	71.9	58.1	67.4

Interestingly, the mean $\Delta\theta$ is negative at small latitudes 60°-70° and positive at large values 75°-85° for almost all MLTs. For intermediate latitudes 70°-75° deg, the negative values of $\Delta\theta$ dominate. In terms of the distribution widths, the lower-latitude magnetic measurements (within 60°-65° CGM) in all the sectors except the two around midnight are characterized by a relatively narrow distribution width of 30°-50°. Particularly low are the widths for all the dayside sectors from 06 to 18 MLT: 30°-40°. The broadest distributions are seen in the midnight sectors at all the latitudes, from 21 to 03 MLT, especially in the morning part from 00 to 03 MLT.

The $\Delta\theta$ distributions for the MLT/latitudinal partitions show systematic shifts of the distribution means. The standard deviations are counted with respect to these shifted means. This means that even though a distribution has narrow width, the magnetometers on average may show a systematic measurement difference. Therefore it is interesting to make a comparison in terms of a number of points with reasonable agreement. We selected the criterion that if the direction difference is less ±45°, then the agreement is reasonable. We calculated the percentage of data points that fall into the ±45° intervals for various magnetic latitudes and magnetic local times. The results are shown in Fig. 5.19, which is organized similar to Fig. 5.18. Again, the numerical data presented for Fig. 5.19 are given in Table 5.3.

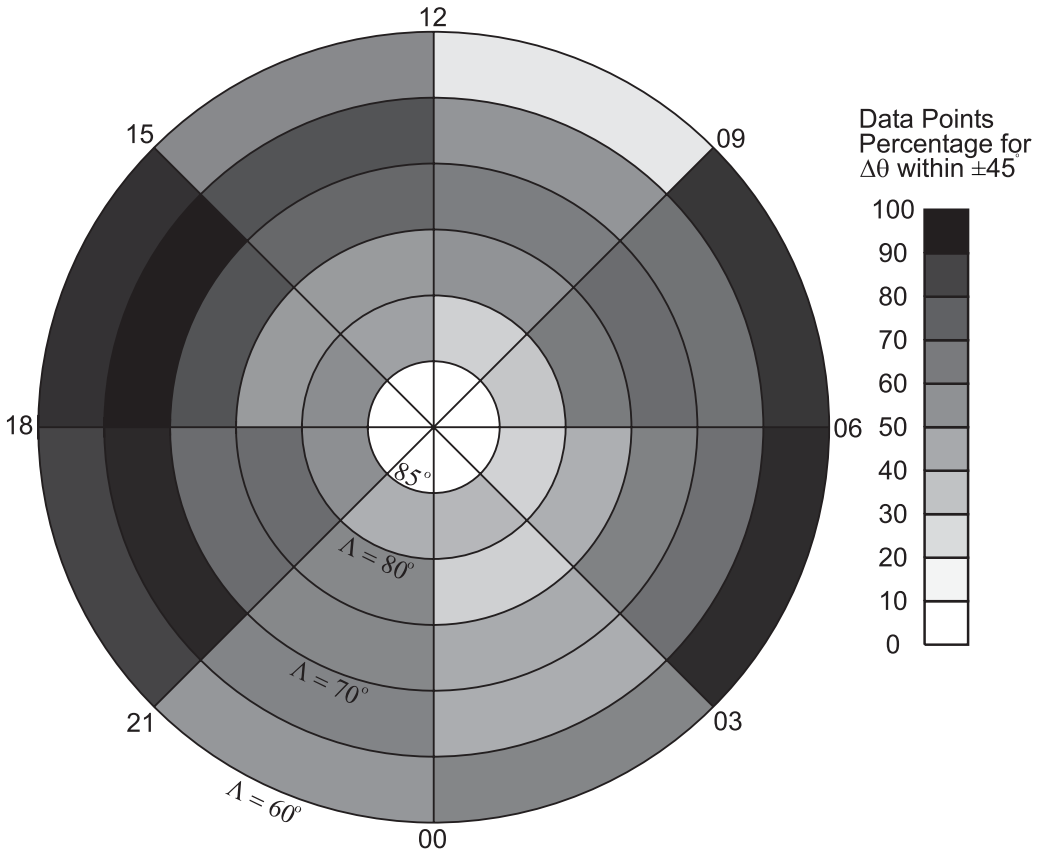

Figure 5.19. The amount of points (in percents) that are within ±45° of difference between the SDC and MEC directions for various MLT/latitudinal segments. The diagram partitioning is the same as in Fig. 5.18.

Table 5.3. The percentage of points that are within ±45° of difference between the SDC and MEC directions for various MLT/latitudinal segments.

MLT / Λ	00-03	03-06	06-09	09-12	12-15	15-18	18-21	21-00
60°-65°	55	87	84	15	53	85	80	48
65°-70°	38	64	64	48	75	90	87	56
70°-75°	39	57	65	58	67	75	66	54
75°-80°	24	37	59	49	46	46	66	54
80°-85°	34	23	28	24	43	52	50	38

According to Fig. 5.19 the best agreement is achieved in the sectors from 03 to 09 MLT and especially from 15 to 21 MLT. The sectors around noon and midnight show worse MEC/SDC agreement. Also, the agreement is worse for the higher latitudes.

5.4 Discussion

In this section we discuss the SuperDARN-magnetometer comparison in several aspects, such as the seasonal effects, magnetic local time and magnetic latitude effects, effects of the photoconductance gradients, and auroral ionospheric cavity effects.

5.4.1 Seasonal effects

Performed magnetometer-radar comparison for the equinox event (Section 5.3.3), for which reasonable amount of data was available for the sunlit, dark and transition ionospheres, showed that, overall, the degree of agreement is the best for the sunlit ionosphere. Indeed, the width of the distribution was smaller for this case. Also, the amount of points with reasonable agreement was much larger here, 63% versus 56% and 20% in other cases. In addition, the distribution was more symmetric, with smaller tails. It is important that shifts in all cases were not significantly different from zero indicating that the MEC gives a satisfactory estimate of the convection most of the time. This conclusion is in agreement with the general expectation that MEC/convection difference would be minimal for the sunlit ionosphere where the ionosphere is more horizontally uniform as compared to the transition and dark ionospheres. Perhaps part of the reason for the small solar radiation effect in the mean shift is the fact that the considered event was relatively quiet so that no strong precipitation occurred. We should mention that the mean shift of the distribution for the sunlit ionosphere was negative while for the transition and dark ionospheres it was positive. We will show later that positive values for the shift in the transition region can be partially explained by presence of gradient of the solar illumination forming a regular gradient in the conductance of the ionosphere.

Our comparison for the winter event (section 5.3.4), for which most of the data were in the dark ionosphere, showed the distribution similar to the nightside one for the equinox event, except that the difference clustering was better (smaller the distribution shift and more points within the gate of reasonable agreement) and the mean shift was negative. For the transition

region, the winter distribution did not have a strong peak, and there was a strong (27°) overall shift of it toward positive $\Delta\theta$. The sign of the shift was again positive.

For the summer event, the best distribution was for the sunlit ionosphere, and the distribution was very similar to the dayside one for the equinox. The summer distributions for the transition region and the dark region were strongly asymmetric, especially for the dark ionosphere. Again, the shift of the distribution for the transition region was positive, consistent with results for the winter and equinox events.

Summarizing all three events, one can state that the MEC differs most from the SD convection direction for the transition region. In terms of seasonal effects, one may conclude that there was not an obvious trend. For the dark ionosphere, winter conditions give slightly better agreement. For the sunlit ionosphere, the distributions are the same for the equinox and summer. These conclusions perhaps indicate that other factors than the sun-related gradient of the conductance influence the MEC-convection differences.

5.4.2 MLT and magnetic latitude effects

The analysis in terms of the MLT and magnetic longitude effects revealed several interesting features. First of all, consider the MLT sectors from 18 to 06 MLT. At the latitudes between 60° and 75°, typical latitudes for the auroral electrojets, all shifts are fairly small (the hatching is close to the vertical), which means that the magnetometers determine the plasma velocity direction more or less well. The certainty of velocity prediction is good within 18-21 MLT (deep-gray colour in the diagram in Fig. 5.18, or width ~30°-60°), whereas the lightness of the hatching in the sectors from 21 to 06 MLT indicates the high level of uncertainty in the velocity direction prediction. The disagreement is strongest in the 00-03 MLT sector, especially between 65° and 70° CGM where it is as high as 97°. The boundary between the good and poor agreement is at 21 MLT. These facts can be explained by the difference in the factors controlling the electrojets in the early-evening and late-morning sectors, as suggested by *Kamide and Kokubun* [1996]. In the evening sector, the Hall conductance is usually low and the northward electric field is strong. While both electric field and conductance contribute to the eastward electrojet intensity, the electric field variations are relatively more important than the conductance variations. This leads to a better agreement between the MEC and SDC. In the region of the Harang discontinuity, from 21 to 00 MLT, a switch from the “electric field

dominant" to the "conductance dominant" electrojet occurs. In the region of the westward electrojet, the southward electric field is relatively weak while the conductance is large. This means that the electrojet intensity is strongly controlled by the Hall conductance variations. This would lead to worse agreement between the MEC and SDC. The disagreement is expected to be even stronger for the periods of substorms during which the ionospheric conductance is highly variable and inhomogeneous.

5.4.3 Sun-related conductance gradients and the MEC/SDC agreement

The sun-related photoconductance gradients can be responsible for the observed differences in the directions of the MEC and SDC, as discussed in Section 5.2. Now we attempt to evaluate this effect in the data statistics for the transition region. The ground-based magnetometers measure the effect from the ionospheric equivalent currents described by the current stream function Ψ, defined as (5.29). The contours of the current function are the equivalent current streamlines. Under the ionospheric regions with relatively uniform conductance the contours of the current function Ψ would coincide with the contours of the SuperDARN electrostatic potential Φ. In the presence of the conductance gradients (e.g., near the terminator) the contours of the current function Ψ and, hence, the equivalent current streamlines would significantly depart from the contours of the SuperDARN potential Φ. The effect can be enhanced by the interhemispheric currents (see the next Chapter).

To consider the effect quantitatively, we recall that the electrostatic potential Φ, the conductances Σ_P and Σ_H , and the current function Ψ are related through the Poisson equation (5.42). This equation should be considered simultaneously with the boundary condition that $\Psi = 0$ at the circumference $\Lambda = 70°$. The latitude $\Lambda = 70°$ is chosen because it is low enough to assume that all the equivalent currents are closed within the spherical cap above 70°. To take the interhemispheric currents into account the technique described in Chapter 3 was applied. Photoconductances Σ_P and Σ_H were calculated using the Moen-Brekke model [*Moen and Brekke*, 1993], as described in Appendix C.

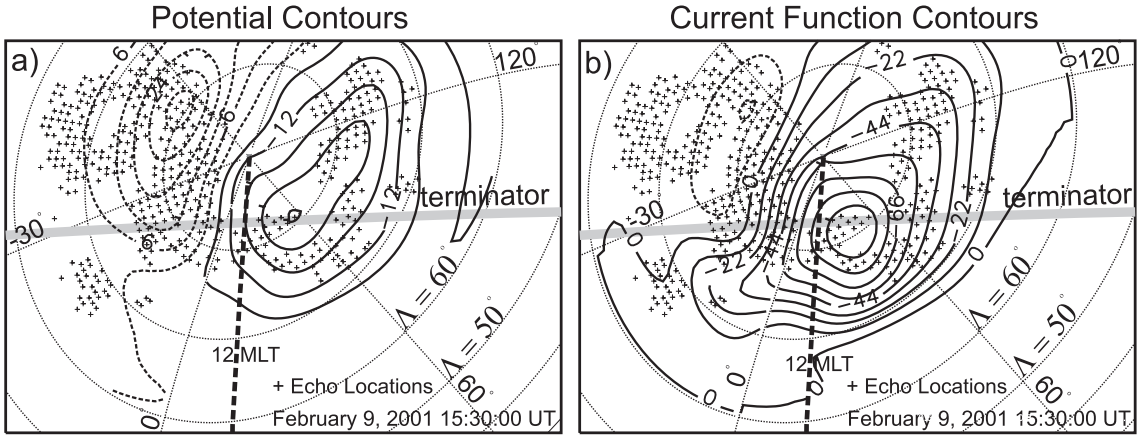

Figure 5.20. An example of (a) the SuperDARN-provided potential map and (b) the equivalent current function map. The functions are shown in contours of constant values. The potential contours are the plasma velocity streamlines, whereas the current function contours are the equivalent current streamlines.

Fig. 5.20 compares the patterns of the original SuperDARN potential in (a) and the current function in (b) computed by solving (5.42) for the equinox event of February 9, 2001. Due to the photoconductance gradients near the terminator, the conductance-corrected equivalent currents depart from the original SuperDARN potential contours. One can see that the equivalent current lines in panel (b) are shifted into the region with higher conductance equatorward of the terminator and displaced westward.

In Fig. 5.21 we statistically compare these SuperDARN-based equivalent currents with the raw MEC data for two dates, January 25 and February 9, 2001, within the sunlit/dark transition zone. Consideration of the conductance gradients somewhat improves the agreement between the radar data and the MEC, mostly in terms of the distribution width and the number of points with reasonable agreement. The fact that the drastic improvement is not pronounced indicates that other factors are probably of importance.

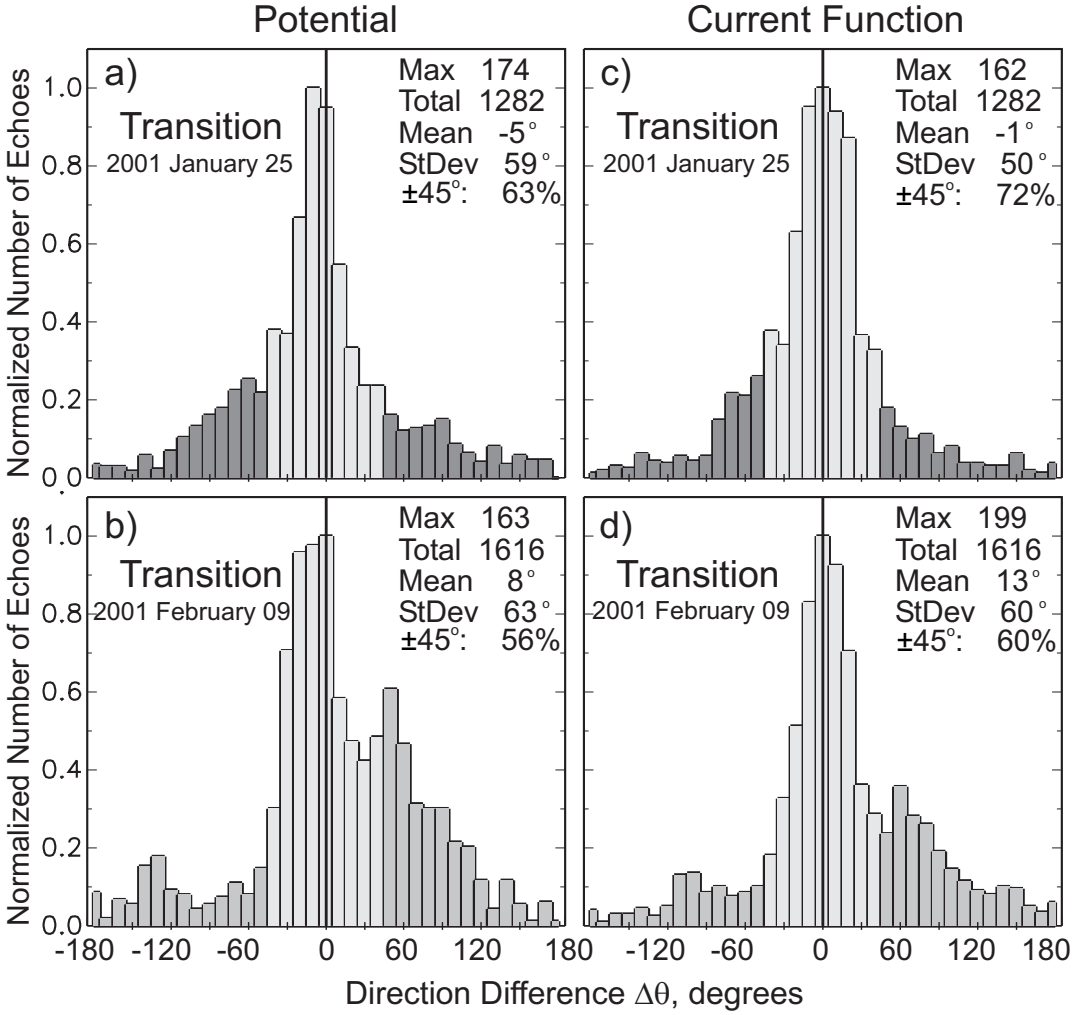

Figure 5.21. a) and b) Statistics for the direction difference Δθ between the original SuperDARN convection direction and the MEC. c) and d) Statistics for the direction difference when the original SuperDARN potential contours were "corrected" by consideration of the ionospheric conductance gradients associated with the solar illumination.

5.4.4 Other potentially important effects

Another possible explanation to the observed discrepancies between the MEC and SDC velocities at the high latitudes has been proposed by *Liang* [2004] and *Liang et al.* [2004]. These authors considered SuperDARN radar observations of the monitored convection vortices and associated equivalent currents, over the same region. It has been shown that the clockwise convection vortices in SDC almost always have their counterparts in MEC, whereas the counterclockwise SDC vortices do not produce their MEC image. The clockwise MEC vortices were often shifted equatorward and westward with respect to the SDC vortices. Within the region of the counterclockwise SDC vortices, the pattern of the MEC was not vortical and rather

poleward. *Liang et al.* [2004] suggested that clockwise and counterclockwise vortices and their associated upward and downward FACs produce different MEC patterns because of two different effects that are involved.

Clockwise vortices are associated with upward FACs and electron precipitations whose ionizing effect enhances the conductance. At the auroral latitudes the resulting Hall conductance is several times larger than the Pedersen conductance [*Aksnes et al.*, 2004]. A strong local Hall conductance enhancement may drastically increase the ratio between the MEC velocity and that of the SDC, which increases the difference in their directions.

Liang [2004] suggested that the observed SDC/MEC disagreement for the counterclockwise vortices may be due to the effect of downward FACs associated with them. A downward FAC may be carried by either proton precipitation or an upward stream of electrons. However, the contribution of proton precipitation to the total auroral particle energy is small: according to *Galand et al*. [2001], it amounts to ~15%. In most cases the downward FACs are carried by the upflowing electrons, which leads to depletion in the ionospheric ionization and formation of the "auroral ionospheric cavities" [*Doe et al*., 1993; 1995; *Aikio et al.*, 2002]. A numerical model by *Doe et al.* [1995] showed that this ionization depletion decreases the Pedersen conductance and almost does not affect the Hall conductance. Formed initially at the FAC footprint, the plasma depletion cavity grows for ~20 s, and then the downward FAC region migrates to the equatorward edge of the cavity. *Liang* [2004a] showed that combination of the Pedersen conductance gradients, pointing outward of the cavity and the convection velocity, leads to emerging of "pseudo-electric field" pointing eastward.

Indeed, consider the equation relating the electric field and the equivalent current:

$$\nabla \cdot \left(\hat{\mathbf{b}} \times \mathbf{J}^{eq} \right) = -\Sigma_H \nabla \cdot \mathbf{E} + \left(\nabla \Sigma_P \times \hat{\mathbf{b}} - \nabla \Sigma_H \right) \cdot \mathbf{E} . \tag{5.45}$$

Grouping $\nabla \Sigma_H \cdot \mathbf{E} - \Sigma_H \nabla \cdot \mathbf{E}$ into $\nabla \cdot \left(\Sigma_H \mathbf{E} \right)$ and changing $\nabla \Sigma_P \times \hat{\mathbf{b}} \cdot \mathbf{E} = \nabla \Sigma_P \cdot \left(\mathbf{E} \times \hat{\mathbf{b}} \right)$ in the right hand side, (5.45) can be rewritten in the form

$$\nabla \cdot \left(\mathbf{J}^{eq} \times \hat{\mathbf{b}} - \Sigma_H \mathbf{E} \right) = \nabla \Sigma_P \cdot \left(\mathbf{E} \times \hat{\mathbf{b}} \right). \tag{5.46}$$

By definition of the equivalent current function Ψ, $\mathbf{J}^{eq} = \nabla \Psi \times \hat{\mathbf{b}}$, so $\mathbf{J}^{eq} \times \hat{\mathbf{b}} = -\nabla \Psi$. Assuming the Hall conductance is unchanged and constant, we obtain a Poisson equation

$$\nabla^2 \left(\Psi - \Sigma_H \nabla \Phi \right) = -\nabla \Sigma_P \cdot \left(\mathbf{E} \times \hat{\mathbf{b}} \right). \tag{5.47}$$

The solution to this equation, $\Psi - \Sigma_H \nabla\Phi$, is a potential function. It has dimensionality of current (Amperes), and it is actually the difference between the equivalent current and the Hall current. Therefore it is possible to introduce a "pseudoelectric" field, $\mathbf{E}^*$, as the gradient of this "pseudopotential":

$$\mathbf{E}^* = -\nabla\left(\Psi - \Sigma_H \nabla\Phi\right). \tag{5.48}$$

The right hand side of the equation (5.48) is negative in the westward part of the cavity and positive in the eastward side, which implies the eastward direction of the "pseudoelectric field" $\mathbf{E}^*$. Due to the Hall conductance this one gives rise to a jet of equatorward equivalent current or poleward MEC stream across the SDC cell. This MEC stream is more pronounced in the region of the plasma depletion cavity not distorting the equatorward part of the MEC cell. Hence the equatorward parts of SDC and MEC patterns are more consistent than the poleward ones.

Fig. 5.22 gives a schematic view of the differences in MEC distortions with respect to SDC for the dusk sector a) and the dawn sector b). The clockwise vortices are predominant in the dusk sectors, whereas the counterclockwise vortices are more frequent in the dawn sectors in accordance to the general two-cell global convection pattern. Therefore it is reasonable to assume

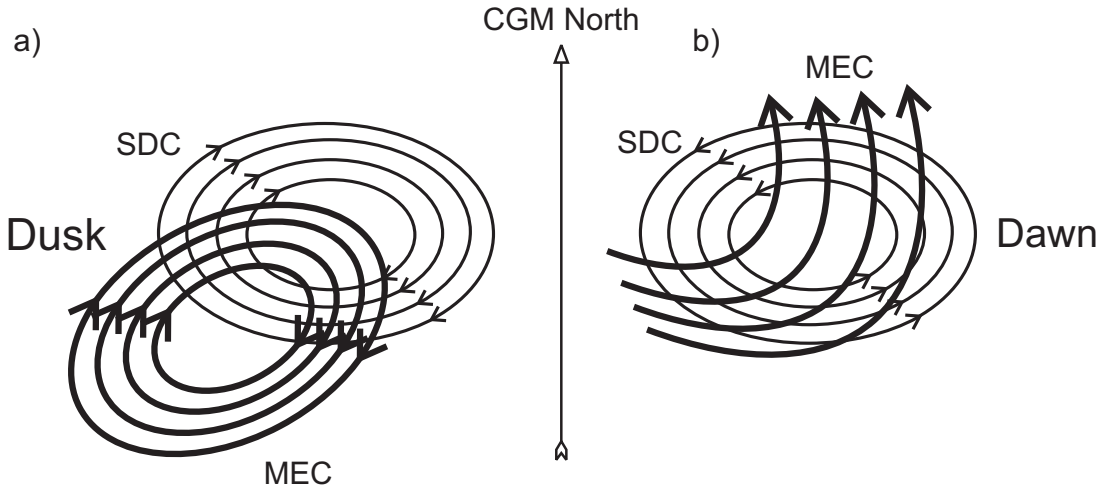

Figure 5.22. Sketch of characteristic differences in magnetic equivalent convection (MEC) patterns with respect to the SuperDARN-produced convection patterns for the dusk sectors (panel a) and the dawn sectors (panel b). It is assumed that the clockwise convection vortices are more frequent in the dusk sectors, while the counterclockwise vortices are more frequent in the dawn sectors in accordance with the general global two-cell convection pattern. The clockwise MEC vortices in the dusk sectors are distorted due to the conductance gradients associated with the terminator and the auroral precipitation zone. The counterclockwise MEC vortices in the dawn sectors are distorted due to the plasma depletion cavity and pseudoelectric field effects.

that the MEC patterns are distorted with respect to those of SDC in the dusk sectors as it is characteristic for the clockwise vortices, whereas the MEC patterns in the dawn sectors are distorted in the way normal for counterclockwise vortices. In the dusk sectors, the clockwise MEC vortices undergo “attraction” to the strong conductance gradients, associated with the sunlit/dark transition region and with the auroral precipitation zone (around 70° CGM). Also, these clockwise vortices are displaced westward as shown in Fig. 5.22a. In the dawn sectors, the counterclockwise MEC vortices are destroyed by the stronger poleward stream of the MEC due to the plasma depletion cavity associated with the downward FACs and the resulting pseudoelectric field as shown in Fig. 5.22b.

In view of these effects it is possible to explain many of the features of Fig. 5.18 using the sketch of a global direction difference between the SDC and MEC vectors presented in Fig. 5.23.

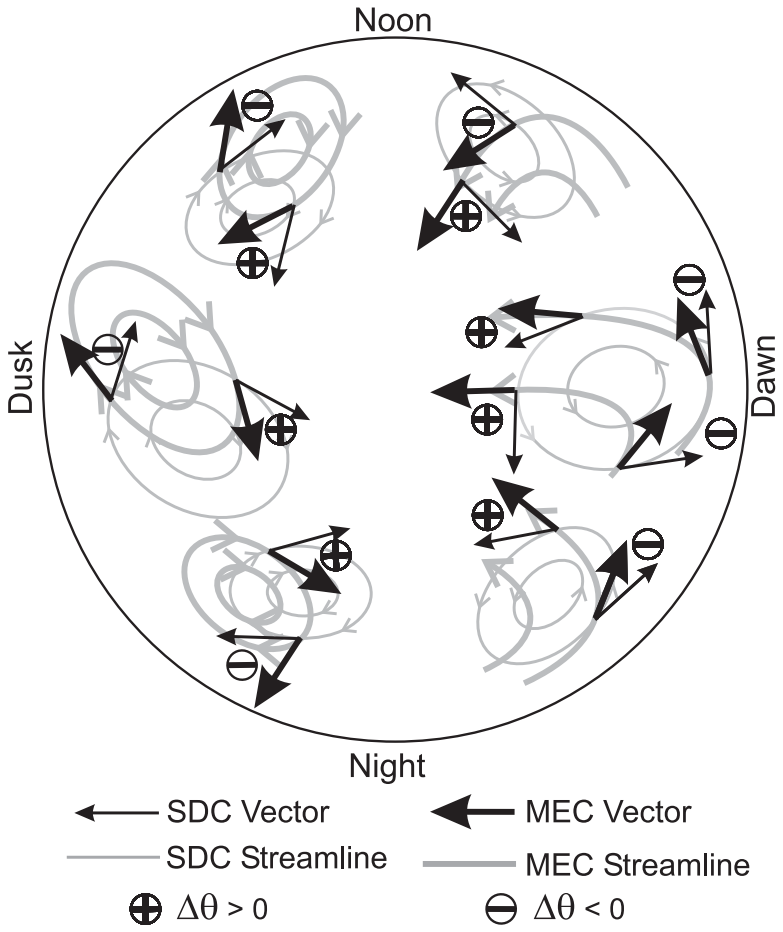

Figure 5.23. Mutual positions of the SDC and distorted MEC patterns on a global perspective and direction differences between the SDC and MEC vectors in various MLT sectors. Due to the character of distortions, the direction differences are in more cases positive in higher latitudes and negative in lower latitudes.

The clockwise tilt of the lining is more characteristic of the higher latitudes, which is confirmed by the character of MEC distortions there for all the sectors. In the sectors close to the noon, from 09 to 15 MLT, the positive $\Delta\theta$ at the high latitudes is gradually changing into the negative $\Delta\theta$ with descending to the lower latitudes. The lining tilt in the dusk semicircle is more definitive (darker color) than the tilt in the dawn semicircle. This effect may be due to the less transient character of the MEC distortion in the dusk sector where the $\Delta\theta$ mean deflection is due to more stable factors like the terminator and the auroral oval. In the dawn sector the distortion appears due to the transient action of the downward FAC associated with the counterclockwise vortices, hence the $\Delta\theta$ mean deflection is most definitive in the highest and the lowest latitudes (darker lining), and less certain in the middle latitudes from 65° to 80° CGM (the lining is light).

5.4.5 One possible scheme of conductance derivation from joint SuperDARN and magnetometer data

In principle, the ionospheric conductance distribution on a global scale can be obtained from the ground-based magnetometer and SuperDARN convection observations. Unfortunately, since the conductance has two components, Pedersen and Hall, and there is only one equation (5.42) that associates the radar-provided potential Φ and the magnetometer-provided equivalent current stream function Ψ, it is impossible to solve it for the two independent variables, Σ_P and Σ_H. However, as a first approximation, one can assume that the conductances are proportional to one another as

$$\Sigma_P = k\Sigma_H \ . \tag{5.49}$$

The magnetometer network supplies equivalent current data. Interpolation over a region of interest yields continuous two-dimensional vector field of the equivalent current $\mathbf{J}^{eq}$, which can be converted into the equivalent current stream function Ψ through numerical solving of the Poisson equation (5.32). The SuperDARN network supplies the electric potential function Φ over the same region. If the Φ and the Ψ are known over the same area, one can find the conductance distribution from these two functions. One can rewrite the equation (5.42) in the form

$$\frac{\partial\Sigma_H}{\partial x}\frac{\partial\Phi}{\partial x}+\frac{\partial\Sigma_H}{\partial y}\frac{\partial\Phi}{\partial y}+k\frac{\partial\Sigma_H}{\partial y}\frac{\partial\Phi}{\partial x}-k\frac{\partial\Sigma_H}{\partial x}\frac{\partial\Phi}{\partial y}+\Sigma_H\nabla^2\Phi=\nabla^2\Psi\ . \tag{5.50}$$

Note that this equation contains only one unknown variable, Σ_H, and all the others are known functions or numbers.

Using the notation $p = \nabla^2\Psi$, $q = \nabla^2\Psi$, and $\mathbf{f} = \begin{Vmatrix} \dfrac{\partial\Phi}{\partial x} - k\dfrac{\partial\Phi}{\partial y} \\ k\dfrac{\partial\Phi}{\partial x} + \dfrac{\partial\Phi}{\partial y} \end{Vmatrix}$, equation (5.20) can be presented in the form

$$\mathbf{f} \cdot (\nabla\Sigma_H) + q\Sigma_H = p, \tag{5.51}$$

or, in more detail,

$$f_x \frac{\partial\Sigma_H}{\partial x} + f_y \frac{\partial\Sigma_H}{\partial y} + q\Sigma_H = p. \tag{5.52}$$

This is a linear partial differential equation of the first order. It can be solved for the Σ_H using the method of characteristics, which decomposes equation (5.52) into a system of two ordinary differential equations. The latter can be solved numerically. A similar technique has been used by *Amm* [1995, 1998]. However, *Amm* [1995, 1998] did not use the idea of current function in his derivations.

We should mention that this approach has several obvious drawbacks. The conductance ratio *k* is not really known and it is not a constant. It can change locally by an order of magnitude, for example, in the region of the aforementioned plasma depletion cavity associated with the downward FACs. Another difficulty is the correct specification of the boundary conditions for Σ_H when solving equation (5.52).

5.5 Conclusions

The results obtained in this chapter can be summarised as follows.

1) Formulation and strict mathematical proof of the Fukushima theorem in a generalised version which allows calculation of the ionospheric equivalent currents as the purely rotational component of the total ionospheric current field. This generalised Fukushima theorem may be used in the studies where the SuperDARN and the ground-based magnetometer measurements are combined to produce more reliable patterns of the ionospheric equivalent current distributions.

2) Suggestion of a method of exact calculation of the ionospheric equivalent currents from the electric potential and conductance distributions. Suggestion of a method of calculation of a

divergence-free equivalent current field from the interpolated ground-based magnetometer measurements.

3) Statistical comparison of the MEC and SD convection directions for 75,241 joint measurements during five relatively quiet days showed that the MEC gives reasonable estimate of the convection direction in about 57% of cases. The strongest magnetometer-radar disagreements were found for the transition region between the sunlit and dark ionospheres. The MEC/SDC agreement for the sunlit and dark ionospheres is about the same. The MEC/SDC differences are about the same order of magnitude for all seasons.

4) Strong disagreement between the MEC and SDC in the transition region can be partially explained by the presence of the conductance gradient produced by solar illumination.

5) In terms of MLT, the MEC/SDC agreement is the best in the evening sector. We interpret this result as a consequence of strong electric field control of the magnetic perturbation as opposite to the morning sector where magnetic perturbations are strongly controlled by the variations in the ionospheric conductance.

6) The MEC/SDC agreement varies with the latitude of observations and magnetic local time. It is the worst at very high latitudes for all MLT and at the low latitudes on the dayside. Evidences were found that support the previously suggested notion that the character of the magnetosphere-ionosphere coupling within the regions of down-flowing and up-flowing field-aligned currents contribute to the MEC-SDC differences.

7)) The MEC/SDC agreement is better for the vertical flows driven by upward FACs than for those driven by downward FACs. The effect takes place because the downward FACs are carried by upflowing electrons, which leads to depletion in the ionospheric ionization and formation of local Pedersen conductance gradients. The latter in turn cause distortions of the vortical flows.

CHAPTER 6

TRAVELING CONVECTION VORTICES

A traveling Convection Vortex (TCV) produces a special type of high-latitude daytime magnetic signature at the ground. For a single magnetic station, a TCV looks like as an isolated magnetic field variation with the H-component demonstrating a bipolar signature. The deflection may be either negative to positive or positive to negative. During the same period, the D-component undergoes a single positive or negative excursion. Thus, the H-component variation is the negative time derivative of the D-component variation. For a longitudinally separated chain of magnetic stations, TCV signatures show tailward propagation; they travel westward in the dawn sector and eastward in the dusk sector, hence the name "traveling" vortex. Data for a network of magnetic stations, spread both latitudinally and longitudinally, reveal a twin-vortex structure in which the two vortices have flows of opposite rotation. It is believed that the two convection cells are driven by field-aligned currents of opposite directions.

The nature of TCVs is not well understood. One popular hypothesis associates TCVs with sudden pulses of the solar wind dynamic pressure or velocity. Such changes can launch a surface wave on the magnetopause or the LLBL inner edge, which in turn can create FACs of alternating directions closing via the ionosphere [*Lyatsky et al.*, 1997]. According to another hypothesis, the sources of TCVs are located deeper within the magnetosphere, inside the plasma sheet [*Yahnin and Moretto,* 1996; *Yahnin et al*., 1997]. This opinion is supported by the fact that TCVs appear at relatively low magnetic latitudes of 67° - 75º CGM while the magnetopause and LLBL ionospheric projections are at ~ 80º CGM. One can argue, however, that the magnetic

disturbances can be detected at lower latitudes because there is a strong latitudinal gradient of the conductance so that the center of the field-aligned current, setting up a TCV, and its focus are shifted equatorward in latitude [*Benkevich and Lyatsky*, 2000].

We consider a very special situation of TCV excitation and propagation near the solar terminator line. We showed that non-uniform conductance distribution near the terminator region can lead to strong interhemispheric currents (Chapter 3) and can drastically modify the pattern of equivalent currents (Chapter 5). This implies that a TCV near terminator should have a very unusual appearance, and we predict the TCV shape theoretically. Finally, we attempt to study TCV with SuperDARN radars. The goal here is just to show experimentally that a TCV is indeed a circular motion of ionospheric plasma. The need for such a proof comes from the fact that, although magnetometer data do clearly show circular motion, there is still a concern that the motion in equivalent currents can be created as a consequence of superposition of a number of special flows.

6.1 TCV: basic features and hypotheses on nature

Fig. 6.1 gives an example of TCV event from *Glassmeier et al.* [1989]. These are H-component traces from the Greenland meridional chain of stations. All stations show similar patterns of changes. One can recognize a bipolar signature lasting ~15 min. The amplitude of the perturbations is of the order of 100 nT. This is a relatively strong event.

Fig. 6.2 taken from *Glassmeier et al.* [1989] is a 2-D plot of magnetic perturbations seen by the magnetometers in northern Scandinavia. Each vector is a magnetic equivalent vector at one instant of time; a set of vectors for each station gives “an image of TCV”. The twin-vortex structure of the feature is obvious. Such vortices move either east or west, typically away from noon, with a velocity of several $\mathrm{km\,s^{-1}}$.

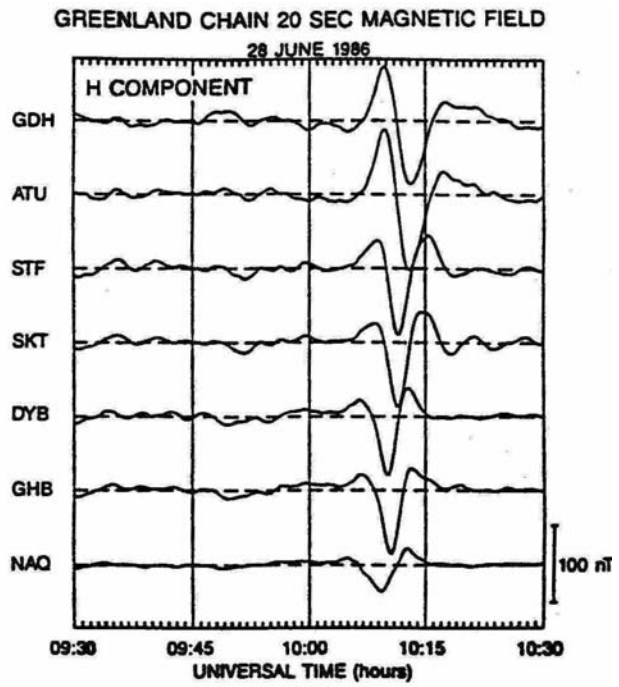

Figure 6.1. TCV event in high-pass (with the cut-off period of 30 min) filtered H-component magnetic traces from the Greenland magnetometer chain. (From *Glassmeier et al.* [1989])

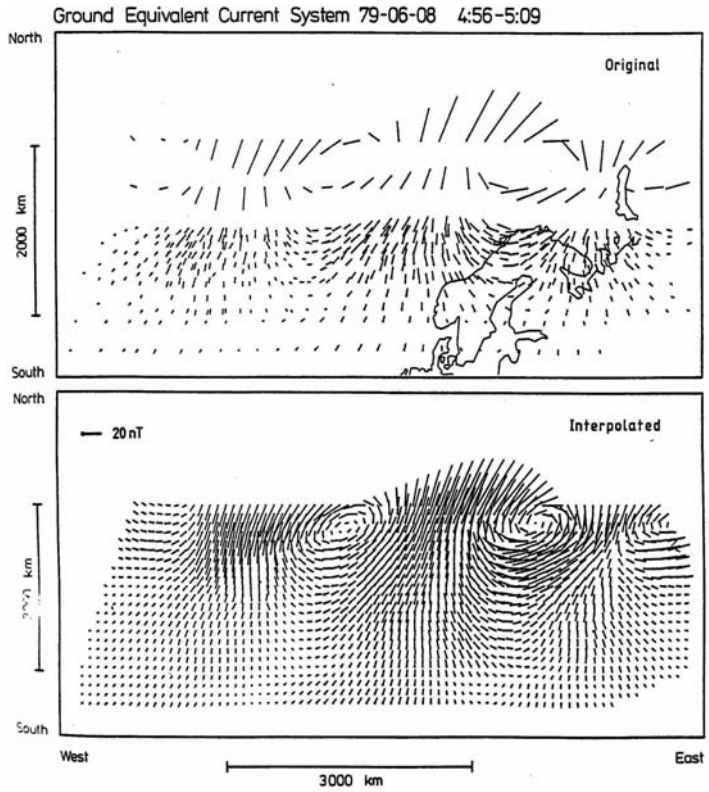

Figure 6.2. TCV event in equivalent current vector hodographs (upper panel) and in interpolated hodographs (lower panel). (From *Glassmeier et al.* [1989])

It is believed that TCVs may appear on both sides of the noon meridian [*Slinker et al.*, 1999]. In this scenario, Fig. 6.3a, a pair of TCVs emerges close to the noon meridian. Both vortices grow and travel antisunward, Fig. 6.3b. While the first pair is reaching the 06 and 18 MLT meridians, another pair can emerge near the noon meridian, Fig. 6.3c. The new vortices have the sense of rotation opposite to their predecessors. The old vortices decay while the new ones grow and follow the first pair, Fig. 6.3d. Eventually, the second pair of TCVs also decays, as shown in Figs. 6.3e and 6.3f.

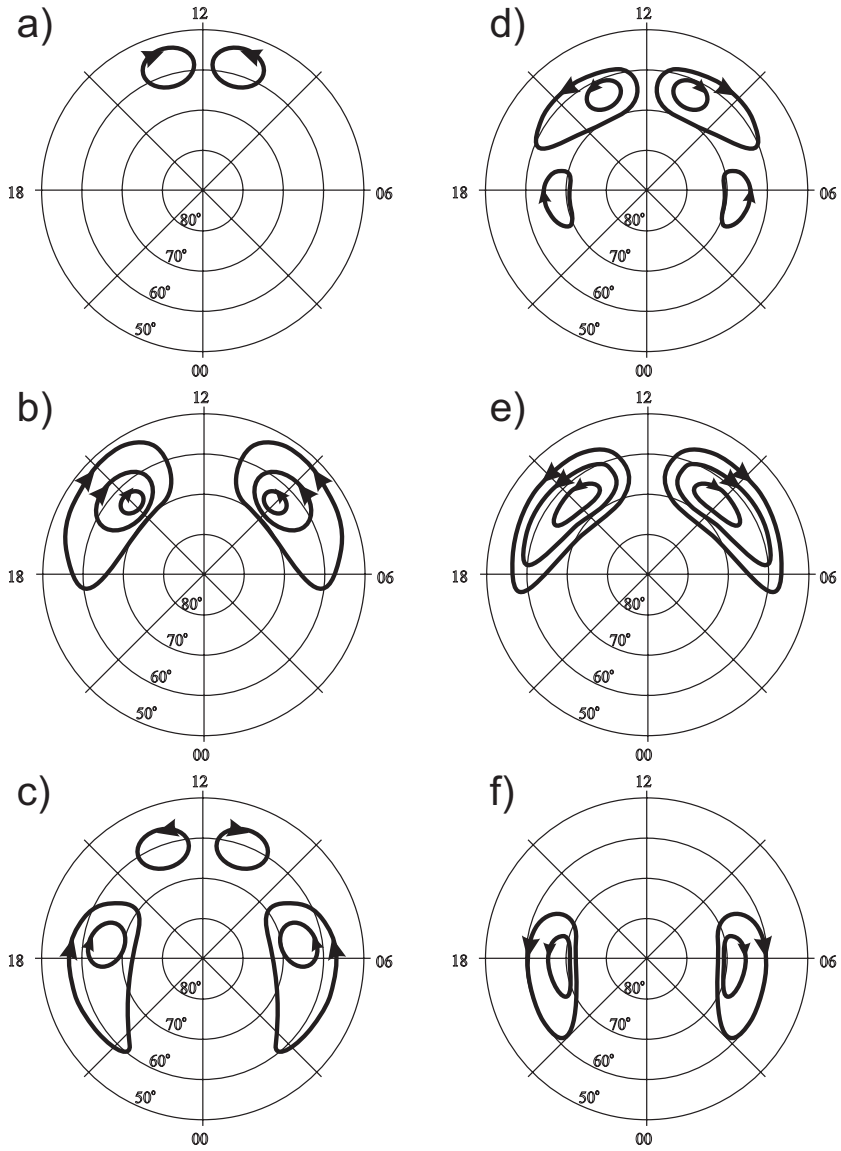

Figure 6.3. Schematics of a twin-vortex TCV event occurring in both morning and evening sectors. Arrows show the plasma flow directions.

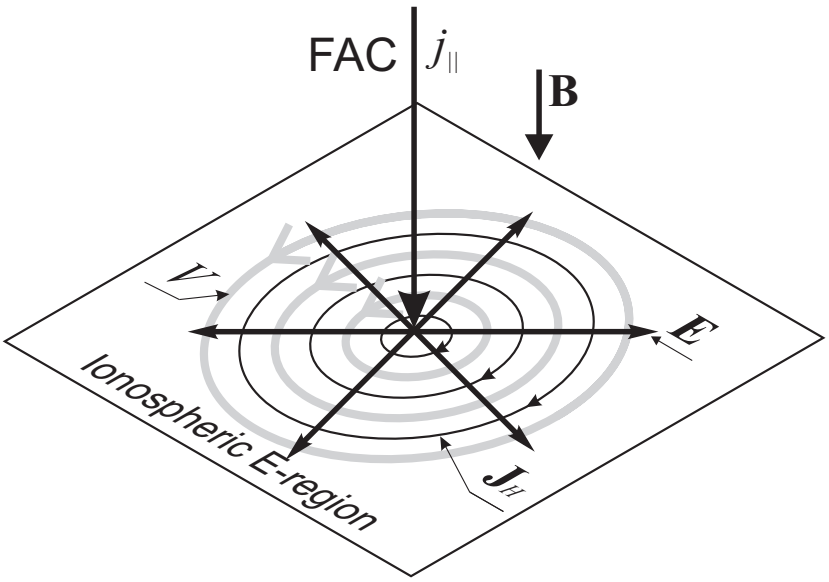

Figure 6.4. TCV as an ionospheric Hall vortex driven by the incident FAC.

A vortical equivalent current structure in ground magnetic observations implies existence of the E-region ionospheric Hall current vortex, which is driven by a filamentary FAC. Fig. 6.4 illustrates the formation of the Hall current vortex. The divergent electric field, supported by the FAC $j_{||}$, causes the drift plasma motion at the velocity $v = B^{-2}\mathbf{E}\times\mathbf{B}$ and forms a vortical plasma flow around the FAC's footprint in the F region. In the E-region, electrons are involved in this vortical motion as well while ions are almost at rest which results in the Hall current $\mathbf{J}_H$, directed opposite to the electron velocity. We would like to stress that vortical drift plasma flows should be seen at F region heights and thus detectable by the SuperDARN HF radars.

Other salient features of TCVs are as follows (according to the website http://www.oulu.fi/~spaceweb/textbook/):

1. Occurrence peaks at about 09 and 14 MLT;
2. Occurrence peaks at about 73° invariant latitude, though TCVs have been observed at the latitudes from 60° to 75°;
3. Morning side vortices seem to occur at lower latitudes than the afternoon ones;
4. Tailward propagation speeds are 0.1-0.3 degrees/s, i.e., 3-10 km/s in the ionosphere and 130-400 km/s at the magnetopause;
5. The foci of vortices are separated by 1000-2000 km;

6. FAC current densities can be several $\mu A/m^2$ in the ionosphere, total FAC amounting to a few hundred Amperes;
7. Conjugate vortices in the two hemispheres have opposite senses of rotation.

There are several hypotheses on the nature of traveling convection vortices:

1. Impulsive penetration of the solar wind plasmoids or plasma blobs into the magnetopause [*Heikkila et al.*,1989]
2. Bursty merging [*Glassmeier et al.*, 1989, 1992]
3. The Kelvin-Helmholtz instability [*McHenry et al.*, 1990]
4. Magnetopause boundary motion driven by abrupt changes in the solar wind dynamic pressure [*Matsushita*, 1957]
5. Tangential discontinuity [*Kataoka et al*., 2002]
6. Magnetospheric vortical driver [*Elphic*, 1988; *Slinker et al.*, 1999]

The above hypotheses explain some specific observations but none can conclusively explain all body of observations. There have been no experimental data supporting the impulsive penetration hypothesis [*Sibeck et al*., 2000; *Owen and Cowley*, 1991]. *Yahnin and Moretto* [1996] and *Yahnin et al*. [1997] presented evidences that the TCV source region could be inside the plasma sheet. The high degree of conjugacy of the events suggests a source close to the equatorial plane, while the MLT distribution implies the source region location close to the subsolar magnetopause. This hypothesis has also been supported by the modelling results by *Slinker et al.* [1999]. Some observations suggest that *multiple* convection vortex systems are related to Pc5 pulsations [*Motoba*, 2002; *Friis-Christensen et al*., 1988a, 1988b] and (most likely) to the accompanying Kelvin-Helmholtz instability in the LLBL) [*McHenry et al*., 1990].

6.2 TCV features around terminator: a model study

It is widely assumed that the convection flow and equivalent ionospheric currents are approximately the same, but oppositely directed. This is true, but only in the case of a homogeneous ionosphere. However, the high-latitude ionosphere is not homogeneous, especially for winter conditions. The conductance inhomogeneity can lead to formation of interhemispheric field-aligned currents in the regions where ionospheric conductance varies, and to very different

patterns in convection flow and equivalent ionospheric currents as we discussed in Chapters 3 and 5.

In this section we study in detail the equivalent ionospheric currents that are expected near the solar terminator line when the conductances in both hemispheres are taken into account. In the winter dayside high-latitude ionosphere the terminator is often located equatorward of the cusp region where the TCV sources are thought to be located. In these cases, secondary field-aligned currents arise at the terminator because of the redistribution of ionospheric currents in the conjugate summer sunlit ionosphere where the conductance is significantly higher, Chapter 3. These secondary FACs create magnetic perturbations that can be detected and studied by magnetometers.

To illustrate the scenario to be studied we refer the reader back to Fig. 3.12a. This figure shows the current system created by dayside field-aligned currents located poleward of the terminator in the northern hemisphere. In this case, secondary field-aligned currents arise on the terminator due to redistribution of ionospheric currents flowing in the conjugate summer sunlit ionosphere, shown in Fig. 3.12b. Part of these ionospheric southern hemisphere currents flows along the magnetic field lines, attached to the terminator position, into the winter ionosphere and close there through the sunlit (well conducting), lower latitude ionospheric region.

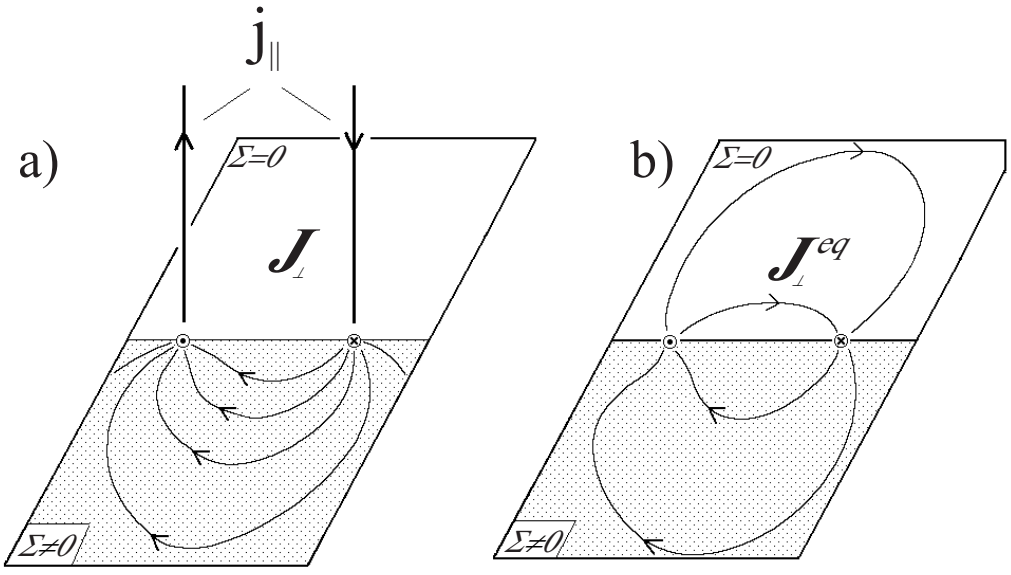

Figure 6.5. A scheme explaining the formation of a vortex in equivalent ionospheric currents when two field-aligned currents are flowing at the boundary of two regions with different conductances. The upper region is assumed to have zero conductance, so that ionospheric currents can flow only in the lower region. Panel (a) shows field-aligned and ionospheric currents, the latter take place only in the lower region. Panel (b) shows resulting equivalent currents forming a vortex attached to the terminator.

Now assume that we have a field-aligned current loop attached to the terminator, Fig. 6.5. For simplicity, the upper region is assumed to have zero conductance so that no ionospheric currents can flow there. Fig. 6.5a shows both the field-aligned and ionospheric currents, the latter occurring only in the lower, conducting region. Fig. 6.5b shows resulting equivalent currents from both ionospheric and field-aligned currents. These equivalent currents would be registered by ground magnetometers.

6.2.1 TCV-like equivalent currents for a sharp conductance gradient, analytical solution

To reveal features in the electric potential and equivalent current distribution around the region of a conductance gradient, we first present results of an analytical solution to the problem. The model to consider is similar to the one investigated in Chapter 3 where field-aligned currents associated with a sharp conductance gradient in one hemisphere have been studied, see Fig. 3.4. We again introduce complex coordinates such that the real axes are the parallels and the imaginary axes are the meridians with the imaginary axis pointing to the North Pole and the real axis pointing to the east. We have four semiplanes, each having different complex conductances: $\Sigma_{N1} = \Sigma_{N1P} - i\Sigma_{N1H}$ and $\Sigma_{N2} = \Sigma_{N2P} - i\Sigma_{N2H}$ in the northern hemisphere and $\Sigma_{S1} = \Sigma_{S1P} - i\Sigma_{S1H}$ and $\Sigma_{S2} = \Sigma_{S2P} - i\Sigma_{S2H}$ in the southern hemisphere. We assume that a magnetospheric source supplies field-aligned current incident on both hemispheres at the points $z_1 = id$. We are seeking the solution for the potential, real current stream function and equivalent current stream function in both hemispheres.

Acting in the same way as in Chapter 3, Section 3.3.2, one can obtain the potential distributions poleward (Φ_1) and equatorward (Φ_2) from the terminator

$$\Phi_1 = \mathrm{Re}\left[F_0 + F_1^{/} \right], \tag{6.1a}$$

$$\Phi_2 = \mathrm{Re}\left[F_0 + F_2^{/} \right] \tag{6.1a}$$

as well as the Ψ-function for the equivalent currents flowing in the ionosphere in all the four semiplanes:

$$\Psi_{N1}^{eq} = \mathrm{Im}\left[\Sigma_{N1}^{*}\left(F_0 + F_1^{/} \right) + \Sigma_{CN} F_{11}^{/} - \Sigma_{N1P} F_0 \right], \tag{6.2a}$$

$$\Psi_{N2}^{eq} = \mathrm{Im}\left[\Sigma_{N2}^{*}\left(F_0 + F_2^{/} \right) + \Sigma_{CN}^{*} F_{22}^{/} - \Sigma_{N1P} F_0 \right] \tag{6.2b}$$

in the northern hemisphere and

$$\Psi_{S1}^{eq} = \mathrm{Im}\left[\Sigma_{S1}^{*}\left(F_0 + F_1^{/}\right) + \Sigma_{CS}F_{11}^{/} - \Sigma_{S1P}F_0\right], \tag{6.2c}$$

$$\Psi_{S2}^{eq} = \mathrm{Im}\left[\Sigma_{S2}^{*}\left(F_0 + F_2^{/}\right) + \Sigma_{CS}^{*}F_{22}^{/} - \Sigma_{S1P}F_0\right] \tag{6.2d}$$

in the southern hemisphere. In these equations, the F_0, $F_1^{/}$, $F_2^{/}$, $F_{11}^{/}$, and $F_{22}^{/}$ are complex potentials. The F_0 is a potential due to the point FAC I. The $F_1^{/}$ is a potential due the point FAC $I^{/}$ which is a "mirror image" of the I over the conductance discontinuity line. The FAC $I^{/}$ is incident on the points $z_2 = -id$. The third complex potential, $F_2^{/}$, is in turn a mirror image of $I^{/}$ at $z_1 = id$. The $F_{11}^{/}$ is a potential due to the FAC I as though the I were incident on the mirror point $z_2 = -id$, and the $F_{22}^{/}$ is the same as F_0. The asterisk superscript (*) denotes the complex conjugate. Also, in equations (6.2) the conductances Σ_{CN} and Σ_{CS} are introduced as:

$$\Sigma_{CN} = \frac{1}{2}\left(\Sigma_{N1} - \Sigma_{N2} - \left(\Sigma_1 - \Sigma_2\right)\frac{\Sigma_{N1}^{*} + \Sigma_{N2}}{\Sigma_1^{*} + \Sigma_2}\right), \tag{6.3a}$$

$$\Sigma_{CS} = \frac{1}{2}\left(\Sigma_{S1} - \Sigma_{S2} - \left(\Sigma_1 - \Sigma_2\right)\frac{\Sigma_{S1}^{*} + \Sigma_{S2}}{\Sigma_1^{*} + \Sigma_2}\right). \tag{6.3b}$$

By using the equations (6.1) and (6.2), one can compute the potential distributions and equivalent currents in both hemispheres.

Consider the solution (6.1) and (6.2) for the conductance in the northern plane of Σ_{N1P} = .88 S, Σ_{N1H} = 1.50 S poleward from the terminator and ten times higher, Σ_{N2P} = 8.8 S, Σ_{N2H} = 15.0 S, equatorward from the terminator. Such a distribution models the conductance drop between the sunlit, equatorward, and the dark, poleward parts of the northern high-latitude ionosphere. In the southern plane the conductance is assumed to be uniform and high, Σ_{S1P}=Σ_{S2P} = 8.8 S, Σ_{S1H}=Σ_{S2H} = 15.0 S, which models the sunlit southern hemisphere. The magnetospheric current sources generate two FACs, I_1 = 1000 A and I_2 = -1000 A, incident at two ionospheric points 810 km away from the terminator and 2000 km away from each other. The potential and equivalent current distributions due to this FAC system are shown in Fig. 6.6 a), b) in the northern hemisphere and c), d) in the southern hemisphere.

According to Figs. 6.6a and 6.6c the potential distribution is "symmetric" in conjugate hemispheres; there are clear vortical potential lines in the highly conducting plane of the southern hemisphere and its projection in the northern hemisphere. Also one can notice a strong "kink" or

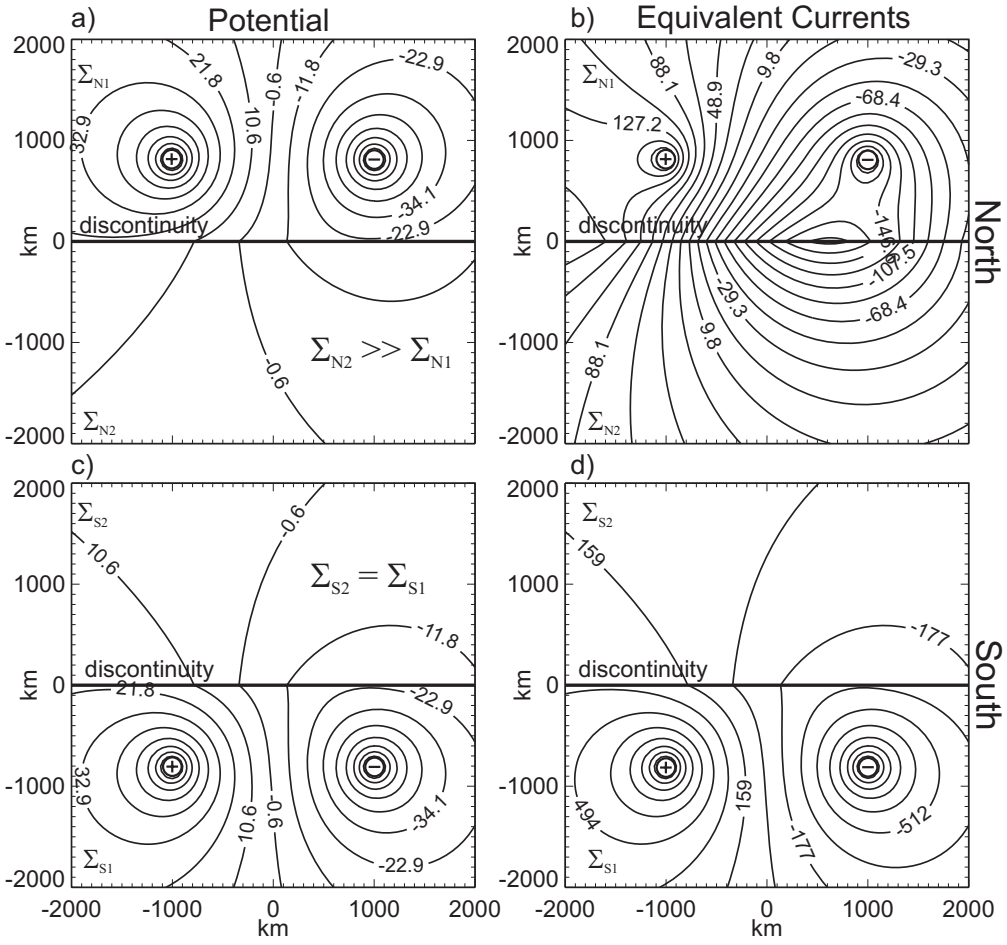

Figure 6.6. Potential contours (a, c) in kV and equivalent current streamlines (b, d) in kA due to a pair of voltage sources 2000 km away from one another. Potential and equivalent currents are shown in a) and b) in the north and in c) and d) in the south.

sudden change of the contour direction at the discontinuity line.

The equivalent current contours, Fig. 6.6b and 6.6d are quite different in opposite hemispheres. In the southern hemisphere, the current contours are very similar to the contours of the electric potential. This is not a surprise since the conductance was assumed uniform in this hemisphere. In the northern hemisphere, one can notice vertical flows around the projections of the FACs, which is also expected. However, there is an additional vertical flow "attached" to the line of the conductance discontinuity. We would call such flow a detached vortex. The detached vortex is weaker than the main vortex centered at the FACs' projections.

It should be noted that the detached vortex *does not* exist in the real Hall currents, whose streamlines look approximately like the potential contours in (a). The vortex at the discontinuity line is an apparent effect caused by the conductance inhomogeneity and by the presence of

interhemispheric currents. Nonetheless, such a vortex in ionospheric equivalent currents would be sensed by ground-based magnetometers.

6.2.2 TCV-like equivalent currents for a smooth conductance gradient, numerical solution

The analytical model considered in the previous section is only applicable to the case of discontinuity in the conductance which is unrealistic. The developed approach cannot be applied to the case of a smooth conductance gradient. In the latter case more powerful, numerical methods can be utilized.

Now we study the equivalent current distribution due to a pair of oppositely directed FACs with the ionospheric conductance distribution close to a real one. The problem setup is similar to the one considered in the previous section except we assume a relatively gradual change of the conductance with latitude near the terminator line. The source is assumed to consist of upward $\boldsymbol{j}_{\|0}{}^{\uparrow}$ and downward $\boldsymbol{j}_{\|0}{}^{\downarrow}$ linear field-aligned currents located poleward of the region with fast changes of the conductance. The potential difference between these two field-aligned current filaments is assumed to be the same in both hemispheres, which implies that the source is a voltage generator. For the ionospheric conductance, a model by *Robinson and Vondrak* [1984] and *Robinson et al.* [1987] was assumed (Refer to Appendix C for its description). We first consider the solution for the winter in the northern hemisphere, more specifically the day of December 29. For this period, conductances in the opposite hemispheres are quite different. According to the model, in the dark northern ionosphere the Hall conductance is ~1.5 S and it rapidly increases equatorward from the terminator to reach ~16 S. In the sunlit southern hemisphere the conductance is more or less homogeneous being between 13 S and 16 S.

Because of the high conductivity along magnetic field lines, the sites in the region of closed field lines may be considered as a single site with a conductance equal to the sum of those of the N and S hemisphere, i.e., $\hat{\Sigma} = \hat{\Sigma}^N + \hat{\Sigma}^S$. The Cartesian coordinates were chosen with X axis pointing eastward, Y axis pointed poleward, and Z axis pointed opposite to the direction of the geomagnetic field.

The ionospheric electric potential Φ and the field-aligned current $j_{\|0}$ are related via the Poisson equation for Φ:

$$\nabla \cdot \left(\hat{\Sigma} \nabla \varphi \right) = j_{\parallel 0} \ . \tag{6.4}$$

For the details of the derivation of this equation see Section 3.3.3, Chapter 3, where equation (6.4) is represented in a more convenient for solution form (3.29). Via solving equation (3.29) with the FACs $j_{\parallel 0}$ given, we obtain the electric potential distribution. Having the latter, we calculate the ionospheric equivalent currents in the dayside northern (N) and southern (S) conjugate ionospheres. The current function for equivalent ionospheric currents (introduced as Ψ in equation (5.29)) is obtained from the equation (5.42). We also calculate the distribution of interhemispheric field-aligned currents arising due to the differences in ionospheric conductance gradient patterns in the conjugate ionospheres. The interhemispheric FACs are obtained by applying the left hand side operator in (6.4) to the potential distribution using individual conductance distribution for each hemisphere. The equations (6.4) and (5.42) have been solved numerically on a rectangular grid of m×n nodes. The method of the solution is described in Appendix A. Fig. 6.7 shows the calculated electric potential distribution in the northern hemisphere around noon on December 29 at the Sondre Stromfjord meridian passing through Greenland. The contours correspond to equipotential curves. In the southern hemisphere in the

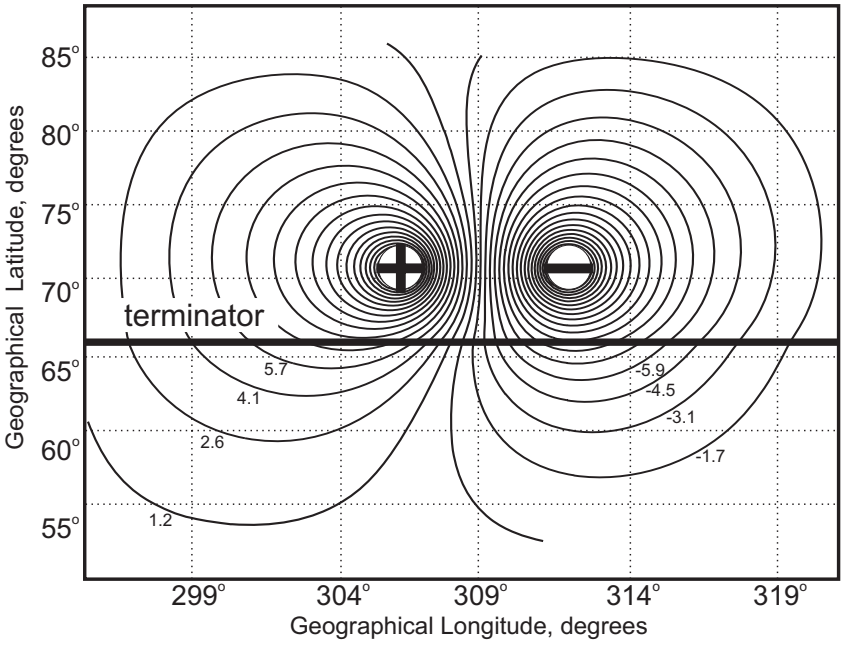

Figure 6.7. Calculated electric potential distribution, kV, in the northern hemisphere around noon on December, 29, near the Sondre Stromfjord (STF) meridian. Contours correspond to equipotential curves. The heavy line shows the terminator position.

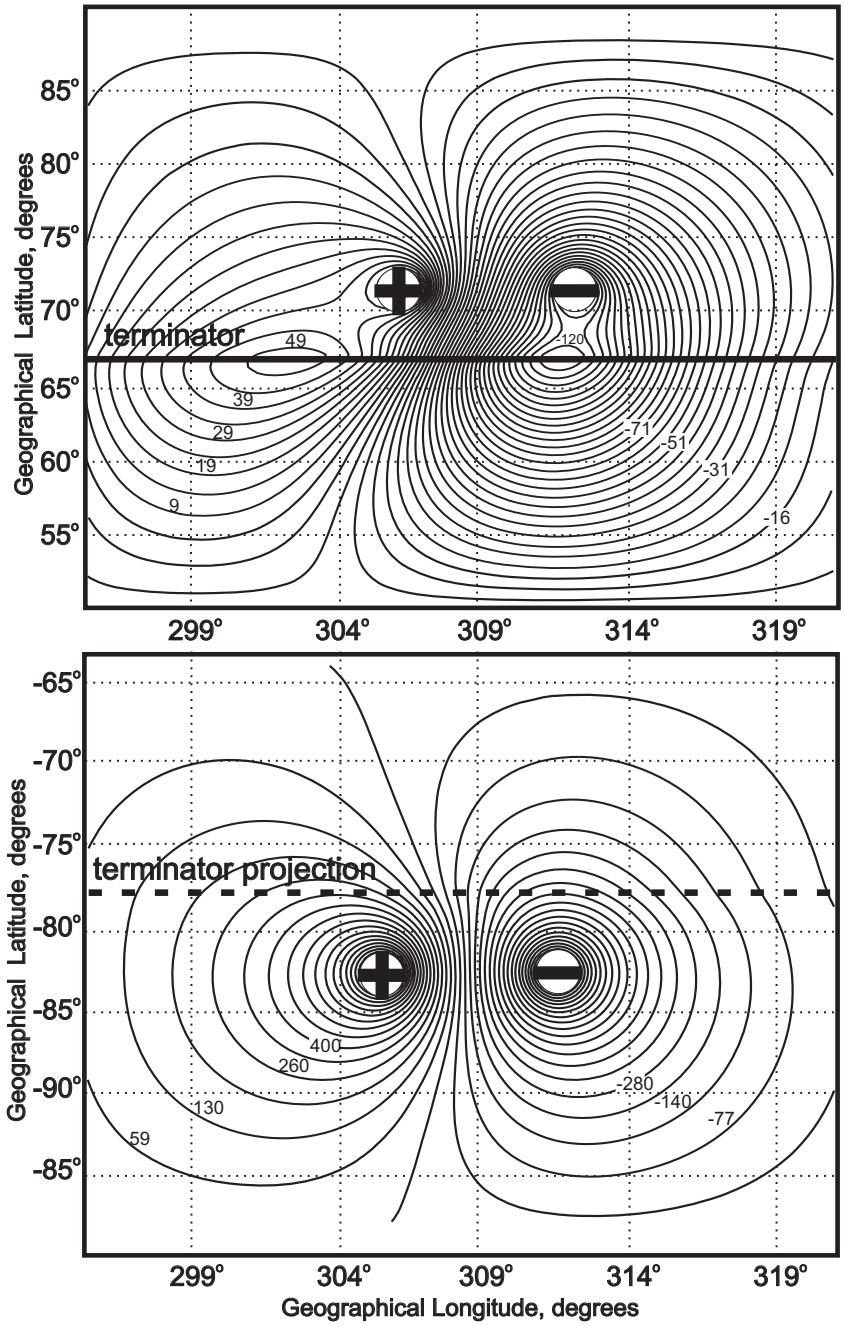

Figure 6.8. Calculated pattern of equivalent ionospheric currents (in the units of kA), in the northern (a) and southern (b) ionospheres for the Sondre Stromfjord (STF) meridian on December 29. The contours are related to the ionospheric equivalent current streamlines. The heavy line shows the terminator position. The downward ($\boldsymbol{j}_{\|0}{}^{\downarrow}$) and upward ($\boldsymbol{j}_{\|0}{}^{\uparrow}$) field-aligned currents are marked with (+) and (-). Two vortices in the equivalent ionospheric currents detached from the potential sources appear at the terminator in the winter northern ionosphere (a), whereas no such vortices can be observed in the summer southern ionosphere (b).

region of closed field lines the potential distribution is the same as that in the northern hemisphere. The heavy line in Fig. 6.7 indicates the terminator position. A small kink in the

potential contours on the terminator implies the appearance of FACs there. Note that the potential distribution in Fig. 6.7 may be referred to quasi-stationary events such as the magnetospheric convection as well as to non-stationary events such as the traveling convection vortices [*Friis-Christensen et al*., 1988; *Clauer and Ridley*, 1995; *Lyatsky et al*., 1999a; 1999b].

Fig. 6.8 shows the calculated distribution of equivalent ionospheric currents in the northern (a) and southern (b) hemispheres. Note that the pattern for equivalent ionospheric currents in the summer southern ionosphere looks like that for the potential distribution but in the northern ionosphere it is very different, and it shows evidently the appearance of two detached vortices with the centers at the terminator.

The performed calculations confirm the possibility of detached equivalent current vortex generation in the vicinity of the terminator line.

6.3 TCV observations with magnetometers and radars

Now we are studying the TCVs by looking at the magnetic and radar observations. The goal of this study is to find out how well the SuperDARN plasma velocity data agree with the magnetic equivalent convection data from the ground-based magnetometers. We consider one particular TCV event occurred on December 4, 1994. More comprehensive SuperDARN/magnetometer study of TCV features, especially the ones near the solar terminator, is left for future work.

We should note that there are difficulties in observing TCV signatures with SuperDARN radars. The SuperDARN velocity maps are 2 (1) min averages. In obtaining these maps, the velocity data for 16 beams separated by 7 (3) s are treated as if they were acquired at the same moment. Two minutes time is sufficient for a vortex to pass through the field of view of a particular radar. Therefore we looked not only at the SuperDARN convection maps, but also at the line-of-sight velocities for individual radar beams and co-located magnetometer data.

6.3.1 December 04, 1994 event overview

The TCV event on December 04, 1994 lasted approximately from 16:35 to 16:50 UT. It was best observed with the Greenland chain of magnetometers. The above period corresponds approximately to 1330 – 1400 MLT for the Greenland chain. Fig. 6.9 shows Greenland magnetometer data, northward B_N and eastward B_E components, for the event. Note that the ~90º

phase shift between B_N and B_E variations implies the circular magnetic perturbation vector rotation. The traces in Fig. 6.9 are high-pass filtered with the cut-off period of 30 min.

The solar wind parameters are also plotted in Fig. 6.9 below the ground-based magnetometer curves. Four parameters are presented: IMF B_Y and B_Z components, solar wind velocity V_X component, and solar wind dynamic pressure P. At the time of measurement the WIND spacecraft was located 289,000 km away from the earth. The SW velocity was ~410 km/s, therefore the propagation delay was about 12 min.

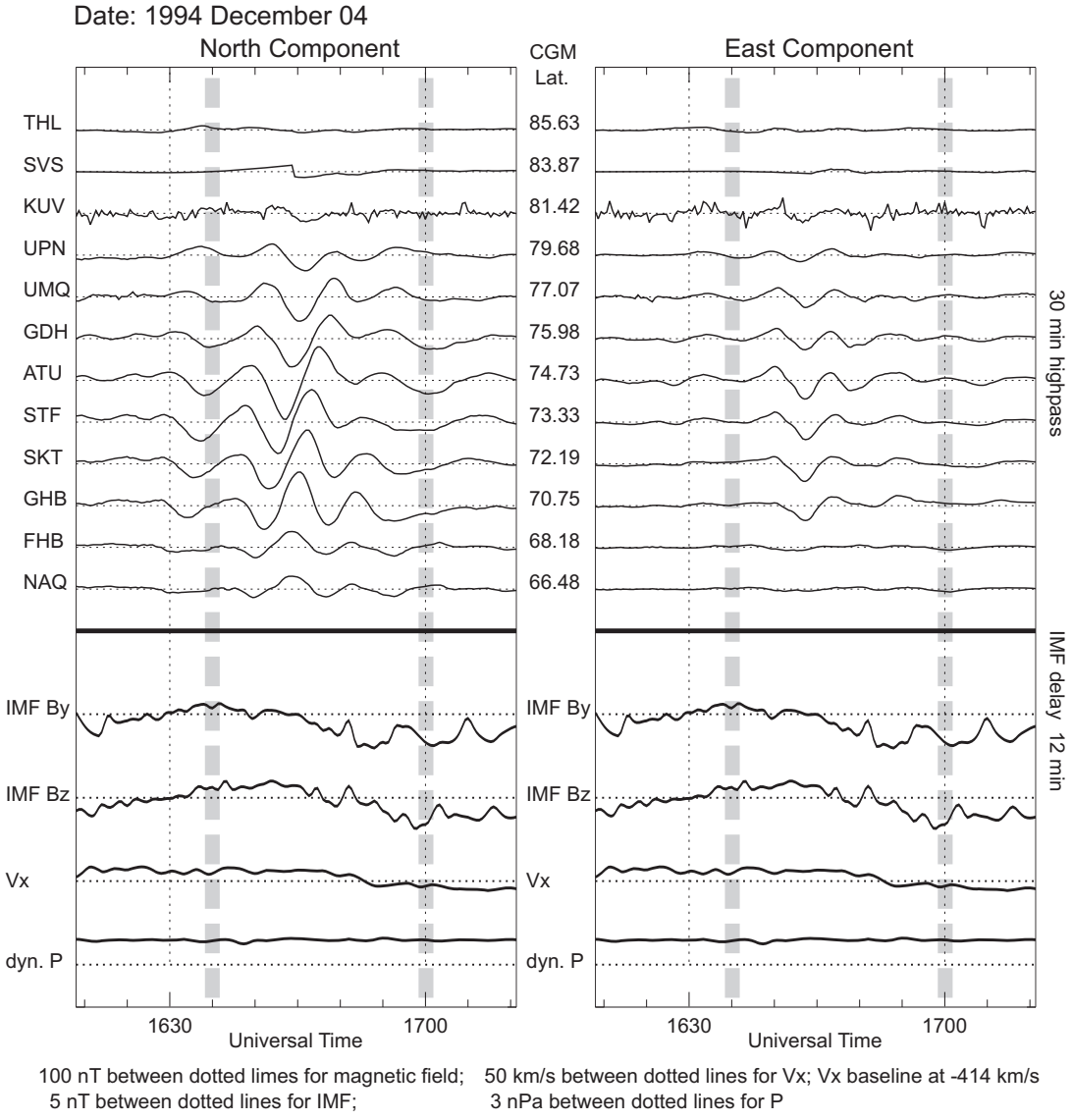

Figure 6.9. TCV event on December 4, 1994 in B_N and B_E magnetic traces from the Greenland west coast magnetometer chain and solar wind data from the WIND satellite (IMF B_Y, B_Z, solar wind velocity V_X and dynamic pressure P. The solar wind data are shifted to allow for the propagation delay from the WIND to the earth's magnetopause (12 min). The event start and end are marked with thick grey dashed vertical lines.

The SWparameter curves in Fig. 6.9 are shifted by 12 min to take the delay into account. The IMF and SW conditions before and during the event were relatively stable, so it is difficult to identify the trigger for the TCV event. Small *positive* B_z (~1 nT) was observed during the event. This fact suggests that some TCVs are not associated with intensification of reconnection.

An evolution of the magnetic equivalent convection vectors measured at the Greenland magnetometer chain is plotted in Fig. 6.10 in the form of a hodogram. The 360º turns of MEC vectors are evident; three TCVs crossed the chain's meridian. The MLAT foci positions of the TCV train can be found as the latitude where the MEC

vectors change the sense of rotation. The idea behind this identification is illustrated in Fig. 6.11. The two magnetometer stations happen to be below and above the foci of a twin TCV. The MEC vectors measured at consecutive moments of time as the TCVs sweep past the stations show the opposite senses of rotation.

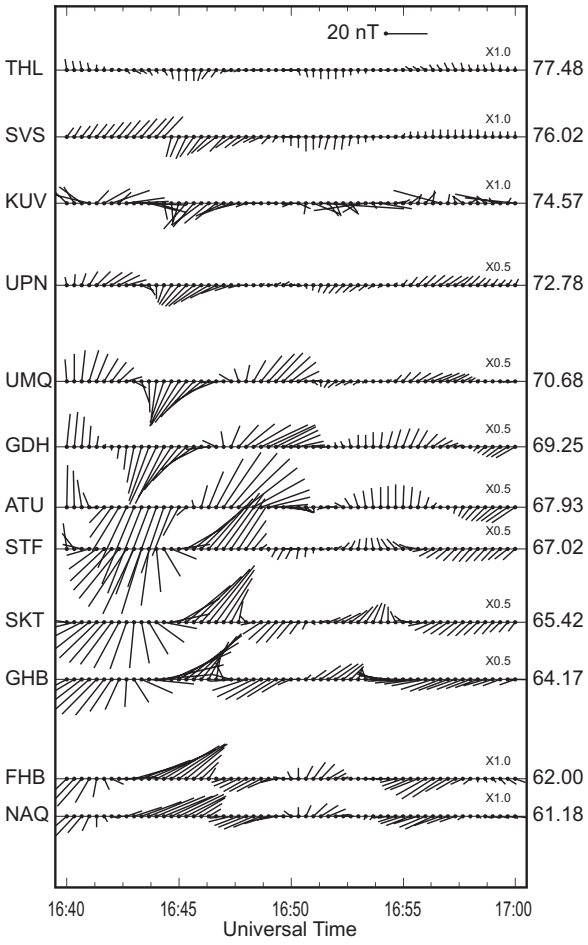

Figure 6.10. Hodograms of the magnetic equivalent convection vectors measured by the magnetometers of the west coast Greenland chain on December 4, 1994. The long vectors between 64°- 71ºCGM have different scales.

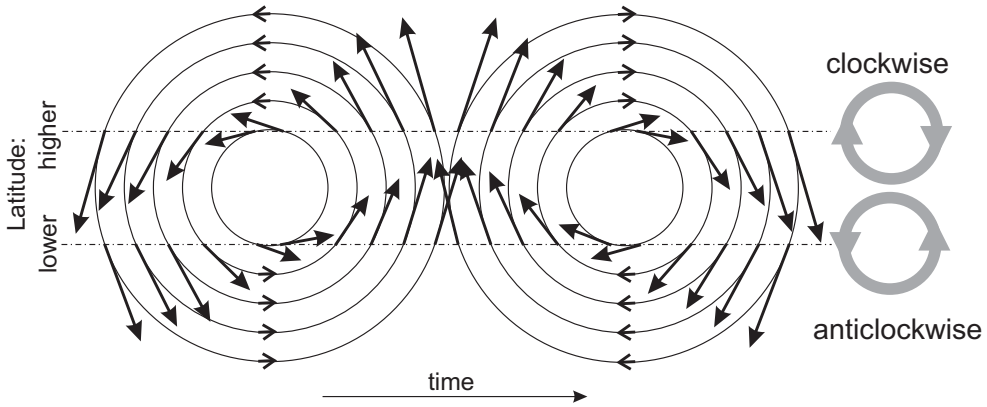

Figure 6.11. A schematic explanation of the method for determining a TCV focus MLAT position. The MEC vectors are measured at two stations, above and below the TCV focus. When the pair of TCVs passes the station locations, the higher latitude station detects clockwise MEC vector rotation, whereas the lower latitude station detects anticlockwise rotation of the MEC vector.

6.3.2 2-D vortex patterns

To visualize the progression of vortices in magnetic equivalent convection (MEC) across the area of observations we plotted the MEC vectors and interpolated them over the observational zone for several moments. Fig. 6.12 shows such a series of TCV snapshots taken with 1 min intervals from 1642 to 1649 UT. Three vortices can be distinguished: counterclockwise A, clockwise B, and counterclockwise C. The TCVs occurred at ~74-75º MLAT and swept along the magnetic parallel to the evening sector (tailward in the magnetosphere).

6.3.3 Magnetometer-radar comparisons

In Fig. 6.13 we compare the MEC patterns with SuperDARN convection maps for three moments: 1643 UT (a, b), 1645 UT (c, d), and 1647 UT(e, f). The SuperDARN patterns are the averages of two-min scans, therefore each was assigned the time in the middle of the scan interval. For example, the pattern at 1643 UT is corresponds to the interval from 1642 to 1644 UT. The clockwise vortex can be seen both in SuperDARN convection, panel (a), and in MEC, panel (b). In two minutes it travels away from noon to the east and slightly poleward. One can see a good agreement between the vortex in SDC, panel (c), and MEC, panel (d). The further TCV displacement in the same direction is also reasonably well reflected in both SDC and MEC, panels (e) and (f). It should be noted that in panels (a) and (b) one can see one more vortex, at later MLT. This is a counterclockwise vortex preceding the one under consideration. This earlier vortices are observed equally well in both SDC and MEC.

As we explained earlier, the two-minute averaging of SuperDARN data may lead to the smearing of fast changing convection patterns. In attempt to make a more credible magnetometer-radar comparison we decided to compare the line-of-sight velocity measured by the Stokkseyri radar and magnetic perturbations associated with the TCV.

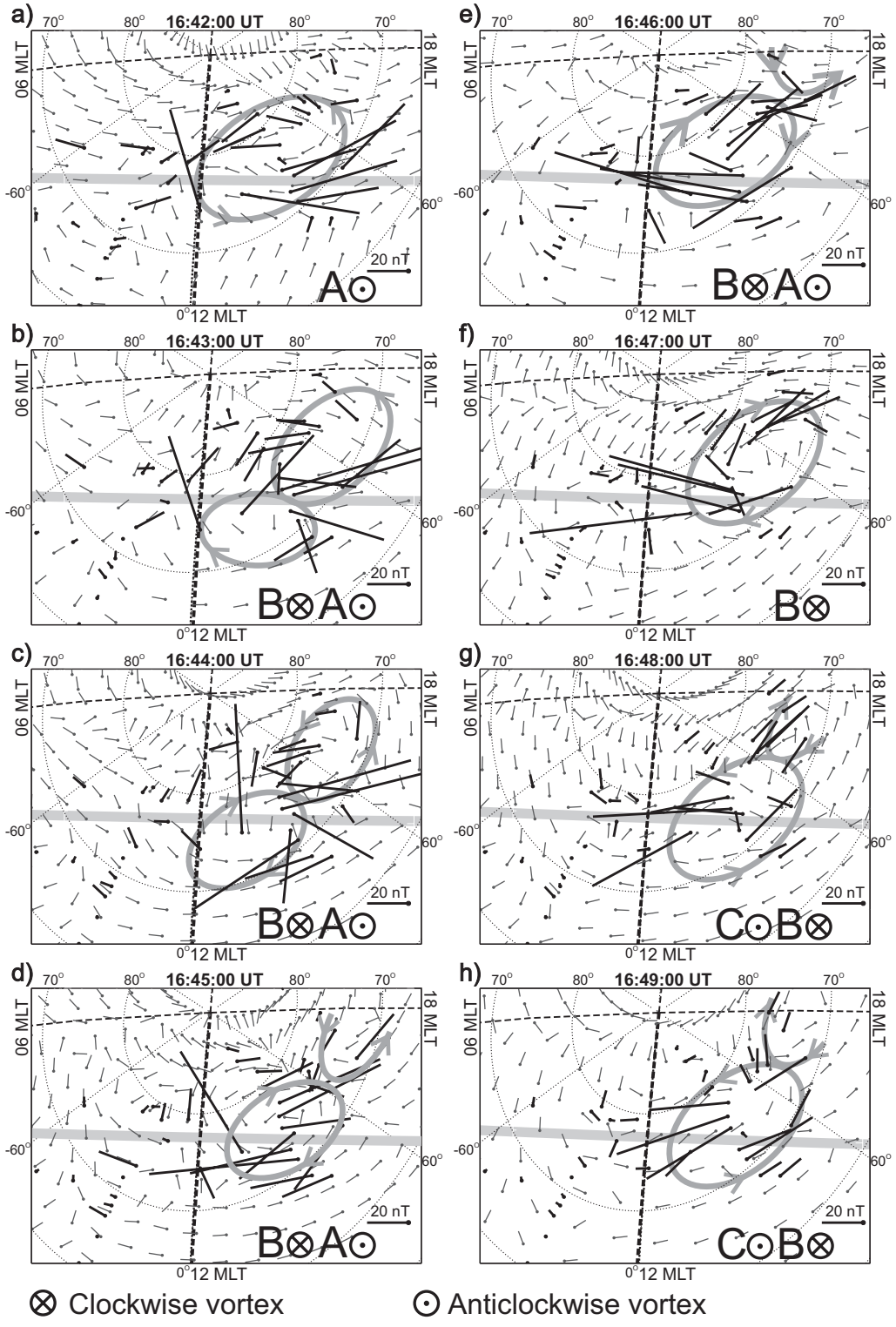

Figure 6.12. TCV progression on December 4, 1994 in ground-based magnetometer measurements. The magnetic equivalent convection is given in thick vectors. The quiver of thin vectors is the interpolation over the region. The interpolation vectors show the direction only, having the same lengths. The terminator is shown as a thick light-grey line. Three distinct TCVs are denoted as A, B, and C.

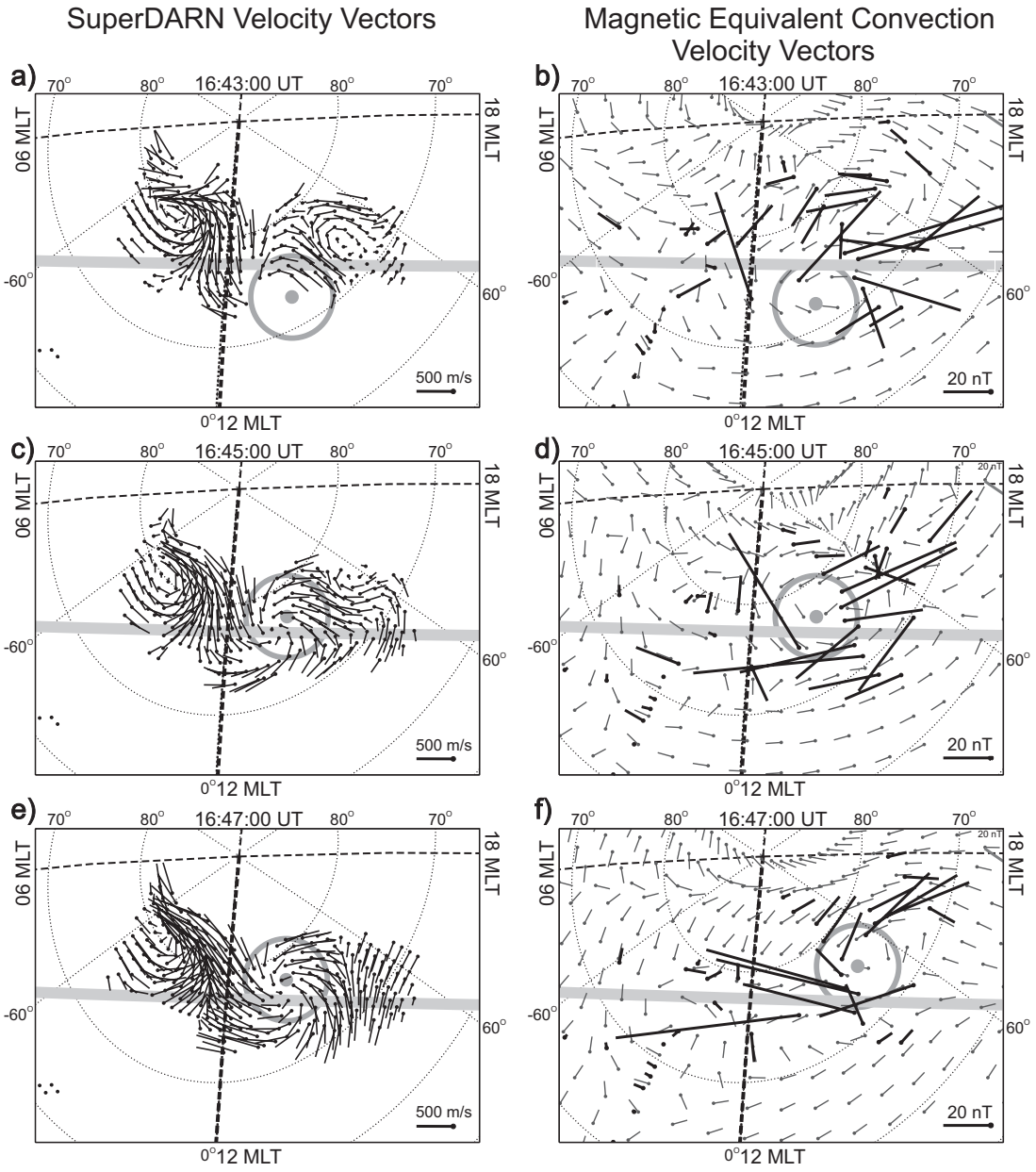

Figure 6.13. A clockwise TCV progression in the juxtaposition of the SuperDARN velocity vectors (left) and the magnetic equivalent convection vectors (right) over the Canadian and Greenland sector at three times, 1643 UT (a, b), 1645 UT (c, d), and 1647 UT (e, f). The panels b), d) and f) have the same legend as in Fig. 6.12.

The reason for the selection of the Stokkseyri radar is that most of the Greenland magnetometer stations are within its field of view. For a comparison we selected the MEC 20-s measurements taken closest in time to the radar measurements in a specific beam and at a specific range. Fig. 6.14 presents a typical comparison of the Stokkseyri line-of-sight velocity over a 2-min scan with the magnetometer equivalent convection measurements for the December 4, 1994 TCV event.

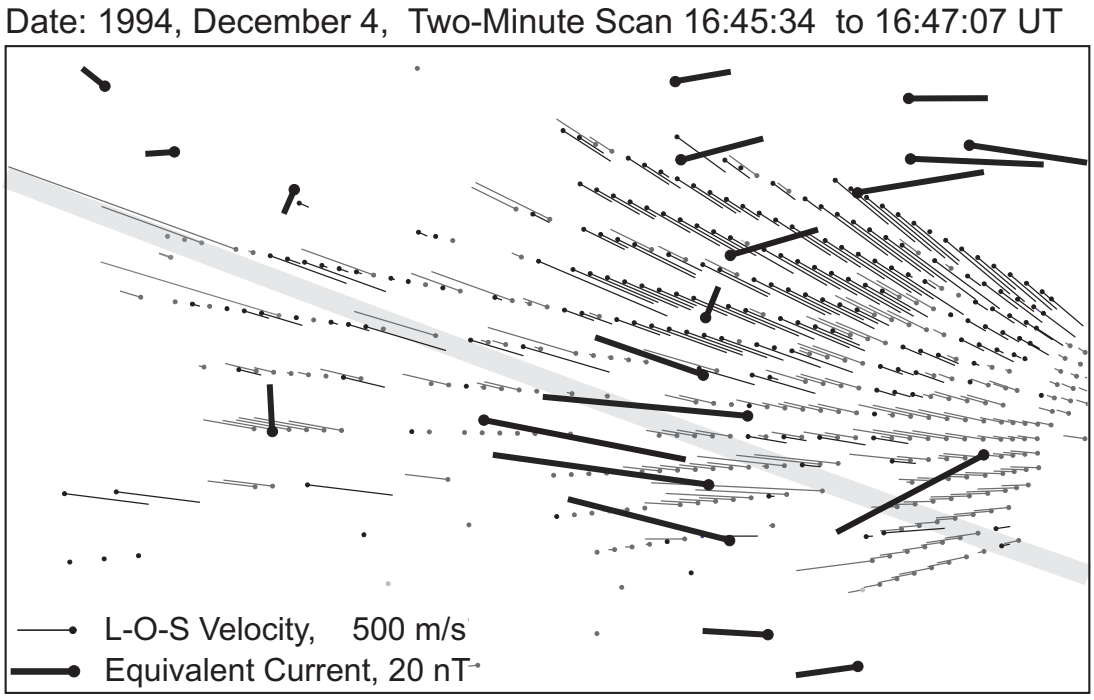

Figure 6.14. The SuperDARN line-of-sight velocities (thin vectors) and the magnetic equivalent convection vectors (thick vectors). The LOS vectors are directed either toward the radar (printed in black) or away from the radar (printed in dark-grey). To prevent the LOS vectors from merging into one line for each beam they are rotated slightly clockwise. Each MEC vector presents the measurement taken at the moment closest to the moment of the spatially closest beam release. The terminator is shown as a thick light-grey line.

Each MEC vector plotted there corresponds to a particular 20-s magnetic measurement that happened to occur near appropriate SuperDARN beam, not more than 10 s apart from the radar echo detection.

An examination of Fig. 6.14 tells us that virtually all of the MEC vectors agree in direction with the SuperDARN LOS vectors. The “directional agreement” means that a MEC vector’s projection on the closest radar beam line has the same signature as a closest LOS vector: towards the radar or from the radar. The agreement between the lengths of projections and LOS vectors is not as good as that for their directions. However, we do not have information on a second component of a LOS velocity; therefore we cannot compare LOS and MEC as vectors.

For some measurements in Fig. 6.14 the differences are obvious. There are several reasons to the discrepancies between the magnetic equivalent ionospheric convection and the SuperDARN LOS velocities. One of these is the ionospheric conductance gradients in the area of observations. As has been shown in previous sections, such gradients can severely change the

equivalent ionospheric current pattern to result in differences in the actual plasma flows measured by the radar and the currents measured by the ground-based magnetometers.

6.4 Conclusions

In this Chapter we have considered several TCV-related issues and suggested solutions to the following problems and questions.

1) We addressed the problem of identification of the magnetospheric region where the TCV-driving FACs are generated. The traveling convection vortices are normally observed with the use of ground-based magnetometers. The measured effects of the ionospheric equivalent currents are used to make conclusions as to the TCVs geometry and their foci locations. A TCV focus position can give the information about the position of the magnetospheric FAC source driving the TCV. We have shown that a TCV focus can appear at the latitudes much lower than those of the driving FACs because of the solar terminator-associated conductance gradients. Strong photoconductance gradients can lead to emergence of apparent TCVs attached to the terminator. Also, in the vicinity of terminator the TCV foci as detected by the ground-based magnetometers are displaced several degrees westward with respect to the driving FACs positions.

2) Two models, analytical and numerical, for the equivalent currents calculation have been developed and implemented. The analytical model allows a TCV simulation near the solar terminator line. The numerical model is more general. It allows calculation of the equivalent currents for arbitrary FAC and ionospheric conductance distributions.

3) A TCV event case study with the use of both ground-based magnetometers and SuperDARN radars has been performed. We demonstrated a reasonable agreement between the traveling vortical flows observed in the SuperDARN plasma velocity data and the TCVs observed in magnetic equivalent convection. Also, we compared the MEC vectors and the line-of-sight velocity vectors for this event and showed a prevailing directional agreement between them. We ascribed some discrepancies between the magnetometer and radar measurements to the ionospheric conductance variations.

CHAPTER 7

CONCLUSIONS AND SUGGESTIONS FOR FURTHER RESEARCH

In this thesis, several high-latitude phenomena have been studied with the emphasis on the effects of the ionospheric conductance and its horizontal gradients. We made several theoretical predictions and studied experimentally some of the expectations. The experimental work was based on the SuperDARN HF radar data and the data from all currently available high-latitude magnetometers. We also used satellite measurements of the solar wind and IMF parameters.

7.1 Conclusions

We considered the role of ionospheric conductance itself and its gradients separately. Therefore we formulate general conclusions for each of these aspects in turn. Fig. 7.1 summarizes what has been studied with respect to each issue. The total conductance effects were considered in substorm, storm sudden commencements and radar aurora echo occurrence. We investigated the conductance gradients' effects in the formation of field-aligned currents, magnetic equivalent convection, and traveling convection vortices.

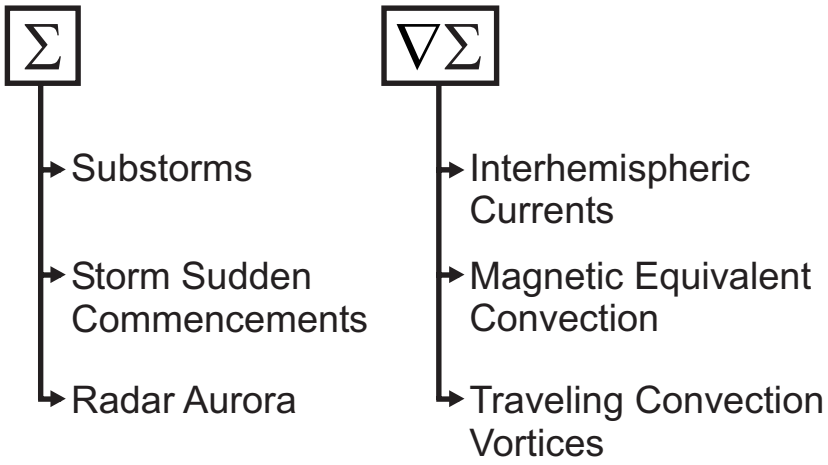

Figure 7.1. Various magnetosphere-ionospheric phenomena dependent on the ionospheric conductance or its horizontal gradients.

7.1.1 Effects of ionospheric conductance

In considering the role of the high-latitude ionospheric conductance, we showed that for some phenomena it is very important to consider conductance of both hemispheres, and for this reason we introduced the *total ionospheric conductance* as the sum of the conductances in conjugate points of both hemispheres over the region of closed geomagnetic lines. These regions are electrically connected through the closed field lines implying equalization of the electrical potentials between the hemispheres. The joint consideration of conductances in both hemispheres makes sense in the view that the magnetospheric current sources that appear in the regions of closed field lines drive the currents through the auroral segments of the conjugate ionospheres. In this case, it is the total conductance magnitude that determines the energy that will dissipate in the earth's ionosphere and also it very likely determines whether the electric potential drop is build up along the magnetic field lines so that magnetospheric particles can be accelerated and precipitate in bursts leading to phenomena such as substorms.

a) Using auroral electrojet index data for over 30 years we introduced new electrojet parameters, the dAE and dAO indices. The dAE and dAO indicate the moments of the fast electrojet increase, which is one of the characteristic features of the substorm onset. We plotted the diagrams of diurnal and annual variations of the dAE and dAO indices and compared them with a corresponding diurnal/annual variation diagram of the *total* ionospheric conductance at the midnight points of the auroral zones in both hemispheres. The dAE/dAO diagrams showed good

agreement with the conductance diagrams; periods of enhanced dAE/dAO indices (substorms) corresponded well to the periods of the small total conductance. The result allowed us to conclude that the substorm onsets are more probable when the conductance in the midnight auroral zones in both hemispheres is low. Such low total conductance is the preferential condition for the onset of the magnetosphere-ionosphere feedback instability, one of the accepted mechanisms of substorm triggering.

b) We showed that the storm sudden commencements also demonstrate sensible variations of the diurnal and annual type. These variations can only be detected when the SSC data for several decades are analyzed by spectral methods. A combination of annual and semiannual harmonics explains most of variability in the SSC occurrence. We showed that the major maxima of SSC occurrence (in the UT-month plot) can be related to the low ionospheric conductance. We suggest that perhaps low total ionospheric conductance sets preferential conditions for the global storm development.

c) The SuperDARN echo occurrence rates were compared with the variations of total ionospheric conductance at the middle points of the radar's field of views. Some radars showed that the echo occurrence rate is maximized at equinoxes when the total conductance experience a local minimum. It is suggested that such a situation is favorable for setting stronger electric fields in the ionosphere. For other radars, there was a clear inverse association between the echo occurrence and the total ionospheric conductance. This fact might indicate that enhanced ionospheric conductance (in the E region) shortens out the polarization electric fields associated with the gradient-drift plasma instability (in the F region) and prevents the irregularity production. The data also indicate that other factors may control the F region echo occurrence, for example the electron density in the ionosphere that controls the amount of radio wave refraction.

7.1.2 Effects of ionospheric conductance gradients

The ionospheric conductance gradients are shown to be responsible for the several phenomena.

a) One of these phenomena is excitation of strong currents flowing between hemispheres on closed field lines. Such currents may play a significant role in the electrodynamics of the high-latitude ionosphere. We performed both analytical and numerical estimates of relative

magnitudes of the interhemispheric currents and their location with respect to magnetospheric sources, which we modeled as current generators. We found that under certain conditions, for example near solstices, the interhemispheric current magnitudes can be of the same order of magnitude as the large-scale Region1/Region2 currents. The interhemispheric currents are attached to the regions of the maximum conductance gradient, and that is where one might expect differences between the true plasma flow and the magnetic equivalent convection inferred from magnetometer measurements.

b) We conducted a statistical assessment of the agreement between the magnetic equivalent convection direction inferred from the ground-based magnetometer data and the true convection direction measured by the SuperDARN radars. The study was global-scale, it included observations in various time sectors and magnetic latitudes of 60^0-85^0 MLAT. We showed that magnetometer predictions are the worst for observations near the terminator line. The data also showed rather poor magnetometer/radar agreement in the midnight sector where strong conductance gradients are expected due to particle precipitation. The developed procedure for taking into account the terminator-associated conductance gradients improved somewhat the agreement in most of the comparisons. Thus we proposed a method of better convection direction estimates from magnetometer data. We expect better results if a real conductance is available, instead of the model one adopted in our calculations.

c) The other interesting phenomenon is the magnetic equivalent convection distortions around the terminator line. We showed that interhemispheric currents can be accompanied by the emergence of an apparent vortex. This vortex does not exist in reality, it is a product of conductance distribution and field-aligned currents structure near the terminator. But the vortex can be detected by a network of magnetometers, and it can be associated with vortical ionospheric structures such as traveling convection vortex.

d) We attempted to find out if the traveling convection vortices are indeed the true circular motions of the ionospheric plasma by comparing magnetometer data and SuperDARN radar measurements of the true convection. Because of limitations of the radar data (scanning through 16 beam positions over 1 or 2 min) and rather scarce magnetometer coverage, we only can claim that the radar data lend some support to the conventional notion that TCVs are indeed the circular plasma flows. The data indicate that TCV foci are located equatorward of the footprints of the magnetospheric current sources. This might be the effect of the conductance

gradient, at least for the considered event. We suggest that the reported location of TCVs at relatively low latitudes can be an apparent effect.

7.2 Suggestions for further research

The research effort described in this thesis cannot be considered as completed in every detail. Here we present some possible extensions of the work.

7.2.1 Detection of interhemispheric currents

The interhemispheric currents excitation due to the conductance discontinuity in one of the hemispheres is one of our theoretical predictions. An important task should be experimental detection of such currents. Our estimates performed in Chapter 3 indicate that the intensity of interhemispheric currents is strong enough to be detected directly. Clearly, this is not an easy task since satellite magnetometers collect signals from all field-aligned currents flowing in the space. One can think of the effects of interhemispheric currents. For example, we discussed in Chapter 6 a TCV-like structures occurring near the solar terminator. We believe that detection of such structures is possible, especially if a network of magnetometers of higher density is available. The other option is investigation of the low-latitude ground-based magnetometer records. We attempted to find signatures of interhemispheric currents in such data, but so far cannot draw definitive conclusions. We also think that it might be useful to involve low-orbiting spacecraft or geostationary satellite measurements.

The other potentially promising way of estimating interhemispheric currents is our suggestion given in Section 3.3.3, Chapter 3, where we proposed to consider SuperDARN convection maps (potential distribution) obtained in both hemispheres. More work in this direction is needed.

7.2.2 Interhemispheric asymmetries in plasma convection patterns

The other potential effect of the interhemispheric currents is distortions in the convection patterns near the terminator lines or near optical forms observable by satellite and ground-based cameras. It would be interesting to take a closer look at the convection vectors distribution around these strong “inhomogeneities” in the conductance distribution. A preliminary, rather

quick analysis does show some promising features, but more detailed, quantitative analysis needs to be done before one can talk about the reality of the effects.

7.2.3 Global-scale estimates of the ionospheric conductance from the radar and magnetometer data

We proposed in Section 5.4.5 one potential way of inferring the global-scale distribution of the ionospheric conductance by combining the radar and magnetometer data. It would be interesting to see the outcome of this approach since conductance is one of the parameters whose distribution is less known to researchers. The advantage of the approach is that it can be applied to the data almost in real time.

7.2.4 Nature of high-latitude TCVs

Our investigation showed that some TCVs can be an apparent effect. This implies their different magnetospheric origin. It is highly desirable to continue investigation of TCVs by considering both magnetometer and radar data. Planned installation by the U of Saskatchewan radar group of new PolarDARN radars capable of echo detection at very high latitudes should be beneficial for this kind of studies as we believe that the TCV sources can be located at high latitudes, they may not be detectable by the current radar systems.

REFERENCES

Ahn, B.-H., H. W. Kroehl, Y. Kamide, and E. A. Kihn, Universal time variations in the auroral electrojet indices, J. Geophys. Res., 105, 267-275, 2000.

Aikio, A. T., V. A. Sergeev, M. A. Shukhtina, L. I. Vagina, V. Angelopoulos, and G. D. Reeves, Characteristics of pseudobreakups and substorms observed in the ionosphere, at the geosynchronous orbit, and in the midtail, J. Geophys. Res, 104, 12,263-12,286, 1999.

Akasofu, S.-I., and S. Chapman, Solar-Terrestrial Physics, *Oxford University Press*, London, 901 pp, 1972.

Akasofu, S.-I., A source of auroral electrons and the magnetospheric substorm current systems, *J. Geophys. Res*, *108(A4)*, 8086, doi:10.1029/2002JA009547, 2003.

Akasofu, S.-I., The development of the auroral substorm, *Planet. Space Sci., 12*, 273-282, 1964.

Aksnes, A., J. Stadsnes, G. Lu, N. Østgaard, R. R. Vondrak, D. L. Detrick, T. J. Rosenberg, G. A. Germany, and M. Schulz, Effects of energetic electrons on the electrodynamics in the ionosphere, *Ann. Geophysicae*, *22*, 475-496, 2004.

Allen, J. H., C. C. Abston, and L. D. Morris, Auroral electrojet magnetic activity indices *AE* (11) for 1974, *Rep. U A G-59*, World Data Center A for Solar Terr. Phys., NOAA, Boulder, Colo., 1976.

Amm, O., Direct determination of the local ionospheric Hall conductance distribution from two-dimensional electric and magnetic field data: Application of the method using models of typical ionospheric electrodynamic situations, *J. Geophys. Res*., *100*, A11, 21,473-21,488, 1995.

Amm, O., Method of characteristics in spherical geometry applied to a Harang-discontinuity situation, *Ann. Geophysicae*, *16*, 413-424, 1998.

André, R., J.-P. Villain, V. Krassnosel'kikh, and C. Hanuise, SuperDARN observations of velocity-divergent structures in the F region ionosphere, *J. Geophys. Res., 105*, 20,899-20,908, 2000.

Atkinson, G., and D. Hutchinson, Effect of the day-night ionospheric conductivity gradient on polar cap convective flow, *J. Geophys. Res., 83*, 725-729, 1978.

Axford, W. I., and C. O. Hines, A unifying theory of high-latitude geophysical phenomena and geomagnetic storms, *Can. J. Phys., 39*, 1433-1464, 1961.

Baker, K. B., and S. Wing, A new magnetic coordinate system for conjugate studies at high latitudes, *J. Geophys. Res*., *94*, 9139-9143, 1989.

Ballatore, P., J.-P. Villain, N. Vilmer, and M. Pick, The influence of the interplanetary medium on SuperDARN radar scattering occurrence, *Ann. Geophysicae., 18*, 1576– 1583, 2001.

Baumjohann, W., R. J. Pellinen, H.J. Opgenoorth, and E. Nielsen, Joint two-dimensional observations of ground magnetic and ionospheric electric fields associated with auroral zone currents: Current systems associated with local auroral break-ups. *Planet. Space Sci*., *29*, 431-447, 1981.

Benkevitch, L., and W. Lyatsky, Detached vortices in equivalent ionospheric currents in the winter dayside ionosphere, *Geophys. Res. Lett*., *27*, 1375-1378, 2000.

Benkevitch, L., W. B. Lyatsky, A. V. Koustov, G. J. Sofko, and A. M. Hamza, Substorm onset times as derived from geomagnetic indices, *Geophys. Res. Lett., 29*, 1496, 10.1029/2001GL014386, 2002.

Benkevitch, L., W. Lyatsky, and L. L. Cogger, Field-aligned currents between conjugate hemispheres, *J. Geophys. Res*., *105*, 27,727- 27,738, 2000.

Birkeland, K., On the cause of magnetic storms and the origin of terrestrial magnetism, *The Norwegian Auroral Polaris Expedition* 1902-1903, Vol. 1, 1st section, pp. 1-315, Christiana(Oslo): H. Aschehoug & Co., 1908.

Bracewell, R. The Fourier Transform and Its Applications, *3rd ed., McGraw-Hill*, New York, 1999.

Burg, J. P., Maximum entropy spectral analysis, *Ph.D. thesis*, Stanford University, 1975.

Chapman, S., and J. Bartels, Geomagnetism, *Oxford University Press*, 1940.

Clauer, C. R., and A. J. Ridley, Ionospheric observations of magnetospheric low-latitude boundary layer waves on August 4, 1991, *J. Geophys. Res., 100*, 21,873-21,884, 1995.

Clauer, C. R., and Y. Kamide, DP 1 and DP 2 current systems for the March 22, 1979 substorms, *J. Geophys. Res., 90(A2)*, 1343-1354, 1985.

Cliver, E. W., Y. Kamide, and A. G. Ling, Mountains versus valleys: Semiannual variation of geomagnetic activity, *J. Geophys. Res., 105*, 2413-2424, 2000.

Clua de Gonzalez, A. L., Silbergleit, V. M., Gonzalez, W. D., and Tsurutani, B. T., Annual variation of geomagnetic activity, *J. Atm. Solar Terr. Phys., 63*, 367-374, 2001.

Clua de Gonzalez, A. L., W. D. Gonzalez, S. L. G. Dutra, and B. T. Tsurutani, Periodic variations in the geomagnetic activity: A study based on the *Ap* index, *J. Geophys. Res. 98*, 9215-9225, 1993.

Cortie, A. L., Sunspots and terrestrial magnetic phenomena, 1898-1911, *Mon. Notic. Roy. Astronom. Soc., 73*, 52-60, 1912.

Cowley, S. W. H., and M. Lockwood, Excitation and decay of solar wind-driven flows in the magnetosphere-ionosphere system, *Ann. Geophysicae, 10*, 103-115, 1992.

Danskin, D. W., A.V. Koustov, R. Makarevitch, and M. Lester, Observations of double-peaked E-region coherent spectra with the CUTLASS Finland HF radar, *Radio Science, 39*, RS2006, doi:10.1029/2003RS0029032, 2004.

Danskin, D. W., HF auroral backscatter from the E and F regions, *PhD Thesis*, University of Saskatchewan, 2004.

Danskin, D.W., Koustov A.V., Ogawa, T., Nozawa, S., Nishitani, N., Milan, S., Lester, M., and André, D., On the factors controlling the occurrence of F-region coherent echoes, *Ann. Geophys., 20*, 1399-1413, 2002.

Davis, T. N., and M. Sigiura, Auroral electrojet activity index AE and its universal time variations, *J. Geophys. Res., 71*, 785-794, 1966.

Doe, R. A., J. F. Vickrey, and M. Mendillo, Electrodynamic model for the formation of auroral ionospheric cavities, *J. Geophys. Res., 100*, 9683-9696, 1995.

Doe, R. A., M. Mendillo, J. F. Vickrey, L. J. Zanetti, and R. W. Eastes, Observations of nightside auroral cavities, *J. Geophys. Res.*, *98*, 293-310, 1993.

Dungey, J. W., Interplanetary magnetic field and the auroral zones, *Phys. Res. Lett.*, *6*, 47-48, 1961.

Elphic, R., Multipoint observations of the magnetopause: Results from ISEE and AMPTE, *Adv. Space Res.*, *8(9)*, 223-238, 1988.

Fasel, G. J., Dayside poleward moving auroral forms: A statistical study, *J. Geophys. Res.*, *100*, 11,891-11,905, 1995.

Friis-Christensen, E., M. A. McHenry, C. R. Clauer, and S. Vennerstrøm, Ionospheric travelling convection vortices observed near the polar cleft: A triggered response to sudden changes in the solar wind, *Geophys. Res. Lett.*, *15*, 253-256, 1988a.

Friis-Christensen, E., S. Vennerstrøm, C. R. Clauer, and M. A. McHenry, Irregular magnetic pulsations in the polar cleft caused by travelling ionospheric convection vortices, *Adv. Space Res.*, *8*, 311-314, 1988b.

Fukushima, N., Equivalence in ground magnetic effect of Chapman - Vestine's and Birkland-Alfven's electric current-systems for polar magnetic storms, *Rep. Ionos. Space Res. Jpn.*, 23, 219-225, 1969.

Fukushima, N., Generalized theorem of no ground magnetic effect of vertical current connected with Pedersen currents in the uniform conductivity ionosphere, *Rep. Ionos. Space. Res. Jap.*, *30*, 35-40, 1976a.

Fukushima, N., Ground magnetic effect of field-aligned currents connected with ionospheric currents, *Geophysics Research Laboratory, Univ. of Tokyo*, Tokyo 113, Japan, 1976b.

Galand, M., T. J. Fuller-Rowell, and M. V. Codrescu, Response of the upper atmosphere to auroral protons, *J. Geophys. Res.*, *106*, 127-139, 2001.

Gasda, S., and A. D. Richmond, Longitudinal and interhemispheric variations of auroral ionospheric electrodynamics in a realistic geomagnetic field, *J. Geophys. Res.*, *103*, 4011-4021, 1998.

Glassmeier, K. H., Ground-based observations of field-aligned currents in the auroral zone: Methods and results, *Ann. Geophysicae*, *5*, 115-125, 1987.

Glassmeier, K.-H., M. Hoenisch, and J. Untiedt, Ground-based and satellite observations of traveling magnetospheric convection twin vortices, *J. Geophys. Res., 94*, 2520-2528, 1989.

Glassmeier, K.-H., Travelling magnetospheric convection twin-vortices: observations and theory, *Ann. Geophysicae, 10*, 547-565, 1992.

Gonzalez, W. D., J. A. Joselyn, Y. Kamide, H. W. Kroehl, G. Rostoker, B. T. Tsurutani, V. M. Vasyliunas, What is a geomagnetic storm?, *J. Geophys. Res.*, 99(A4), 5771-5792, 10.1029/93JA02867, 1994.

Granzow, K. D., Spherical harmonic representation of the magnetic field in the presence of a current density, Geophys. J. R., *Astr. Soc., 74*, 489-505, 1983.

Greenwald, R. A., K. B. Baker, J. R. Dudeney, M. Pinnock, T. B. Jones, C. Thomas, J.-P. Villain, J.-C. Cerisier, C. Hanuise, R. D. Hunsucker. G. J. Sofko, J. Koehler, E. Nielsen, and R. Pellinen, DARN/SUPERDARN, A global view of the dynamics of high-latitude convection, *Space Sci. Rev., 71*, 761-796, 1995.

Haines, G. V., and J. M. Torta, Determination of equivalent current sources from spherical cap harmonic models of geomagnetic field variations, *Geophys. J. Int., 118*, 499-514, 1994.

Hajkowicz, L. A., Longitudinal (UT) effect in the onset of auroral disturbances over two solar cycles as deduced from the AE-index, *Ann. Geophyicae, 16*, 1573-1579, 1998.

Harang, L., The mean field of disturbance of polar geomagnetic storms, *Terr., Magn., Atmos. Electr., 51,* 353-380, 1946.

Hardy, D. A., M. S. Gussenhoven, R. Raistrick, and W. J. McNeil, Statistical and functional representations of the pattern of auroral energy flux, number flux, and conductivity, *J. Geophys. Res., 92,* 12,275-12,294, 1987.

Hargreaves, J. K., The solar-terrestrial environment, *Cambridge atmospheric and space science series, 5, Cambridge university press*, 1992.

Heikkila, W. J., T. S. Jorgensen, L. J. Lanzerotti, and C. G. Maclennan, A transient auroral event on the dayside, *J. Geophys. Res., 94,* 15,291-15,305, 1989.

Hosokawa, K., T. Iyemori, A. S. Yukimatu, and N. Sato (2001), Source of field-aligned irregularities in the subauroral F region as observed by the SuperDARN radars, *J. Geophys. Res., 106*, 24,713–24,731.

Huang, C. S., D. Murr, G. J. Sofko, W. J. Hughes, and T. Moretto, Ionospheric convection response to changes of interplanetary magnetic field Bz component during strong By component, *J. Geophys. Res., 105*, 5231-5243, 2000.

Huber, M., and G. J. Sofko, Small-scale vortices in the high-latitude F region, *J. Geophys. Res. 105*, 20,885-20,897, 2000.

Iijima, T., and T. A. Potemra, Large-scale characteristics of field-aligned currents associated with substorms, *J. Geophys. Res., 83*, 599-615, 1978.

Jackson, J. D., Classical electrodynamics, *monograph, John Willey & Sons,, Inc*., second edition, 1975.

Kalitkin, Numerical methods, Moscow, *Nauka*, 1980. (in Russian)

Kamide, Y., A. D. Richmond, and S. Matsushita, Estimation of ionospheric electric fields, ionospheric currents, and field-aligned currents from ground magnetic records, *J. Geophys. Res., 86*, 801-813, 1981.

Kamide, Y., and S. Kokubun, Two-component auroral electrojet: Importance for substorm studies, *J. Geophys. Res., 101*, 13,027-13,046, 1996.

Kan, J. R., A global magnetosphere-ionosphere coupling model of substorms, *J. Geophys. Res., 98*, 17,263-17,276, 1993.

Kataoka, R., H. Fukunishi, L. J. Lanzerotti, T. J. Rosenberg, A. T. Weatherwax, M. J. Engebretson, and J. Watermann, Traveling convection vortices induced by solar wind tangential discontinuities, *J. Geophys. Res.*, 10.1029/2002JA009459, 2002.

Kelley, M. C., The earth's ionosphere: Plasma physics and electrodynamics, *Academic Press, San Diego*, 1989.

Khachikyan, G. Ya., G. J. Sofko, A. V. Koustov, and L. V. Benkevitch, 2005. Dependence of the occurrence frequency and time of storm sudden commencements on heliogeophysical conditions, *Geomagnetism and Aeronomy, 45*, No. 6, 720–729, 2005. *Translated from Geomagnetizm i Aeronomiya, 45*, No. 6, 764–773, 2005.

Khan, H., and S. W. H. Cowley, Observations of the response time of high-latitude ionospheric convection to variations in the interplanetary magnetic field using EISCAT and IMP-8 data, *Ann. Geophysicae, 17*, 1305-1335, 1999.

Kikuchi, T., H. Luhr, T. Kitamura, O. Saka, and K. Schlegel, Direct penetration of the polar electric field to the equator during a DP2 event as detected by the auroral and equatorial magnetometer chains and the EISCAT radar, *J. Geophys. Res*., *101*, 17,161-17,173, 1996.

Kikuchi, T., S. Tsunomura, K. Hashimoto, and K. Nozaki, Field-aligned current effects on midlatitude geomagnetic sudden commencements, *J. Geophys. Res., 106*, 15,555-15,566, 10.1029/2001JA900030, 2001.

Kivelson, M. G., and C. T. Russell (editors), Introduction to space physics, *Cambridge University Press*, 1995, reprinted in 1996.

Kivelson, M. G., K. K. Khurana, R. J. Walker, L. Kepko, and D. Xu, Flux ropes, interhemispheric conjugacy, and magnetospheric current closure, *J. Geophys. Res., 101*, 27,341-27,350, 1996.

Koustov A. V., G. J. Sofko, D. André, D. W. Danskin, L. V. Benkevitch, 2004. Seasonal variation of HF radar F region echo occurrence in the midnight sector, *J. Geophys. Res., 109*, A06305, doi:10.1029/2003JA010337.

Kozlovsky, A., and W. Lyatsky, Finite Larmor radius convection instability in the near-Earth plasma sheet, *J. Geophys. Res., 104*, 2443-2449, 1999.

Lee, L. C., and G. J. Fasel, Patchy multiple X-line reconnection and poleward-moving auroral forms, in *Physical Signatures of Magnetospheric Boundary-Layer Processes*, ed. by A. Egeland and J. Holtet, 291-306, *Kluwer Academic Publishers*, the Netherlands, 1994.

Leontyev, S. V., and W. B. Lyatsky, Electric field and currents connected with the Y-component of the interplanetary magnetic field, *Planet. Space Sci., 22*, 811-819, 1974.

Lester, M., S. Milan, V. Besser, and R. Smith, A case study of HF radar spectra and 630.0 nm auroral emission in the pre-midnight sector, *Ann. Geophysicae, 19*, 327-339, 2001.

Levy, R. H., and G. S. Janes, Plasma Radiation Shielding, *AIAA Journal* 2:10, 1835-1838; also presented at Second Symposium on Protection Against Radiations in Space, Gatlinburg, TN, NASA SP-71, 211-215, Oct. 1964.

Liang, J., L. Benkevitch, G. Sofko, and A.V. Koustov, Comparison between ionospheric convection vortices and the associated equivalent currents *Eos Trans. AGU, 85*(47), Fall Meet. Suppl., Abstract SM51C-0383, 2004.

Liang, J., Multi-instrument studies of ionospheric and magnetospheric processes, *Ph.D. thesis*, Univ. of Saskatchewan, Saskatoon, Saskatchewan, Canada, 2004.

Liu A. T. Y., R. W. McEntire, and S. M. Krimigis, Evolution of the ring current during two geomagnetic storms, *J. Geophys. Res., 92*, 7459-7470, 1987.

Lockwood, M., A.P. van Eyken, B.J.I. Bromage, D.M. Willis, and S.W.H. Cowley, Eastward propagation of a convection enhancement following a southward turning of the interplanetary magnetic field, *Geophys. Res. Lett., 13*, 72 – 85, 1986.

Lockwood, M., and S. W. H. Cowley, Comment on "A statistical study of the ionospheric convection response to changing interplanetary magnetic field conditions using the assimilative mapping of ionospheric electro-dynamics technique" by A. J. Ridley et al., *J. Geophys. Res., 104*, 4387-4391, 1999.

Lu, G., A. D. Richmond, B. A. Emery, and R. G. Roble, Magnetosphere-ionosphere-thermosphere coupling: Effect of neutral winds on energy transfer and field-aligned current, *J. Geophys. Res., 100(A10)*, 19643-19660, 10.1029/95JA00766, 1995.

Lu, G., A. D. Richmond, B. A. Emery, P. H. Reiff, O. de la Beaujardière, F. J. Rich, W. F. Denig, H. W. Kroehl, L. R. Lyons, J. M. Ruohoniemi, E. Friis-Christensen, H. Opgenoorth, M. A. L. Persson, R. P. Lepping, A. S. Rodger, T. Hughes, A. McEwin, S. Dennis, R. Morris, G. Burns, and L. Tomlinson, Interhemispheric asymmetry of the high-latitude ionospheric convection pattern, *J. Geophys. Res., 99*, 6491-6510, 10.1029/93JA03441, 1994.

Lu, G., B. A. Emery, A. S. Rodger, M. Lester, J. R. Taylor, D. S. Evans, J. M. Ruohoniemi, W. F. Denig, O. de la Beaujardière, R. A. Frahm, J. D. Winningham, and D. L. Chenette, High-latitude ionospheric electrodynamics as determined by the assimilative mapping of ionospheric electrodynamics procedure for the conjunctive SUNDIAL/ATLAS 1/GEM period of March 28-29, 1992, *J. Geophys. Res., 101*, 26,697-26,718, 1996.

Lühr, H., and W. Blawert, Ground signatures of travelling convection vortices, *in Solar Wind Sources of Magnetospheric Ultra-Low-Frequency Waves*, Geophysical Monograph, 81, 231-251, 1994.

Lühr, H., M. Lockwood, P. E. Sandholt T. L. Hansen, and T. Moretto, Multi-instrument ground-based observations of a travelling convection vortices event, *Ann. Geophysicae, 14*, 162-181, 1996.

Lundin, R., I. Sandahl, J. Woch, and R. Elphinstone, The contribution of the boundary layer IMF to Magnetospheric Substorms, Magnetospheric Substorms, *Geoph. Monograph* 64, 355 pp, AGU 1991.

Lyatsky, W. B., Current systems of magnetosphere-ionosphere disturbances, Nauka, Leningrad, 1978. (in Russian)

Lyatsky, W. B., and Y. P. Maltsev, Magnetosphere-Ionosphere Interaction, *monograph, Publ. House "Nauka", Moscow,* 1983, 192 p. (in Russian)

Lyatsky, W. B., and D. G. Sibeck, Surface waves on the low-latitude boundary layer inner edge and travelling convection vortices, *J. Geophys. Res., 102*, 17,643-17,647, 1997.

Lyatsky, W. B., G. J. Sofko, A. V. Kustov, D. Andre, W. J. Hughes, and D. Murr, Traveling convection vortices as seen by the SuperDARN HF radars, *J. Geophys. Res., 104*, 2591-2601, 1999a.

Lyatsky, W., A. V. Kustov, G. J. Sofko, B. Jacobsen, D. Andre, and L. L. Cogger, Ionospheric convection and equivalent ionospheric currents in the dayside high-latitude winter ionosphere, *J. Geophys. Res., 104*, 22,525-22,533, 1999b.

Lyatsky, W., and A. M. Hamza, Seasonal and diurnal variations of geomagnetic activity and their role in space weather forecast, *Can. J. Phys., 76*, 907-920, 2001.

Lyatsky, W., P. T. Newell, and A. Hamza, Solar illumination as cause of the equinoctial preference for geomagnetic activity, *Geophys. Res. Lett., 28*, 2353-2356, 2001.

Lyons, L. R., D.S. Evans, and R. Lundin, An observed relationship between magnetic field-aligned electric fields and downward electron energy fluxes in the vicinity of auroral forms, *J. Geophys. Res., 84*, 457-461, 1979.

Lyons, L. R., Discrete auroras as the direct result of an inferred high-altitude generating potential distribution, *J. Geophys. Res., 86*, 1-8, 1981.

Lysak, R. L., Feedback instability of the ionospheric resonant cavity, *J. Geophys. Res., 96*, 1553-1568, 1991.

Maltsev, Y. P., Electric field and current system of the magnetospheric substorm, *PhD thesis, the Leningrad State University*, Leningrad, 1973. (in Russian)

Maltsev, Y. P., and W. B. Lyatsky, Penetration of geomagnetic pulsations from one polar cap into the other, *Geomagn. Aeron., 22*, 985-990, 1982a.

Maltsev, Y. P., and W. B. Lyatsky, Effect of the terminator on electric field and field-aligned currents, *Kosmicheskie Issledovanija* (in Russian), *20*, 304-308, 1982b.

Matsushita, S., On sudden commencements of magnetic storms at higher latitudes, *J. Geophys. Res., 62*, 162-166, 1957.

Mayaud, P. N., A hundred year series of geomagnetic data, 1868-1967, indices *aa*, Storm sudden commencements, IAGA Bull. 33, 1-252, 1973

Mayaud, P. N., Derivation, meaning, and use of geomagnetic indices, *Geophysical Monograph, 22*, AGU, Washington, D. C., 1980.

McHenry, M. A., C. R. Clauer, and E. Friis-Christensen, Relationship of solar wind parameters to continuous, dayside, high-latitude travelling ionospheric convection vortices, *J. Geophys. Res., 95*, 15,007-15,022, 1990.

McIntosh, D. H., On the annual variation of magnetic disturbances, *Phil. Trans. Roy. Soc. London*, Ser. A, 251, 525-552, 1959.

McPherron, R. L., C. T. Russell, and M. Aubry, Satellite studies of magnetospheric substorms on August 15, 1978. Phenomenological model for substorms, *J. Geophys. Res., 78*, 3131-3149, 1973.

McWilliams, K. A., Multi-Pulse Sequence Optimization and Testing: A Tutorial, *SuperDARN Workshop*, Kiljava, Finland, 2003.

Milan, S.E., T.K. Yeoman, M. Lester, E.C. Thomas, and T.B. Jones, Initial backscatter occurrence statistics for the CUTLASS HF radars, *Ann. Geophysicae, 15*, 703-718, 1997.

Moen, J., and A. Brekke, The solar flux influence on quiet time conductivities in the auroral ionosphere, *Geophys, Res. Lett., 20*, 971-974, 1993.

Moretto, T., E. Friis-Christensen, H. Lühr, and E. Zesta, Global perspective of ionospheric traveling convection vortices: Case studies of two Geospace environmental modeling events, *J. Geophys. Res., 102*, 11,597-11,610, 10.1029/97JA00324, 1997.

Motoba T., T. Kikuchi, H. Lühr, H. Tachihara, T.-I. Kitamura, and T. Okuzawa, Equatorial Pc5 associated with moving current vortices in the high-latitude ionosphere, *COSPAR Colloquia series on Space Weather Study Using Multipoint Techniques, edited by L.-H. Lyu, 12*, 255-258, 2002.

Murr, D. L., and W. J. Hughes, Reconfiguration timescales of ionospheric convection, *Geophys. Res. Lett., 28*, 2145-2149, 2001.

Ness, N. F., C. S. Scearce, and J. B. Seek, Initial Results of the IMP I Magnetic Field Experiment, *J. Geophys. Res., 69*, 3531-3569., 1964.

Newell P. T., T. Sotirelis, J. P. Skura, C.-I. Meng, and W. Lyatsky, Ultraviolet insolation drives seasonal and diurnal space weather variations, *J. Geophys. Res.*, 107 (A10), 1305, doi:10.1029/2001JA000296, 2002.

Newell, P. T., and C.-I. Meng, Ionospheric projection of magnetospheric regions under low and high solar wind pressure conditions, *J. Geophys. Res.*, 99, 273-286, 1994.

Newell, P. T., C.-I. Meng, and K. M. Lyons, Suppression of discrete aurorae by sunlight, *Nature, 381*, 766-767, 1996.

Newell, P. T., Y. I. Feldstein, Y. I. Galperin, and C.-I. Meng, Morphology of nightside precipitation, *J. Geophys. Res., 101*, 10,737-10,748, 1996.

Newell, P., and D. Sibeck, Upper limits on the contribution of the flux transfer events to ionospheric convection, *Geophys. Res. Lett., 20*, 2829-2832, 1993.

Nishida, A., Geomagnetic DP2 fluctuations and associated magnetospheric phenomena, *J. Geophys. Res., 73*, 1795-1803, 1968.

Olsen, W. P., The geomagnetic field and its extension into space, *Adv. Space Res., 2*, 13-17, 1982.

Olson, J. V., and G. Rostoker, Pi2 pulsations and the auroral electrojet, *Planet. Space. Sci., 23*, 1129-1139, 1975.

Owen, C. J., and Cowley S. W. H., Heikkila's mechanism for impulsive transport through the magnetopause: a re-examination, *J. Geophys. Res., 96*, 5565-5574, 1991.

Parker, E. N., Extension of the solar corona into interplanetary space, *J. Geophys. Res., 64*, 1675-1681, 1959.

Parkinson M. L., The importance of ionospheric Pedersen conductivity in the control of ionospheric irregularities and their Doppler characteristics, *SuperDARN Workshop*, Saskatoon, Canada, 2004.

Parkinson, M. L., J. C. Devlin, H. Ye, C. J. Waters, P. L. Dyson, A. M. Breed, and R. J. Morris , On the occurrence and motion of decameter-scale irregularities in the sub-auroral, auroral, and polar cap ionosphere, *Ann. Geophysicae, 21*, 1847–1868, 2003.

Potemra, T. A., Sources of large-scale Birkeland currents, in *Physical Signatures of Magnetospheric Boundary Layer Processes*, edited by J. A. Holtet and A. Egeland, pp. 3-27, Kluwer Acad. Norwell, Mass., 1994.

Press, W.H., S. A. Teukolsky, W. T. Vetterling, B. P. Flannery, Numerical recipes in C. The art of scientific computing. Second edition, *Cambridge University Press*, 1992, *reprinted* 1993, 1994, 1995, 1997, 2002.

Renka, R. J., Algorithm 772: STRIPACK: Delaunay Triangulation and Voronoy Diagram on the Surface of a Sphere, *ACM Transactions on Mathematical Software, 23, N 3*, 416-434, September 1997.

Renka, R. J., Interpolation of data on the surface of a sphere, *ACM Transactions on Mathematical Software, 10, N 4*, 417-436, December 1984.

Richmond A. D., and Y. Kamide, Mapping electrodynamic features of the high-latitude ionosphere from localized observations: Technique, *J. Geophys. Res., 93*, 5741-5759, 1988.

Richmond, A. D., and R. G. Roble, Electrodynamic effects of thermospheric winds from the NCAR thermospheric general circulation model, *J. Geophys. Res., 92*, 12,365-12,376, 1987.

Richmond, A. D., Assimilative mapping of ionospheric electrodynamics, *Adv. Space Res., 12*, 59-68, 1992.

Ridley, A. J., G. Lu, C. R. Clauer, and V. O. Papitashvili, A statistical study of the ionospheric convection response to changing interplanetary magnetic field conditions using the

assimilative mapping of ionospheric electrodynamics technique, *J. Geophys. Res*., 103(A3), 4023-4040, 10.1029/97JA03328, 1998.

Ridley, A. J., G. Lu, C. R. Clauer, and V. O. Papitashvili, Ionospheric convection during nonsteady interplanetary magnetic field conditions, *J. Geophys. Res., 102*, 14563-14580, 10.1029/97JA00940, 1997.

Robinson, R. M., and R. R. Vondrak, Measurements of E-region ionization and conductivity produced by solar illumination at high latitudes, *J. Geophys. Res., 89*, 3951-3956, 1984.

Robinson, R. M., R. R. Vondrak, K. Miller, T. Dabbs, and D. Hardy, On calculating ionospheric conductances from the flux and energy of precipitating electrons, *J. Geophys. Res*., *92*, 2565-2569, 1987.

Rostoker, G., The evolving concept of a magnetospheric substorm, *J. Atmos. Terr. Phys., 61*, 85, 1999.

Rostoker, G., Identification of substorm expansive phase onsets, *J. Geophys. Res., 107 (A7)*, doi:10.1029/2001JA003504, 2002.

Rostoker, G., S.-I. Akasofu, J. Foster, R. A. Greenwald, Y. Kamide, K. Kawasaki, A. T. Y. Lui, R. L. McPherron, and C. T. Russell, Magnetospheric substorms - Definition and signatures, *J. Geophys. Res.*, *85*, 1663-1668, 1980.

Ruohoniemi, J. M., and K. B. Baker, Large-scale imaging of high-latitude convection with Super Dual Auroral Radar Network HF radar observations, *J. Geophys. Res*., *103*, 20,797-20,811, 1998.

Ruohoniemi, J. M., and R. A. Greenwald, Rates of scattering occurrence in routine HF radar observations during solar cycle maximum, *Radio Sci., 32*, 1051-1070, 1997.

Ruohoniemi, J. M., and R. A. Greenwald, Statistical patterns of high-latitude convection obtained from Goose Bay HF radar observations, *J. Geophys. Res., 101*, 21,743-21,763, 1996.

Ruohoniemi, J. M., and R. A. Greenwald, The response of high-latitude convection to a sudden southward IMF turning, *Geophys. Res. Lett*., *25*, 2913-2916, 1998.

Ruohoniemi, J. M., S. G. Shepherd, and R. A. Greenwald, The response of the high-latitude ionosphere to IMF variations, *J. Atmos. Solar-Terr. Phys, 64*, 159– 171, 2002.

Russell, C. T., and R. L. McPherron, Semi-annual variation of geomagnetic activity, *J. Geophys. Res., 78,* 92-108, 1973.

Russell, C. T., Critical problems of magnetospheric physics, Monograph, Ed E.R. Dyer, *National Academy of Science*s, Washington, D. C., 1972.

Sandholt, P. E., and M. Lockwood, Periodic events at the high-latitude convection reversal in the 16 MLT region, *Geophys. Res. Lett., 17,* 1877-1880, 1990.

Sandholt, P. E., J. Moen, P. Stauning, J. A. Holtet, S. W. H. Cowley, M. Lockwood, U. P. Lovhaug, T. Hansen, and A. Egeland, Temporal and spatial variability of auroral forms in the 10-14 MLT sector: Relationship to plasma convection and solar wind-magnetosphere coupling, *Earth Planets Space, 50,* 663-682, 1998.

Saunders, M. A., M. P. Freeman, D. J. Southwood, S. W. H. Cowley, M. Lockwood, J. C. Samson, C. J. Farrugia, and T. J. Hughes, Dayside ionospheric convection changes in response to long-period interplanetary magnetic field oscillations: Determination of the ionospheric phase velocity, *J. Geophys. Res.*, 97, 19,373-19,380, 1992.

Schiffler, A., SuperDARN measurements of double-peaked velocity spectra, *M. Sc. Thesis, Univ. of Saskatchewan,* Saskatoon, Canada, 1996.

Sibeck, D. G., A model for the transient magnetospheric response to sudden solar wind dynamic pressure variations, *J. Geophys. Res., 95,* 3755-3771, 1990.

Sibeck, D.G., T. D. Phan, R. Lin, R. P. Lepping, A. Szabo, Wind observations of foreshock cavities: A case study, *J. Geophys. Res., 107,* 1271, doi:10.1029/2001JA007539, 2002.

Siscoe, G.L., W. Lotko, and B.U.O. Sonnerup, A high-latitude, low- latitude boundary layer model of the convection current system, *J. Geophys. Res., 96,* 3487-3496, 1991.

Slinker, S. P., J. A. Fedder, W. J. Hughes, and J. G. Lyon, Response of the ionosphere to a density pulse in the solar wind: simulation of traveling convection vortices, *Geophys. Res. Lett., 26,* 3549-3552, 1999.

Smith, E.J., The heliospheric current sheet, *J. Geophys. Res., 106,* 15,819-15,831, 2001.

Stauning, P., E. Friis-Christensen, O. Rasmussen, and S. Vennerstrøm, Progressing polar convection disturbances: Signature of an open magnetosphere, *J. Geophys. Res., 99,* 11,303-11,317, 1994.

Stenbaek-Nielsen, H. C., and A. Otto, Conjugate auroras and the interplanetary magnetic field, *J. Geophys. Res., 102*, 2223-2232, 1997.

Stoker, P. H., M. J. Mathews, M. J., M. W. J. Scourfield, Coordinated measurements of auroral light intensities and riometric radio-wave absorption, *Geophys. Res. Lett., 23*, 641-644, 1996.

Sturrock, P. A., Plasma Physics. An introduction to the theory of astrophysical, geophysical, and laboratory plasmas, *Cambridge University Press*, 1994.

Svalgaard, L., Geomagnetic responses to the solar wind and to solar activity, *NASA Report SP-366*, 1975.

Sugiura, M., and S. Chapman, The average morphology of geomagnetic storms with sudden commencements, *Abh. Akad. Wiss. Gottingen. Math. -Phys. K1, 4*, 1-53, 1960.

Tsunoda, R.T., High latitude irregularities: A review and synthesis, *Rev. Geophys., 26*, 719-760, 1988.

Tsyganenko, N. A., Modeling the inner magnetosphere: The asymmetric ring current and Region 2 Birkeland currents revisited, *J. Geophys. Res., 105*, 27739-27754, 10.1029/2000JA000138, 2000.

Untiedt, A. J., and W. Baumjohann, Studies of polar current systems using the IMS Scandinavian Magnetometer Array, *Space Sci. Rev., 63*, 245-390, 1993.

Vasyliunas, V. M., Interaction between the magnetospheric boundary layers and the ionosphere, in *Proceedings of the Magnetospheric Boundary Layer Symposium*, ESA SP-148, ed. B. Battrick (p. 387), Noordwijk: ESA, 1979.

Vasyliunas, V.M., Large-scale morphology of the magnetosphere, in *Solar-Terrestrial Physics: Principles and Theoretical Foundations*, Ed R.L.a.F. Carovillano, J.M., pp. 243-254, *D. Reidel Publishing Company*, Dordrecht, 1983.

Villain, J.-P., R. A. Greenwald, K. B. Baker, and J. M. Ruohoniemi, HF radar observations of E region plasma irregularities produced by oblique electron streaming, *J. Geophys. Res., 92*, 12,327-12,342, 1987.

Villain, J.-P., R. Andre, M. Pinnock, R. A. Greenwald, and C. Hanuise, A statistical study of the Doppler spectral width of high-latitude ionospheric F-region echoes recorded with SuperDARN coherent HF radars, *Ann. Geophysicae, 20*, 1769–1781, 2002.

Vorobjev, V. G., Dynamics of Hall current vortices in the daytime high-latitudes, *Geomag. Aeron., 33,* 612-620, 1994.

Watanabe, M., N. Sato, R. A. Greenwald, M. Pinnock, M. R. Hairston, R.L. Rairden, and D. J. McEwen, The ionospheric response to interplanetary magnetic field variations: Evidence for rapid global change and the role of preconditioning in the magnetosphere, *J. Geophys. Res., 105,* 22,955–22,977, 2000.

Xu, L., SuperDARN plasma convection: Comparison with other data and application to field-aligned current measurements, *Ph.D. thesis,* Univ. of Saskatchewan, Saskatoon, Saskatchewan, Canada, 2003.

Yahnin, A. G., and T. Moretto, Traveling convection vortices in the ionosphere map to the central plasma sheet, *Ann. Geophysicae, 14*, 1025-1031, 1996.

Yahnin, A. G., V. G. Vorobjev, T. Bösinger R. Rasinkangas, D. G. Sibeck, and P. T. Newell, On the source region of travelling convection vortices, *Geophys. Res. Lett., 24*, 237-240, 1997.

Zesta, E., W. J. Hughes, M. J. Engebretson, T. J. Hughes, A. J. Lazarus, and K. I. Paularena, The November 9, 1993, traveling convection vortex event: A case study, *J. Geophys. Res., 104*, 28,041-28,058, 1999.

Zhu, L., P. Gifford, J. J. Sojka, and R. W. Schunk, Model study of ground magnetic signatures of travelling convection vortices, *J. Geophys. Res., 102*, 7449-7459, 1997.

APPENDIX A

Numerical analysis of 3-D current systems

Spatial distribution of various electrodynamical parameters in the magnetosphere-ionosphere system is governed by the second order partial differential equations. Numerical solution of these equations with appropriate boundary conditions can be done in a variety of ways. In this Appendix we describe three problems that have been considered in this thesis and present details on their numerical solution. In all cases, the problem was reduced to a solution of a system of linear algebraic equations. We also analyze the accuracy of the obtained solutions.

A1: Distribution of electrostatic potential on a spherical cap

Distribution of the electric potential Φ that is established on a conducting ionosphere by a FAC flowing into it can be found by solving the elliptic boundary-value problem for the Poisson equation (3.29):

$$\begin{cases} \Sigma_P \nabla^2 \Phi + (\nabla \Sigma_P)\cdot(\nabla \Phi) + [(\nabla \Sigma_H)\times(\nabla \Phi)]_z = -j_\parallel \\ \Phi(\theta_0) = \Phi_0 \end{cases}. \qquad (A.1)$$

The potential Φ_0 is given at the circular cap border drawn at some colatitude θ_0. It is assumed that the Pedersen and Hall conductance tensor components Σ_P and Σ_H as well as the FACs $j_\parallel$ are given, too. Denote the potential being sought as u (instead of Φ, just for convenience). Because of sphericity of the problem, it is convenient to consider (A.1) in spherical coordinates; in this way the vector operators are replaced by partial derivatives:

$$\Sigma_P \cos\theta \sin\theta \frac{\partial u}{\partial \theta} + \Sigma_P \sin^2\theta \frac{\partial^2 u}{\partial \theta^2} + \Sigma_P \frac{\partial^2 u}{\partial \varphi^2} + \sin^2\theta \frac{\partial \Sigma_P}{\partial \theta}\frac{\partial u}{\partial \theta} + \frac{\partial \Sigma_P}{\partial \varphi}\frac{\partial u}{\partial \varphi} + \sin\theta \frac{\partial \Sigma_H}{\partial \theta}\frac{\partial u}{\partial \varphi} - \sin\theta \frac{\partial \Sigma_H}{\partial \varphi}\frac{\partial u}{\partial \theta} = -j_\parallel r^2 \sin^2\theta. \qquad (A.2)$$

The numerical solution to (A.2) is sought on a spherical cap with the radius θ_0 as shown in Figure A.1, covered by a grid of parallels and meridians with even angular steps: the longitudinal step h_θ and the colatitudinal step h_φ. The solution is obtained at each (i,j)-th node of the spherical grid as a set of values of the unknown function u_{ij}. A grid of m longitudes and n colatitudes results in $m \times n$ nodal variables u_{ij} and hence in a set of $m \times n$ algebraic equations for these variables. Only the u_{ij} values at interior nodes of the numerical domain are calculated in the process of the solution. The spherical cap boundary nodes are not considered as nodal variables because their values are fixed.

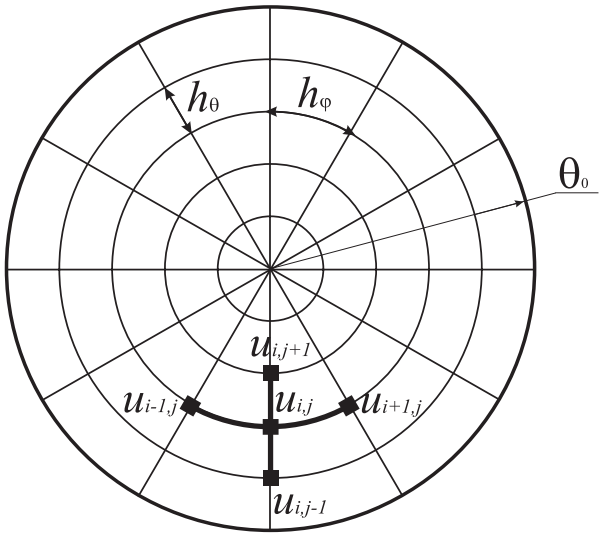

Figure A.1. Spherical cap of the radius θ_0 as a numerical domain with the spherical coordinate grid. The numerical stencil is shown as a bold cross.

The partial derivatives in equation (A.2) are approximated by appropriate difference quotients with the use of a numerical stencil shown in Figure A.1 as a bold cross. The stencil approximates the vicinity of a (*i*,*j*)-th grid point containing five closest variables: the centre u_{ij}, west $u_{i-1,j}$, east $u_{i+1,j}$, south $u_{i,j-1}$, and north $u_{i,j+1}$ neighbors. Function values at these points are sufficient to approximate any second order linear differential operator at the (*i*,*j*)-th point using the following difference quotients :

$$\frac{\partial u}{\partial \varphi}=\frac{u_{i+1j}-u_{i-1j}}{2h_\varphi};\qquad \frac{\partial u}{\partial \theta}=\frac{u_{ij+1}-u_{ij-1}}{2h_\theta};\qquad \frac{\partial^2 u}{\partial \theta^2}=\frac{u_{ij+1}-2u_{ij}+u_{ij-1}}{h_\theta{}^2}$$
$$\frac{\partial^2 u}{\partial \varphi^2}=\frac{u_{i+1j}-2u_{ij}+u_{i-1j}}{h_\varphi{}^2};\qquad \frac{\partial \Sigma^P}{\partial \theta}=\frac{\Sigma^P_{ij+1}-\Sigma^P_{ij-1}}{2h_\theta};\qquad \frac{\partial \Sigma^H}{\partial \theta}=\frac{\Sigma^H_{ij+1}-\Sigma^H_{ij-1}}{2h_\theta};\qquad (A.3)$$
$$\frac{\partial \Sigma^P}{\partial \varphi}=\frac{\Sigma^P_{i+1j}-\Sigma^P_{i-1j}}{2h_\varphi};\quad \frac{\partial \Sigma^H}{\partial \varphi}=\frac{\Sigma^H_{i+1j}-\Sigma^H_{i-1j}}{2h_\varphi}\ .$$

Replacement of the derivatives in (A.2) by the difference quotients (A.3) reduces the problem to a system of algebraic equations:

$$-8\left(h_\theta^2+h_\varphi^2\sin^2\theta\right)\Sigma^P_{ij}u_{ij}+$$
$$\left[2h_\theta h_\varphi^2\cos\theta\sin\theta\,\Sigma^P_{ij}+4h_\varphi^2\sin^2\theta\,\Sigma^P_{ij}+h_\varphi^2\sin^2\theta\left(\Sigma^P_{ij+1}-\Sigma^P_{ij-1}\right)-h_\theta h_\varphi\sin\theta\left(\Sigma^H_{i+1j}-\Sigma^H_{i-1j}\right)\right]u_{ij+1}+$$
$$\left[-2h_\theta h_\varphi^2\cos\theta\sin\theta\,\Sigma^P_{ij}+4h_\varphi^2\sin^2\theta\,\Sigma^P_{ij}+h_\varphi^2\sin^2\theta\left(\Sigma^P_{ij+1}-\Sigma^P_{ij-1}\right)+h_\theta h_\varphi\sin\theta\left(\Sigma^H_{i+1j}-\Sigma^H_{i-1j}\right)\right]u_{ij-1}+$$
$$\left[4h_\theta^2\Sigma^P_{ij}+h_\theta^2\left(\Sigma^P_{i+1j}-\Sigma^P_{i-1j}\right)+h_\theta h_\varphi\sin\theta\left(\Sigma^H_{ij+1}-\Sigma^H_{ij-1}\right)\right]u_{i+1j}+$$
$$\left[4h_\theta^2\Sigma^P_{ij}-h_\theta^2\left(\Sigma^P_{i+1j}-\Sigma^P_{i-1j}\right)-h_\theta h_\varphi\sin\theta\left(\Sigma^H_{ij+1}-\Sigma^H_{ij-1}\right)\right]u_{i-1j}=-4\,j_\parallel r^2h_\theta^2h_\varphi^2\sin^2\theta.\qquad (A.4)$$

Each (*i*,*j*)-th equation (A.4) has up to five unknowns : u_{ij}, $u_{i-1,j}$, $u_{i+1,j}$, $u_{i,j-1}$, and $u_{i,j+1}$, the potential values around the (*i*,*j*)-th node. A set of equations (A.4) written for every interior grid node makes up a system of $m\times n$ linear algebraic equations with $m\times n$ unknowns, which allows an

exact solution. It can be solved by the standard numerical methods. We used the iterative biconjugate gradient method (routine *linbcg*, *Press et al.*, [2002]).

A2: Distribution of current function on a spherical cap

In section 5.2.2 it has been shown that the current stream function Ψ satisfies the Poisson equation $\nabla^2\Psi = (\nabla\times\mathbf{J})_z$, where the right hand part is the vorticity of the ionospheric sheet currents. To solve this equation for Ψ one does not actually need to know the actual distribution of ionospheric currents **J**; instead one can involve the electric potential Φ and the conductance tensor $\hat{\Sigma}$ at every node of the numeric domain because

$$(\nabla\times\mathbf{J})_z = \Sigma_H\nabla^2\Phi + (\nabla\Sigma_H)\cdot(\nabla\Phi) - \left[(\nabla\Sigma_P)\times(\nabla\Phi)\right]_z, \tag{A.5}$$

where Σ_P and Σ_H are the Pedersen and Hall conductance tensor components (given at every node). The problem then can be formulated as the Dirichlet's problem for the Poisson equation (5.42):

$$\begin{cases} \nabla^2\Psi = \Sigma_H\nabla^2\Phi + (\nabla\Sigma_H)\cdot(\nabla\Phi) - \left[(\nabla\Sigma_P)\times(\nabla\Phi)\right]_z \\ \Psi(\theta_0) = \Psi_0 \end{cases}. \tag{A.6}$$

In (A.6), Ψ_0 is the current function specified at the spherical cap boundary, similar to the one considered in the previous section. To numerically obtain the ionospheric currents vorticity (A.5) on a grid, the difference operator should be applied to Φ and Σ. Such an operator was obtained from the right hand part of the Poisson equation in (A.6) by considering it in the spherical coordinates

$$\begin{aligned}(\nabla\times\mathbf{J})_z = \Sigma_H\nabla^2\Phi + (\nabla\Sigma_H)\cdot(\nabla\Phi) - \left[(\nabla\Sigma_P)\times(\nabla\Phi)\right]_z = \\ \frac{\Sigma_H}{r^2}\left(\frac{1}{\tan\theta}\frac{\partial u}{\partial\theta} + \frac{\partial^2 u}{\partial\theta^2} + \frac{1}{\sin^2\theta}\frac{\partial^2 u}{\partial\varphi^2}\right) + \frac{1}{r^2}\left(\frac{\partial\Sigma_H}{\partial\theta}\frac{\partial u}{\partial\theta} + \frac{1}{\sin\theta}\frac{\partial\Sigma_H}{\partial\varphi}\frac{\partial u}{\partial\varphi}\right) - , \\ \frac{1}{r^2\sin\theta}\left(\frac{\partial\Sigma_P}{\partial\theta}\frac{\partial u}{\partial\varphi} - \frac{\partial\Sigma_P}{\partial\varphi}\frac{\partial u}{\partial\theta}\right)\end{aligned} \tag{A.7}$$

and by replacing the partial derivatives by the difference quotients (A.3) in a similar to (A.2) way. The difference operator for the current vorticity (A.7) has the form:

$$\begin{aligned}(\nabla\times\mathbf{J})_z \cong \frac{\Sigma^H_{ij}}{r^2}\left(\frac{1}{\tan\theta}\frac{u_{ij+1}-u_{ij-1}}{2h_\theta} + \frac{u_{ij+1}-2u_{ij}+u_{ij-1}}{{h_\theta}^2} + \frac{1}{\sin^2\theta}\frac{u_{i+1j}-2u_{ij}+u_{i-1j}}{{h_\varphi}^2}\right) + \\ \frac{1}{r^2}\left(\frac{\Sigma^H_{ij+1}-\Sigma^H_{ij-1}}{2h_\theta}\frac{u_{ij+1}-u_{ij-1}}{2h_\theta} + \frac{1}{\sin\theta}\frac{\Sigma^H_{i+1j}-\Sigma^H_{i-1j}}{2h_\varphi}\frac{u_{i+1j}-u_{i-1j}}{2h_\varphi}\right) - \\ \frac{1}{r^2\sin\theta}\left(\frac{\Sigma^P_{ij+1}-\Sigma^P_{ij-1}}{2h_\theta}\frac{u_{i+1j}-u_{i-1j}}{2h_\varphi} - \frac{\Sigma^P_{i+1j}-\Sigma^P_{i-1j}}{2h_\varphi}\frac{u_{ij+1}-u_{ij-1}}{2h_\theta}\right) .\end{aligned} \tag{A.8}$$

Now that we know how to calculate the right hand part of the Poisson equation (A.6) we can build a difference scheme for the Laplacian on the surface of a sphere. Again, we denote the current function sought by *u* instead of Ψ, and the right hand side of equation in (A.6) as $-f$. Since the spherical Laplacian given the constant radius *r* is

$$\nabla^2 u = \frac{1}{r^2 \tan\theta}\frac{\partial u}{\partial \theta} + \frac{1}{r^2}\frac{\partial^2 u}{\partial \theta^2} + \frac{1}{r^2 \sin^2\theta}\frac{\partial^2 u}{\partial \varphi^2} \ , \tag{A.9}$$

the Poisson equation in (A.6) takes the form:

$$\frac{1}{r^2 \tan\theta}\frac{\partial u}{\partial \theta} + \frac{1}{r^2}\frac{\partial^2 u}{\partial \theta^2} + \frac{1}{r^2 \sin^2\theta}\frac{\partial^2 u}{\partial \varphi^2} = -f \ . \tag{A.10}$$

Approximating the partial derivatives by the difference quotients yields the equation

$$\begin{aligned} &-4\left(h_\theta^2 + h_\varphi^2 \sin^2\theta \right) u_{ij} + \\ &h_\varphi^2 \sin\theta \left(2\sin\theta - h_\theta \cos\theta\right) u_{ij-1} + h_\varphi^2 \sin\theta \left(2\sin\theta + h_\theta \cos\theta\right) u_{ij+1} + \\ &2h_\theta^2 u_{i-1\,j} + 2h_\theta^2 u_{i+1\,j} = -2r^2 h_\theta^2 h_\varphi^2 \sin^2\theta \cdot f_{ij} \quad . \end{aligned} \tag{A.11}$$

This is a linear algebraic equation with up to five unknowns: u_{ij}, $u_{i-1,j}$, $u_{i+1,j}$, $u_{i,j-1}$, and $u_{i,j+1}$, which are the current function values from the (i,j)-th node vicinity. A linear system composed of $m \times n$ equations for each of the $m \times n$ interior nodes can be solved for a vector containing the values of current function at every interior node.

A3: Calculations of FACs from known potential and conductance on a spherical cap

The elliptical equation (A.1) can be used in a reversed way. Namely, if the potential and conductances are known, the FACs $j_\parallel$ associated with them can be calculated as

$$-j_\parallel = \Sigma_P \nabla^2 \Phi + (\nabla \Sigma_P)\cdot(\nabla \Phi) + [(\nabla \Sigma_H)\times(\nabla \Phi)]_z \ . \tag{A.12}$$

The FACs are calculated by applying the right-hand-part vector operator to the potential distribution Φ. Rewriting (A.12) in explicit partial derivatives gives:

$$\begin{aligned} -j_\parallel = \ & \frac{\Sigma_P}{r^2}\left(\frac{1}{\tan\theta}\frac{\partial u}{\partial \theta} + \frac{\partial^2 u}{\partial \theta^2} + \frac{1}{\sin^2\theta}\frac{\partial^2 u}{\partial \varphi^2} \right) + \frac{1}{r^2}\left(\frac{\partial \Sigma_P}{\partial \theta}\frac{\partial u}{\partial \theta} + \frac{1}{\sin\theta}\frac{\partial \Sigma_P}{\partial \varphi}\frac{\partial u}{\partial \varphi} \right) + \\ & \frac{1}{r^2 \sin\theta}\left(\frac{\partial \Sigma_H}{\partial \theta}\frac{\partial u}{\partial \varphi} - \frac{\partial \Sigma_H}{\partial \varphi}\frac{\partial u}{\partial \theta} \right) \quad . \end{aligned} \tag{A.13}$$

After replacing partial derivatives by the difference quotients (A.3), we get the formula for the numerical calculation of the FACs at an (i,j)-th grid node:

$$\begin{aligned} j_\parallel^{i,j} \cong & \frac{\Sigma_{ij}^P}{r^2}\left(\frac{1}{\tan\theta}\frac{u_{ij+1} - u_{ij-1}}{2h_\theta} + \frac{u_{ij+1} - 2u_{ij} + u_{ij-1}}{{h_\theta}^2} + \frac{1}{\sin^2\theta}\frac{u_{i+1\,j} - 2u_{ij} + u_{i-1\,j}}{{h_\varphi}^2} \right) + \\ & \frac{1}{r^2}\left(\frac{\Sigma_{ij+1}^P - \Sigma_{ij-1}^P}{2h_\theta}\frac{u_{ij+1} - u_{ij-1}}{2h_\theta} + \frac{1}{\sin\theta}\frac{\Sigma_{i+1\,j}^P - \Sigma_{i-1\,j}^P}{2h_\varphi}\frac{u_{i+1\,j} - u_{i-1\,j}}{2h_\varphi} \right) - \\ & \frac{1}{r^2 \sin\theta}\left(\frac{\Sigma_{ij+1}^H - \Sigma_{ij-1}^H}{2h_\theta}\frac{u_{i+1\,j} - u_{i-1\,j}}{2h_\varphi} - \frac{\Sigma_{i+1\,j}^H - \Sigma_{i-1\,j}^H}{2h_\varphi}\frac{u_{ij+1} - u_{ij-1}}{2h_\theta} \right) \quad . \end{aligned} \tag{A.14}$$

A4: Precision of the numerical solutions

The numerical solution of the elliptic equations on a grid has inherent sources of errors. The machine rounding error is small enough: modern computers allow calculations at the

absolute precision of ~10^{-16} (called also "machine epsilon"). More serious danger for the solution is originated from poorly conditioned matrix of the linear system. The methods that we use are implicit; for $m\times n$ nodes, a linear system of the order of $(m\times n)^2$ is to be solved. If this system has the matrix with too high a condition number, say ~10^{-13}, then its solution on a computer with machine epsilon at 10^{-16} would have only 16-13=3 significant digits. Of course, the conditional numbers may be monitored in the course of solution. However, the major systematic errors arise from the approximation of the differential operator by the combination of difference quotients (A.3).

In our estimation of the error in the solution due to approximation we do not take into account the boundary conditions since they are considered to be specified exactly. Expansion of the solution for $u_{i,j}$ within a vicinity of (i,j)-th node into the Taylor series with the remainder term gives:

$$u_{i,j\pm1} = u_{i,j} \pm h_\theta u_\theta^{i,j} + \frac{1}{2}h_\theta^2 u_{\theta\theta}^{i,j} \pm \frac{1}{6}h_\theta^3 u_{\theta\theta\theta}^{i,j} + \frac{1}{24}h_\theta^4 u_{\theta\theta\theta\theta}^{i,j}\left(\varphi_i, \eta_{j\pm1}\right), \tag{A.15a}$$

$$u_{i\pm1,j} = u_{i,j} \pm h_\varphi u_\varphi^{i,j} + \frac{1}{2}h_\varphi^2 u_{\varphi\varphi}^{i,j} \pm \frac{1}{6}h_\varphi^3 u_{\varphi\varphi\varphi}^{i,j} + \frac{1}{24}h_\varphi^4 u_{\varphi\varphi\varphi\varphi}^{i,j}\left(\xi_{i\pm1}, \theta_j\right), \tag{A.15b}$$

where h_θ and h_φ are steps along colatitude and longitude. In the remainder the $\eta_{j\pm1}$ and $\xi_{i\pm1}$ are some intermediate points such that $\varphi_{i-1} < \xi_{i-1} < \varphi_i < \xi_{i+1} < \varphi_{i+1}$ and $\theta_{i-1} < \eta_{i-1} < \theta_i < \eta_{i+1} < \theta_{i+1}$.

Hereafter we assume that
$u_{\theta\theta\theta\theta}^{i,j}\left(\varphi_i, \eta_{j\pm1}\right) \approx u_{\theta\theta\theta\theta}^{i,j}\left(\varphi_i, \theta_j\right) = u_{\theta\theta\theta\theta}^{i,j}$ and $u_{\varphi\varphi\varphi\varphi}^{i,j}\left(\xi_{i\pm1}, \theta_j\right) \approx u_{\varphi\varphi\varphi\varphi}^{i,j}\left(\varphi_i, \theta_j\right) = u_{\varphi\varphi\varphi\varphi}^{i,j}$.
Using (A.3) we can write down the approximations for the difference quotients:

$$\begin{aligned}
\frac{u_{i,j+1} - 2u_{i,j} + u_{i,j-1}}{h_\theta^2} &\approx \frac{1}{h_\theta^2}\left(h_\theta^2 u_{\theta\theta}^{i,j} + \frac{1}{12}h_\theta^4 u_{\theta\theta\theta\theta}^{i,j}\right)\\
\frac{u_{i+1,j} - 2u_{i,j} + u_{i-1,j}}{h_\varphi^2} &\approx \frac{1}{h_\varphi^2}\left(h_\varphi^2 u_{\varphi\varphi}^{i,j} + \frac{1}{12}h_\theta^4 u_{\varphi\varphi\varphi\varphi}^{i,j}\right)\\
\frac{u_{i,j+1} - u_{i,j-1}}{2h_\theta} &= \frac{1}{2h_\theta}\left(2h_\theta u_\theta^{i,j} + \frac{1}{3}h_\theta^3 u_{\theta\theta\theta}^{i,j}\right)\\
\frac{u_{i+1,j} - u_{i-1,j}}{2h_\varphi} &= \frac{1}{2h_\varphi}\left(2h_\varphi u_\varphi^{i,j} + \frac{1}{3}h_\varphi^3 u_{\varphi\varphi\varphi}^{i,j}\right).
\end{aligned} \tag{A.16}$$

The approximations for conductances Σ_P and Σ_H are similar.

The differential equation can be represented as $Au = f$, A being a differential operator, $A_h u = f$ its difference approximation, and A_h the difference operator. By denoting the approximation error at (i,j)-th node as $\psi_{i,j}$, where

$$\psi = Au - A_h u_h, \tag{A.17}$$

and the error in solution as

$$\varepsilon = u - u_h, \tag{A.18}$$

the following theorem [*Kalitkin*, 1980] can be used to estimate the error in solution ε using the approximation error ψ.

Theorem A.1. Let the operators A and A_h be linear and A_h approximate A so that there exists the limit

$$\overline{\psi} = \lim_{h\to 0} h^{-p}\psi . \tag{A.19}$$

Then the error in the solution has the asymptotics

$$\varepsilon = h^p \bar{z} + o\left(h^p\right), \tag{A.20}$$

where $\bar{z}$ is the solution to the equation

$$A\bar{z} = \overline{\psi} . \tag{A.21}$$

A4.1: Error estimate for the spherical Poisson equation numerical solution

Substitution of the Taylor approximations for derivatives (A.16) into the expression for the approximation error (A.17) gives

$$\psi_{i,j} = \nabla^2 u - \nabla_h^2 u_h = -\frac{1}{12r^2}\left(\frac{2}{tg\theta_j} h_\theta^2 u_{\theta\theta\theta}^{i,j} + h_\theta^2 u_{\theta\theta\theta\theta}^{i,j} + \frac{1}{\sin^2\theta} h_\varphi^2 u_{\varphi\varphi\varphi\varphi}^{i,j}\right). \tag{A.22}$$

Changing the angular variables for the metric variables using

$$h_\varphi = \frac{h}{r\sin\theta} \text{ and } h_\theta = \frac{h}{r}, \tag{A.23}$$

where for simplicity the metric steps along both dimensions are assumed the same and equal h, yields:

$$-\psi_{i,j} = \frac{h^2}{12r^4}\left(\frac{2}{tg\theta_j} u_{\theta\theta\theta}^{i,j} + u_{\theta\theta\theta\theta}^{i,j} + \frac{1}{\sin^4\theta} u_{\varphi\varphi\varphi\varphi}^{i,j}\right) . \tag{A.24}$$

The limit (A.19) then is

$$-\overline{\psi}_{i,j} = -\lim_{h\to 0} h^{-2}\psi_{i,j} = \frac{1}{12r^4}\left(\frac{2}{tg\theta_j} u_{\theta\theta\theta}^{i,j} + u_{\theta\theta\theta\theta}^{i,j} + \frac{1}{\sin^4\theta} u_{\varphi\varphi\varphi\varphi}^{i,j}\right). \tag{A.25}$$

Let us introduce the characteristic scale length λ (again, we assume the same scale length for both dimensions). In order to rougly estimate the derivatives in relation to this scale, we assume the following relationships:

$$\lambda_\theta = \frac{\lambda}{r}; \quad \lambda_\varphi = \frac{\lambda}{r\sin\theta}; \quad \frac{\partial^n u}{\partial\theta^n} = \frac{r^n}{\lambda^n} u ; \quad \frac{\partial^n u}{\partial\varphi^n} = \frac{r^n \sin^n\theta}{\lambda^n} u . \tag{A.26}$$

Using these, we can find $\bar{z}$ as a solution to the equation (A.21), here $\nabla^2\bar{z} = -\overline{\psi}$:

$$\nabla^2\bar{z} \approx \left(\frac{1}{r\tan\theta}\frac{1}{\lambda} + 2\frac{1}{\lambda^2}\right)\bar{z} , \tag{A.27a}$$

$$-\overline{\psi} \approx \frac{1}{6}\left(\frac{1}{r\tan\theta}\frac{1}{\lambda^3} + \frac{1}{\lambda^4}\right)\bar{u} , \text{ so} \tag{A.27b}$$

$$\left(\frac{1}{r\tan\theta}\frac{1}{\lambda} + 2\frac{1}{\lambda^2}\right)\bar{z} = \frac{1}{6}\left(\frac{1}{r\tan\theta}\frac{1}{\lambda^3} + \frac{1}{\lambda^4}\right)\bar{u} . \tag{A.27c}$$

We assume that the characteristic length scale is significantly less than the earth's radius $r = R_E$. Therefore

$$\bar{z} = \lim_{r\to\infty} \frac{\frac{1}{6}\left(\frac{1}{r\tan\theta}\frac{1}{\lambda^3}+\frac{1}{\lambda^4}\right)\bar{u}}{\left(\frac{1}{r\tan\theta}\frac{1}{\lambda}+2\frac{1}{\lambda^2}\right)} = \frac{1}{12}\frac{1}{\lambda^2}\bar{u}\,, \tag{A.28}$$

and we get the solution error estimate (A.20) as

$$\varepsilon = h^2\frac{1}{12}\frac{1}{\lambda^2}\bar{u} + o\left(h^2\right)\,. \tag{A.29}$$

This result says that on the scale length equal to grid step the numerical solution may be by 1/12 = 8.33% different from the exact solution. However, if one sets the grid step equal to 1/3 of the characteristic scale, then the solution error becomes less than 1%, because 1/(12x9) = 0.9%.

A4.2. Error estimate for the spherical elliptic equation numerical solution

We start from the equation

$$\Sigma_P\nabla^2\Phi + (\nabla\Sigma_P)\cdot(\nabla\Phi) + [(\nabla\Sigma_H)\times(\nabla\Phi)]_z = -j_\parallel \tag{A.30}$$

that can be represented in the form $Au = -j_\parallel$, where

$$Au = \Sigma_P\nabla^2 u + (\nabla\Sigma_P)\cdot(\nabla u) + [(\nabla\Sigma_H)\times(\nabla u)]_z\,. \tag{A.31}$$

Substituting the derivative Taylor approximations (A.16) into the expression for the approximation error (A.17) one obtains

$$\psi_{i,j} = Au - A_h u_h = -\frac{h_\theta^2}{12r^2}\left(2\frac{\Sigma^P}{\tan\theta_j}u^{i,j}_{\theta\theta\theta} + \Sigma^P u^{i,j}_{\theta\theta\theta\theta} + 2\Sigma^P_\theta u^{i,j}_{\theta\theta\theta} - 2\frac{\Sigma^H_\varphi}{\sin\theta}u^{i,j}_{\theta\theta\theta}\right) - \frac{h_\varphi^2}{12r^2\sin^2\theta_j}\left(\Sigma^P u^{i,j}_{\varphi\varphi\varphi\varphi} + 2\Sigma^P_\varphi u^{i,j}_{\varphi\varphi\varphi} - 2\sin\theta_j\Sigma^H_\theta u^{i,j}_{\varphi\varphi\varphi}\right)\,. \tag{A.32}$$

Changing the angular variables for the metric variables using

$$h_\varphi = \frac{h}{r\sin\theta} \text{ and } h_\theta = \frac{h}{r}, \tag{A.33}$$

and assuming for simplicity that the metric steps *h* along both dimensions are the same and equal, yields

$$\psi_{i,j} = \frac{h^2}{12r^4}\left(2\frac{\Sigma^P}{\tan\theta_j}u^{i,j}_{\theta\theta\theta} + \Sigma^P u^{i,j}_{\theta\theta\theta\theta} + 2\Sigma^P_\theta u^{i,j}_{\theta\theta\theta} - 2\frac{\Sigma^H_\varphi}{\sin\theta}u^{i,j}_{\theta\theta\theta}\right) + \frac{h^2}{12r^4\sin^4\theta_j}\left(\Sigma^P u^{i,j}_{\varphi\varphi\varphi\varphi} + 2\Sigma^P_\varphi u^{i,j}_{\varphi\varphi\varphi} - 2\sin\theta_j\Sigma^H_\theta u^{i,j}_{\varphi\varphi\varphi}\right) \tag{A.34}$$

Similarly, by introducing the characteristic scale length λ, one obtains

$$\lambda_\theta = \frac{\lambda}{r};\quad \lambda_\varphi = \frac{\lambda}{r\sin\theta};\quad \frac{\partial^n u}{\partial\theta^n} = \frac{r^n}{\lambda^n}u;\quad \frac{\partial^n u}{\partial\varphi^n} = \frac{r^n\sin^n\theta}{\lambda^n}u\,. \tag{A.35}$$

Using these, one can find $\bar{z}$ as a solution to the equation (A.21):

$$A\bar{z} \approx \left(\frac{\Sigma^P}{r\tan\theta}\frac{1}{\lambda} + 4\Sigma^P\frac{1}{\lambda^2}\right)\bar{z}\,, \tag{A.36a}$$

$$-\overline{\psi} \approx \frac{1}{12}\left(2\frac{\Sigma^P}{r\tan\theta}\frac{1}{\lambda^3}+6\Sigma_P\frac{1}{\lambda^4}\right)\overline{u}\text{ , so} \tag{A.36a}$$

$$\left(\frac{\Sigma^P}{r\tan\theta}\frac{1}{\lambda}+4\Sigma^P\frac{1}{\lambda^2}\right)\overline{z}=\frac{h^2}{12}\left(2\frac{\Sigma^P}{r\tan\theta}\frac{1}{\lambda^3}+6\Sigma_P\frac{1}{\lambda^4}\right)\overline{u} \tag{A.36c}$$

By assuming that the characteristic length scale is significantly less than the earth's radius $r = R_E$, one arrives to

$$\overline{z}=\lim_{r\to\infty}\frac{\frac{1}{12}\left(2\frac{\Sigma^P}{r\tan\theta}\frac{1}{\lambda^3}+6\Sigma_P\frac{1}{\lambda^4}\right)}{\left(\frac{\Sigma^P}{r\tan\theta}\frac{1}{\lambda}+4\Sigma^P\frac{1}{\lambda^2}\right)}\overline{u}=\frac{1}{8}\frac{1}{\lambda^2}\overline{u}\,, \tag{A.37}$$

and the solution error estimate (A.20) as:

$$\varepsilon = h^2\frac{1}{8}\frac{1}{\lambda^2}\overline{u}+o\left(h^2\right)\,. \tag{A.38}$$

Equation (A.37) means that to ensure the solution precision at the level less than 1% the step h must be shorter than 0.28λ. For $h = (1/4)\lambda$, the error is 1/(8x16)=0.8%.

APPENDIX B

Zenith angle as function of coordinates and time of year and position of the solar terminator

The zenith angle χ is the angle between the incident sunlight direction and the vector normal to the point of the incidence. Generally, the zenith angle depends on the latitude λ the longitude φ and the time of a year *t*. We can consider the sunlight beams everywhere parallel to the line connecting the sun and the earth centres. Therefore, at each geographical point (λ,φ) the zenith angle will be defined as the angle between two unit vectors: the vector **g = g**$(1,\lambda,\varphi)$ and the vector **s**, pointing at the sun. Here we derive the formula for the cosine of zenith angle through several coordinate transformations reducing the vectors **g** and **s** to the same coordinate system.

Denote the frequency of diurnal earth rotation around its axis as ω and the frequency of its annual rotation around the sun as ν:

$$\omega = 2\pi / 31557600 \text{ s}^{-1}, \quad \nu = 2\pi / 86400 \text{ s}^{-1}, \tag{A.1}$$

where 86400 = 24*3600 is the number of seconds in one day, and 31557600 = 365.25*86400 is the number of seconds in one revolution of the earth around the sun.

Determine the coordinates of **g** in the geographical coordinate system (GEO) system *XYZ*. Its *Z* axis is the earth's axis of rotation:

$$\begin{cases} x = \cos\lambda\cos\varphi \\ y = \cos\lambda\sin\varphi \\ z = \sin\lambda \end{cases}. \tag{A.2}$$

We first find the coordinates of **g** in the system $X'Y'Z'$, whose Z' axis is the same as *Z*, but the X' axis is always in the plane containing the Z' axis and the sun-earth line. Using the rotational matrix we take into account the earth's diurnal rotation:

$$\begin{pmatrix} x' \\ y' \\ z' \end{pmatrix} = \begin{pmatrix} \cos\omega t & -\sin\omega t & 0 \\ \sin\omega t & \cos\omega t & 0 \\ 0 & 0 & 1 \end{pmatrix} \cdot \begin{pmatrix} x \\ y \\ z \end{pmatrix}. \tag{A.3}$$

To find the coordinates in the right-handed orthogonal system $X''Y''Z''$, whose X'' axis points toward the sun, the Z'' axis lies in the $X''Z$ plane, and the Y'' axis points duskward, consider the annual variation of the angle α between the axis of rotation, *Z* and the GSE Z'' axis:

$$\begin{cases} \sin\alpha = \sin\alpha_0\cos\nu t \\ \cos\alpha = -\sqrt{1-\left(\sin\alpha_0\cos\nu t\right)^2} \end{cases}, \tag{A.4}$$

where α_0 = 23.45° is the Eart's axis inclination angle. The "minus" sign in front of the square root symbol means that in the earth initial position at the winter solstice the earth's axis is inclined

"from" the sun and its projection on the X'' axis is negative (and maximum). The transformation is rotation around Y' by the angle α:

$$\begin{pmatrix} z'' \\ x'' \end{pmatrix} = \begin{pmatrix} \cos\alpha & \sin\alpha \\ -\sin\alpha & \cos\alpha \end{pmatrix} \cdot \begin{pmatrix} z' \\ x' \end{pmatrix}. \qquad \text{(A.5)}$$

$$y' = y'$$

Substitutions of the **g** coordinates into all the transformation yields the formula for x'':

$$\begin{aligned} x'' &= \left(\cos\lambda\cos\varphi\cos\omega t - \sin\lambda\sin\varphi\sin\omega t\right)\cos\alpha - \sin\lambda\sin\alpha \\ &= -\cos\lambda\cos\left(\varphi+\omega t\right)\sqrt{1-\left(\sin\alpha_0\cos\nu t\right)^2} - \sin\lambda\sin\alpha_0\cos\nu t \end{aligned} . \qquad \text{(A.6)}$$

The cosine of zenith angle is determined from the **s** and **g** scalar product

$$\mathbf{s}\cdot\mathbf{g} = |s||g|\cos\chi\,, \qquad \text{(A.7)}$$

where $\mathbf{s} = \|1,\ 0,\ 0\|$, and $\mathbf{g} = \|x'',\ y'',\ z''\|$, both being vectors of unit length. Therefore $|s||g| = 1$ and $\cos\chi = \mathbf{s}\cdot\mathbf{g} = x''$. Eventually we get the formula

$$\cos\chi = -\cos\lambda\cos\left(\varphi+\omega t\right)\sqrt{1-\left(\sin\alpha_0\cos\nu t\right)^2} - \sin\lambda\sin\alpha_0\cos\nu t \quad . \qquad \text{(A.8)}$$

This formula allows one to calculate cosine of the zenith angle for any point of the earth or the ionosphere at any second of a year.

Using the zenith angle formula (A.8), one can derive the equation for the latitude and longitude at any point of the terminator. Defining the terminator as locus with the latitudes and longitudes in radians $(\lambda_{term}, \varphi_{term})$ where the zenith angle χ is zero, gives

$$\sin\lambda_{term}\sin\alpha_0\cos\nu t = -\cos\lambda_{term}\cos\left(\varphi_{term}+\omega t\right)\sqrt{1-\left(\sin\alpha_0\cos\nu t\right)^2}\,, \qquad \text{(A.9)}$$

and, after appropriate grouping, one obtains

$$\lambda_{term} = -\arctan\left(\frac{\cos\left(\varphi_{term}+\omega t\right)\sqrt{1-\left(\sin\alpha_0\cos\nu t\right)^2}}{\sin\alpha_0\cos\nu t}\right). \qquad \text{(A.10)}$$

APPENDIX C

Ionospheric conductance models and their modifications

The ionospheric conductance depends strongly on the height profile of the ionization (Figure 1.7). There are two major ionization factors: the solar radiation and particle precipitation. The ionospheric conductance due to precipitation is highly variable; its values span two orders of magnitude from fractions of Siemens up to tens of Siemens. The photoconductance due to the solar radiation is very stable and predictable. It is possible to consider the solar photoconductance as a large-scale background against which the precipitation conductance variations of smaller scale are added. All currently available instruments provide local measurements of the conductance while for studies of the large-scale high-latitude electrodynamics, such as calculations of the FACs, current function, and potential, the conductance distribution over the globe is required. Having no chances to measure the conductance distribution of the high-latitude ionosphere, we considered in this thesis only the photoconductance implying that the obtained result are only applicable to relatively quiet conditions.

Two models of the solar photoconductance were considered: an earlier one by *Robinson and Vondrak* [1984] and a newer one by *Moen and Brekke* [1993]. Both these models describe the photoconductance as a function of the zenith angle χ and solar power flux at wavelength 10.7 cm (in units of 10^{-22} W/m^2), S_a. The solar radiation at this wavelength depends on the solar activity and typically takes values from 60 to 240.

According to the models, the ionospheric conductance is proportional to square root of the cosine of the zenith angle χ. This means that the conductance has infinite gradient at the terminator where the χ equals zero, which is unphysical. To make the models more realistic we have considered replacement of the cosine square root by a cut of the Gaussian distribution function within several degrees vicinity of the terminator. The initial conductance function and the Gaussian "bell-shaped" curve were merged so that both their values and their first spatial derivatives are equal at the seam. The merging parameters were, of course, different for the models.

C1: Robinson-Vondrak conductance model

The Hall and Pedersen ionospheric conductances in this model are

$$\begin{aligned} \Sigma_P &= 0.88\sqrt{S_a \cos\chi} \\ \Sigma_H &= 1.50\sqrt{S_a \cos\chi} \end{aligned} . \qquad \text{(C.1)}$$

The solar zenith angle χ (an angle between the normal to ionosphere and the direction towards the sun) changes from negative to positive values with the motion along a meridian. The

Robinson-Vondrak model assumes zero conductance beyond the interval [-90°;+90°], as shown by solid curve in Figure C.1.

In order to remove the singularity at the points $\chi = \pm 90°$ we introduced a smooth "Gaussian-like" decrease of the conductance over the transition region from sunlit to dark ionospheres. Mathematically it means merging of the conductance function with the Gaussian function $G = Ce^{-k\left(\chi^2 - \chi_0^2\right)}$

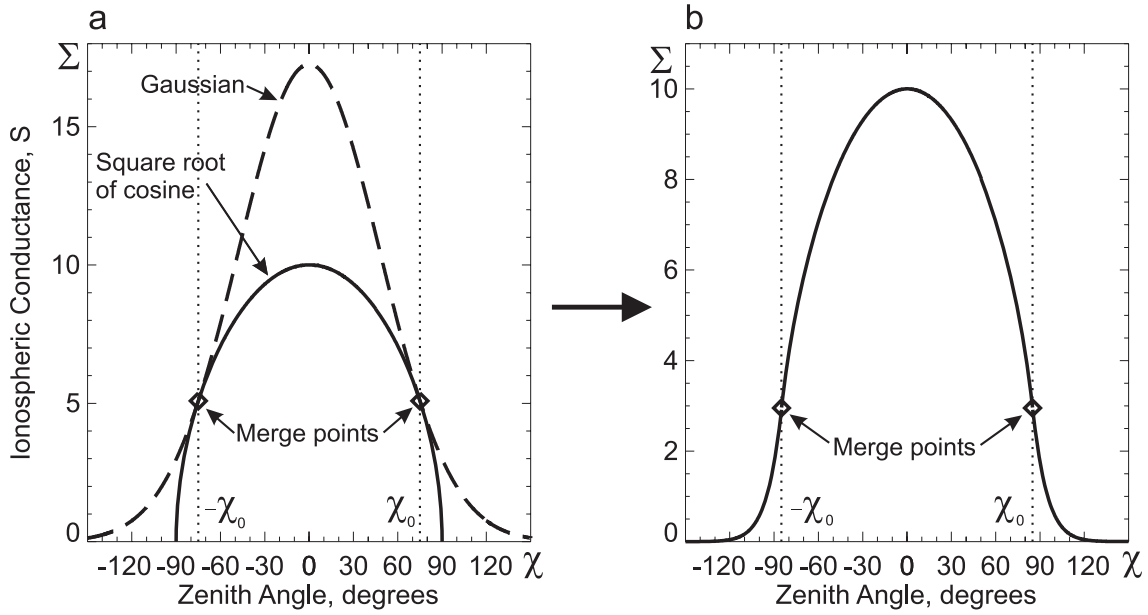

Figure C.1. a) The ionospheric conductance as dependent on the zenith angle according to the Robinson-Vondrak model (solid curve) and the fitted Gaussian curve to ensure the smooth conductance fall off in the terminator region. b) Same functions merged at the points several degrees away from the terminator.

(shown as dashed curve in Figure C.1a) at the points $\pm\chi_0$. After the merging, the conductance will change according to Robinson-Vondrak model within the limits $[-\chi_0;\chi_0]$ and according to the Gaussian function beyond the interval, as shown in Figure C.1b. For the resultant curve to be smooth at the merge points both functions and their first derivatives must have the same values.

To find the parameters C and k satisfying the merging conditions, we first equate the conductance values at $\chi = \pm\chi_0$. This gives

$$C = \sqrt{S_a \cos\chi_0}\,. \tag{C.2}$$

Equality of the first derivatives at $\chi = \pm\chi_0$ yields

$$-\frac{S_a \sin\chi_0}{2\sqrt{S_a \cos\chi_0}} = -2\sqrt{S_a \cos\chi_0}\cdot k\chi_0 e^{-k\left(\chi_0^2 - \chi_0^2\right)}, \tag{C.3}$$

which after solving for *k* gives

$$k = \frac{\tan\chi_0}{4\chi_0}. \tag{C.4}$$

Finally, the Gaussian function $G = Ce^{-k\left(\chi^2 - \chi_0^2\right)}$ smoothly merging with the conductance function (C.1) is

$$G(\chi)=\sqrt{S_a\cos\chi}\,e^{-\frac{\tan\chi_0}{4\chi_0}\left(\chi^2-\chi_0^2\right)}. \tag{C.5}$$

Figure C.1b shows the resultant curve.

The conductivity of the night side ionosphere is non-zero, it is ~1 S for the quiet, precipitation-free conditions. This background conductance was added by introducing the terms Σ_P^0 and Σ_H^0 so that the modified Robinson-Vondrak model takes the form

$$\begin{aligned}
&\Sigma_P=\Sigma_P^0+0.88\Sigma(\chi), \quad \chi<\chi_0\\
&\Sigma_P=\Sigma_P^0+0.88G(\chi), \quad \chi>\chi_0\\
&\Sigma_H=\Sigma_H^0+1.50\Sigma(\chi), \quad \chi<\chi_0\\
&\Sigma_H=\Sigma_H^0+1.50G(\chi), \quad \chi>\chi_0
\end{aligned}, \tag{C.6}$$

where

$$\Sigma(\chi)=\sqrt{S_a\cos\chi}\,. \tag{C.7}$$

C2: Moen-Brekke conductance model

The ionospheric conductances in this model are given as

$$\begin{aligned}
&\Sigma_P=S_a^{0.49}\left(0.34\cos\chi+0.93\sqrt{\cos\chi}\right)\\
&\Sigma_H=S_a^{0.53}\left(0.81\cos\chi+0.54\sqrt{\cos\chi}\right)
\end{aligned}. \tag{C.8}$$

To find the Gaussian functions $G=Ce^{-k\left(\chi^2-\chi_0^2\right)}$ merged with the conductance functions (C.7) at the points $\chi=\pm\chi_0$ we used the common template for $\Sigma(\chi)$:

$$\Sigma(\chi)=p\cos\chi+q\sqrt{\cos\chi}\,. \tag{C.9}$$

Equality of values for $\Sigma(\chi)$ and $G(\chi)$ means that

$$C=p\cos\chi_0+q\sqrt{\cos\chi_0}\,. \tag{C.10}$$

Equality of the first derivatives of $\Sigma(\chi)$ and $G(\chi)$ at the points $\chi=\pm\chi_0$ leads to the equations

$$-p\sin\chi_0+q\frac{\sin\chi_0}{2\sqrt{\cos\chi_0}}=-2\left(p\cos\chi_0+q\sqrt{\cos\chi_0}\right)k\chi_0e^{-k\left(\chi_0^2-\chi_0^2\right)}, \tag{C.11}$$

whose solution for k is

$$k=\frac{p\sin\chi_0+q\dfrac{\sin\chi_0}{2\sqrt{\cos\chi_0}}}{2\chi_0\left(p\cos\chi_0+q\sqrt{\cos\chi_0}\right)}. \tag{C.12}$$

The Gaussian function merging smoothly with the conductance function at the points $\chi=\pm\chi_0$ is therefore

$$G(\chi)=\left(p\cos\chi_0+q\sqrt{\cos\chi_0}\right)\cdot\exp\left(-\frac{p\sin\chi_0+q\dfrac{\sin\chi_0}{2\sqrt{\cos\chi_0}}}{2\chi_0\left(p\cos\chi_0+q\sqrt{\cos\chi_0}\right)}\left(\chi^2-\chi_0^2\right)\right). \tag{C.13}$$

The conductivity of the night side ionosphere is non-zero, amounting in absence of the auroral precipitations. Allowing of the background conductance of ~1 S for Σ_P^0 and Σ_H^0, leads to the modified Moen-Brekke model in the form

$$\begin{aligned}
\Sigma_P &= \Sigma_P^0 + S_a^{0.49}\Sigma(\chi), \quad \chi < \chi_0 \\
\Sigma_P &= \Sigma_P^0 + S_a^{0.49}G(\chi), \quad \chi > \chi_0 \\
\Sigma_H &= \Sigma_H^0 + S_a^{0.53}\Sigma(\chi), \quad \chi < \chi_0 \\
\Sigma_H &= \Sigma_H^0 + S_a^{0.53}G(\chi), \quad \chi > \chi_0
\end{aligned}, \tag{C.14}$$

where $\Sigma(\chi)$ is given in (C.9).